CATALYTIC REDOX REACTIONS OF NITRIC OXIDE AND CARBON MONOXIDE OVER MIXED METAL OXIDE NANOPARTICLES

THESIS

Submitted to the **Goa University**

For the degree of

DOCTOR OF PHILOSOPHY

IN CHEMISTRY

By

Mr. Rahul D. Kerkar

Research Scholar

School of Chemical Sciences,

Goa University

Under the Guidance

of

Prof. A.V. Salker

School of Chemical Sciences

Goa University, Goa 403206, India

SEPTEMBER 2020

DECLARATION

I hereby declare that the work presented in the thesis entitled "**Catalytic redox reactions of nitric oxide and carbon monoxide over mixed metal oxide nanoparticles**" is the result of investigations carried out by me under the guidance of **Prof. A.V. Salker** at Department of Chemistry, Goa University and that it has not previously formed the basis for the award of any degree or diploma or other similar titles.

In keeping with the general practice of reporting scientific observations, due acknowledgement has been made wherever the work described is based on the findings of other investigations. I further state that the thesis has been prepared by me and it is my original work and free of any plagiarism. This document has been duly checked through a Plagiarism detection tool approved by the Goa University and confirms to the provisions of OA-19.

Mr. Rahul D. Kerkar
Research Student
School of Chemical Sciences
Goa University
Goa - 403206, India.

SCHOOL OF CHEMICAL SCIENCES

CERTIFICATE

This is to certify that the thesis entitled, "**Catalytic redox reactions of nitric oxide and carbon monoxide over mixed metal oxide nanoparticles**" submitted by **Mr. Rahul Damu Kerkar**, for the award of Doctor of Philosophy in Chemistry is a record of research work carried out by the candidate during the period of study under my supervision and that it has not previously formed the basis for the award of any degree or diploma or other similar titles.

Prof. A.V. Salker
Research Guide
School of chemical Sciences
Goa University
Goa - 403206, India
September 2020

ACKNOWLEDGEMENT

I have achieved a milestone in my life not only because of my hard work, but the credit goes to all the people who have made me what I am today. Thus, let me accept this opportunity to express gratitude toward every last one, who has been a part of this PhD journey and have helped me complete this endeavor.

First and the foremost, I would like to thank my supervisor and mentor ***Prof. A. V. Salker,*** *who with exemplary work and ethics has guided me throughout my thesis tenure in Goa University. You are a true example of how the qualities of perseverance, hard-work, and sincerity towards work can lead oneself to a succeeding career. Working under your guidance has made me grow not only professionally but intellectually as well.*

I would like to thank my subject expert ***Prof. V. M. S. Verenkar*** *and* ***Dr. S. N. Dhuri*** *for their scientific and motivational support. I thank to all my teachers from School of Chemical sciences,* ***Prof. B.R. Srinivasan, Prof. V.S. Nadkarni, Prof. R.N. Shirsat, Prof. J.B. Fernandes, and Prof. S.G. Tilve*** *for the timely help and constant encouragement. In person I deeply thank to* ***Dr. R. K. Kunkalkar, Dr. Mahesh Majik, Dr. Sandeep Dey, Dr. P. P. Morajkar****,and* ***Dr. G. Santosh*** *for their constant support, help and encouragement.*

I wish to thank ***Prof. Varun Sahni****, Hon'ble Vice chancellor, Goa University and* ***Prof. Y. V. Reddy****, Registrar, Goa University, for their valuable support. Also, I would like to thank* ***Dr. Satish Shetye****, Former Vice chancellor, Goa University and* ***Prof. Vijayendra P. Kamat,*** *former Registrar of Goa University.*

I am grateful to my department and Goa University for providing equipments and space in the infrastructure. I am also thankful to entire teaching and non-teaching staff of School of Chemical Sciences-Goa University, for the necessary help whenever asked for.

A sincere thanks to ***UGC-New Delhi*** *for providing me* ***RGNF Fellowship*** *and also* ***UGC-CSIR*** *for providing* ***NET-JRF****.*

In person I deeply thank ***Mr. G. Prabhu****, NIO for all the XRD characterization,* ***Mr. Lanjewar****, USIC, Goa University for SEM characterizations,* ***Mr. Agnelo Lopes*** *from the*

glass blowing section, ***Mr. Jagadish*** *for helping in surface studies,* ***SAIF Bombay*** *for TEM studies and* ***SAIF Kanpur*** *for XPS analysis.*

I owe my greatest gratitude toward my senior research colleagues ***Dr. Mira, Dr. Shambu, Dr. Mithil, Dr. Madhavi, Dr. Celia and Dr. Sudershana*** *for motivating and helping me during my PhD and also teaching various instrumental techniques. I would also like to thank all my other senior colleagues at the department* ***Dr. Daniel, Dr. Satu, Dr. Savita, Dr. Rita, Dr. Dattaprasad, Dr. Diptesh, Dr. Sandesh, Dr. Sagar, Dr. Hari, Dr. Prajesh, Dr. Durga, Dr. Mayuri*** *for helping me whenever in need. I would like to thank all my research colleagues and my juniors* ***Vipul, Sudesh, Pooja, Neha, Mangala, Seneca, Luann, Nikita, Ketan, Shashank, Lima, Joette, Savio, Pratibha, Johnross, Apurva, Amarja, Akshay, Wilma, Vishal, Dinesh, Ratan, Keraba, Geeta*** *for helping me in need and keeping the environment at department very helpful.*

Ph. D life is difficult without friends which made my research journey a wonderful memory. A special thank you for being with me whenever I needed, ***Mr. Vishnu Chari****,* ***Dr. Prajyoti Gauns Dessai, Dr. Vishal Pawar, Dr. Jayakanthan, Mr. Pratik Asogekar, Mr. Sarvesh Harmalkar, Mr. Kedar Narvekar, Mr. Abhijit Shetgaonkar, Dr. Narayan Vatrekar, Dr. Kiran Dhavskar, Mr. Milind Mutnale, Mr. Pratik Surlekar, Mr. Shankar, Mr. Jayesh, Mr. Prakash, Mr. Prem and Mr Uddhav Kerkar*** *for always helping, motivating and inspiring me.*

A special thank-you to all my hostel mates ***Santhosh, Praveen, Mahendra, Ranjeet, Jostin, Dillan, Laximan, Charan, Marlon, Aniket, Sanket, Marconi, Rohatash, Manojit, Chetan, Nilesh*** *for making the hostel-stay worthwhile in all the enduring times.*

1 *indebt thank my best teachers* ***Dr. Pradeepesh Bhattacharya*** *and* ***Mr. Viren Dangui*** *for motivational support. Whatever I am today, it is because of the blessings from my parents and my siblings. I would like to acknowledge parents for always supporting me. Also, I am grateful to my entire family for the love, understanding and support during testing times.*

Finally, the blessings from the almighty are always needed, thank you God for surrounding me with good teachers, good friends and finally good human beings.

Mr. Rahul Kerkar

Research Scholar

CONTENT

CHAPTER 4: THERMAL, DIFFRACTION, SPECTROSCOPIC AND MICROSCOPIC STUDIES

CHAPTER 5: SURFACE AND CATALYTIC STUDIES

1.1 Introduction

Increase in industrial activity and heavy transportation lead to contamination of air by pollutants, which is a major concern towards the public health. Since several decades, gaseous pollutants such as oxides of nitrogen (NO_x), carbon monoxide (CO), hydrocarbons (HC), etc. are released into the atmosphere causing different health hazards and environmental issues [1, 2]. In automobiles, exhaust contributes towards major part in releasing air pollutants. Potentially, exhaust system should prevent any gaseous pollutants. But this happens only when there is complete combustion with high efficiency of the fuel. Generally, partial combustion of fuel takes place and it tends to generate harmful pollutants like NO_x, CO, HC etc. [3]. According to the study, over 80% of the total world population is getting exposed to the air pollutants beyond the recommendation level set by the World Health Organization (WHO) and also millions of death have been claimed due to air pollution [4, 5]. In this regard, eliminating such air pollutants is very important before they enter in the environment.

The pollutants like nitrogen oxide (NO) and carbon monoxide (CO) are the colorless gases generally produced and released into the environment by the transportation and industrial processes. Nitric oxide is not harmful till a certain concentration, but when it combines with O_2 in the exhaust system it forms NO_x which is more toxic. Acid rain and photochemical smog are the consequences of the reaction of NO_x in the environment. The exposure to CO leads in poisoning in humans and animals as it attacks the hemoglobin from the blood, thus depriving supply of oxygen to different organs [6, 7]. Thus, conversion of NO and CO into N_2 and CO_2 is essential to overcome such issue. With respect to the final products from the conversion of CO and NO i.e. N_2 and CO_2, CO_2 is an ingredient of air and required for the growth of plants but in higher concentration it is considered as greenhouse gas which develops issues like global warming. The presence of CO_2 cannot harm the human health as concerned due to non-toxicity of CO_2 and can readily associate and dissociate from hemoglobin while CO cannot. Oxygen has lower affinity towards hemoglobin than CO, as a result CO binds to hemoglobin in higher amount as that of O_2 which causes very little transportation of O_2 in the body. Also, CO being poisonous, colorless and odorless it is impossible to detect when emitted from various sources such as industries and automobiles. This is a main reason why the extensive research is being carried out to develop improved

catalysts to convert these toxic gases to non-toxic products before being released into the atmosphere. Although, lot of study has been carried out with respect to conversion of NO using ammonia, urea etc. [8–11] and conversion of CO with O_2 [12–14], the simultaneous conversion of NO with CO is considered as an efficient way, wherein both the pollutants can be detoxified at one step. In these detoxification processes, catalyst plays an important role in converting such toxic gases like NO and CO to its nontoxic N_2 and CO_2 forms, respectively.

Heterogeneous catalytic system has a wide scope on the account of engineering benefits by designing/modification of the catalysts. For this reason, a heterogeneous catalyst is one such significant tool which is financially very helpful from industrial application point of view. Catalytic oxidation of CO by oxidizing gases and catalytic reduction of NO by reducing gases are widely studied over different types of heterogeneous catalysts such as doped oxides, mix-metal oxides and supported oxides. Transition metal oxides are important candidates for such catalytic detoxification reactions. Among them, oxides of manganese, cobalt, copper, iron, and chromium in combination with precious metals are extensively used in oxidation-reduction of these pollutants [15–22]. Also, oxides of aluminum and cerium are widely studied for such types of gas phase reactions [23–29].

The performance of catalytic reaction is greatly associated with the probable mechanism which is acting during the CO oxidation and NO-CO redox process. Since, heterogeneous catalysis deals with the solid catalyst, Langmuir - Hinshelwood and Rideal – Eley are the two widely accepted mechanism which can take place during the catalytic process [30–32]. Besides these, Mars van Krevelen (MvK) mechanism is also widely accepted mechanism for oxidation of carbon monoxide in oxidizing environment. When, CO gets chemisorbed on the catalyst surface which desorbs leaving behind the vacant oxygen site and this vacant site is stabilized by O_2 or NO. This is what exactly happens when a reaction path is followed via MvK mechanism. Oxides of Cr, Mn, Co, Cu are some of the non-precious catalyst that has been known for high oxygen mobility and have good impact in CO-O_2 and NO-CO reaction [20, 31, 33–37]. Although, transition metal oxides offer good catalytic performance but cannot compete with that of precious metals due to its unique electronic property. Such unique property of precious metal, when combined with transition metal holding redox pair, can create a high synergy which contributes a major impact in catalyzing

exhaust related reactions [38–40]. Such combining can be opted as support, doping, etc. to non-precious catalytic oxide system.

1.2 Highlights of the Thesis

- Preparation of Monophasic chromium oxide and cerium oxide catalysts using combustion method and sol-gel auto-combustion methods.
- Preparation of composite oxide catalysts via combustion, sol-gel auto-combustion, impregnation and physical grinding routes.
- Characterization of these prepared catalysts using various characterizing tools such as powder XRD, IR spectroscopy, TG-DTA, SEM, TEM, XPS, BET, H_2-TPR, CO-TPD, NH_3-TPD, CO_2-TPD and CO pulse titration techniques.
- Catalytic oxidation of carbon monoxide using oxygen over prepared catalyst was studied.
- Simultaneous NO - CO conversion reaction over the prepared catalyst and also, reaction stability and recyclability studies over he prepared catalyst has been discussed.

1.3 Organization of thesis

Chapter 1: Introduction

Chapter 2: Literature Studies

Chapter 3: Experimental Part

Chapter 4: Thermal, Diffraction, Spectroscopic and Microscopic studies

Chapter 5: Surface and Catalytic Studies

Chapter 6: Summery and Conclusion

Literature Studies

2.1 Nitrogen monoxide (NO)

Nitrogen monoxide, also known as nitric oxide (NO) is a neutral gaseous molecule which is paramagnetic in nature. It has a melting point of -164 °C and boiling point of -152 °C. The unusual nature of nitrogen monoxide results from an unpaired electron which is present in HOMO (highest occupied molecular orbit). The molecular orbital diagram of NO is given in Fig. 2.1., where in it can be observed that nitrogen possesses 5 valence electrons and oxygen possesses 6 valence electrons. Thus, nitric oxide (NO) holds a total number of 11 valence electrons as seen from Fig. 2.1. According to the molecular orbital theory (MOT), nitric oxide contains 3 fully occupied bonding orbitals and 1 unpaired electron in anti-bonding π orbital. The weakening of overall bonding is a resultant of 1 unpaired electron. Thus, oxygen and nitrogen are held together by the bond order of 2.5 [41, 42].

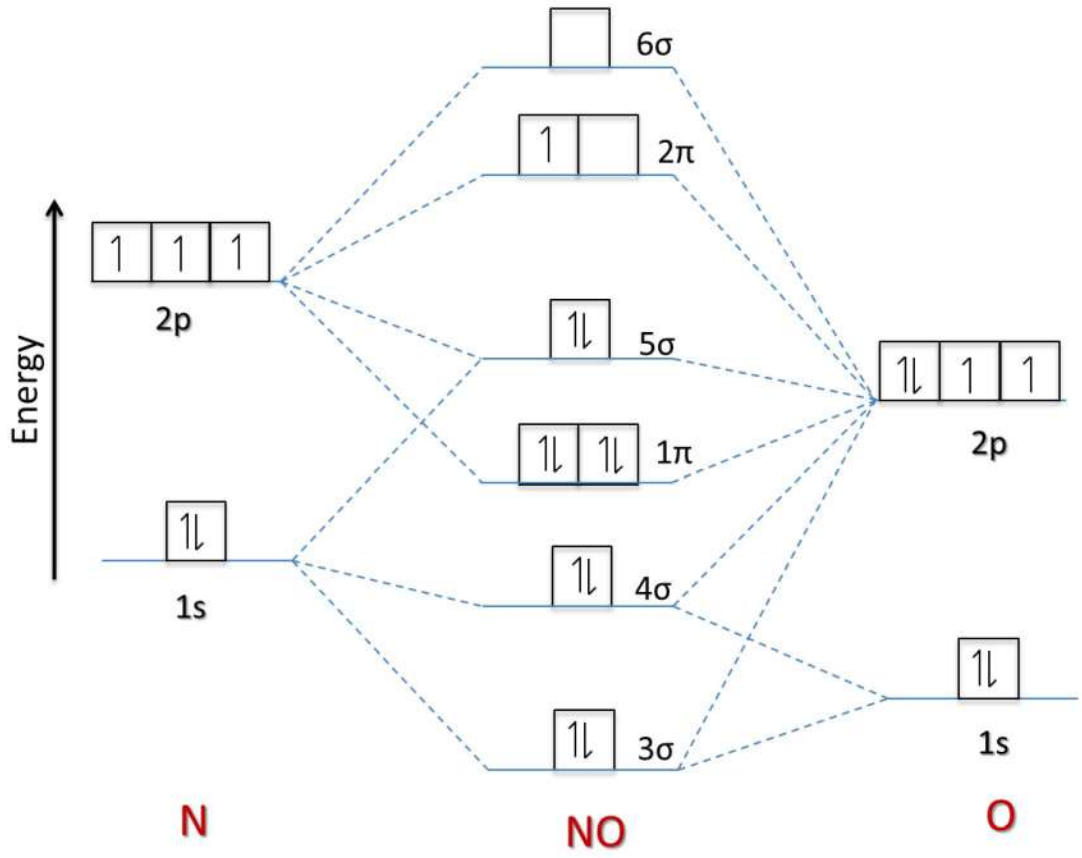

Fig. 2.1: *The molecular orbital diagram of nitrogen monoxide.*

The incomplete combustion of the fuel leads in the production of nitric oxide in today's industrial era. Also, in nature it forms by natural calamities like lightning, earthquake, etc. In the laboratory, nitric oxide can be synthesized by various methods as follows:

$$NaNO_2 + H_2SO_4 + NaI \rightarrow NO + H_2O + Na_2SO_4 + {}^1/_2 I_2 \quad \ldots\ldots\ldots\ldots (2.1)$$

$$3Cu + 8HNO_3 \rightarrow 2NO + 4H_2O + 3\,Cu(NO_3)_2 \quad \ldots\ldots\ldots\ldots (2.2)$$

$$2NaNO_2 + 2H_2SO_4 + 2FeSO_4 \rightarrow 2NO + 2H_2O + Na_2SO_4 + Fe_2(SO_4)_3 \quad \ldots\ldots (2.3)$$

When nitrogen oxide (NO) is produced in the exhaust system, it reacts with oxygen present in the system and forms NO_2 (NOx). However NO is not considered as harmful at ambient concentration, whereas NO_x can be toxic at ambient concentration. Also, it has negative effect on vegetation, it damages the leaf and reduces growth rate.

2.2 Carbon Monoxide (CO)

Carbon monoxide was discovered in 1799 by Priestley, and was found to be toxic for humans. It has been proven that CO directly attacks hemoglobin and causes slow poisoning. This is because of affinity of hemoglobin towards CO is 250 times higher than that of O_2 [43]. Carbon monoxide is a colorless gas having molecular formula CO. It is odorless and toxic gas and can be fatal in higher concentration. It is having a molecular weight of 28.01 g/mol with a melting point (M.P.) of -205 °C and boiling point (B.P.) of -191 °C. In CO, carbon is bonded to oxygen with a triple bond, which is known to be strongest chemical bond. Detailed understanding of the electronic structure of CO is given in energy level diagram and presented in Fig. 2.2.

Carbon monoxide is considerably weak Lewis acid and has ability to donate 2 electrons towards metals from transition series to form metal carbonyl. This property makes carbon monoxide an influential molecule in the field of coordination and organometallic chemistry. Among the different molecules present, CO is one of the commonly and vastly studied molecules in the organometallic chemistry. When CO is bonded to transition metal there is decrease in bond order of CO from 3 (C≡ O) to 2 (C=O) through phenomenon called back bonding. In the purification of nickel, CO plays an important role wherein Ni can be purified

by coordinating it with CO. This process is known as the carbonyl process, discovered by Ludwig Mond in 1890 for the extraction of nickel from its ore.

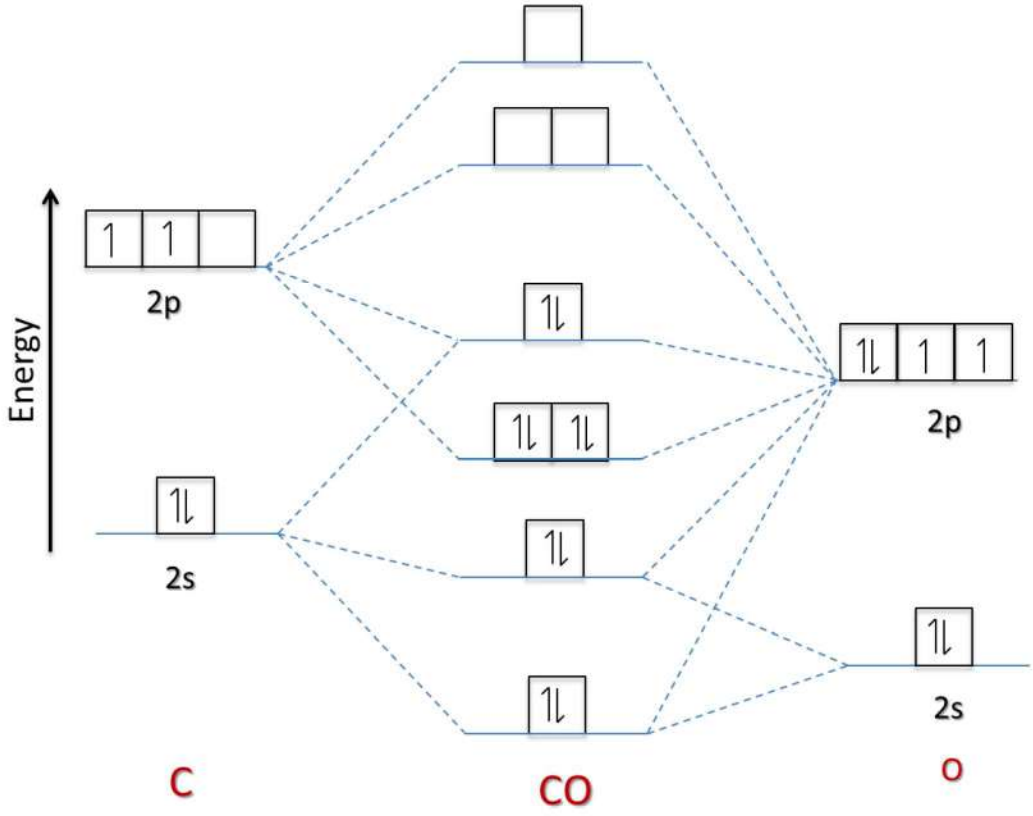

Fig. 2.2: *The molecular orbital diagram of carbon monoxide.*

Carbon monoxide is produced when carbon species are incompletely burned. Carbon monoxide has always been present in the air before urbanization. In nature, existence of CO is a consequence of volcanic activities, bushfire, etc. In the present scenario, the increase in the carbon monoxide in the ambient air is from automobile exhaust. The increasing level of CO in the atmosphere creates a major issue toward human health and environment. When internal vehicle engine is unable to burn fuel completely, it produces CO along with other pollutants. Also combustion of biomass equally contributes in the raising level of CO in the atmosphere. In laboratory, CO is produced by reacting formic acid with sulfuric acid wherein formic acid is disproportionate to CO and H_2O.

2.3 Catalysis

The process of catalysis has been employed for many centuries. In 1835, the concept of catalysis was first recognized and discussed by Swedish scientist called Berzelius. The industrial catalytic field began with the huge scope in sulfuric acid production using platinum catalyst in the year 1875. In 1903, Ostwald produced nitric acid by oxidizing ammonia on platinum gauge. Another significant advancement was proposed by Mittasch, Bosch and Haber in 1908- 1914 where they synthesized ammonia with iron based catalyst.

Catalysis is a process wherein the rate of chemical reaction is enhanced by the addition of an external substance called as catalyst. A catalyst is one which accelerates the rate of a chemical reaction. Catalyst primarily forms a bond with the reactant and reacts with it to give a product, which can be later detached from the catalyst surface by leaving behind unaltered catalyst. In fact, catalytic process is a cyclic event wherein catalyst reacts in initial step and in final stage it gains its original structure as demonstrated in Fig. 2.3. It can be observed from the Fig. 2.3 that the two reactants, 'A' and 'B' in catalytic reaction reacts together to yield product P. The catalytic cycle starts with bonding of a reacting molecule (A and B) to the catalyst. The reactant A and B then forms a product which is attached to the catalyst. Later in the final step of catalytic process, product (P) gets separated leaving behind the catalyst in its original structure.

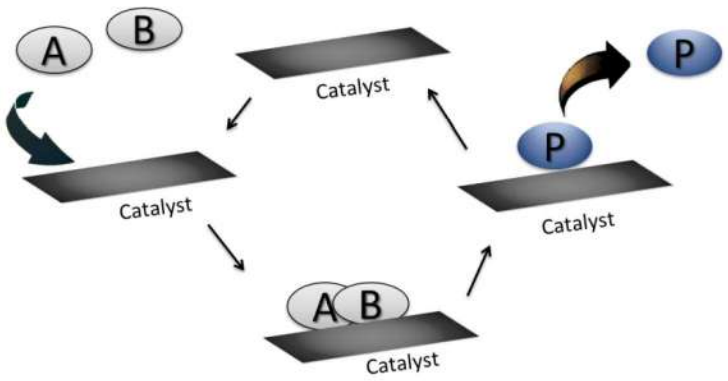

Fig, 2.3: *The pictorial representation of a catalysis process.*

Thermodynamically, activation energy plays an important role in a chemical reaction. Fig. 2.4 displays a comparison plot of activation energy in presence and absence of a catalyst. If a

reaction is carried out without catalyst, than it requires large amount of activation energy to complete the reaction, but in the presence of catalyst the energy required to activate the reaction is much lesser. The fundamental favorable circumstance of catalysis is that you get the preferred product quicker, utilizing less assets and creating less waste. Based on the types of catalyst, catalysis is divided into two categories i.e. Homogenous and heterogeneous catalysis.

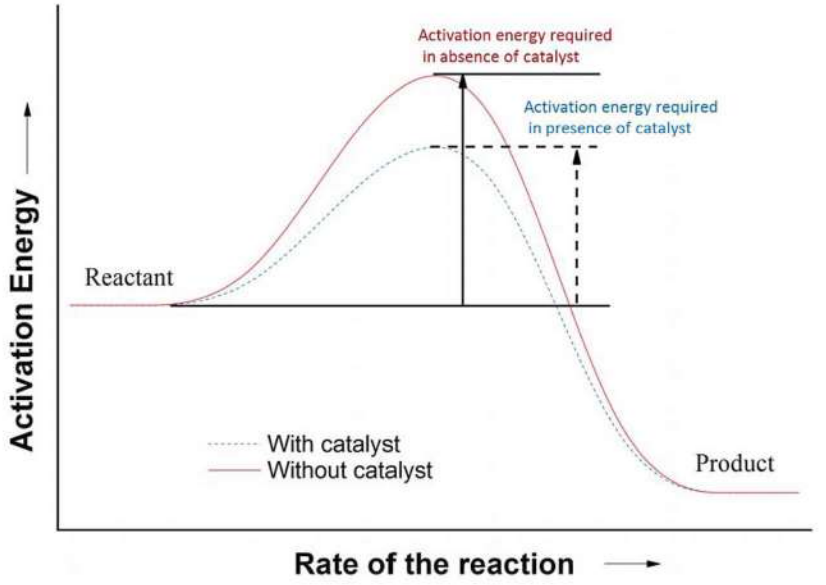

Fig. 2.4: *The plot of activation energy v/s rate of the reaction for a reaction carried out in presence and absence of catalyst.*

2.3.1 Homogenous Catalysis

In a catalytic reaction, when the catalyst is in the same form as that of reactants than the reaction is called as a homogeneous catalytic reaction. Commonly, the catalyst and reactant are either in gaseous form or in liquid form. In most of the industries, the homogeneous catalytic reactions are performed on liquid system. For example, catalytic conversion of methanol to acetic acid, production of polyethylene using organometallic compounds as a catalysts and also some of the enzymatic reaction wherein enzyme act as catalyst, etc. Similarly, in atmospheric chemistry decomposition of ozone by chlorine is common example where reactant and catalyst is in gaseous phase. The reaction is given as follows:

$$Cl + O_3 \rightarrow ClO_3 \quad \cdots\cdots (2.4)$$

$$ClO_3 \rightarrow ClO + O_2 \quad \cdots\cdots (2.5)$$

$$ClO + O \rightarrow O_2 + Cl \quad \cdots\cdots (2.6)$$

Under the influence of sunlight the ozone gets decomposed but in the presence of Cl the rate of decomposition tremendously increases [44].

Homogeneous catalysts are very advantageous due to factors like high activity and selectivity. Also, Catalytic mechanism and chemistry involved in homogeneous catalysis can be studied in better aspect and because of this it is very helpful in controlling and manipulating the parameters of the process. However, homogeneous catalytic processes are associated with some major drawbacks. Sometimes homogeneous catalysts are very sensitive towards pH, temperature, etc. which intern can spoil the catalytic performance of the reaction. Since the homogenous catalysts are molecularly dispersed by getting homogenized with that of reactant and product, the separation of catalyst becomes difficult or sometimes expensive. Similarly, in many cases it is very difficult to recover the catalyst for reusing in next reaction.

2.3.2 Heterogeneous Catalysis

Heterogeneous catalysis is a reaction where catalyst is present in different physical phase as that of reactant and product. Mostly heterogeneous catalyst are composed of inorganic materials like metal salt, metal oxides, metals, MOF, zeolites etc. but it can be also from organic materials like enzymes, ion exchanger, etc. Heterogeneous catalysis is very efficient in converting raw materials into valuable substances in eco-friendly manner. Ease of catalyst separation is one of the significant benefits of heterogeneous catalysis over homogeneous catalysis. In gas - solid catalytic systems the catalyst can be easily separated and cleaned giving heat treatment, whereas in liquid - solid catalytic systems both can be easily separated by simple filtration method. This makes heterogeneous catalysis a crucial for world's economy.

It has been found out that more than 50% of chemical processes are dependent on heterogeneous catalysts. Heterogeneous catalysis finds importance in several industrial

applications such as in automobiles, food production, petrochemical industries, pharmaceutical industries, etc. One of the common examples is synthesis of ammonia, where iron based catalyst, elemental nitrogen and hydrogen are combined to yield NH_3. Similarly, Heterogeneous catalysis is gaining importance in new areas such as green chemistry, fuel cells, nanotechnology, etc. Moreover, the wide range application of heterogeneous catalysis makes it highly interdisciplinary in nature.

Adsorption is a key step involved in the catalytic process. In adsorption process, the reactant binds to the catalyst surface via physical or chemical bond. Based on the type of bonding, adsorption can be divided as physisorption type (weak bonding) or chemisorption type (strong bond). In physisorption, a reacting molecule is attracted towards the catalyst surface by weak forces like van der Waals forces. While in the chemisorption, the molecule bounds to the catalyst surface by sharing the electron. The energy required to desorb the physisorbed molecule is very less, whereas for chemisorbed species a huge amount of energy is needed as it bonds strongly toward the surface.

Discussing the principals involved in heterogeneous process is complicated as wide range of catalyst applications covers different surface chemistries. Most of the catalysis processes are carried out on the metal surface of the catalyst, but not all the heterogeneous processes take place on surfaces of metal. One of the common examples is zeolite, which is an excellent material used as solid-acid catalyst. The Zeolite structure is mainly developed from aluminum, silicon, titanium and oxygen.

2.3.2.1 Heterogeneous catalysis for environment

The existence of environmental pollution was known from centuries but its intensity provoked drastically with industrial revolution. Varieties of processes are employed to convert raw material into fuels and chemical goods which are essential to modern life. However, it results in increased stress on the environment through pollution as most efficient processes which have been used in day today life result in pollution as by-products. This slowly took major part in contamination of soil, water and atmosphere. Therefore to overcome this situation, catalysis played a key role by giving realistic solution towards many environmental related issues. With respect to the pollutant type, both homogeneous and heterogeneous

catalysts are being used for reducing the pollutants. More than 80% of the catalytic practices are often observed in heterogeneous catalysis route. Although, homogeneous catalysis assists in detoxifying the pollutants, it is sometimes less eco-friendly and found less efficient as compared to heterogeneous form.

During 1970s, oxide of titanium and zinc gained attention in field of water and soil pollution research due to their enhanced chemical stability, high photo-catalytic property, low toxicity, etc. Similarly, other transition metal oxides were also in demand during mid-1970s for air cleaning purpose. The perspective of those heterogeneous catalyst is to eliminate the gaseous pollutants like CO, NO_x, HC, etc., which is formed in the course of the fuel combustion.

2.3.2.2 CO and NO detoxification by heterogeneous catalysis

Atmospheric pollutants like carbon monoxide (CO), oxides of nitrogen (NO_x) and hydrocarbon (HC), the chief byproducts which originates from different industrial and automobile activities, are very harmful to the environment and human health. Thus, the most appropriate solution for reducing emissions at the exhaust outlet with the help of catalytic converter composed of heterogeneous catalyst. Heterogeneous catalysis process is one of the most effective techniques used to control air pollution. In heterogeneous catalytic process, nano-sized or porous materials are more abundantly used as they possesses good surface areas or pores, compared to bulk materials.

Three-way catalytic convertor is used to convert these pollutants to non-toxic CO_2, N_2 and H_2O products before releasing in the atmosphere. Wide literature is available on low temperature oxidation of CO by O_2 [45, 46] and reduction of NO using H_2 and NH_3 as reducing agent[47–49]. Selective catalytic reduction of nitric oxide with ammonia (NH_3-SCR) [50, 51] and selective catalytic reduction using H_2 (H_2-SCR) [52, 53] are widely studied over different types of oxide catalysts (Doped Oxides, mix metal oxide, supported oxide). In NH_3-SCR, main drawback is observed in the form of NH_3 slip, incomplete combustion of NO_x [54, 55] also H_2-SCR gives less selectivity and tends to generate more N_2O than N_2 [54, 56]. Thus, Reacting nitric oxide and carbon monoxide via redox pathway is significant route to convert nitric oxide - carbon monoxide (NO-CO) simultaneously [20, 57]

As both CO and NO exist in exhaust, simultaneous elimination of these pollutants is economical technique which is extensively studied by researchers[58–60]. Engineering an economical catalyst for low temperature detoxification of NO and CO is challenging objective worldwide because the stability of NO increases above 300 ^{o}C. Below are the reactions demonstrating the detoxification of CO and NO over the heterogeneous catalyst system.

$$2\,CO + O_2 \xrightarrow{Catalyst} 2\,CO_2 \qquad \text{Oxidation of CO With } O_2 \qquad \cdots\cdots (2.7)$$

$$2\,CO + 2\,NO \xrightarrow{Catalyst} 2\,CO_2 + N_2$$

Or

$$CO + 2\,NO \xrightarrow{Catalyst} CO_2 + N_2O$$

$$CO + N_2O \xrightarrow{Catalyst} 2\,CO_2 + N_2$$

Simultaneous NO-CO Conversion ····· (2.8)

In early 1970s, a major query was identifying the catalyst materials which would be appropriate to drive the detoxification reaction. At the time, platinum group metals such as platinum (Pt) and palladium (Pd), were known for its excellent oxidation performance. Later, it has also been observed that exhaust system gets rich in reducing gases like CO and HC, which results in lowering of exhaust catalyst performance. This is the reason why ceria (Ce) or ceria-zirconia (Ce-Zr) enters the picture as they are good oxygen reservoir and depending on size and type of lattice dopants, Ce or Ce/Zr can alter its lattice oxygen storing capacity [61]. Similarly, transition metals are highly preferred as heterogeneous catalysts for detoxification of exhaust pollutants. Due to variable oxidation states, oxides of manganese, cobalt, copper, iron, and chromium are extensively used in oxidation reduction of these pollutants [60, 62, 63]

Later, for developing an effective catalyst at low price for emission control, the concept of dilution of precious metal in transition metals or metal oxides came in existence like $Pd/Co_3O_4–CeO_2$ [64], $Pd/La_{0.9}Ba_{0.1}AlO_3$ [65], Au/CeO_2-Al_2O_3 [66], $M_{0.05}Co_{2.95}O_4$ (M = Rh, Pd & Ru) spinel [20], etc.

2.4 Mechanism in heterogeneous catalysis

As Known earlier, catalyst is the one which takes part in the reaction, however is not getting consumed within the reaction. During the reaction, the catalyst reacts with the reactant in first step of mechanism and also with product in the last step of mechanism. In this way the catalytic cycle continues and the catalyst can be used again and again. Several reaction mechanisms are found, which discusses the reaction pathway of a chemical reaction based on experimental result observed. Two types of reaction mechanisms had been proposed for the heterogeneous catalysis, which are known as Langmuir- Hinshelwood mechanism and Eley-Rideal mechanisms [67].

In 1921, Langmuir came up with the idea of the adsorption of molecules on the solid surfaces, which later correlated by Hinshelwood to explain the reaction between two reacting molecules over the surface of a heterogeneous catalyst. In the Langmuir– Hinshelwood (L-H) mechanism, the two reacting molecules are primarily chemisorbed on the surface of the catalyst before the occurrence of the chemical reaction. The steps involved in the L-H mechanism are as follows

1. Adsorption of the reacting molecule on the catalyst surface.
2. Dissociation of reactants on the catalyst surface
3. Reactions between adsorbed molecules
4. Desorption of the product from the catalyst surface.

In the Eley–Rideal mechanism, only one reacting molecule reacts with the catalyst surface directly (Chemisorbed) and other one reacts with the chemisorbed molecule without getting adsorbed on the catalyst surface. The steps involved in the E-R mechanism are as follows:

1. Adsorption of one of the reacting molecule on catalyst surface.
2. Dissociation of adsorbed molecules at the catalyst surface.
3. Reactions between adsorbed molecules and the molecule present in gaseous phase in reaction stream.
4. Desorption of the formed product.

Another mechanism which is widely accepted for the oxidation reaction in heterogeneous catalysis is Mars Van Krevelen (MvK) mechanism, where it deals with the lattice oxygen. In Mar van Krevelen mechanism, reactants gets adsorbed on the catalyst surface, and reacts with the lattice oxygen of a catalyst and get desorbed as a product. Later, this oxygen vacancy is stabilized by oxidizing species present in the catalytic stream and thus regenerating the catalyst for next cycle.

2.4.1 Mechanism involved in CO-O_2 reaction

Mostly, Oxidation of carbon monoxide may occur on the metal surface via either the Langmuir–Hinshelwood (LH) mechanism or the Eley–Rideal (ER) mechanism. When oxidation of carbon monoxide proceeds with the Langmuir–Hinshelwood (L-H) mechanism, the chemisorption of CO molecule and chemisorption of O_2 (dissociative) on surfaces of the catalyst takes place [68, 69].

In the Eley–Rideal (ER) mechanism, the O_2 molecule gets chemisorbed and dissociates on the catalyst surface which later directly reacts with CO molecule to yield CO_2 [70, 71]. The schematic representation of CO oxidation via L-H Mechanism and E-R Mechanism are given in Fig. 2.5 and Fig. 2.6.

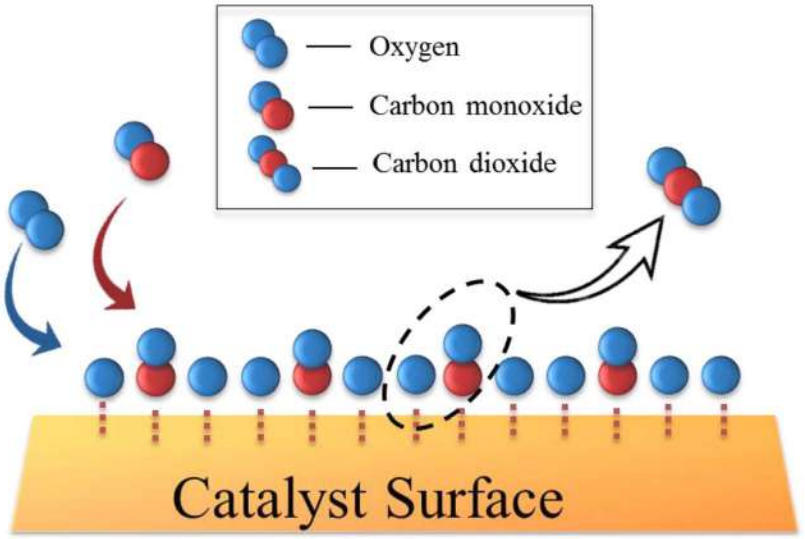

Fig. 2.5: *The Schematic representation of Langmuir–Hinshelwood (L-H) mechanism.*

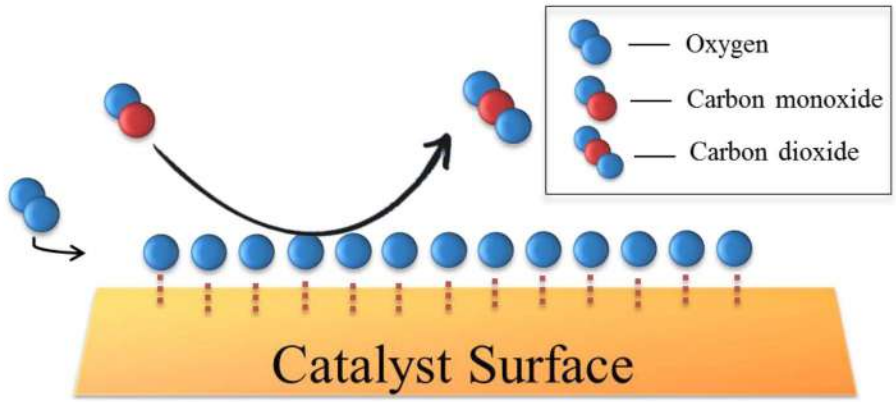

Fig. 2.6: *The Schematic representation of Eley–Rideal (ER) mechanism.*

Literature shows an alternative mechanism which is projected for CO oxidation over various heterogeneous catalyst called Mars van Krevelen mechanism (MvK) [33, 72]. Oxygen storing material like Ce, Zr, transition metals, etc. tends to hold huge amount of oxygen in its lattice which thereby acts as good exhaust catalyst. According to MvK mechanism, lattice oxygen takes part in oxidizing the CO and creates oxygen vacancy on the catalyst surface which is replenished by oxygen from the reaction stream. The schematic representation of CO oxidation via Mars van Krevelen Mechanism is given in Fig. 2.7.

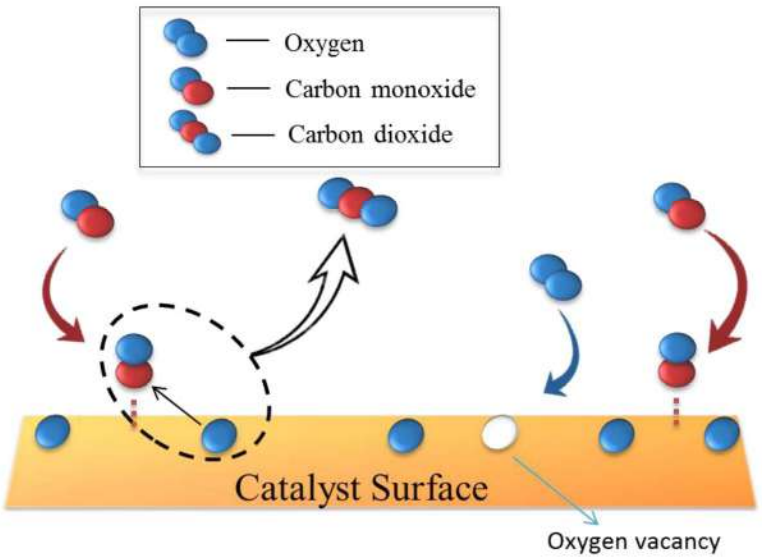

Fig. 2.7: *The Schematic representation of Mars van Krevelen Mechanism (MvK) mechanism.*

Recently, Bing Han and others presented a promising effect of Rh/CeO_2 catalyst for CO oxidation [72]. With several experimental findings they proposed reaction pathway via Mars van Krevelen (MvK) mechanism for low temperature CO oxidation. Studies by Katsaounis and others demonstrated the key importance of lattice oxygen in oxidation reaction [73] and the report of He et al. gave the evidence of increasing lattice oxygen for enhancing the catalytic performance [73]. It cannot be neglected that the CO oxidation can also be proceeded via a Langmuir− Hinshelwood (L−H) mechanism as well as Mars−van Krevelen mechanism depending on the surface character [74, 75].

2.4.2 Mechanism involved in NO-CO reaction

Predicting the NO-CO catalytic pathway over the catalyst surface is considered to be a difficult task as many channels could be possible if a catalyst is composed of complex material. S. Carlotto et al. proposed four mechanisms for NO-CO reaction based on Mars van Krevelen assumption [31]. These four mechanisms are presented below as (a) Mechanism I, (b) Mechanism II (c) Mechanism III, and (d) Mechanism IV.

In mechanism I, both the reactant gets adsorbed on the surface of the catalyst following L-H mechanistic approach. Primarily, he showed formation of CO to CO_2 by surface O species creating a vacant site. This site is later occupied by NO and finally N_2 gets released giving oxygen to the vacant Site.

$$O_s + CO(g) \rightarrow V_O + CO_2(g) \quad (a1)$$

$$V_O + O_s + CO(g) \rightarrow 2V_O + CO_2(g) \quad (a2)$$

$$2V_O + NO(g) \rightarrow V_O + [V_O—NO] \quad (a3)$$

$$V_O + [V_O—NO] + NO(g) \rightarrow 2[V_O—NO] \quad (a4)$$

$$2[V_O—NO] \rightarrow N_2(g) + 2O_s \quad (a5)$$

(a) Mechanism I

Mechanism II is reported based on E-R pathway wherein only one species gets chemisorbed on the surface and in this case NO was the chemisorbed species. CO from the reaction atmosphere reacts to O from the catalyst surface creating a vacant site for NO. This

vacant site in final step was stabilized by oxygen from NO. Also N_2O formation was accounted from N_2O_2 species.

$$O_s + CO(g) \rightarrow V_O + CO_2(g) \quad (b1)$$
$$V_O + O_s + CO(g) \rightarrow 2V_O + CO_2(g) \quad (b2)$$
$$2V_O + NO(g) \rightarrow V_O + [V_O—NO] \quad (b3)$$
$$V_O + [V_O—NO] + NO(g) \rightarrow Vo + [V_O—N_2O_2] \quad (b4)$$
$$Vo + [V_O—N_2O_2] \rightarrow [V_O—N_2O] + O_s \quad (b5)$$
$$[V_O—N_2O] \rightarrow N_2(g) + 2O_s \quad (b6)$$

(b) Mechanism II

While in case of mechanism III, first three steps were adapting mechanism to form CO_2. Wherein, the adsorption of NO molecule gets dissociated into N and O to stabilize the previous oxygen vacancy. In second step of NO adsorption, adsorption of NO takes place on surface incorporated N (nitrogen) to yield N_2O species. Finally this N_2O decomposes to N_2 gas and then desorbed back in gaseous phase.

$$O_s + CO(g) \rightarrow V_O + CO_2(g) \quad (c1)$$
$$V_O + O_s + CO(g) \rightarrow 2V_O + CO_2(g) \quad (c2)$$
$$2V_O + NO(g) \rightarrow V_O + [V_O—NO] \quad (c3)$$
$$V_O + [V_O—NO] \rightarrow O_s + N_s \quad (c4)$$
$$N_s + NO(g) \rightarrow N_2O(ads)\ (N\text{-down}) \quad (c5)$$
$$N_2O(ads)\ (N\text{-down}) \rightarrow N_2O(ads)\ (O\text{-down}) \quad (c6)$$
$$N_2O(ads)\ (O\text{-down}) \rightarrow N_2(g) + 2O_s \quad (c7)$$

(b) Mechanism III

In mechanism IV, the vacancies generated after CO oxidation strongly supports the NO reduction where dependency was seen with NO reduction and formed vacancies. Also, partial reduced surface and equal NO/CO ratio dependency with N_2O formation was discussed

$$O_s + CO(g) \rightarrow V_O + CO_2(g) \quad (d1)$$
$$V_O + NO(g) \rightarrow [V_O—NO] \quad (d2)$$
$$[V_O—NO] + NO(g) \rightarrow [V_O—N_2O_2] \quad (d3)$$
$$[V_O—N_2O_2] \rightarrow N_2O(g) + O_s \quad (d4)$$

(b) Mechanism IV

M. Esrafili reported NO reduction to N_2O via dimer mechanism, wherein two NO molecules were attached to get $(NO)_2$ dimer. Later this dimer dissociates into O and N_2O possessing an activation energy of 0.39 eV. Also, he showed unfeasibility in direct NO dissociation to N_2 and O_2 as it requires very high activation energy at ambient condition [76]. A.K. Ladavos et al. showed two reaction pathway wherein in one case NO-CO gets decomposed to N_2 and O_2 (occurs at higher temperature) whereas in second route the reaction proceeds via N_2O formation (occurs at lower temperature) as shown below in route 1 and route 2 [77].

$$Route\ 1: 2NO + 2\,CO \rightarrow N_2 + 2CO_2 \quad \text{(2.9)}$$

$$Route\ 2: 2NO + CO \rightarrow N_2O + CO_2 \quad \text{(2.10)}$$

2.5. Preparative routes of catalyst material

Over the years, catalyst development has become a center of attraction in the catalytic research around the globe. A variety of nano sized materials are found in the literature which has been synthesized with different synthesis routes [78, 79]. Since the catalyst size and morphology plays a significant impact on their performances, selecting a specific method for catalyst preparation is very important. Depending on the type of synthesis, it has been divided into wet chemical methods and solid-state methods. Some of the preparative methods are been discussed in the following sub-sections.

2.5.1. Co-precipitation method

Co-precipitation is a simple method for the preparation of pure or mixed metal oxide nanoparticles using metal salt and precipitating agent. Here, metal salt such as metal nitrate, metal chloride, metal sulfate, etc. are dissolved in distilled water and then precipitated by adjusting basic pH using sodium hydroxide or ammonium hydroxide. After precipitating the

metal hydroxide, it is then filtered and calcined above metal hydroxide decomposition temperature to yield metal oxide.

Pure metal oxide or mix metal oxide nanoparticles composed of Fe, Cu, Co, Ni etc. are conveniently synthesized with respective metal salt and base [50, 64, 80]. Min li et al. prepared $AlPO_4$ using co-precipitation route for Rh support and the interaction of metal support was evaluated over NO-CO reaction [81]. Additionally, Behrens et al. studied magnetic and catalytic properties of ternary transition metal oxide composed of Cu-Fe-Mn produced by co-precipitation route and calcined above 500 °C [82].

2.5.2. Sol-gel method

The Sol-gel synthesis is a useful technique for the production of metal oxide nanoparticles possessing an interesting catalytic property [83, 84]. This preparative method is considered as an effective method in modifying the catalyst surface. The basic of sol-gel method is inorganic polymerization reaction including hydrolysis, poly-condensation, drying and thermal decomposition [85]. After the condensation of a solution, the formed gel is kept at calcination temperature to decompose the gel to metal oxide. The rate of condensation and hydrolysis are the important phenomenon which decides the surface property of the metal oxides. Formation of smaller particle size in sol gel method is mostly due to controlled hydrolysis process. This method was used for preparation of various metal oxides such as $Co_{2-x}Fe_xWO_6$, CeO_2, TiO_2, CeO_2-Al_2O_3, etc. [86–89]. Recently, Syvorotka et al. investigated the structural and photoluminescence behavior of Yb doped $Y_3Al_5O_{12}$ which has been synthesized via citrate sol-gel method [90].

2.5.3. Combustion method

Combustion synthesis method is also called as self-propagating high-temperature synthesis (SHS) which is economical and effective method for the preparation of various kinds of metal oxide nano particles. In combustion synthesis, the oxidant and fuel is combined to form mixture which is later combusted by providing little heat to produce metal oxide. Combustion gives huge amount of heat during the process which helps in combusting the metal precursor to metal oxide. The oxidant such as nitrate and fuel such as glycine, urea, and citrate are the essential component to carry out this reaction.

Several complex metal oxides were prepared with combustion method. T. Nien et. al. synthesized $CuCrO_2$ [91] in which mixture of copper, chromium nitrate and glycine was dissolved in minimum amount of water and then was heated at 175 °C at which self-ignition takes place to give $CuCrO_2$. The fine powder was obtained due to evolution of gas during the combustion process and it also helped in preventing the particle agglomeration.

2.5.4. Impregnation method

Impregnation is a method commonly used to prepare supported catalyst where the active species is placed on the substrate as a support. In this method, the support material is immersed in the metal precursor solution. Metal precursor is directly adsorbed on the surface of the substrate or can be precipitated by adjusting the pH of the solution. This is further dried and heated to desired temperature to yield supported catalyst. For example, Rh/SiO_2 is prepared by mixing silica and rhodium nitrate in aqueous solution. The solvent is dried and heated in reducing atmosphere to yield supported catalyst [92]. Similarly Platinum supported on alumina (Pt/Al_2O_3) were conventionally prepared via wet impregnation route, where Pt salt is dissolved in aqueous solvent and alumina is dipped into that solution which was further processed to get Pt/Al_2O_3 [93].

2.5.5. Ceramic method

Ceramic method is an oldest known method for the synthesis of metal oxide. The ceramic method is a solid state method where metal oxides are prepared with solid material such as oxides, carbonate, sulfate, etc. where solid powder are mixed by means of mortar-pestle or ball milling and heating at a desired temperature. However, in this route maintaining a uniform homogeneity is a challenging task and due to this reason chemical methods are more favorable.

Many researchers have already shown a successful preparation of a desired material with the solid state method [94–97]. Report from Rajadurai et al. showed the preparation of $La_{2-x}Sr_xCuO_4$ via ceramic method and applied for the oxidation of CO [98]. Main agenda for development of a material using solid state method is for generating new defects. Also, this method is considered as an environmentally viable in synthesizing new material.

2.5.6. Hydrothermal method

Hydrothermal synthesis is a technique where materials can be synthesized in presence of high temperature and pressure. Generally, this process deals with the heating of a reacting sample at high pressure and temperature. These reactions are carried out in special unit called autoclave at a temperature between 100-300 °C.

Synthesizing a zeolite is the most important application of hydrothermal method. Zeolites can be synthesized by heating the precursor of aluminum and silicate gels in hydrothermal unit. Single crystals of GeO_2, SiO_2 (quartz), etc. was grown with the help of hydrothermal method for piezoelectric application [99]. In past decades, a wide variety of nano-sized catalytic materials has been synthesized through hydrothermal methods such as CuO–CeO_2 [100], MnM_2O_4 (M=Co, Ni, Cu) [32], Fe and Co binary metal oxide [101], Na–SSZ-13 [102], etc.

2.6. Metal oxide catalyst

Metal oxides are cited as successful heterogeneous catalysts that has countless benefits for society and the environment. Oxides of transition metal are observed as one of the important candidate for NO-CO redox reactions [20, 103] and CO oxidation by O_2 [14, 104, 105] due to their variable oxidation state, easy availability and low cost. Most of the time, these oxides are strategically modified by doping with alternate metal ion to improve the performance of the catalyst. Literature also shows the alternative catalyst modification such as composite oxide catalyst, metal/metal oxide supported catalyst for improving the oxidation-reduction property of the catalyst [73, 82, 86, 93, 100].

2.6.1 Single phase metal oxide catalyst

2.6.1.1 Chromium (III) Oxide (Cr_2O_3)

Chromium (III) oxide is known to be a remarkable material which has potential application in pigment and material industries. Mineral eskolaite is a naturally occurring form of chromium oxide and has rhombohedral corundum structure. In 1797, the French Chemist named Louis prepared Cr_2O_3 by reacting the $PbCrO_4$ (crocoite) with hydrochloric acid (HCl).

Although Cr_2O_3 has been widely used in pigment and semiconducting devices, it has also shown a prominent effect in catalysis.

With concentrating on chromium oxide, it has been observed that, considerably fewer reports are detected with respect to exhaust related reactions. During 1968, M. Shelef and co-worker studied the oxidation of CO using NO and O_2 on chromium oxide catalyst, where they reported T_{50} for CO oxidation at 220 °C (with NO) and 265 °C (with O_2) [106]. Yu Ren et. al. reported 50% CO conversion at 151 °C over Cr_2O_3 (pretreated at 200 °C) and further enhancement was produced which showed T_{50} at 147 °C by pretreating Cr_2O_3 at 400 °C [107]. Nasr E. et al. reported that formation of redox couple (Cr^{+3}/Cr^{+6}) on the surface of α-Cr_2O_3 is accountable for the high activity for CO oxidation [108]. Parameters such as oxygen mobility and active surface for adsorption-desorption process majorly decides the catalytic activity of these catalyst [109]. In respect of CO oxidation on Cr_2O_3 surface, the presence of two oxygen species was demonstrated by Masayoshi Kobayash et al. [110]. Here they reported the involvement of mobile oxygen for immediate conversion of CO to CO_2 as that of labile one.

Various sources have reported that the copper containing systems are one of the probable species for increasing the catalytic activity. When copper interact with the surfaces like CeO_2, ZrO_2, Al_2O_3, Fe_2O_3, it increases the surface oxygen mobility and surface reducibility was seen [111]. Mixture of Cu-Cr oxide [112] and supported Cu-Cr [113] are also known to generate active surface with high oxygen mobility for oxidation-reduction of carbon monoxide and nitric oxide. Such catalytic enhancement follows when different active sites from Cu and Cr_2O_3 synergistically contributes in the process of CO conversion [114].

2.6.1.2 Cerium (IV) oxide (CeO_2)

Cerium is a most commonly used rare earth metal as oxidation catalyst from the lanthanide series. Cerium in oxide form can exist in both +4 and +3 oxidation state giving CeO_2 and Ce_2O_3. The most stable form of cerium oxide is considered to be CeO_2 which adopts fluorite structure. Cerium dioxide has a wide application in oxidation catalysis, hydrogen production, oxygen sensing unit, solar cell, exhaust catalytic unit, etc.

From the literature it is observed that, among the various catalysts, cerium has generated a wide attention due to its electronic and redox property, which makes it a good oxygen

exchanging candidate [115, 116]. Cerium when modified with appropriate substituent cation, it can behave as oxygen efficient or oxygen deficient material. This substitution directly alters the redox nature of ceria, which disturbs their Ce^{+3}/Ce^{+4} redox cycles. In spite of extensive studies on cerium, it is still gaining continuous attention in recent detoxification studies.[115, 117, 118]

Cerium is known for its very good oxygen storing property, which can be easily made available during the reaction period with the help of redox nature of Ce^{+3}/ Ce^{+4}. Additionally, use of transition metal in CeO_2 can further be used to improve the oxygen storing –releasing property and to generate active sites for the reactants like CO which intern helps in triggering the CO oxidation reaction at much lower temperature.

It has been reported that the addition of metals like Ag, Ru, Pd, Pt, Rh, Cu, Mn, Co and Fe leads to enhancement in oxygen storage capacity and improved catalytic performance of a material. Recent literature shows variety of research on cerium based catalyst wherein its redox character is improved by addition of another oxide system such as CeO_2-CuO,[119–121] Co_3O_4-CeO_2,[122–124] Ce-Zr-O, [125, 126] M/CeO_2 (M=Au, Pd, Pt) [125, 127] etc. for CO and NO detoxification. A series of Fe_2O_3-CeO_2 composite prepared by Huizhi Bao et al. showed that coupling of oxides of iron and cerium provides a good platform for oxidizing CO than individual oxides [128]. Among the precious metals, Pd substitution in cerium oxide shows the highest amount of exhaust gas conversion at a lower temperature. S. Roy and Hegde reported 100% catalytic conversion of NO and CO over $Ce_{0.98}Pd_{0.02}O_2$ [129]. They also observed that performance of Pd on catalytic conversion was much higher than that of Rh and Pt substituted CeO_2. Also, enhanced redox nature formed by addition of transition metal was observed by incorporation more than one type of metal ions. Such multi doping has greater impact in converting CO compared to singly doped. Hongjian Zhu et al. reported that the co-doping Mn/Cu in CeO_2 solid solution can produce much better conversion by synergistic interaction as compared to Mn or Cu doped CeO_2 alone.[117] Salker et al. studied carbon monoxide oxidation with oxygen over Cu, Mn, Ag substituted CeO_2 and found that the catalyst composted of tri-metallic substitution showed higher activity than the catalyst containing only one dopant [130]. However, oxidation of CO to CO_2 requires material which has active sites and high oxygen storing-releasing capability to complete the oxidation process

more efficiently[131, 132]. A strategic way for developing a catalyst for both active sites and enhancing redox character can be achieved by using a small amount of precious metal in co-doped oxide system. Therefore incorporation of precious metal is believed to improve the CO adsorption on the surface and also helps in stabilizing the active host surface.

2.6.1.3 Copper (II) Oxide (CuO)

Copper (II) oxide is an inorganic compound with monoclinic crystal structure. Copper oxide (CuO) is black to brownish powder which is found in nature as melaconite, tenorite and paramelaconite mineral. In laboratory, it can be prepared using various methods like precipitation, combustion, sol-gel, etc. CuO is used in several technological fields, such as, gas sensor, catalytic processes, solar cell application and so on.

Copper oxide is extensively studied catalyst for the exhaust related catalytic reaction, more specifically detoxification of CO, NO and HC due to its high catalytic property. Even though copper oxide possesses a lower activity than Pt, Pd, Ag and Rh, it is much cheaper and is abundantly present as that of precious metals. From the Literature, it has been observed that, CuO when combined with CeO_2 [15, 119, 133–135], Al_2O_3 [136–138] and TiO_2 [139] can have higher catalytic conversion as compared to pure copper oxide. Such collective performance between Cu and other host metal provides high surface area and excellent oxygen mobility. In addition, when precious metals like Rh and Pd mixed with metal oxides, they exhibit a superior CO adsorption capacity and improve the conversion of NO and CO [27, 134, 140, 141] Recent investigations on Pd and Rh substituted CuO showed improved performance in CO-O_2 and NO-CO redox reaction [142].

In many reports, increased concentration of Cu in CuO-CeO_2 composite is seen to have enhanced its catalytic activity for detoxification reactions. Cu acts as promoter and improves the adsorption of CO due to its electron rich nature. Pristine CuO shows lower catalytic activity compared to metallic Cu or cuprous oxide [143]. However, it is well known that metallic Cu and Cu_2O tend to oxidizes as CuO [144]. Cu loading on TiO_2 is found to be effective for NO reduction to N_2 [145]. Cu dispersed on inert support like silica is also reported to increase the catalytic performance for nitric oxide reduction [145–147]. Substitution of Cu in transition metal oxides enhances the catalytic activity due to better CO

chemisorption property. Cu^{2+} substituted in Co_3O_4 is found to increase the oxygen mobility in it [148]. Recently, A. Glisenti and coworkers studied NO-CO redox reaction over $LaCo_{1-x}Cu_xO_3$ prepared by sol-gel method and observed that Cu substitution enhances the catalytic activity [149]. Promotional effect of Cu on detoxification of CO is also evident from the recent investigation of J. Gao et al., where they studied the effect of various transition metal like Fe, Co, Ni, and Cu substituted in MnO_2 [150].

2.6.2 Composite metal oxide

Metal oxides are considered as one of the most potential heterogeneous catalysts employed in different industrial applications. Most of the metal oxides holds both redox and acid-base character which is a significant property of superior catalyst. Generally, performance of the single metal oxides catalyst are comparatively low and due to this reason a foreign impurity is added to it for enhancing the performance of the catalyst. Recently, development in metal oxide composite catalyst has gain a huge importance all around the globe for generating high catalytic performance. In concern with environment, plenty of research is going on for developing a stable and highly efficient catalyst using various composition of transition metals along with precious metals to remove toxic gases like NO and CO [20, 27, 151–153].

Transition metal oxides and the metals composed of more than one oxidation state are important candidate for NO-CO redox reactions [20, 103] and CO oxidation by O_2 [14, 104, 105, 154] due to variable oxidation states, easy availability and low cost. Therein, manganese oxide [14, 155] and cobalt oxide [18, 20] have received considerable attention because of their redox capability. Studies showed that the system containing more than one metal have tendency to generate more conversion activity by increasing surface oxygen mobility. In recent research, Zang et al. studied NO conversion over CoO_x/Al_2O_3 system at 350 °C wherein it can reach less than 30% conversion; further bimetallic oxide supported aluminum oxide ($CuO\text{-}CoO_x/Al_2O_3$) was able to achieve 100% conversion at 350 °C [136]. Jiang et al. studied the $CeO_2\text{-}MoO_3\text{-}WO_3/TiO_2$ system, which showed the excellent catalytic performance for the NO conversion due to its high redox property and stronger adsorption property generated by strong interaction among Ce, Mo, W and Ti [156]. Similarly, studies on the composite system also showed that the addition of copper to CeO_2–Fe_2O_3 mixed metal oxides

produced a more significant impact on NO and CO conversion as that of Cu containing CeO_2 or Fe_2O_3 [19].

Although, metal oxides like manganese, chromium, copper and cobalt offer excellent catalytic performance but most of the time cannot compete with that of precious metals due to unique electronic property possessed by precious metals. The work of Lui et al. on Cu-Mn composite shows the requirement of 250 °C of temperature to achieve 100% NO conversion [157]. However, main disadvantage is the requirement of high temperature to convert NO efficiently, as stability of NO increases at higher temperature. Therefore developing a catalyst for lower temperature reaction is specifically significant. Loading Precious metal in the host oxide system can increase the efficiency of the catalyst material at lower temperature [158, 159]. Mergler et al. showed that the addition of Pt to CoO_x-SiO_2 composite system boosts the surface property of the catalyst which promotes the redox reaction [160]. Due to this reason, precious metals are combined with transition metals that contributes a significant impact in catalyzing exhaust related reactions [38–40, 161, 162]. From the literature, it has been also observed that instead of using single type of precious metal if pair of precious metal is used it can provide more synergy which can therefore enhance the catalytic process [163, 164].

Another way to enhance the catalytic performance of the composite catalyst is a method of catalyst preparation. Several types of approaches have been found in literature to prepare composite oxide catalyst for detoxification of CO, NO etc. such as hydrothermal method [135, 165, 166], self-template method [167], co-precipitation [15, 168], impregnation method [169–171] etc. In addition, ceramic method is also known to develop the insoluble inorganic materials for such catalytic processes [97, 172]. Kamolphop and others reported a comparison study on the silver/aluminum catalyst prepared via mechano-chemical method and silver/aluminum catalyst prepared via wet impregnation method for NO_x reduction [173]. They observed that the catalyst prepared with mechano-chemical route produced a significant activity at a lower temperature as compared to catalyst prepared via wet impregnation method. Jentoft et al. prepared the mixed metal oxides via mechano-chemical method and observed active for NOx reduction [174]. Recently, Salker et al prepared Ce-Cu nano-composite oxide catalyst via simple grinding method where they observed a superior activity in CO oxidation [175]. Such catalyst designing is a green and promising way for enhancing the catalytic performance towards a catalytic redox reaction as it helps in altering surface property and oxygen mobility.

3.1 Preparation of the catalyst

3.1.1. Preparation of monophasic oxides

3.1.1.1 $Cr_{2-x}Cu_xO_3$ (x = 0.00, 0.04, 0.08 and 0.16)

Combustion method was employed to synthesize the nano-sized $Cr_{1-x}Cu_xO_3$ (x = 0.00, 0.04, 0.08 and 0.16) catalysts. Weighed amount of Cr $(NO_3)_3 \cdot 9H_2O$ (Sigma Aldrich) and Cu $(NO_3)_2 \cdot 2.5H_2O$ (Sigma Aldrich) were dissolved in double distilled water and stirred for 15 minutes. Stoichiometric amount of glycine (metal nitrate: glycine, i.e., 1: 0.5) (Thomas baker) was added to the above solution with stirring. The resultant homogeneous solution was then slowly evaporated, which resulted in viscous gel. Further, the gel was heated in electric oven at 200 °C which resulted in auto-ignition to form foamy oxide. This oxide was then collected, grinded and calcined at 550 °C for 5 hours.

3.1.1.2 $Ce_{1-x}M_xO_2$ (M = Mn, Cu and Ag)

CeO_2 and Mn, Cu and Ag doped CeO_2 were prepared via tartaric acid assisted solution combustion method. The preparations were carried out by dissolving the stoichiometric amount of $Ce(NH_4)_2(NO_3)_6$ (Sigma Aldrich) and respective metal nitrate salts i.e. $AgNO_3$ (Sigma Aldrich), $Mn(NO_3)_2 \cdot 4H_2O$ (Sigma Aldrich) and $Cu(NO_3)_2 \cdot 3H_2O$ (Sigma Aldrich) in double distilled water. Weighed amount of tartaric acid was added to this mixture with constant stirring and heating on a hot plate cum stirrer and then was kept at 80 °C in an electric oven. The formed gel was than heated at 220 °C for 2 h and then calcined at 500 °C for 4 h to get the respective metal oxides.

3.1.1.3 $Ce_{1-x}Ru_xO_2$ (x =0, 0.01, 0.025 and 0.05)

In this case also the tartaric acid assisted solution combustion preparative route was employed to synthesize Ru substituted CeO_2 series. First and foremost, a stoichiometric amount of $Ce(NH_4)_2(NO_3)_6$ (Sigma Aldrich) and $RuCl_3$ (Sigma Aldrich) were dissolved in double distilled water. To the resultant mixture, weighed amount of Tartaric acid was added which was further kept on hot plate equipped with stirrer. Obtained gel was than combusted at 220 °C and kept at 500 °C for calcination for 4 h to produce 1%, 2.5% and 5% Ruthenium substituted Cerium oxide.

3.1.2. Preparation of composite oxides

3.1.2.1 CoO_x-MnO_x –X% PdO (X = 0, 1, 3 and 5)

Composite oxides with mole % Co:Mn ratio 1:1 (MM′) and palladium-containing Co–Mn oxide (MM′–X% PdO, where X = 1, 3 and 5) were prepared via the glycine combustion method. In this method, required amount of pure $Co(NO_3)_2 \cdot 6H_2O$ (Sigma-Aldrich), $Mn(NO_3)_2 \cdot 4H_2O$ (Sigma- Aldrich) and $PdCl_2$ (Sigma-Aldrich) were dissolved in pure double-distilled water. The glycine solution was initially prepared by dissolving weighed amount of glycine (Thomas baker) in double-distilled water and added to the metal–salt solution with constant stirring and heating. This mixture was then stirred for 4 h at 60 °C. Further, the solution was kept in electric oven at 80 °C for 8 h and then combusted at 200 °C. Combusted product was than calcined in muffle furnace at 500 °C for 4 h in air to obtain the final oxide.

3.1.2.2 CoO_x-MnO_x –X% Ag – y% Rh (X =0 and 5; y=0 and 1)

CoO_x-MnO_x composite system was prepared by combustion method using glycine as a combustion fuel. CoO_x-MnO_x with 1: 1 weight ratio of Co: Mn and CoO_x-MnO_x containing 5% Ag and/or 1% Rh was prepared by following method. Metal salts such as $Co(NO_3)_2 \cdot 6H_2O$ (Sigma-Aldrich), $Mn(NO_3)_2 \cdot 4H_2O$ (Sigma-Aldrich), $Ag(NO_3)$ (Sigma-Aldrich) and $Rh_2(OOCCH_3)_4$ was used as a source of Co, Mn, Ag and Rh, respectively. A known amount of respective metal salts were dissolved in double distilled water and to it appropriate amount of glycine (Thomas baker) was added. The mixture was heated with constant stirring for 2 h on hot plate cum stirrer and was then kept in oven at 80 °C for removing excess of water and further heated at 200 °C for 2 h where it gets combusted. Obtained product was then again heated at 500 °C for 4 h to remove any unburned species. The prepared CoO_x-MnO_x, CoO_x-MnO_x-5%Ag, and CoO_x-MnO_x-5%Ag-1%Rh were denoted as MM′, MM′-5%Ag, and MM′-5%Ag-1%Rh.

3.1.2.3 CuO-MnO_x –X% Al_2O_3 -y% Pd (X= 0 and 10; y = 0 and 2.5)

The series of aluminum and palladium containing composite oxide of copper – manganese were prepared by glycine combustion method. A required amount of $Cu(NO_3)_2 \cdot 3H_2O$ (Sigma Aldrich), $Mn(NO_3)_2 \cdot 4H_2O$ (Sigma Aldrich), $Al(NO_3)_3 \cdot 9H_2O$ (Sigma Aldrich) and $PdCl_2$ as a

source of Cu, Mn, Al, and Pd were dissolved into the double- distilled water. The obtained solution mixture was then added to the previously prepared glycine solution which was then subjected to heating and stirring. After 1 h of stirring, the solution was kept at 80° C in an electric oven to remove excess of water. Later, the metal nitrate-glycine gel was combusted at 200 °C for 2 h followed by calcining at 500 °C for 4 h to get the desired composite oxide. The composite catalyst CuO-MnO_x, CuO-MnO_x-Pd and CuO-MnO_x-Al_2O_3-Pd were named as CM, CMP and CMAP, respectively.

3.1.2.4 CoO_x-CuO- X% Mn (X=0, 10, 20, and 30)

A Similar glycine assisted combustion method was employed to prepare the cobalt- copper – manganese composite oxide by varying the amount of manganese. Metal source such as $Co(NO_3)_2 \cdot 6H_2O$ (Sigma Aldrich), $Cu(NO_3)_2 \cdot 3H_2O$ (Sigma Aldrich) and $Mn(NO_3)_2 \cdot 4H_2O$ (Sigma Aldrich) were used. The respective metal salts were dissolved using double distilled water, thereafter weighed amount of glycine was added with stirring and was then kept on hot plate cum stirrer. The mixture was then dried at 80 °C which was further kept at 200 °C for combustion process. Finally, the obtained oxide was heated to 500 °C for 4 h in muffle furnace. CoO_x-CuO, CoO_x-CuO- 10% Mn, CoO_x-CuO- 20% Mn and CoO_x-CuO- 30% Mn are abbreviated as Co-Cu, Co-Cu- 10% Mn, Co-Cu- 20% Mn and Co-Cu- 30% Mn, respectively.

3.1.2.5 Pd-Based metal Oxides

$Co_{0.95}Pd_{0.05}Cr_2O_4$ was synthesized using glycine as a combustion fuel. The calculated amount of $Co(NO_3)_2 \cdot 6H_2O$ (Sigma Aldrich), $Cr(NO_3)_3 \cdot 9H_2O$ (Sigma Aldrich), and $PdCl_2$ (Sigma Aldrich) was dissolved in double distilled-water. Glycine (Thomas Baker) was added to the above-prepared metal nitrate mixture and kept for heating with stirring for 4 h. Further, the above mixture was allowed to heat at 80 °C in an electric oven to form a gel which was then combusted at 200 °C followed by heating at 500 °C for 4 h to get Pd substituted Cobalt Chromite.

The PdO (2.5%) supported $Co_{0.95}Pd_{0.05}Cr_2O_4$ (PdO/$Co_{0.95}Pd_{0.05}Cr_2O_4$) was prepared using simple impregnation method. Weighed amount of $PdCl_2$ dissolved in the double-distilled water was added to the tartaric acid solution. Further, prepared $Co_{0.95}Pd_{0.05}Cr_2O_4$ was added to

Pd-Tartaric acid solution. Then the prepared sample was dried in an oven for 8 h at 90 °C and calcined at 400 °C for 4 h.

Similar glycine combustion method was employed to prepare the $Mn_{1.96}Pd_{0.04}O_3$ using $Mn(NO_3)_3 \cdot 3H_2O$ (Sigma Aldrich) as source of Mn ion. A weighed amount of metal salt and glycine (Thomas Baker) was dissolved with distilled water and kept for heating and stirring. Above mixture was allowed to form a gel which was then kept in an oven at 200 °C for 2 h. The obtained product was then calcined at 500 °C for 4 h to get $Mn_{1.96}Pd_{0.04}O_3$.

Preparation of $MnPdO_X/PdO/Co_{0.95}Pd_{0.05}Cr_2O_4$ was carried out by introducing $PdO/Co_{0.95}Pd_{0.05}Cr_2O_4$ powder in Mn-Pd-glycine solution, which was further followed by combustion route. The calculated amount of $Mn(NO_3)_3 \cdot 3H_2O$, $PdCl_2$, and glycine were dissolved in double-distilled water and kept for heating with stirring at 70-80 °C. To the above mixture, previously prepared $PdO/Co_{0.95}Pd_{0.05}Cr_2O_4$ powder was added with continuous stirring. The mixture was then kept at 80 °C to remove excess water. This precursor was then subjected to 200 °C for 2 h followed by heating at 500 °C for 4 h to produce $MnPdO_X/PdO/Co_{0.95}Pd_{0.05}Cr_2O_4$.

Series of all the catalysts prepared are $Co_{0.95}Pd_{0.05}Cr_2O_4$, $PdO/Co_{0.95}Pd_{0.05}Cr_2O_4$, $Mn_{1.96}Pd_{0.04}O_3$ and $MnPdO_X/PdO/Co_{0.95}Pd_{0.05}Cr_2O_4$ which are denoted as PdR1, PdR2, PdR3, and PdR3-PdR2, respectively.

3.1.2.6 Al_2O_3 modified $Cu_{0.95}Pd_{0.05}O$

Nano sized Pd substituted copper oxide ($Cu_{0.95}Pd_{0.05}O$) were prepared by glycine combustion method. $Cu(NO_3)_2 \cdot 3H_2O$ (Sigma Aldrich), $PdCl_2$ (Sigma Aldrich) and glycine (Thomas Baker) were used for obtaining the desired metal oxide nanoparticles. Suitable amount of $Cu(NO_3)_2 \cdot 3H_2O$ and $PdCl_2$ were dissolved in double distilled water followed by addition of glycine with a vigorous stirring and heating on hot plate. Obtained mixture was then subjected to 80 °C in an electric oven and then formed gel was heated at 200 °C for 2 h. Finally, the oxide was calcined at 500 °C for 5 h.

20% $Al_2O_3/Cu_{0.95}Pd_{0.05}O$ was prepared using aluminum nitrate and previously prepared $Cu_{0.95}Pd_{0.05}O$ powder. Weighed amount of aluminum nitrate was dissolved in double distilled

water, to it 2 g of $Cu_{0.95}Pd_{0.05}O$ powder and citric acid (1:2 ratio of Al : Citric acid) was added. Above mixture was then kept on heater cum stirrer and removed once the water gets evaporated completely. Obtained solid mixture was later heated at 200 °C for 3 h followed by heating at 450 °C for 4 h to yield 20% $Al_2O_3/Cu_{0.95}Pd_{0.05}O$

Later, glycine combustion method was employed to prepare 10%Al_2O_3-$Cu0_{.95}Pd_{0.05}O$ composite oxide wherein previously prepared 20% $Al_2O_3/Cu_{0.95}Pd_{0.05}O$ powder was used. $Cu(NO_3)_2 \cdot 3H_2O$ and $PdCl_2$ were dissolved in water and to that glycine and 20% $Al_2O_3/Cu_{0.95}Pd_{0.05}O$ were added. This mixture was then heated to 200 °C and later heated at 500 °C for 4 h to produce 10%Al_2O_3–$Cu_{0.95}Pd_{0.05}O$.

Series of all the catalysts prepared are $Cu_{0.95}Pd_{0.05}O$, 20% $Al_2O_3/Cu_{0.95}Pd_{0.05}O$ and 10%Al_2O_3-$Cu0_{.95}Pd_{0.05}O$ which are denoted as $Cu_{0.95}Pd_{0.05}O$, 20Al/$Cu_{0.95}Pd_{0.05}O$ and 10Al-$Cu_{0.95}Pd_{0.05}O$ respectively.

3.1.2.6 Ce-Cu Composite oxide

Cerium oxide was prepared using solution combustion method using tartaric acid as a fuel. Ammonium Cerium (IV) nitrate (Sigma Aldrich) was used as a source of cerium salt which was dissolved in double distilled water. To above solution, tartaric acid (Thomas baker) was added with constant stirring and heating. Further, the formed mixture was kept at 80 °C for 12 h and then it was combusted at 200 °C. Finally, calcination was done at 500 °C for 4 h to yield CeO_2.

Copper oxide was prepared from its nitrate precursor via glycine combustion method. The calculated amount of copper (II) nitrate (Sigma Aldrich) and glycine (Thomas baker) were dissolved in double distilled water and then above solution mixture was kept for heating with stirring. After saturation of the solution, it was then kept at 80 °C in electric oven until it forms a gel. Obtained gel was then heated at 200 °C for 2 h. Further, the obtained compound was kept at 500 °C for 4 h to yield CuO.

The CeO_2-CuO nano composite was prepared by physical grinding of previously prepared CeO_2 and CuO. The weighed amount of CeO_2 and CuO (1: 0.25) were ground using mortar

and pestle for 1 h. After grinding, the mixture was kept at 300 °C for 1 h to get CeO_2-CuO nano composite oxide.

3.1.2.7 CeRu - CuPd composite oxide

$Ce_{0.95}Ru_{0.05}O_2$ prepared via tartaric acid combustion method and $Cu_{0.95}Pd_{0.05}O$ prepared by glycine combustion method, was used to prepare the CeRu-CuPd composite oxide. $Ce_{0.95}Ru_{0.05}O_2$ and $Cu_{0.95}Pd_{0.05}O$ were taken with a weight ratio 1: 1 and grounded with mortar and pestle for 1 h. The grinded oxide was then kept at 300 °C for 1 h in muffle furnace to obtain CeRu-CuPd nano-composite oxide.

3.2. Preparation of the Gases

3.2.1. Preparation of the carbon monoxide (CO)

A chemical reaction is given as follow:

$$HCOOH \xrightarrow{H_2SO_4} CO + H_2O \quad \cdots\cdots\cdots\cdots (3.1)$$

CO was prepared by reacting formic acid and sulfuric acid in a controlled manner through dehydration process. When suitable amount of formic acid reacts with sulphuric acid, CO gets released which was passed through various traps to remove any impurity formed. Finally, it is stored in air tight glass bottle.

3.2.2. Preparation of the Nitric oxide (NO)

Nitric oxide (NO) is a colorless gas which is produced by using sodium nitrite, ferrous sulphate and sulphuric acid. Appropriate amount of ferrous sulphate is added to the sulphuric acid in two-neck round bottom flask. To above mixture, sodium nitrite solution was added with a calculated flow rate. The NO gas generated were passed over appropriate trap to yield pure NO gas which was later stored in an air tight glass bottle

3.3. Characterization Techniques

3.3.1. Powder X-ray diffraction (XRD)

The X-ray diffraction technique is a powerful tool which is used to characterize the crystalline materials. This technique is also useful in identifying the phase purity, average grain size, strain, crystal defect and crystal structure. The X rays generated by cathode rays, when interact with the electrons from an atom, gets scattered which gives the information regarding the electronic distribution within the material [176]. Constructive interference produced by the interaction of incident rays with the sample satisfies when it fulfills the Bragg's law:

$$n\lambda = 2d \sin\theta \qquad \text{.....} (3.2)$$

Where

n is an integer,

λ is wavelength of the X-rays,

d is the inter planner spacing and

θ is diffraction angle

The X- rays when bombarded on target material, the characteristic diffraction spectra is produced as intensity v/s 2 theta.

RIGAKU Ultima IV (X-Ray diffractometer) was employed to study the prepared oxide catalyst using Cu Kα as a target source having λ= 1.5418 Å. All the samples were recorded from angle 20° to 80° with a scanning step of 0.02.

3.3.2. Thermogravimetry/Differential Thermal Analysis (TG-DTA)

Thermal studies are an important study which provides the information regarding the structural changes with respect to temperature. Thermo- gravimetric analysis (TG) is mostly used to understand the thermal stability of material and is stated as change in the mass of sample as a function of temperature.

Another thermal method used is Differential Thermal Analysis (DTA) which has wide application to understand the material's structural behavior such as crystallization, sublimation, glass transitions and melting. The processes like melting shows endothermic peak due to positive ΔH value whereas when ΔH is negative exothermic peaks are observed (such as oxidation) [177].

To understand the decomposition behavior of the metal precursor and the stabilities of prepared oxide catalyst TG-DTA were performed. All the analyses were carried out on NETZCHSTA 409PC instrument at heating rate of 10 K min^{-1} in air atmosphere.

3.3.3. Infrared Spectroscopy (IR)

IR spectroscopy is a vibrational spectroscopy and is used to identify the various functional groups in a compound. In metal oxide system, it gives vibrational bands below 1000 cm^{-1}. In the preparative methods such as sol-gel, combustion, co-precipitation etc., formation of the metal oxide can be monitored by comparing the metal precursor and final metal oxide as metal oxides has a characteristic vibration bands below 1000 cm^{-1}. For IR analysis, SHIMADZU FTIR Prestige-21 spectrophotometer was used to record the IR spectra of the prepared samples. Oxide samples were previously ground with potassium bromide (KBr) and mounted in the instrument where IR radiations will interact with the sample to produce the spectra.

3.3.4. X-ray Photoelectron spectroscopy (XPS)

X-ray Photoelectron spectroscopy (XPS) studies is performed in vacuumed chamber wherein non-monochromatic source (X-Ray) is used. The XPS analyses are done to understand the chemical state and surface composition of the element. PHI 5000 Versa Probe II instrument were used to record the XPS spectra of the catalyst to examine the oxidation states of the elements present.

3.3.5. Scanning Electron microscopy (SEM)

SEM is a common tool to inspect the surface morphology of material. In principle, Scanning is processed by focusing a beam of light to the surface of a material which interacts with the sample surface to give surface morphology and elemental composition.

Scanning electron microscopic studies were performed on Zeiss evo18 instrument for morphologic view of the prepared catalysts. Samples were well dried before analysis at 150 °C.

3.3.6. Transmission Electron Microscopy (TEM)

Transmission electron microscope (TEM) is a powerful tool for understanding the particle shape and sizes of sample in the field at a nano-scale level. Here, a beam of energetic light is passed through the thin sample which later interacts with the analyzing sample to produce image.

Philips CM 200 instrument was used to record the TEM images and the HR-TEM studies were carried out on Jeol/JEM 2100 instrument operating at 200 kV.

3.3.7. BET (Brunauer–Emmett–Teller) Surface area studies

Surface area of a catalytic material is an important method which can be determined by physisorption of a gaseous molecule on a solid. It is observed that the catalyst with a nano size shows a high surface area as compared to the material in bigger size which makes nano size material highly reactive. Brunauer-Emmett- Teller (BET) theory extends Langmuir adsorption theory for adsorption of inert gases on the surface of solid. Absorption isotherm is given by inert gases like N_2, Ar, CO_2 etc. at a low pressure.

N_2-sorption studies were performed on the QUANTACHORME AUTOSORB iQ-MP-C instrument at liquid nitrogen temperature. The samples were degassed at 200 °C for 2 h to remove any adsorbed molecule from analyzing sample.

3.4 Temperature Programmed studies

3.4.1 Temperature Programmed Reduction studies

Temperature programmed reduction (TPR) is a material characterization technique used to examine the surface reduction pattern of a catalyst under various thermal conditions. This experiment is performed by placing fixed amount of catalyst in quartz tube. A reducing gas such as hydrogen is passed over the prepared bed by varying the temperature and results are

recorded. TPR pattern always depends on the surface oxygen mobility as more mobile oxygen can shift the TPR pattern to a lower temperature.

H_2-TPR was performed on Quantachrome Autosorb iQ-MP-C instrument for determining the oxygen mobility from the prepared catalyst. The samples were degassed at 250 ºC under inert atmosphere (He) prior to the analysis.

3.4.2 Temperature Programmed Oxidation studies

Temperature programmed oxidation (TPO) is a technique to examine the oxidation character of a sample with respect to the temperature. Oxidizing gas like oxygen is used to study the surface oxidation of the material. Here, suitable amount of catalyst was loaded in quartz tube and oxidizing gas, like O_2, was passed to carry out the measurement.

O_2-TPO studies were conducted on Quantachrome Autosorb iQ-MP-C instrument from 50-500 ºC on prepared catalyst. The acquired data was plotted as TCD signals v/s temperature.

3.4.3 Temperature Programmed Desorption studies

A temperature programmed desorption (TPD) process has been focused particularly in the field of catalysis as it allows one to understand the interaction between the solid catalyst and adsorbate which makes it a powerful tool to study the active sites present on the surface of the catalyst. TPD experiments are performed by placing a calculated amount of catalyst in analyzing tube. After cleaning the catalyst surface under inert atmosphere, the gases are adsorbed on its surface and later their desorption pattern were recorded with respect to temperature. To analyze the surface acidity, basic gases like NH_3 is used whereas CO_2 is used to monitor the basic sites present on the surface. Also many other desorption profiles can be studied depending upon the type of the information required such as CO-TPD, NO-TPD, NH_3-TPD, CO_2-TPD etc.

All TPD studies were performed on Quantachrome Autosorb iQ-MP-C instrument and the data in the form of TCD signals v/s temperature were recorded. For CO/NO/NH_3/CO_2-TPD studies respective gas was adsorbed on the catalyst and later desorption profile was recorded with linear increase in temperature. All the catalyst sample were activated before TPD run at 250 °C under inert atmosphere to remove any previously adsorbed species.

3.5 CO Chemisorption

A phenomenon wherein strong interaction occurs between adsorbate and adsorbent is known as chemisorption. Chemisorption occurs when any gaseous molecule irreversibly bound to the solid surface which cannot desorb at an ambient temperature. Amount of gas adsorbed is directly proportional to the active site present on the catalyst surface and when those active sites are consumed no further gas can chemically get adsorbed on the surface. Experimentally two types of chemisorption pathways can be used to study the chemisorption behavior i.e. static and dynamic. In static chemisorption, gas is adsorbed by as a function of pressure at constant temperature which gives two isotherms. One for amount of gas adsorbed and other one is irreversible adsorption. In dynamic chemisorption, a fixed amount of gas is passed over catalyst surface and amount of gas adsorbed can be detected via thermal conductivity detector.

CO Pulse titration method was used for CO chemisorption study on same Quantachrome Autosorb instrument. 100 mg catalyst was sandwiched between two quartz wool plugs in a reactor. After degassing the sample, 250 µL of CO was used for one pulse.

3.6 Catalytic Activity Measurement

3.6.1 CO oxidation Study using O_2

The catalytic detoxification of CO was carried out using continuous flow fixed bed reactor. 0.5-1.2 g of catalyst was packed in between glass wool plugs. Prior to analysis, catalysts were heated at 100 °C in inert atmosphere to remove any adsorbed species. Later, the reactor loaded with catalyst was placed in an electric furnace and the reaction temperature were measured using thermocouple placed just above the catalyst. The gases like N_2, O_2, H_2 required during the analysis were used from commercial source whereas the CO gas was prepared in the laboratory using standard preparative route. The feed gas for CO oxidation comprised of 5% CO and 5% O_2 in 90% of N_2 with a flow rate of 5000 mL h^{-1}. The reaction was monitored using online gas chromatography over molecular sieves 13x column for CO/O_2 and Porapak Q column to detect CO_2. The detail schematic representation of $CO\text{-}O_2$ reaction is presented below in Fig. 3.3.1.

.,

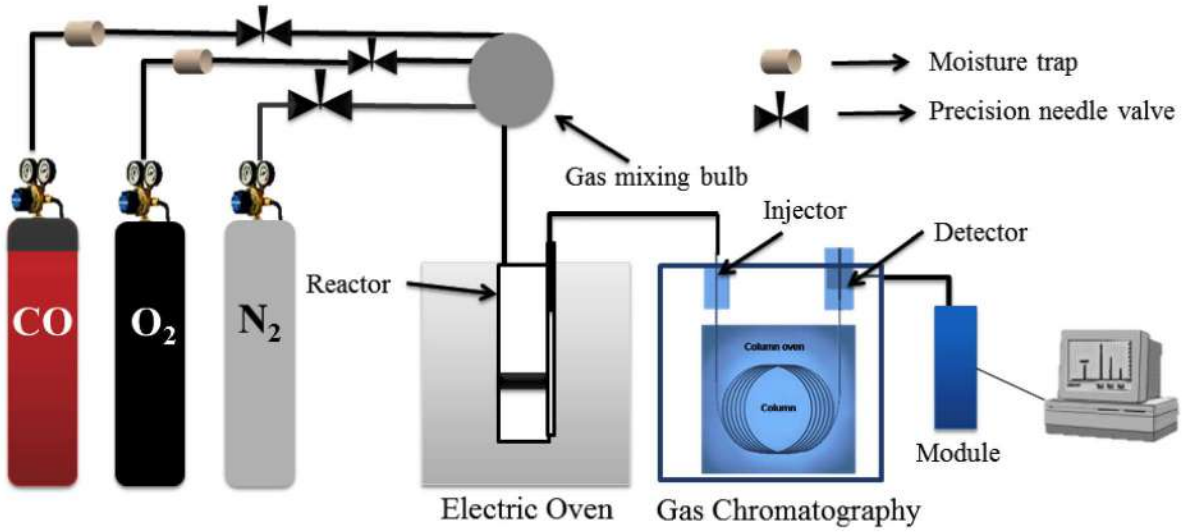

Fig. 3.3.1: *Schematic representation of CO-O_2 catalytic reaction set-up.*

3.6.2 NO-CO redox reaction study

The NO–CO reaction was studied in continuous flow fix bed reactor. The schematic representation of NO-CO redox reaction set-up is presented in Fig. 3.3.2. Both carbon monoxide and nitric oxide were prepared in the laboratory using standard preparative method; appropriate trap was used to purify the gases. Nitrogen (99.9%), oxygen (99.8%), hydrogen (99.9) and argon (99.99%) were used from pure commercial source. Catalytic redox reaction of NO–CO was studied using 5% NO and 5% CO in an argon atmosphere at the rate of 5000 ml h−1. About 0.5 - 1.2 g of the catalyst powder was sandwiched between glass wool plugs. Prior to the reaction, the catalyst was heated at 200 °C for 1 h in N_2 atmosphere. Further, the reactor was kept in electric oven to study its activity with respect to temperature. The feed gas and obtained product were monitored using online GC equipped with TCD detector over molecular sieve 13× and Porapak Q columns.

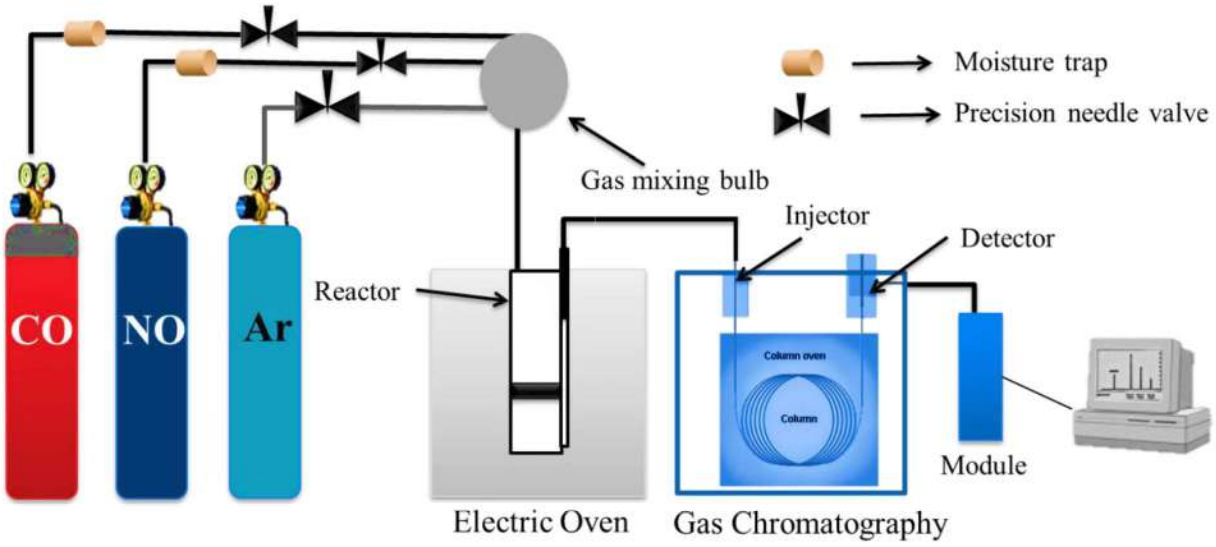

Fig.3.3.2: *Schematic representation of NO-CO catalytic reaction set-up.*

4.1 Thermal Studies (TG/DTA)

The TG/DTA technique was employed to study the thermal decomposition pattern of the precursor synthesized during the preparation of the oxide. Based on the produced data combustion temperature was determined of this precursor. Also, the thermal stability of some compounds was studied, as the thermal property is an important property in exhaust catalytic system.

TG-DTA studies was performed to examine the decomposition temperature of the prepared metal-tartarate precursor and also to study the temperature stability of the prepared oxide. TG-DTA of the Cerium-tartaric acid precursor has been shown in Fig. 4.1(a), which showed the complete decomposition of the precursor at around 220 °C. Endothermic (Endo) peak in the DTA studies at around 100 °C reveals the removal of water molecules from the precursor and the strong exothermic (Exo) peak at around 220 °C corresponds to the decomposition of carbon moiety from the system. In Fig. 4.1(b) a straight line in TG concludes the stability of CeO_2 till 800 °C. Also no phase change was seen from the DTA plot.

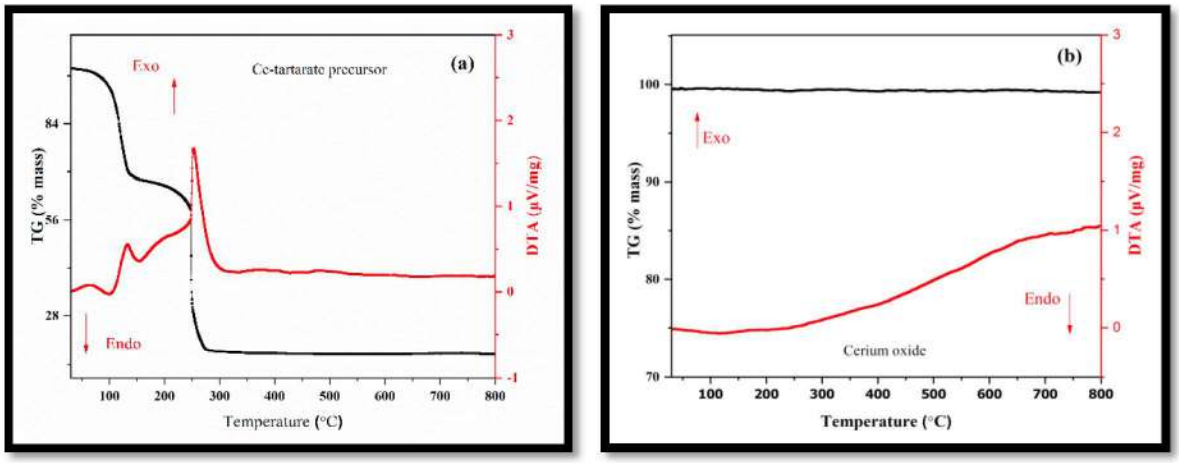

Fig. 4.1: *TG/DTA plots of (a) Ce-tartarate precursor and (b) CeO_2.*

The TG-DTA study was performed on the cobalt-manganese-glycine precursor and the trace of the same is shown in Fig. 4.2(a). From TG plot, it can be interpreted that the first drop in weight is due to dehydration of the precursor mixture. The second drop in weight at around 200 °C can be attributed to the loss of organic matter. This precursor shows the two peaks in DTA plot, wherein dehydration process showed a broad endothermic peak at around 100 °C

and a rapid combustion of precursor produced sharp exothermic peak at 160 °C. In Fig. 4.2(b) a straight line in TG up to 550 °C concludes the stability of Co-Mn composite oxide and further loss in weight observed can be due to conversion of Mn^{+4} to Mn^{+3}.

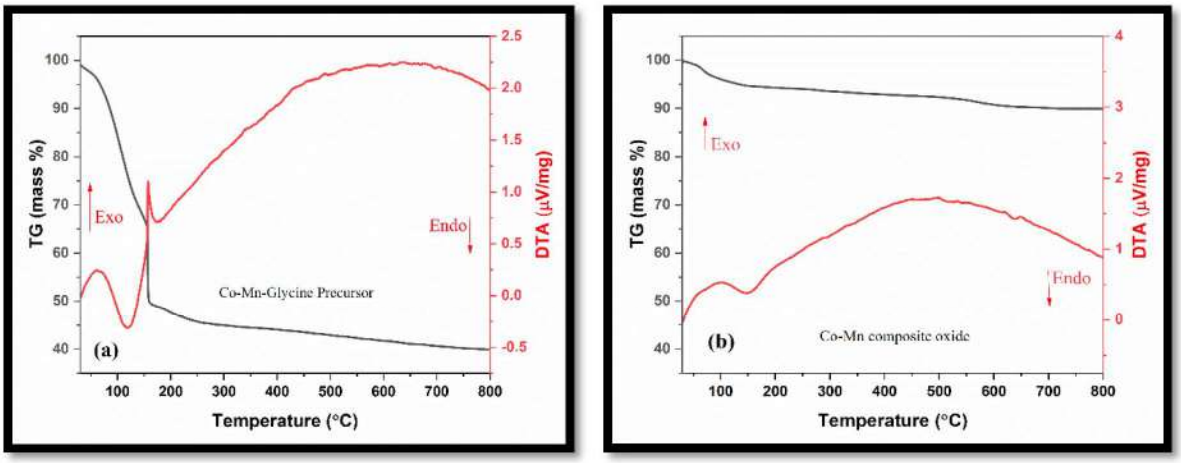

Fig. 4.2: *TG/DTA plots of (a) Co-Mn-glycine precursor and (b) Co-Mn composite oxide.*

A representative metal glycine precursor was studied from the Al and Pd containing copper-manganese series and presented in Fig. 4.3(a). Thermal decomposition of the Cu-Mn-Glycine precursor showed several steps.

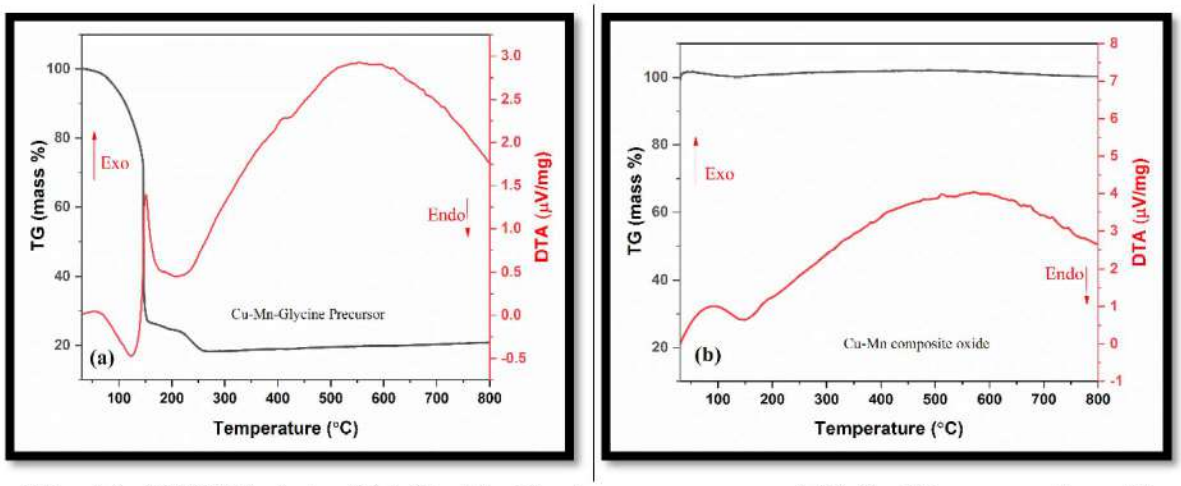

Fig. 4.3: *TG/DTA plots of (a) Cu-Mn-Glycine precursor and (b) Cu-Mn composite oxide.*

An initial loss in weight can be attributed to the removal of water from the precursor which can be confirmed from the endothermic peak observed in the DTA curve. Second drastic weight loss observed as a consequence of combustion process was evident from exothermic

peak in DTA curve. In Fig. 4.3(b) a straight line in TG concludes the stability of Cu-Mn composite oxide till 800 °C. Also no phase change was seen from the DTA plot.

Thermal studies were carried out from 30 to 800 ºC on Pd containing Cu-Glycine precursor and depicted in Fig. 4.4(a).

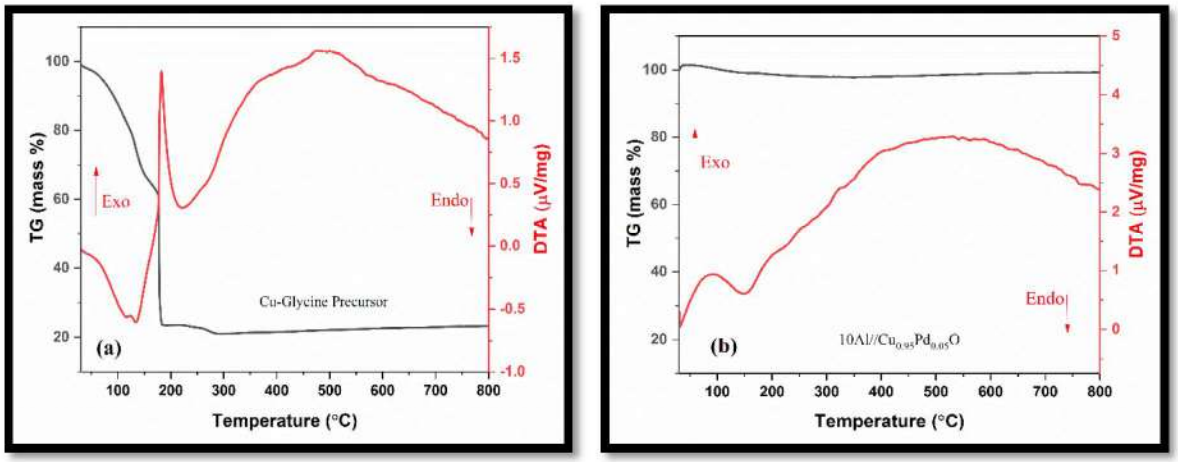

Fig. 4.4: *TG/DTA plots of (a) Cu-Glycine precursor and (b) 10Al-$Cu_{0.95}Pd_{0.05}O$ composite oxide.*

Here in Fig. 4.4 (a), DTA showed an endothermic peak below 150 ºC which can be attributed to the dehydration process. Further, loss in weight above 160 ºC and exothermic peak explains the combustion process wherein decomposition of a metal precursor occurs. Additionally, a straight line from 300 to 800 ºC suggests no weight loss concluding the excellent thermal stability of the final oxide. In Fig. 4.4(b), stability of 10Al-$Cu_{0.95}Pd_{0.5}O$ was reported, where a straight line in TG concludes the stability of 10Al-$Cu_{0.95}Pd_{0.5}O$ till 800 °C. Also, no phase change was seen from the DTA plot.

The thermal pattern of the $Ce_{0.95}Ru_{0.5}O_2$- $Cu_{0.95}Pd_{0.05}O$ (CeRu-CuPd) composite oxide is shown in Fig. 4.5. Initial thermal loss in weight was observed in the composite oxide, which corresponds to the loss of adsorbed water molecule. This further can be confirmed from the endothermic peak at around 150 °C in DTA profile.

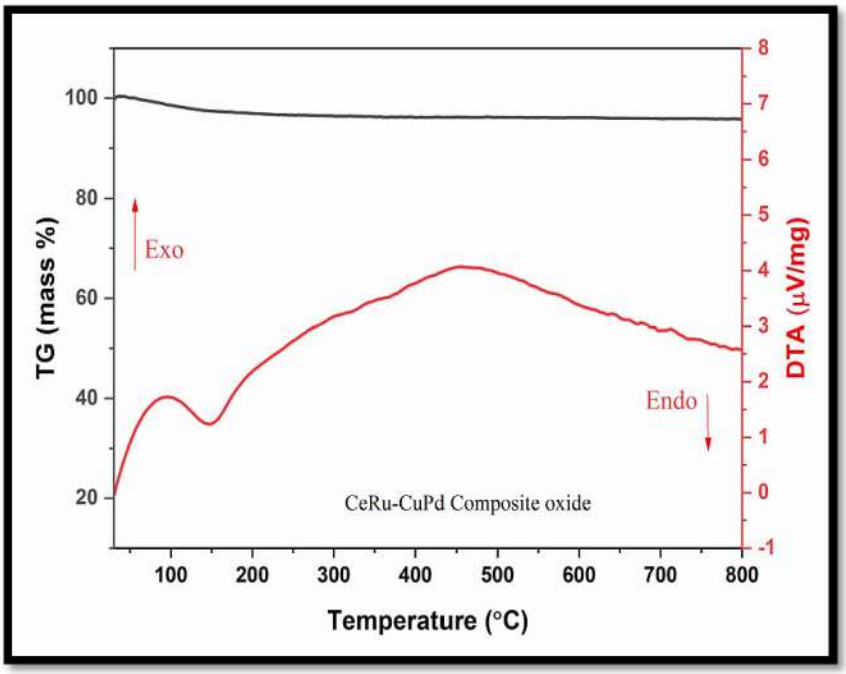

Fig. 4.5: *TG/DTA plots of CeRu–CuPd composite oxide.*

Thus, result suggests the excellent thermal stability of a composite oxide as no weight loss was observed till 800 °C.

4.2 X-ray Diffraction studies

Figure 4.6 shows the X-ray diffraction (XRD) pattern of Cr_2O_3 and series of Cu containing Cr_2O_3. X-ray diffraction pattern substantiates the formation of monophasic rhombohedral Cr_2O_3, which is confirmed with the JCPDS data file (01-084-1616) [178, 179]. X-ray diffraction pattern of $Cr_{1.96}Cu_{0.04}O_3$ shows no characteristic extra peaks of Cu, CuO, and Cu_2O whereas CuO impurity was observed with the increase of Cu content in Cr_2O_3. X-ray diffraction technique was carefully run to check for any impurity peak at selected 2θ values. Peak magnification of $Cr_{1.96}Cu_{0.04}O_3$ depicts a small shift in peak position (in all major peaks), which was not observed in higher concentration of copper-substituted biphasic Cr_2O_3, thus confirming the copper incorporation in chromium oxide. Also, no extra reflection was observed in XRD on slow scanning.

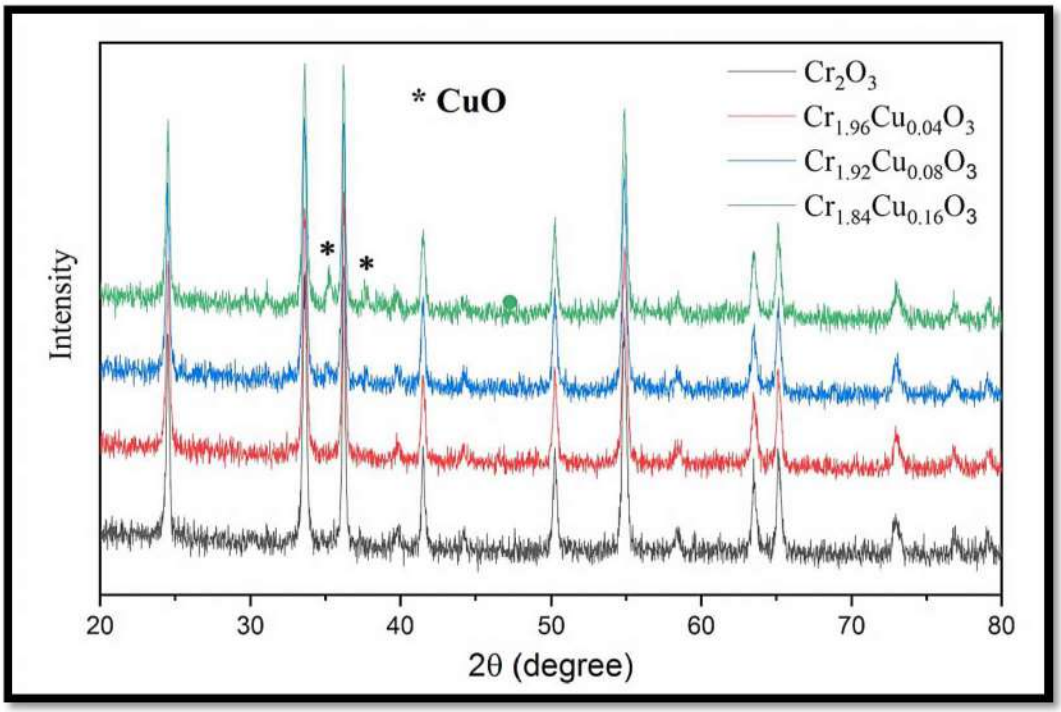

Fig. 4.6: *XRD pattern of Cu substituted Cr_2O_3 ($Cr_{2-x}Cu_xO_3$ (x=0, 0.04, 0.08, and 0.16)).*

Average crystalline particle sizes of $Cr_{2-x}Cu_xO_3$ (x = 0, 0.04, 0.08, and 0.16) were calculated using Scherrer's equation and the same is given in Table 4.1. Result showed the decrease in the crystallite size from 35 to 33 nm as Cu was incorporated into the Cr_2O_3 lattice.

Table 4.1: *Average crystallite Size of $Cr_{2-x}Cu_xO_3$ (x=0, 0.04, 0.08 and 0.16).*

Catalyst	Average crystallite size (nm)
Cr_2O_3	35
$Cr_{1.96}Cu_{0.04}O_3$	33
$Cr_{1.92}Cu_{0.8}O_3$	33
$Cr_{1.84}Cu_{0.16}O_3$	33

The XRD pattern of the prepared Mn, Cu and Ag substituted cerium oxides are displayed in Fig. 4.7. The crystallographic planes observed at ~ 28.51° (111), ~ 33.01° (200), ~ 47.55° (220), ~ 56.23° (311), ~ 59.23° (222), ~ 69.33° (400), ~ 76.75° (331) and ~ 79.06° (420) are matched with the JCPDS data card no. 00-034-0394 showing the characteristic plans of CeO_2.

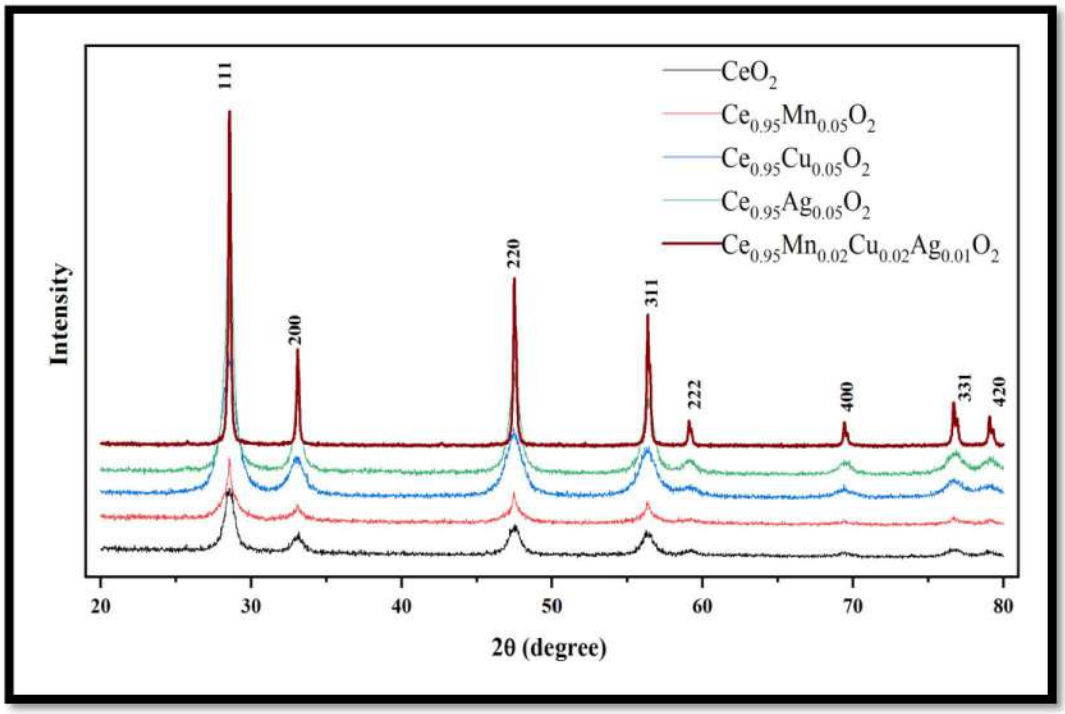

Fig. 4.7: *XRD pattern of CeO_2 and Cu, Mn and Ag substituted CeO_2.*

On carefully matching the peaks, the absence of extra reflections of impurity was observed, implying the incorporation of Mn, Cu and Ag in the CeO_2 lattice. Thus, confirms the formation of monophasic cerium oxide, which can be perfectly indexed to a cubic structure [180, 181].

Table 4.2: *Average crystallite Size of Mn, Cu and Ag substituted CeO_2.*

Catalyst	Average crystallite size (nm)
CeO_2	10
$Ce_{0.95}Mn_{0.05}O_2$	8
$Ce_{0.95}Cu_{0.05}O_2$	7
$Ce_{0.95}Ag_{0.05}O_2$	13
$Ce_{0.95}Mn_{0.05}Cu_{0.02}Ag_{0.01}O_2$	41

Average crystallite size of Mn, Cu and Ag substituted CeO_2 were calculated using Scherrer's formula and the same is tabulated in Table 4.2. Result showed decrease in average

crystallite size with addition of Cu and Mn while with the addition of Ag, it was found to increase.

The powder X-ray diffraction pattern of Ru substituted CeO_2 are depicted in Fig. 4.8.

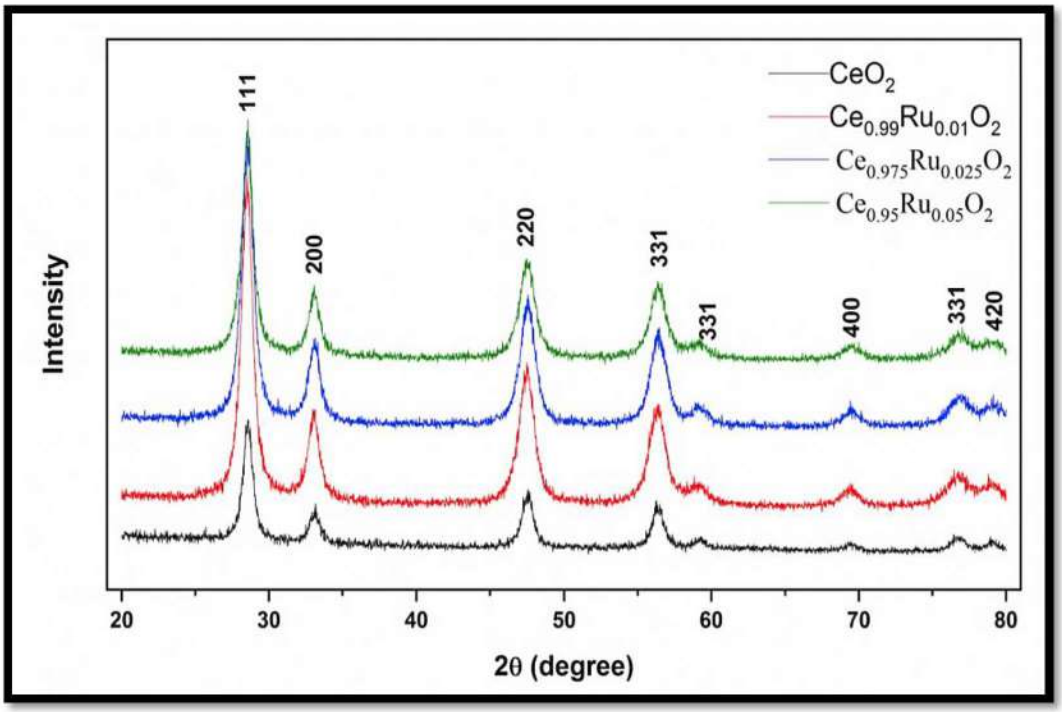

Fig. 4.8: *XRD pattern of CeO_2 and Ru substituted CeO_2 ($Ce_{1-x}Ru_xO_2$ (x=0.01, 0.025 and 0.05).*

The peaks at 2θ= ~ 28.51°, ~ 33.01°, ~ 47.55°, ~ 56.23°, ~ 59.23°, ~ 69.33°, ~ 76.75° and ~ 79.06° is an indication of the typical CeO_2 phase (JCPDS 00-034-0394).

Table 4.3: *Average crystallite Size of $Ce_{1-x}Ru_xO_2$ (0, 0.01, 0.025 and 0.05).*

Catalyst	Average Crystallite size (nm)
CeO_2	10
$Ce_{0.99}Ru_{0.01}O_2$	8
$Ce_{0.975}Ru_{0.025}O_2$	8
$Ce_{0.95}Ru_{0.05}O_2$	9

The absence of crystalline phase of Ru in studied XRD pattern confirms the monophasic CeO_2 formation. The average crystallite size calculated using Scherer's equation for series of

Ru substituted CeO_2 was in the range of 10 nm to 8 nm. The data pertaining to the same is given in Table 4.3.

XRD studies were carried out to examine the phases present in the Co-Mn composite oxide system and the results of MM′, MM′–5% PdO are exhibited in Fig. 4.9. XRD peaks of low crystalline sample resulted in weak diffraction pattern. Since the catalyst is a composite mixture, the representative oxides will be always there and because of their fine particle size all the diffraction peaks will not emerge; however, the constituent oxides will be always present. The standard JCPDS data cards for MnO_2, Mn_2O_3 and Co_3O_4 are 00-002-0567, 00-002-0909 and 01-080-1540, respectively.

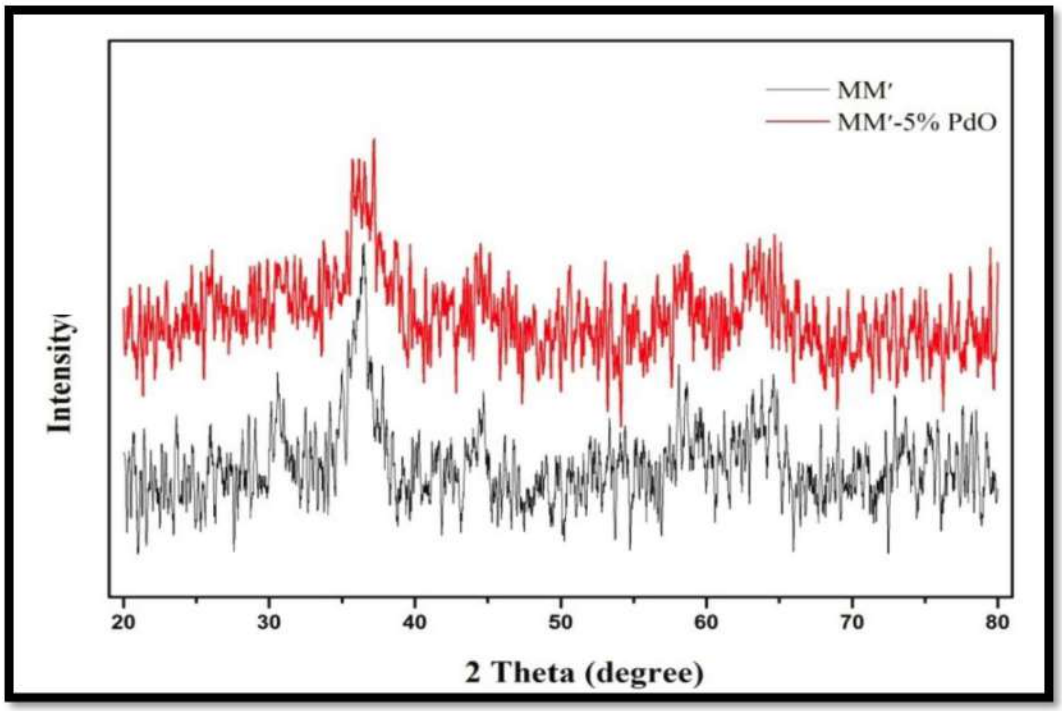

Fig. 4.9: *XRD patterns of MM′ and MM′–5% PdO.*

The X-ray diffraction pattern of MM′ and MM′-5%Ag-1%Rh composite catalysts were recorded to understand its crystallinity behavior and phases present in the system. The diffractograms of composite system is given in Fig. 4.10.

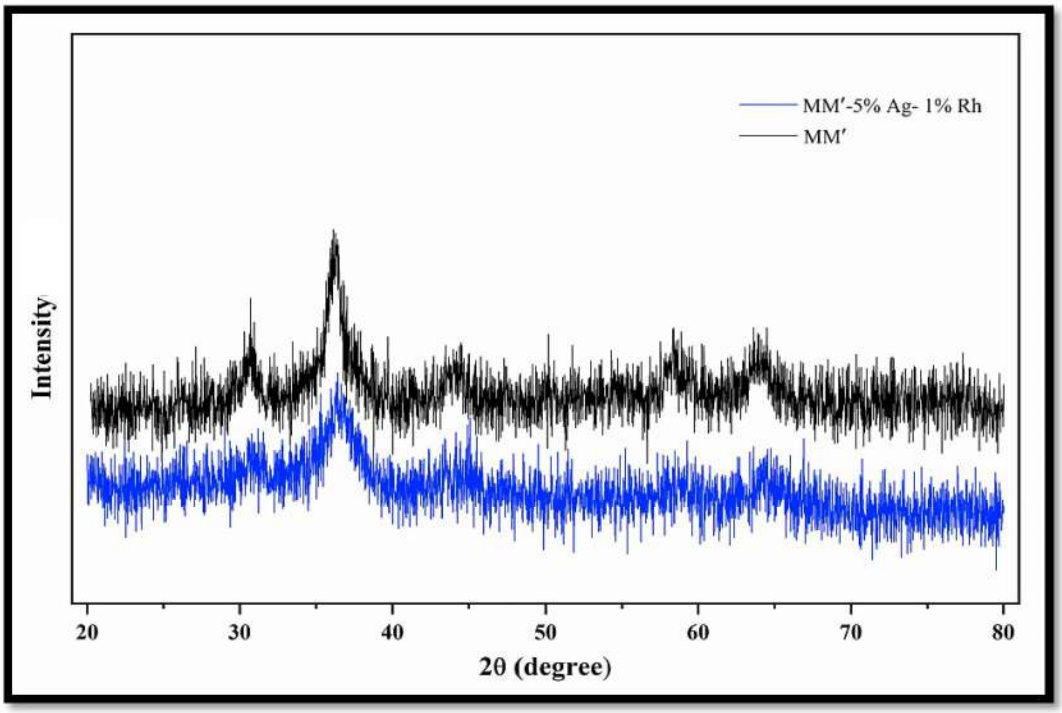

Fig. 4.10: *XRD patterns of MM′ and MM′-5%Ag-1%Rh.*

The presence of Co_3O_4, MnO_2 and Mn_2O_3 phases were detected which were matched with the standard JCDPS data 01-080-1540, 00-002-0567 and 00-002-0909, respectively. The low crystalline nature of the composite exhibiting broad peaks indicates the nano nature of the prepared composite catalyst.

The crystallographic data of the Cu-Mn and Cu-Mn-Al-Pd composite oxide were studied through X-ray diffraction tool (XRD) and their spectra are depicted in Fig. 4.11. The spectrum of Cu-Mn composite oxide shows well-defined peaks, which indicates the formation of different types of phases in composite oxide system. By carefully observing diffraction peaks of composite oxides, the occurrence of $Cu_{1.5}Mn_{1.5}O_4$, CuO and Mn_2O_3 was confirmed with JCPDS data 00-035-1171, 01-080-0076 and 01-089-2809, respectively. Additionally, some more peaks of Al_2O_3 were detected (JCPDS card No.00-010-0173) in Cu-Mn-Al-Pd oxide system and observed to be merging with the Cu-Mn oxide peaks. Further, a broad XRD peak and decrease in the intensity of diffraction peaks was seen by addition of Al and Pd in Cu-Mn composite as that of Cu-Mn composite oxide. This result confirms the nano nature of the Cu-Mn-Al-Pd composite oxide.

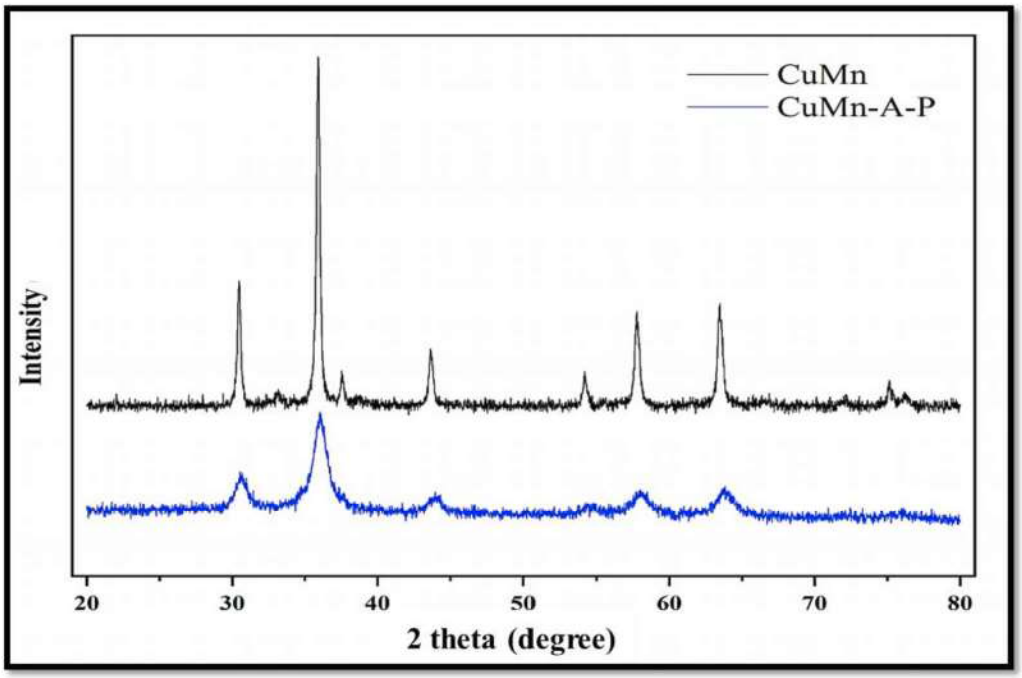

Fig. 4.11: *XRD patterns of Cu-Mn and Cu-Mn-A-P composite oxide.*

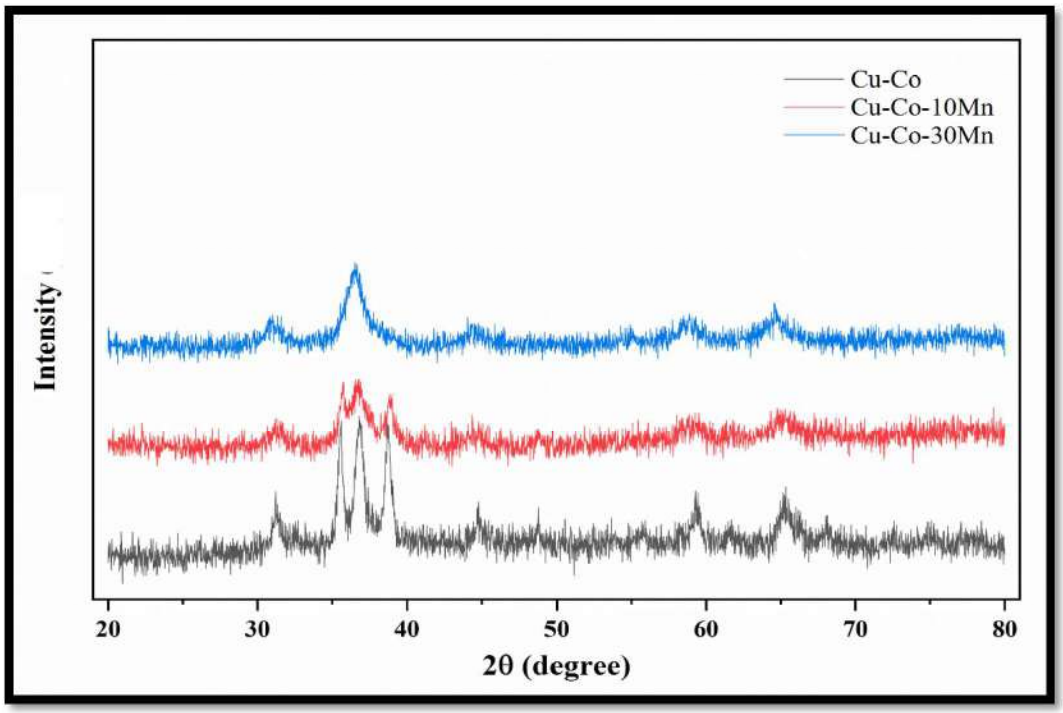

Fig. 4.12: *XRD patterns of Cu-Co, Cu-Co-10Mn and Cu-Co-30Mn composite oxide.*

XRD pattern of Mn containing Cu-Co composite oxide series prepared by glycine combustion route are shown in Fig. 4.12. The strong diffraction peaks of cobalt oxide (Co_3O_4)

and Copper oxide (CuO) were distinctively confirmed with JCPDS No. 01-080-1540 and 00-048-1548, respectively. As Mn is added to Cu-Co composite oxide system, a slow disappearance of some peaks has been observed. This can be attributed to the formation of extra phase of Mn in the Cu-Co-10Mn and Cu-Co-30Mn composite oxide. Furthermore, poor crystallinity in all the prepared series demonstrates the nano nature of the composite oxide catalysts.

XRD pattern of PdR1, PdR3 and PdR3-PdR2 are shown in Fig. 4.13. The formation of monophasic $Mn_{1.96}Pd_{0.04}O_3$ was confirmed by the XRD pattern, which shows the absence of any impurity phase with the highest intensity peak at 32.93 ° [182, 183].

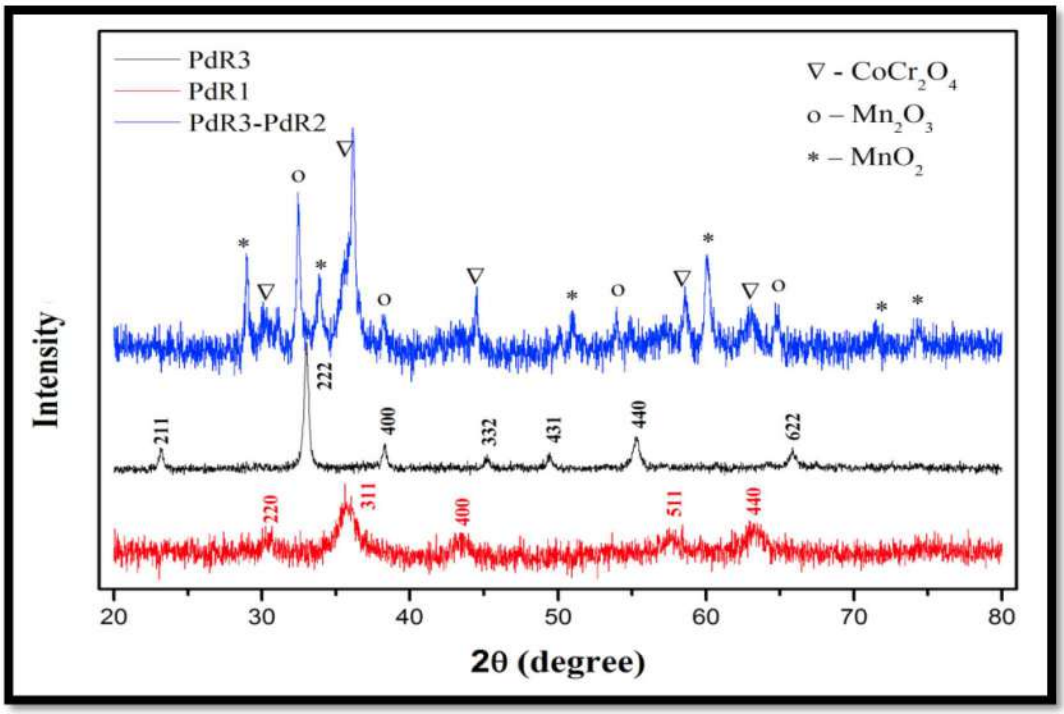

Fig. 4.13: *XRD patterns of PdR1, PdR3, and PdR3-PdR2.*

Further, its phase formation was confirmed by matching 2 theta values with JCPDS data card No 00-041-1442. Similarly, a phase of $Co_{0.95}Pd_{0.05}Cr_2O_4$ was carefully matched with JCPDS data card No. 00-022-1084 with the main peak at 35.62° [184]. No extra reflections were observed, thus confirming monophasic $Co_{0.95}Pd_{0.05}Cr_2O_4$. A well designed Pd containing manganese oxide engineered cobalt chromite showed the presence of $CoCr_2O_4$, Mn_2O_3 and

MnO_2 (JCPDS data card No. 00-044-0141) phases. Poor crystallinity by the XRD data attributes to the nano nature of the prepared samples.

The X-Ray diffraction pattern of Pd doped copper oxide and Al modified $Cu_{0.95}Pd_{0.05}O$ are displayed in Fig. 4.14.

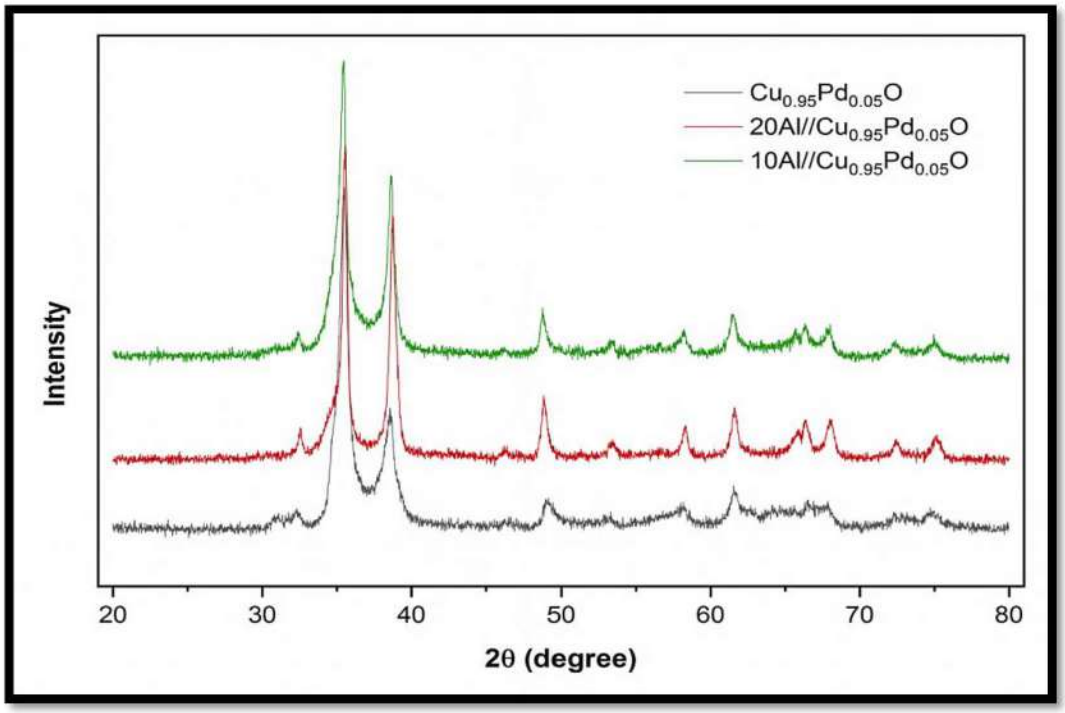

Fig. 4.14: *XRD patterns of $Cu_{0.95}Pd_{0.05}O$ and Al modified $Cu_{0.95}Pd_{0.05}O$.*

The peak intensity of $Cu_{0.95}Pd_{0.05}O$ is observed as less intense which may be due to the poor crystallinity of the sample. Although, the peaks are poorly diffracted in XRD pattern of $Cu_{0.95}Pd_{0.05}O$, no extra reflection of Pd is seen. This has been confirmed by comparing the diffraction pattern of $Cu_{0.95}Pd_{0.05}O$ with the standard JCPDS card no. 01-080-0076. While in Al modified $Cu_{0.95}Pd_{0.05}O$, the intensity of the peak is slightly enhanced and also a small hump has been observed at 35°, which occurred due to the formation of Al_2O_3 (JCPDS card no. 00-010-0173) in the composite oxide system.

The XRD patterns of the prepared CeO_2, CuO and CeO_2-CuO nano composite are shown in Fig. 4.15. The cubic structure demonstrated by CeO_2 [185, 186] and the monoclinic structure by pure CuO has been displayed in the powder patterns [187, 188]. Respective

phases was also matched with the JCPDS data card No. 00-034-0394 for CeO_2 and 00-048-1548 for CuO.

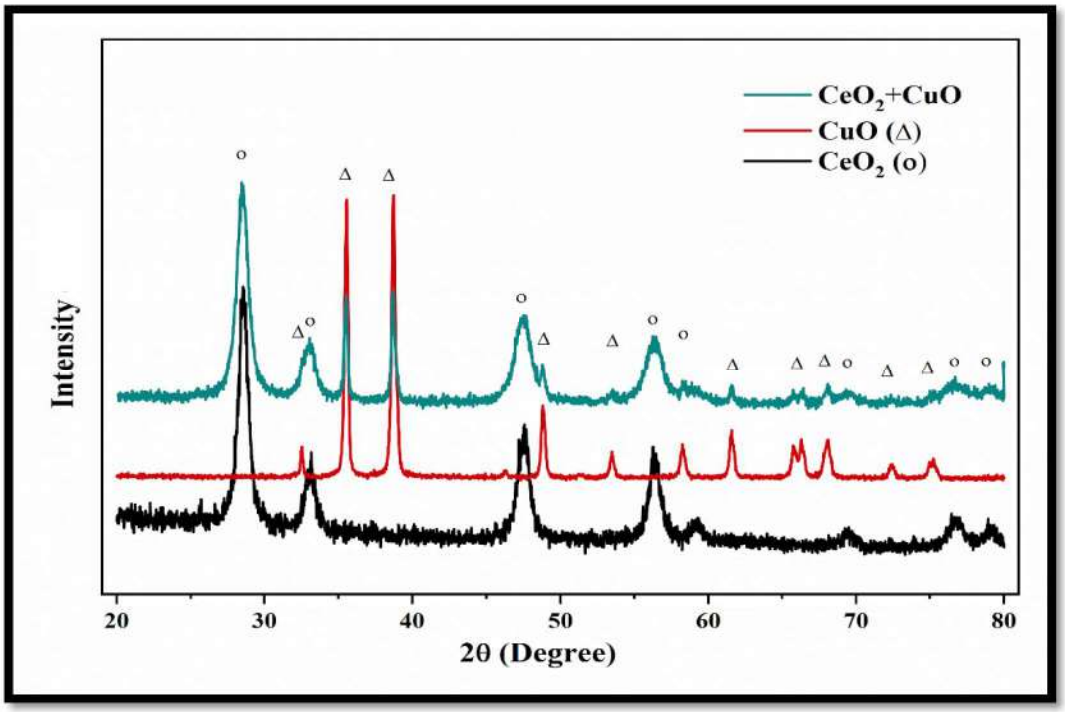

Fig. 4.15: *XRD patterns of CeO_2, CuO and CeO_2-CuO composite oxide.*

CeO_2-CuO composite oxide showed the presence of both the phases of CeO_2 and CuO in the XRD pattern indicating the presence of cerium oxide and copper oxide. Although, the composite were prepared by grinding for 1 h and heating at 300 °C for 1 h, extra impurity phases were not detected as can be ascribed from the XRD data.

4.3 IR spectroscopy studies

IR spectra of the metal precursor and the prepared oxides were recorded. The IR spectra of metal-oxygen vibrations observe below 1000 cm^{-1}. Thus, comparing the IR spectra of precursor with that of metal oxide helps in confirming the complete decomposition of metal precursor to their respective metal oxide.

Infrared spectra of metal-glycine precursor and $Cr_{2-x}Cu_xO_3$ (x = 0.04, 0.08 and 0.16) are shown in Fig. 4.16. The metal precursor shows the IR bands which are the characteristics of

glycine. The peaks observed in the 3000 – 3500 cm $^{-1}$ region of IR spectra is attributed to the presence of moisture and N-H group [189].

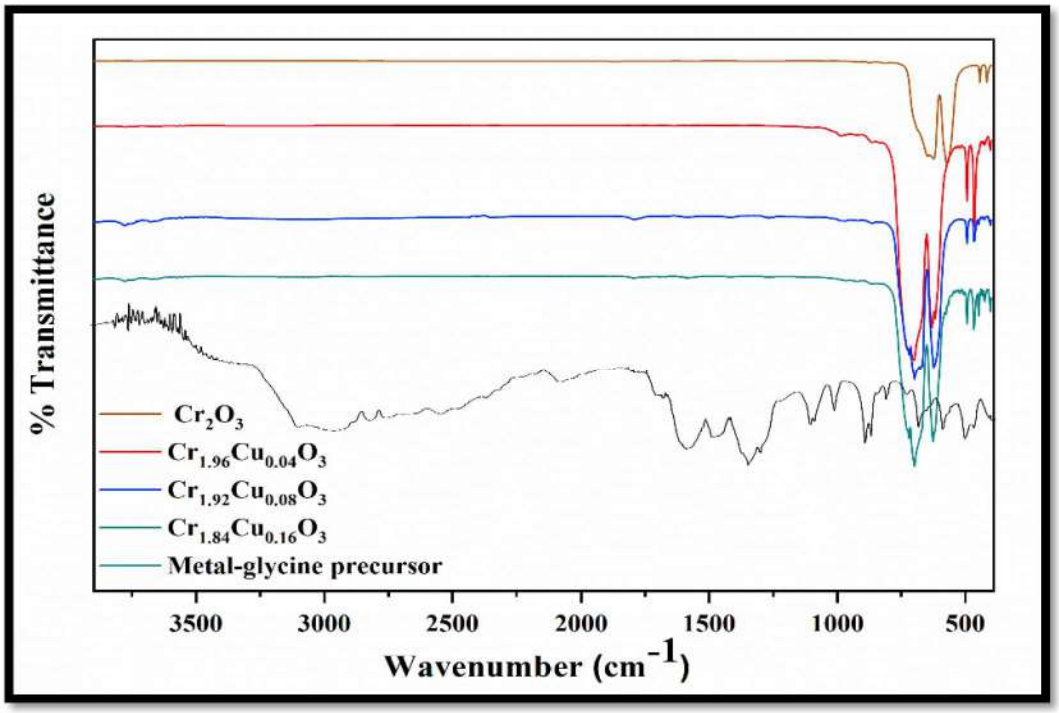

Fig. 4.16: *IR spectra of Cr-glycine precursor and $Cr_{2-x}Cu_xO_3$ (x=0.04, 0.08 and 0.16).*

The disappearance of the organic peaks after the combustion of metal precursor was observed which can be seen from the given chromium oxide spectra. The IR bands appear below 600 cm^{-1}. These are the characteristics vibrations of the metal oxides. The spectrum shows 2 strong peaks at 624 and 572 cm^{-1} due to Cr-O stretching vibration (symmetric and asymmetric) and 2 sharp bands of O^{2-} displacement in lattice at 445 and 415 cm^{-1}, which confirms the presence of Cr_2O_3 phase [190–192].

Figure 4.17 shows the IR spectra of metal-tartaric acid precursor, cerium oxide and metal substituted (Mn, Cu, and Ag) cerium oxide. IR spectra were recorded in the region from 400 to 4000 cm^{-1}. Typical IR vibrations were observed for prepared precursor which can be assigned for IR bands of tartaric acid. IR spectra of tartaric acid showed various peaks in the studied region. Final compound produced after combustion of precursor showed absence of tartaric acid peaks and showed only metal-oxygen vibration as reported for cerium oxide [193, 194].

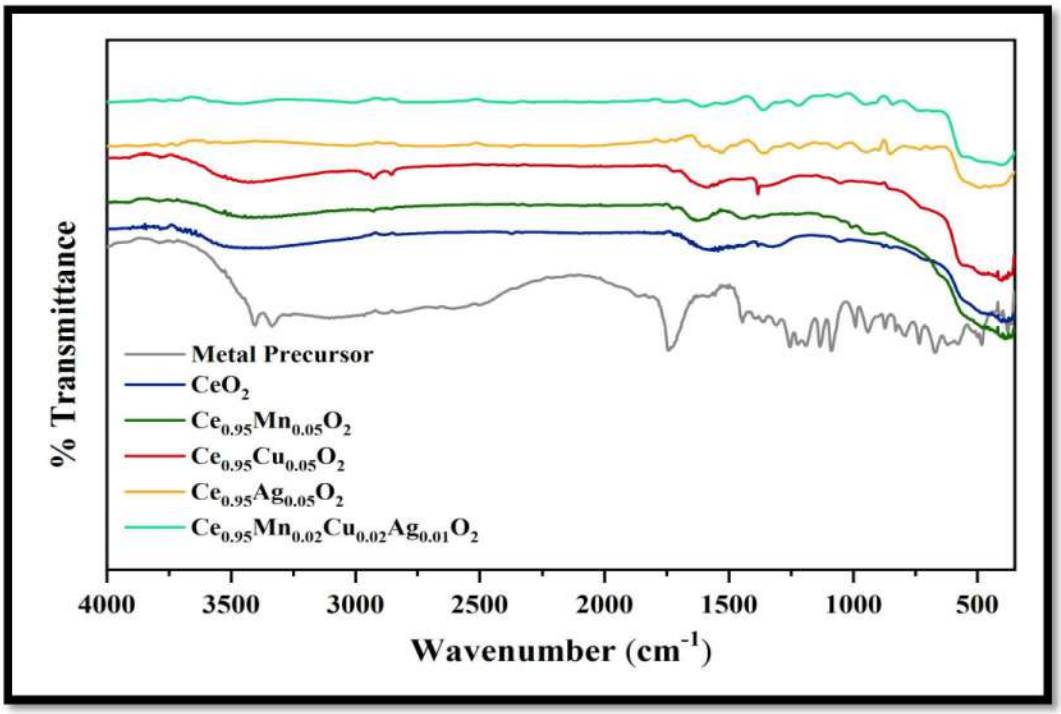

Fig. 4.17: *IR spectra of Ce-tartrate precursor and Cu, Mn, Ag containing CeO_2.*

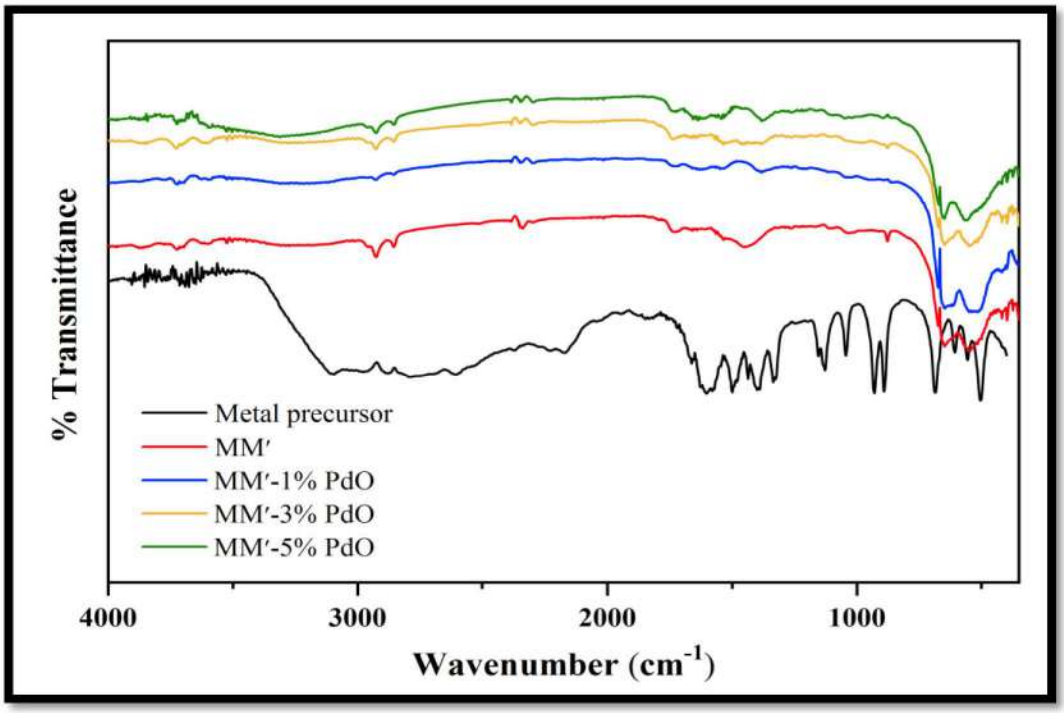

Fig. 4.18: *IR spectra of metal precursor and palladium containing cobalt-manganese composite oxide.*

The IR spectra of the palladium containing cobalt-manganese composite oxide series (MM′) and glycine precursor are presented in Fig. 4.18. IR spectra were recorded in the region from 400 to 4000 cm^{-1}. Characteristic glycine peaks are observed for the metal-glycine precursor. Decomposition of this precursor at 200 °C leads to disappearance of these peaks and formation of new metal-oxygen vibrations as depicted in IR spectra in Fig. 4.18.

The IR scanning for all the composite oxides were carried out from 4000 to 400 cm^{-1}. The characteristic IR vibration bands of mix metal oxides are presented in Fig. 4.19. The IR peaks which observed in finger print region are not found in metal oxide system, which mostly arises in metal precursor. When metal precursor gets decomposed, all the carbon species gets oxidizes leaving behind the metal oxide. Therefore, such disappearance of organic peak confirms the conversion of metal precursor to metal oxide as shown by the metal-oxygen vibration band below 1000 cm^{-1}.

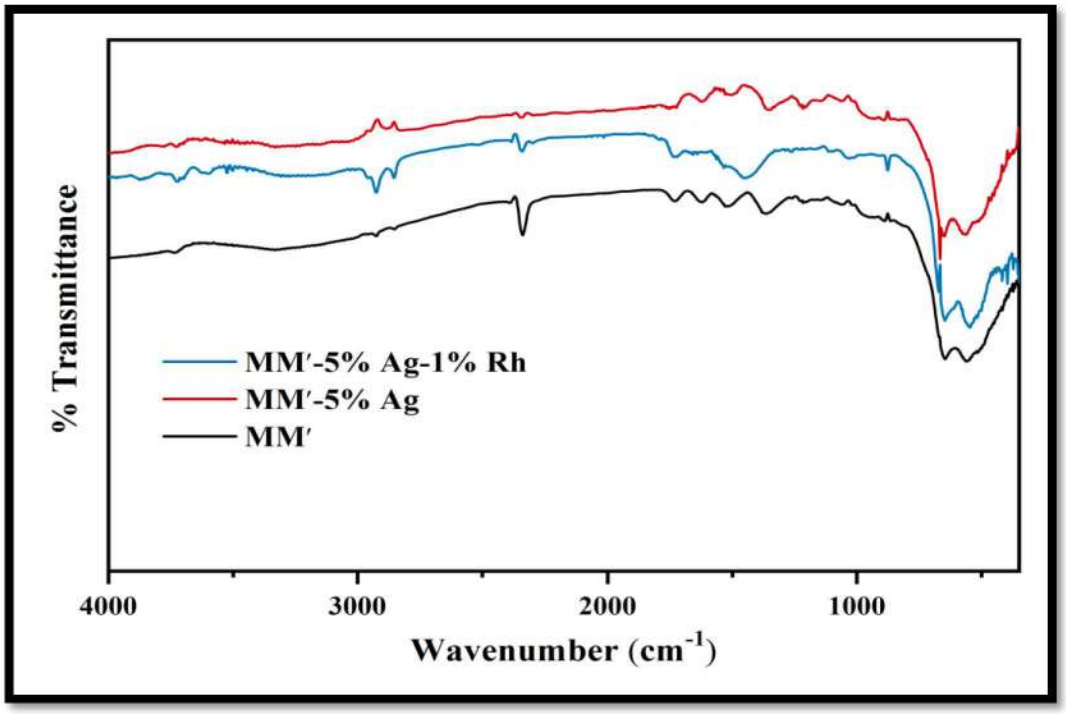

Fig. 4.19: *IR spectra of Co-Mn and precious metal containing Co-Mn composite oxide.*

In the IR spectra of manganese containing copper-cobalt composite oxide and glycine precursor, absence of spectral similarity was seen implying the proper combustion of metal-glycine precursor as depicted in Fig 4.20. The IR spectrum of precursor shows a broad peak (3600 to 3000 cm^{-1}) of O-H and N-H species. IR spectra of the composite oxide shows change in the IR vibration in the region 750-400 cm^{-1} when manganese is added to the Cu-Co composite oxide, conveying the formation of a new phase.

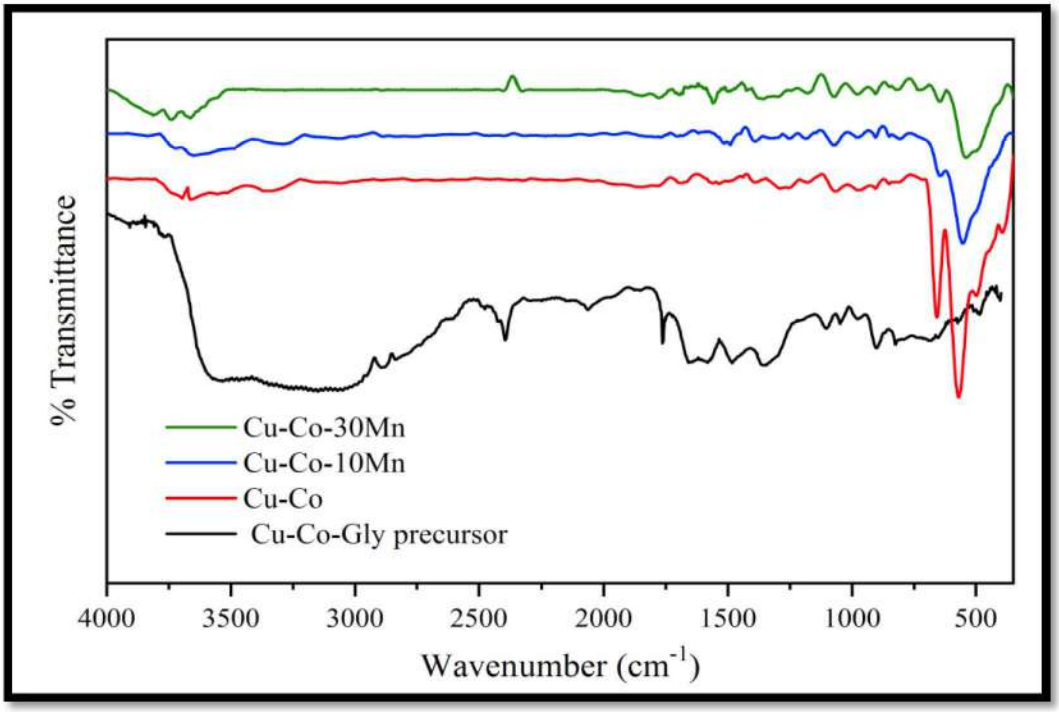

Fig. 4.20: *IR spectra of Cu-Co-gly precursor and Mn containing Cu-Co composite oxide.*

IR spectra of Al modified $Cu_{0.95}Pd_{0.05}O$ oxide series after the combustion process is depicted in Fig. 4.21. The spectra of oxides showed no characteristic peaks of glycine, which confirms the decomposition of glycine precursor to oxide. The intense peak at around 500 cm^{-1} can be ascribed for metal-oxygen bond vibration; also broad peak of adsorbed moisture was seen arising from O-H vibration.

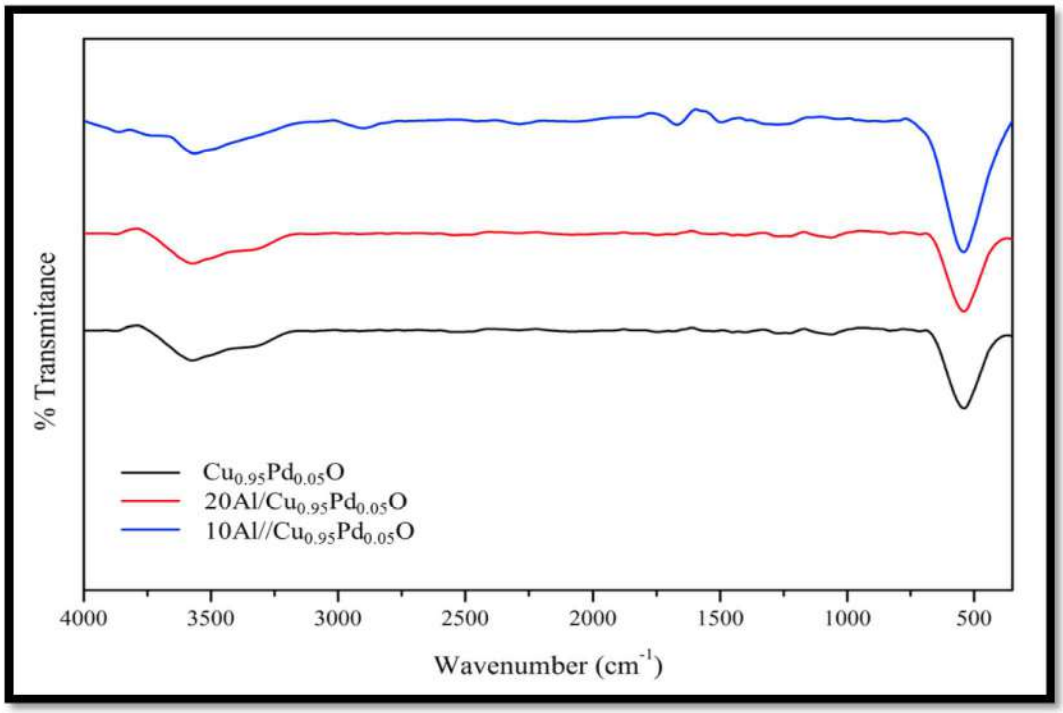

Fig. 4.21: *IR spectra of $Cu_{0.95}Pd_{0.05}O$ and Al modified $Cu_{0.95}Pd_{0.05}O$.*

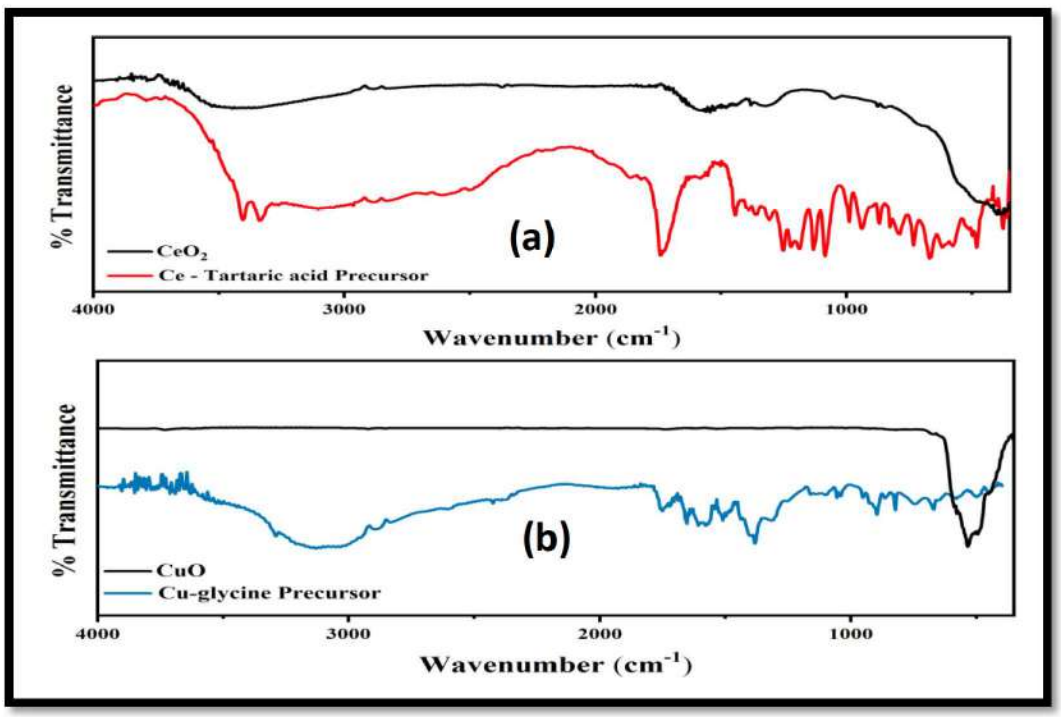

Fig. 4.22: *IR spectra of Ce-tartarate precursor (a), Cu-glycine precursor (b), CeO_2 (a) and CuO (b).*

IR spectra of metal precursors (Ce-tartaric acid and Cu-glycine) and respective metal oxides (CeO_2 and CuO) are displayed in Fig. 4.22. IR spectra of metal precursor showed the characteristic peaks of respective organic moiety, which were than compared with the spectra of metal oxide. Absence of organic peaks in the metal oxide spectrum confirms the complete removal of the organic species from the system.

The IR spectra of the prepared $Ce_{0.95}Ru_{0.05}O_2$, $Cu_{0.95}Pd_{0.05}O$ and CeRu-CuPd composite oxide are recorded from 400-4000 cm^{-1} and are presented in Fig. 4.23. The broad vibrational band at 3000-3600 cm^{-1} is of hydroxyl group from the surface adsorbed water.

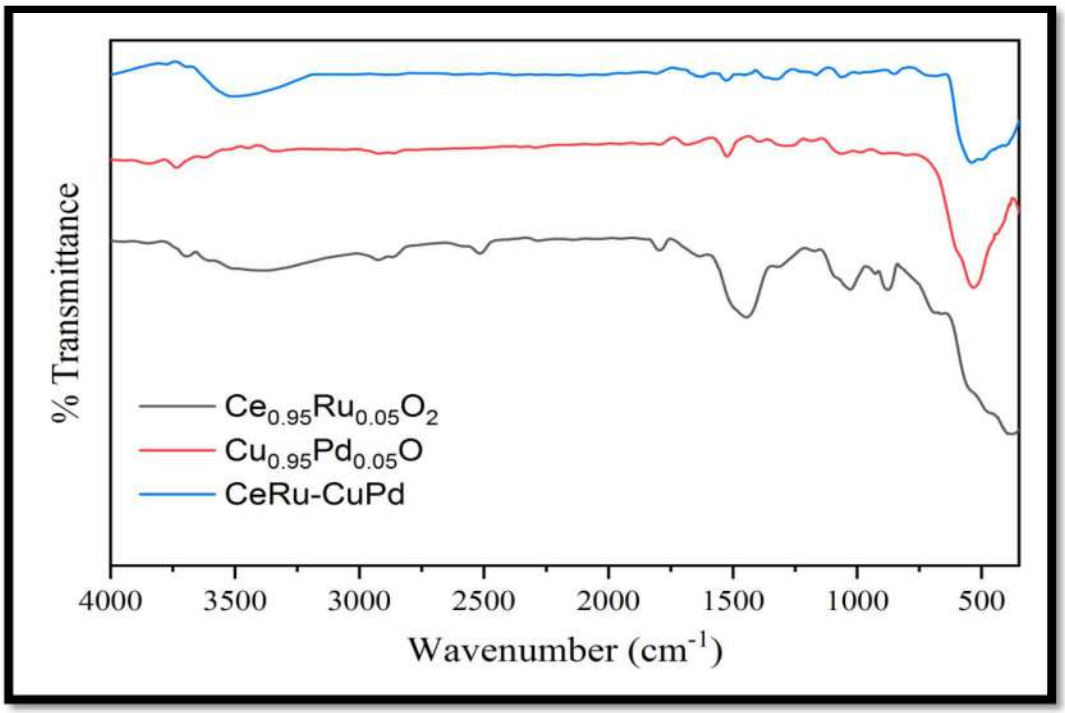

Fig. 4.23: *IR spectra of $Ce_{0.95}Ru_{0.05}O_2$, $Cu_{0.95}Pd_{0.05}O$ and CeRu-CuPd composite oxide.*

In the presented spectra the broad band observed below 750 cm^{-1} can be ascribed to the metal-oxygen vibration (Ce-O and Cu-O) of oxides.

4.4 X–Ray Photoelectron spectroscopy studies

The Chemical state and surface composition of nanostructured $Cr_{1.96}Cu_{0.04}O_3$ was studied through XPS. The XPS spectra of Cr 2p, Cu 2p, and O 1s are presented in Fig. 4.24. Asymmetric peaks from the spectra were resolved using Gaussian curve fitting method. The

Cr 2p splits into two peaks i.e. Cr $2p_{3/2}$ and Cr $2p_{1/2}$ at 576.10 and 585.52 eV respectively showing chromium in Cr^{+3} in agreement with literature [195, 196]. Cr $2p_{3/2}$ spectra can be fitted into two peaks at 576.10 eV indicating presence of Cr^{+3} and 578.01 eV showing presence of higher oxidation Cr species in the system. Further an energy difference of 9.42 eV between Cr $2p_{3/2}$ and Cr $2p_{1/2}$ confirms the presence of Cr_2O_3 species in the system [196, 197].

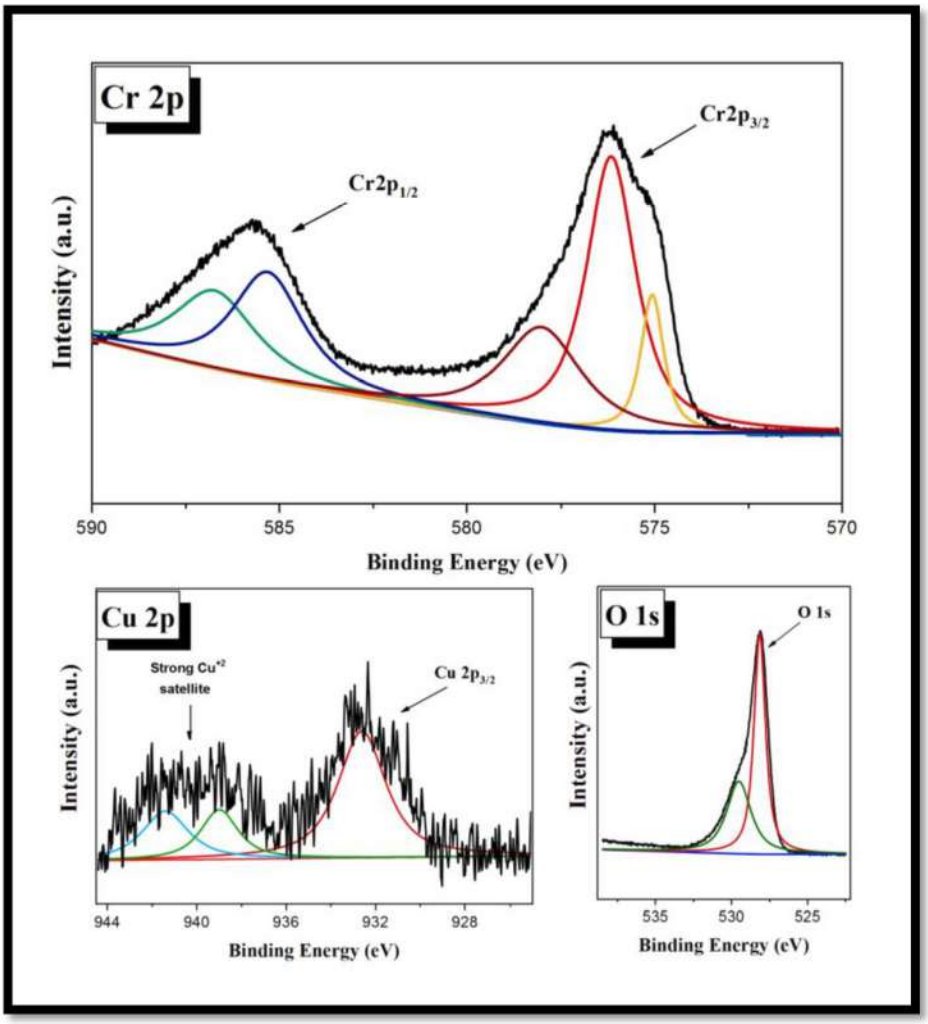

Fig. 4.24: *X-ray photoemission spectra of Cr 2p, Cu 2p and O 1s from* $Cr_{1.96}Cu_{0.04}O_3$.

The de-convolution of Cu $2p_{3/2}$ spectra demonstrates the peak at 933.53 eV and strong satellite peaks at 939.92 and 942.39 eV in higher binding energy region confirming that copper is in Cu^{+2} state. Also presence of shake-up satellite peak is an evidence of Cu^{+2} species in the system [198, 199].

To understand the type of oxygen present in $Cr_{1.96}Cu_{0.04}O_3$, O 1s is de-convoluted and depicted in Fig. 4.24. Gaussian fitting of asymmetric O 1s peak shows the existence of two peaks at 529.37 and 530.50 eV. The peak with BE of 529.37 eV is attributed to O^{2-} ion and the small peak at higher B.E is due to surface defect as also seen in literature studies [20, 200].

XPS analyses were conducted in order to understand the chemical valence state of the elements present in $Ce_{0.95}Ru_{0.05}O_2$. As shown in Fig. 4.25, the existence of Ce, Ru and O in analysed sample were confirmed through XPS studies.

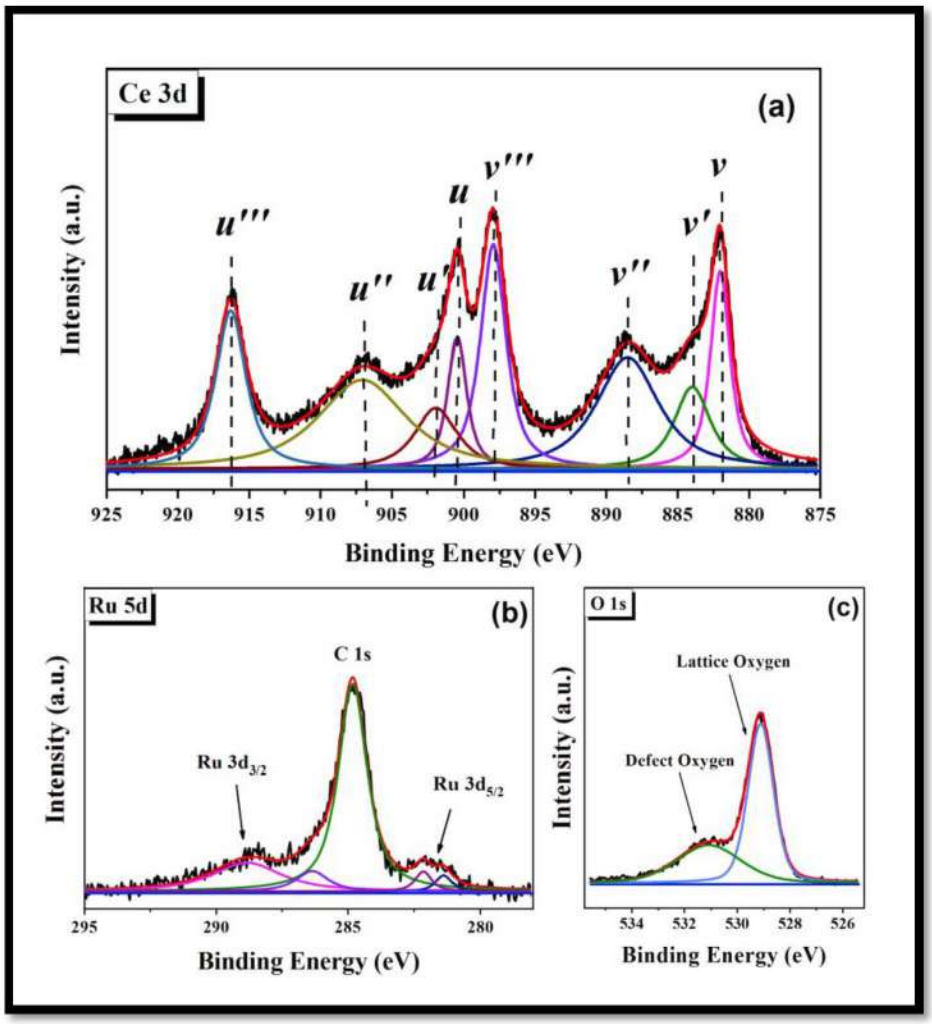

Fig. 4.25: *XPS spectra of (a) Ce 3d, (b) Ru 5d and (c) O 1s from* $Ce_{0.95}Ru_{0.05}O_2$.

Ce 3d spectrum of $Ce_{0.95}Ru_{0.05}O_2$ shows the presence of both Ce^{+4} and Ce^{+3} as depicted in Fig. 4.25a. The Ce 3d spectrum was fitted with Gaussian-Lorentz fitting, which showed eight photo-electrons splitting. From observed peaks, 3 $d_{5/2}$ spin orbit state was labelled as 'v' and

$3d_{3/2}$ orbital states was denoted as 'u' symbol. Ce is often observed as an important component due to its typical redox pair. The peaks labelled as v′ and u′ were attributed to +3 state of Ce and the remaining six photoemission peaks (i.e. v, v″, v‴, u, u″ and u‴) confirms the presence of Ce^{+4} state [201, 202].

Figure 4.25b shows the Ru 3d spectra along with C 1s peak. The existence of Ru species was clearly identified by peak fitting procedure wherein presence of Ru^{+4} was revealed [202, 203].

The XPS spectrum of O 1s is shown in Fig. 4.25c and various kinds of oxygen present were investigated. The main peak appeared at lower binding energy i.e. 529 eV is attributed to lattice oxygen and the oxygen which appears at higher binding energy at 531.22 eV is considered to be due to defect oxygen [21, 190].

The XPS of MM′-5% PdO was performed in order to carry out its chemical characterization. The oxidation state and its chemical environment are represented in Fig. 4.26. The Fig. 4.26a shows the Co 2p spectra (Co $2p_{3/2}$ and Co $2p_{1/2}$) which is fitted in six photoelectron peaks. Co $2p_{3/2}$ splits into two peaks with binding energy of 779.6 eV and 781.7 eV which corresponds to Co^{+3} and Co^{+2} , respectively [204]. Appearance of satellite peak at 769.9 eV is due to the surface Co^{+2} species [204].

XPS spectra of Mn 2p (Fig. 4.26b) showing peaks of Mn $2p_{3/2}$ and two peaks of Mn $2p_{1/2}$ conclude the presence of two oxidation states of Mn. Photo emission at BE 640.6 eV (Mn $2p_{3/2}$) and 651.9 eV (Mn $2p_{1/2}$) confirms the 3+ oxidation state of Mn. The Mn 3/2 and Mn 1/2 peaks appears at 643.4 eV and 653.07 eV , respectively, confirming the coexistence of Mn^{+3}/Mn^{+4} in the system [204, 205].

The characteristic peaks of Pd^{+2} are depicted in Fig. 4.26c. The peak at binding energy of 337.6 eV (Pd $3d_{5/2}$) and 343 eV (Pd $3d_{3/2}$) are found to be characteristic of Pd^{+2} species which are similar to the literature data [57, 206].

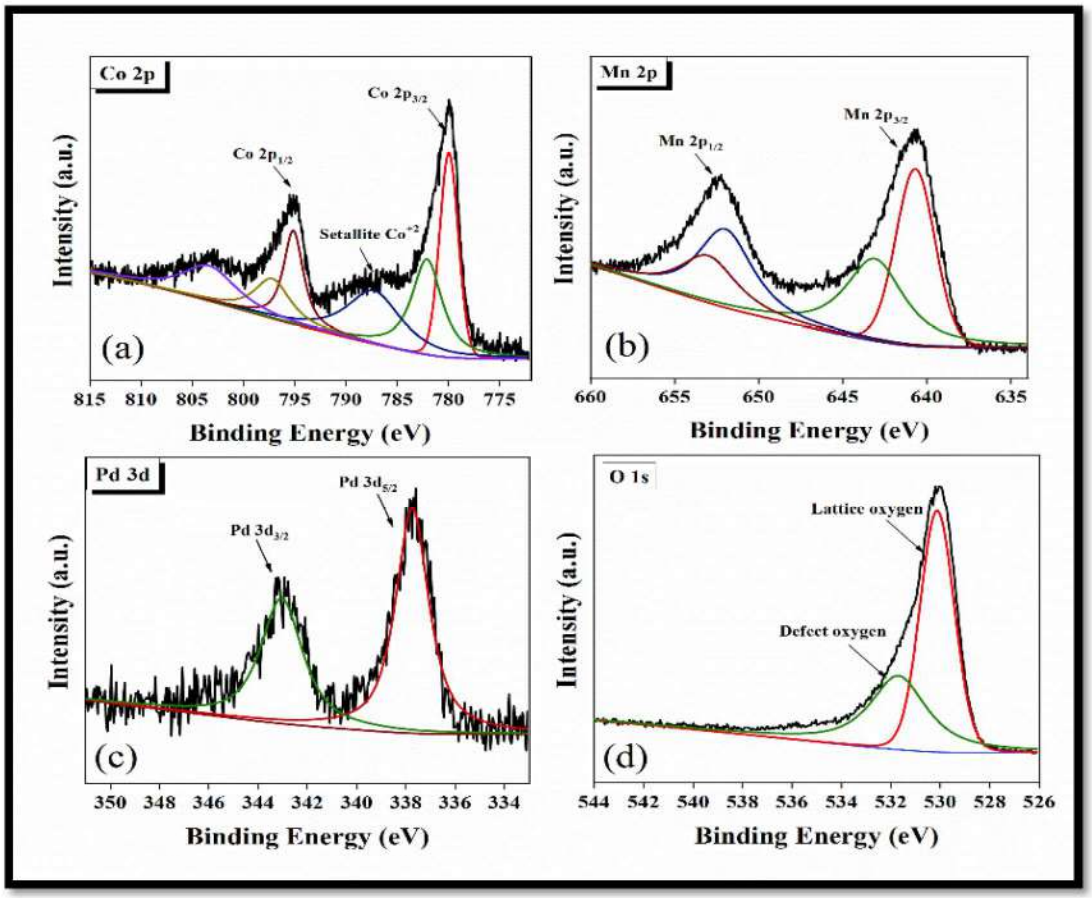

Fig. 4.26: *XPS spectra of (a) Co 2p, (b) Mn 2p, (c) Pd 3d and (d) O 1s from MM'-5% PdO.*

The various surface oxygen species from Co-Mn-Pd oxide catalysts are given in Fig. 4.26d. The O1s spectra with two BE shows the presence of two forms of oxygen species on the surface of the catalyst. The O1s with lower BE i.e. 530 eV have been regarded as due to lattice oxygen and the one with higher BE, 531.6 eV may be attributed to defect oxygen [39, 205].

The X-ray photoelectron spectra (XPS) of Co 2p, Mn 2p, Ag 3d, Rh 3d, and O 1s are studied to understand their electronic state in the prepared MM-5%Ag-1%Rh sample. The peaks obtained are de-convoluted using XPSPEAK software, and the splitted spectra are presented in Fig. 4.27. The high-resolution Mn 2p spectrum shows Mn $2p_{3/2}$ and Mn $2p_{1/2}$, which can be resolved into four peaks (Fig. 4.27a). The photoelectron peaks located at 642.07 eV and 653.6 eV were attributed to $Mn^{+3,}$ whereas the presence of peaks at 644.87 eV and 656.3 eV shows the existence of Mn^{+4} [155, 207]. However, the presence of the Mn^{+3}/Mn^{+4} couple may be the resultant of a preparative route that was chosen for composite synthesis.

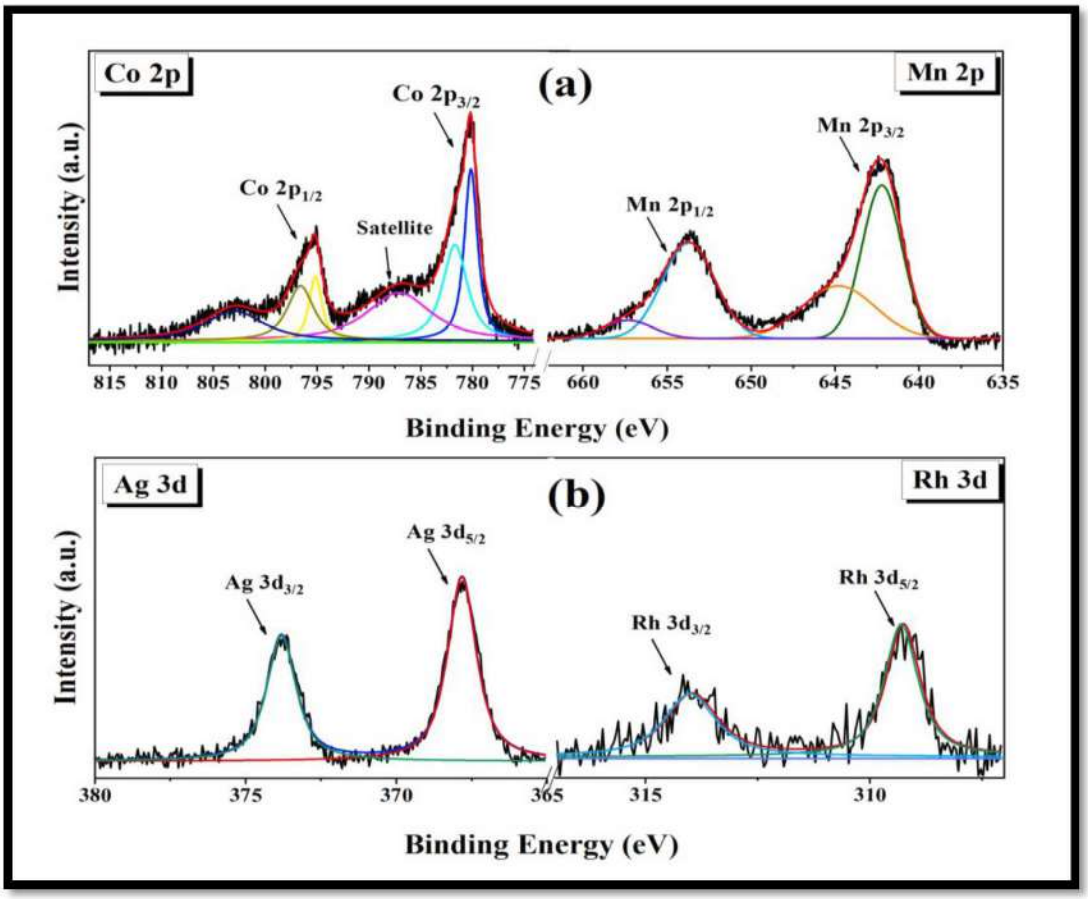

Fig. 4.27: *XPS spectra of (a) Co 2p, Mn 2p and (b) Ag 3d, Rh 3d from MM-5%Ag-1%Rh.*

Figure 4.27a depicts the chemical state of cobalt present in the MM-5%Ag-1%Rh catalytic system. The peaks having a binding energy of 780.03 eV and 781.55 eV from the Co $2p_{3/2}$ shows the presence of $Co^{+2/+3}$ redox pair in the catalyst system. Further, the presence of shoulder peak at a binding energy of 787.02 eV and 803.30 eV confirms the existence of $Co^{+2,}$ which are the characteristic shake-up peaks of Co^{+2} species [208, 209].

In Fig. 4.27b, the Ag 3d spectrum shows the splitting of Ag $3d_{5/2}$ and Ag $3d_{3/2}$, respectively. The photoemission at 367.8 eV and 373.8 eV were assigned for the Ag^{+1} state instead of metallic Ag [210, 211].

Further, the evaluation of the Rh spectrum shows the existence of only Rh^{+3} [212, 213] (309.2 eV for Rh $3d_{5/2}$ and 313.9 eV for Rh $3d_{3/2}$) as depicted in Fig. 4.27b.

The surface chemical composition of PdR3-PdR2 was determined using XPS and photoelectron spectra of Co 2p, Mn 2p, Cr 2p, Pd 3d, and O 1s is represented in Fig. 4.28. The calibrations of all the spectra were done with C 1s peak. Raw data of analyzed elements were fitted with a Gaussian curve fitting method to ascertain the oxidation state.

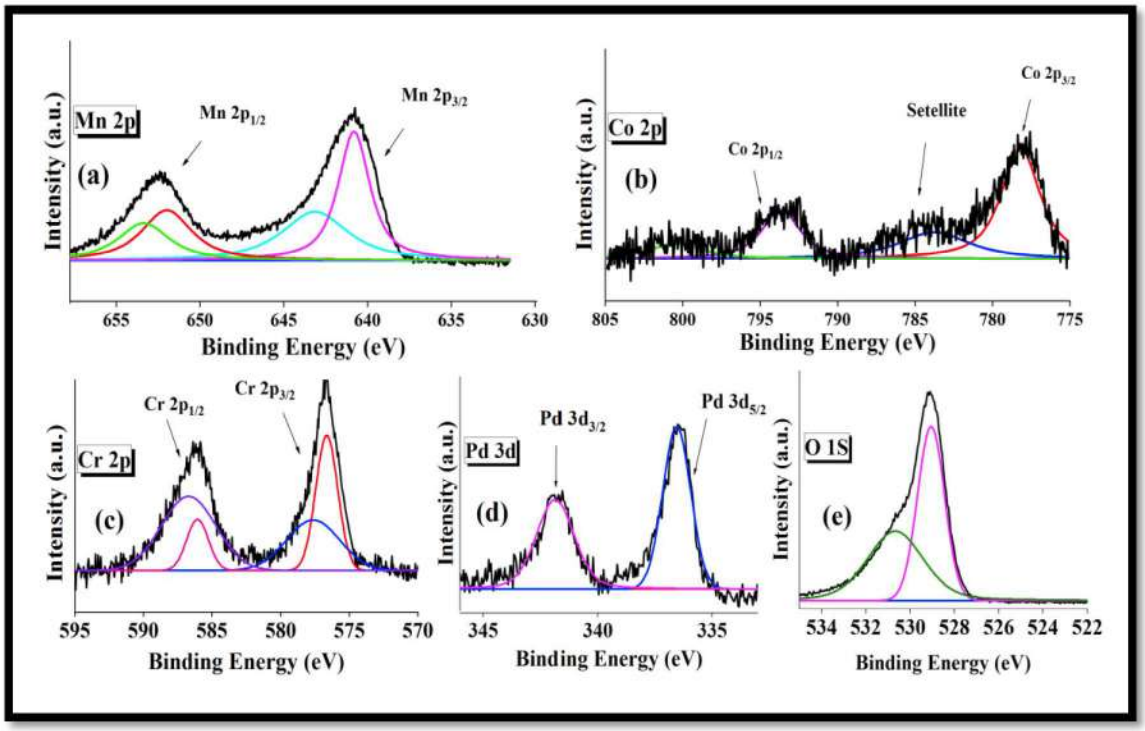

Fig. 4.28: *XPS spectra of (a) Mn 2p, (b) Co 2p, (c) Cr 2p, (d) Pd 3d and (e) O 1s from PdR3-PdR2.*

Mn spectral peaks are given in Fig. 4.28a. The Mn $2p_{3/2}$ peaks having BE of 640.8 eV and 651.9 eV of $2p_{1/2}$ correspond to Mn^{+3} of Mn_2O_3. [214]. Also, the peak at higher binding energy was observed, showing the formation of Mn^{+4} species of MnO_2, which also confirmed from the XRD pattern. Fig. 4.28b shows the photoelectron splitting of Co $2p_{3/2}$ and $2p_{1/2}$. The peaks at 778.23 eV ($2p_{3/2}$) and 793.5 eV ($2p_{1/2}$) observed implies the presence of cobalt in the +2 oxidation state [215]. Also, a shakeup satellite peak was seen, which is another evidence of Co^{+2} in the system [215, 216]. Fig. 4.28c presents Cr $2p_{3/2}$ and $2p_{1/2}$ photoelectron spectra. B.E. of 576.6 eV ($2p_{3/2}$) and 586.1 eV ($2p_{1/2}$) shown in the spectra confirms that Cr is in +3 oxidation state [217]. A high-resolution scan of Pd 5d is depicted in Fig. 4.28d. Resolution of photoelectron spectra shows two peaks at 336.5 eV and 341.8 eV i.e. $3d_{5/2}$ and $3d_{3/2}$. Absence

of peak at a lower B.E. (335 eV) [218] of reduced Pd species indicates the presence of Pd in only +2 oxidation states [152]. Further, the oxygen 1s core level spectrum is shown in Fig. 4.28e. In the O 1s spectrum, two peaks are observed with a binding energy of 529 eV and 530.6 eV. The peak at lower B.E. can be assigned to lattice oxygen and one with higher B.E. for defect oxygen or surface defect [20, 219] .

The chemical states of the elements present in the Cu-Mn-Al-Pd composite oxide are examined with XPS data and XPS spectra of Cu 2p, Mn 2p, Al 2p, Pd 3d and O 1s are presented in Fig. 4.29. All the spectra have been calibrated against C 1s (284.4 eV) which is later fitted using XPSPEAK software.

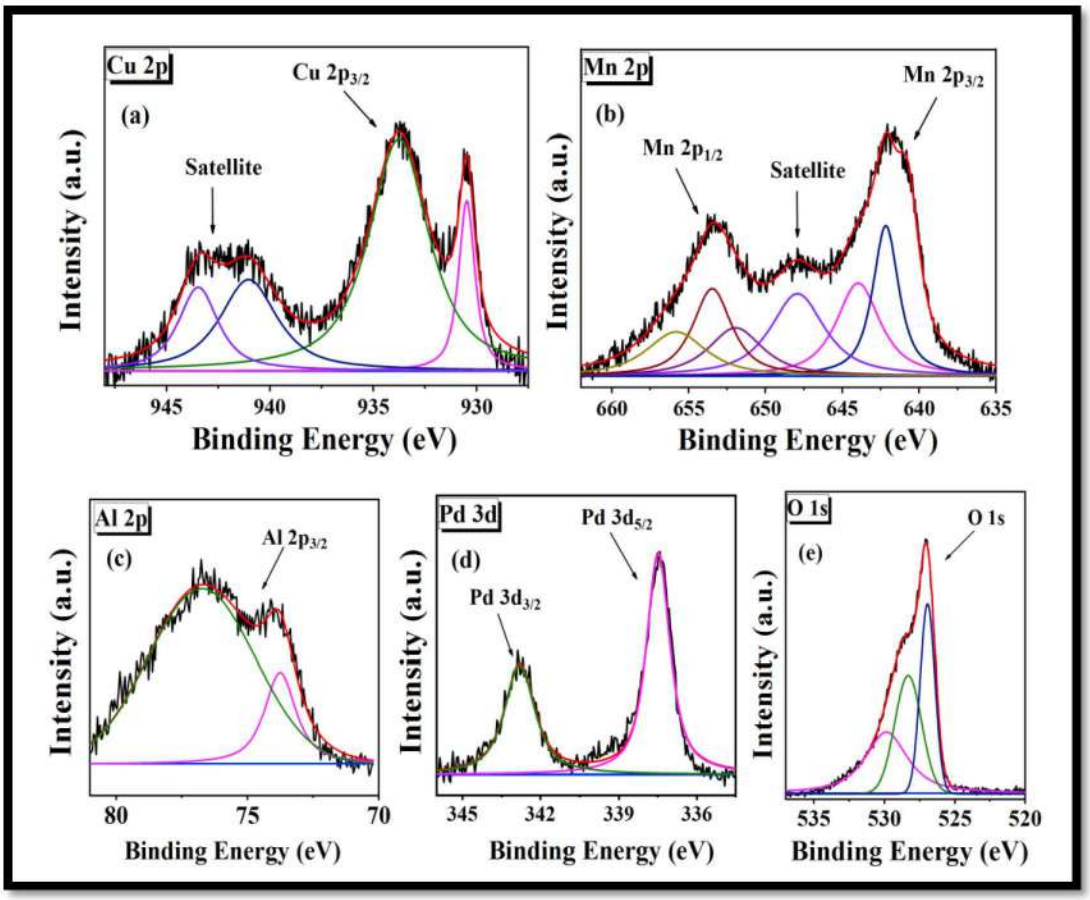

Fig. 4.29: *XPS spectra of (a) Cu 2p, (b) Mn 2p, (c) Al 2p, (d) Pd 3d and (e) O 1s from Cu-Mn-Al-Pd composite oxide.*

In Fig. 4.29a, the distinguishable peaks of CuO and Cu_2O belonging to $2p_{3/2}$ can be seen. After de-convolution of Cu $2p_{3/2}$ peak, the peaks at binding energy (B.E.) 933.59 eV and

930.50 eV confirms the presence of the Cu^{+2} and Cu^{+1}, respectively [220, 221]. Also, the existence of satellite peaks (943.59 eV and 941.12 eV) were observed, which is a characteristic of the Cu^{+2}.

Mn 2p peak splits into Mn $2p_{3/2}$ and Mn $2p_{1/2}$ as depicted in Fig. 4.29b. Further, Mn $2p_{3/2}$ can be splited into three photoelectron peaks which corresponds to Mn^{+4}, Mn^{+3} and Mn^{+2} at B.E. of 643.81, 641.98 and 640.61 eV, respectively [155, 220]. Additionally, satellite peak appears at a binding energy of 648 eV which is an evidence of Mn^{+2} state.

The photoelectron spectra of Al 2p region are shown in Fig. 4.29c. After carefully de-convoluting Al $2p_{3/2}$, two peaks were observed having binding energy of 76.76 eV and 73.92 eV which can be assigned to Al^{+3}. Such difference in binding energy of Al^{+3} can be justified by the presence of different electronic environment which surrounds the Al species [137].

As shown in Fig. 4.29d, Pd in Cu-Mn-Al-Pd composite oxide exists in +2 oxidation state. XPS peak of Pd 3d can be fitted into two peaks (i.e. Pd $3d_{5/2}$ and Pd $3d_{3/2}$) at a binding energy of 337.45 eV and 342.75 eV, respectively [152, 222].

From Fig. 4.29e, three different kinds of oxygen species can be seen by fitting O 1s peak. The peak at lower binding energy i.e. 527 eV and 528.40 eV corresponds to oxygen associated to metal (lattice oxygen) and XPS peak at higher binding energy i.e. 529.9 eV can be accounted for the defect oxygen.

The XPS studies are employed to portray the presence of respective elements (Cu, Al and Pd) and their electronic state in the 10% Al-$Cu_{0.95}Pd_{0.05}O$. The photoelectron peaks of Cu 2p, Al 2p and O1s are de-convoluted and presented in Fig. 4.30.

Figure 4.30a shows the XPS spectra of Cu $2p_{3/2}$ showing the peaks ranging from 946 eV to 929 eV. Cu $2p_{3/2}$ shows single peak at binding energy of 933.82 eV which can be related to Cu^{+2} species. Additionally, association of satellite peak at 943.47 eV and 941.04 eV is an evidence of presence of Cu^{+2} [220, 221].

The XPS peak of Al 2p is presented in Fig. 4.30b which consist of a single peak at B.E. of 76.9 eV that can be assigned to Al^{+3} [137].

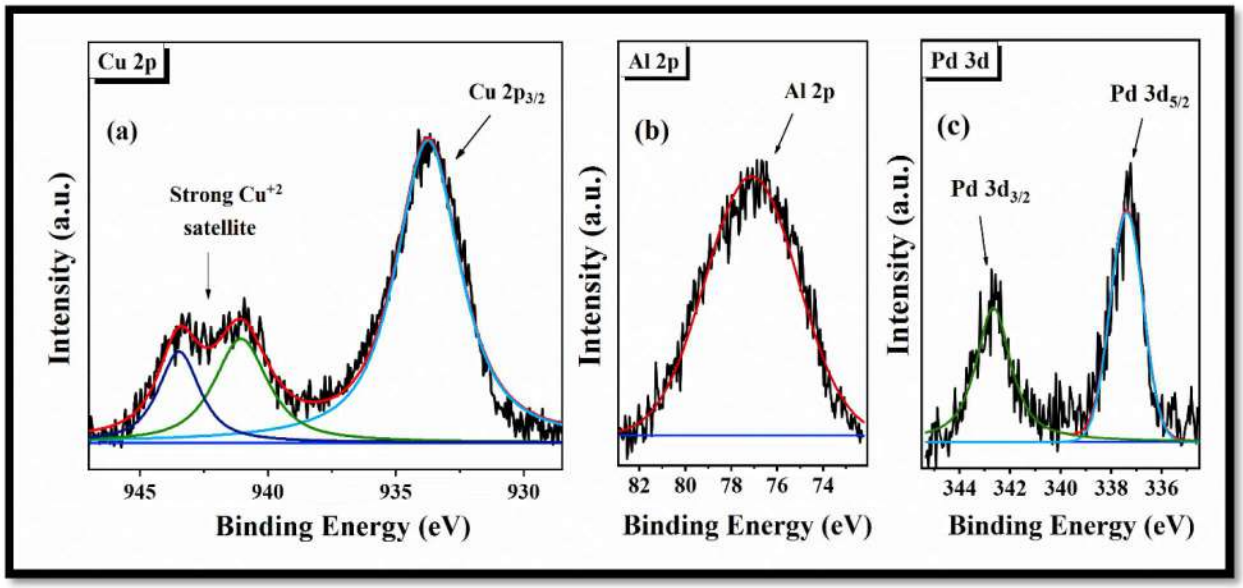

Fig. 4.30: *XPS spectra of (a) Cu 2p, (b) Al 2p and (c) Pd 3d from 10% Al-*$Cu_{0.95}Pd_{0.05}O$.

As shown in Fig. 4.30c, XPS of Pd is composed of two peaks at B.E. of 337.24 eV and 342.46 eV which is attributed to Pd $3d_{5/2}$ and Pd $3d_{3/2}$, respectively [152, 222]. After carefully fitting these peaks, no extra signals were observed conveying the presence of only +2 species of Pd.

The elemental oxidation state of the Ce, Cu and O from the prepared Ce-Cu composite oxide was investigated through X-ray photoelectron spectroscopy and XPS spectra of the same are presented in Fig. 4.31. A Ce 3d spectrum is de-convoluted into eight photoelectron peaks as presented in Fig. 4.31(e). The splitted peaks are labeled as v (v, v′, v″, v‴) and u (u, u′, u″ and u‴) from which v, v′, v″and v‴ represents the Ce $3d_{5/2}$ and peaks which are labeled as u, u′, u″ and u‴ symbolizes the Ce $3d_{3/2}$. Among the above observed peaks v, v″ and v‴ of Ce $3d_{5/2}$ and u, u″ and u‴ of Ce $3d_{3/2}$ signifies the cerium in +4 oxidation state whereas v′ and u′ is assigned for Ce^{+3} state [8, 120]. An XPS spectrum of pristine CeO_2 was also recorded to compare the electronic state of the cerium from Ce-Cu composite which showed no difference in the peak splitting (Fig. 4.31a).

It is well-known that the BE of Cu^{+2} is in between 933 eV to 934 eV depending on the nature of its surrounding [223–226] and also presence of strong shake-up peaks is

characteristic of Cu^{+2} existence, while a peak at a binding energy below 933 eV are mostly determined for reduced copper species (Cu^{+1} and Cu^{o}) [225, 226].

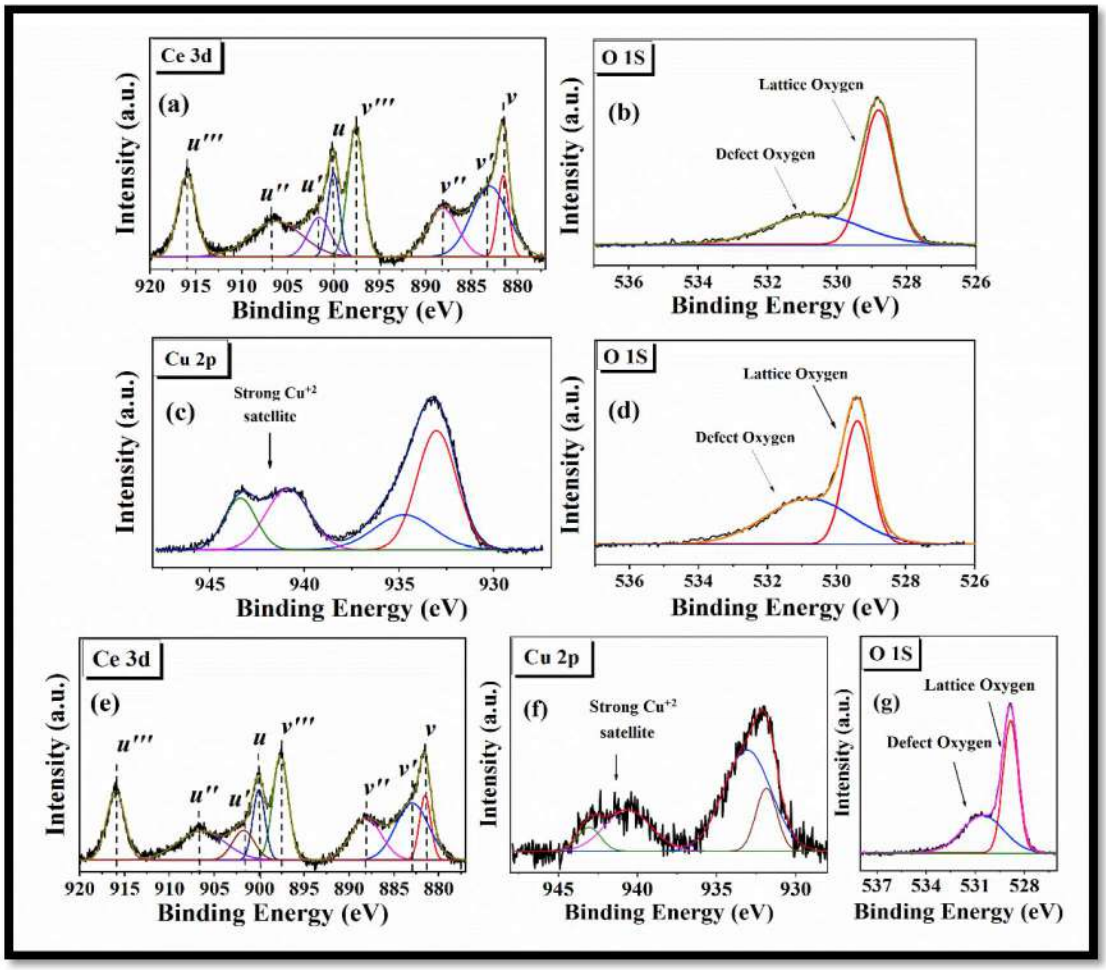

Fig. 4.31: *XPS spectra of (a) Ce 3d and (b) O 1s from CeO_2 (c) Cu 2p and (d) O 1s from CuO (e) Ce 3d (f) Cu 2p and (g) O 1s from Ce-Cu composite oxide.*

Figure 4.31f shows the Cu $2p_{3/2}$ spectra which has been fitted into two peaks. The photoelectron peaks with binding energy of 933.27 eV corresponds to Cu^{+2} which is also supported by the presence of shake up peak at 940.43 eV and 942.75 eV which are characteristic peaks observed when copper is in +2 oxidation state [112, 199, 226, 227]. Further, the occurrence of the peak at a binding energy of 931.92 eV shows the co-existence of $Cu^{+1/0}$ oxidation state [180, 228]. Such formation of $Cu^{+1/0}$ species in Ce-Cu composite oxide may be a result of surface interaction of cerium and copper within composite. Studies

by Jiahui Ma et. al. also showed that as cerium concentration increases in CuO-CeO_2 composite, it leads to decrease in the binding energy of Cu^{+2} to Cu^{+1} [229].

Similar de-convoluting procedure was employed to fit the O 1s spectrum which is depicted in Fig. 4.31(b, d and g). XPS profile of oxygen displays two photoemission peaks at binding energy of 530.75 eV and 528.81 eV. XPS peak at a lower binding energy corresponds to the oxygen attached to the metal species which is labeled as a lattice oxygen and the peak observed at higher binding energy corresponds to the defect oxygen or surface oxygen species [7, 43, 44, 8].

X-ray photoemission studies of $Ce_{0.95}Ru_{0.05}O_2$-$Cu_{0.95}Pd_{0.05}O$ were illustrated in Fig. 4.32. No reflection other than Ce, Ru, Cu, Pd, O and C were detected in the studied compound. All the peaks observed were calibrated with C 1s value of 284.6 eV and de-convoluted using Gaussian- Lorentz procedure.

The presence of Ce was seen having distinct peaks in the range of 878 eV - 922 eV. Further, de-convolution of these peaks revealed the presence of Ce^{+4} along with the small amount of Ce^{+3} oxidation state. As shown in Fig. 4.32a, Ce 3d splits as Ce $3d_{5/2}$ and Ce $3d_{3/2}$ which was after de-convolution labelled as v (v, v′, v″ and v‴) and u(u, u′, u″ and u‴), respectively. The XPS peaks of v, v″ and v‴ (Ce $3d_{5/2}$) and u, u″ and u‴ (Ce 3 $d_{3/2}$) were assigned for Ce^{+4} oxidation state and the v′ (Ce $3d_{5/2}$) and u′ (Ce $3d_{3/2}$) were ascribed for +3 oxidation state of cerium [175].

The Cu $2p_{3/2}$ photoelectron spectrum was de-convoluted and fitted peaks are shown in Fig. 4.32c. After fitting Cu $2p_{3/2}$, two peaks were observed. The One at a binding energy of 933.12 eV and other at 935.08 eV showing the presence of copper in Cu^{+2} oxidation state. The peak observed at lower binding energy corresponds to the Cu-O whereas peak at higher binding energy arise due to Cu which is surrounded with Ce-O. Similar results were also discussed by G Cordoba and others wherein Cu in Cu-O-Ti-O showed B.E. of 935.1 eV [233]. Further, the characteristic satellite peaks confirms the existence of Cu^{+2} oxidation state.

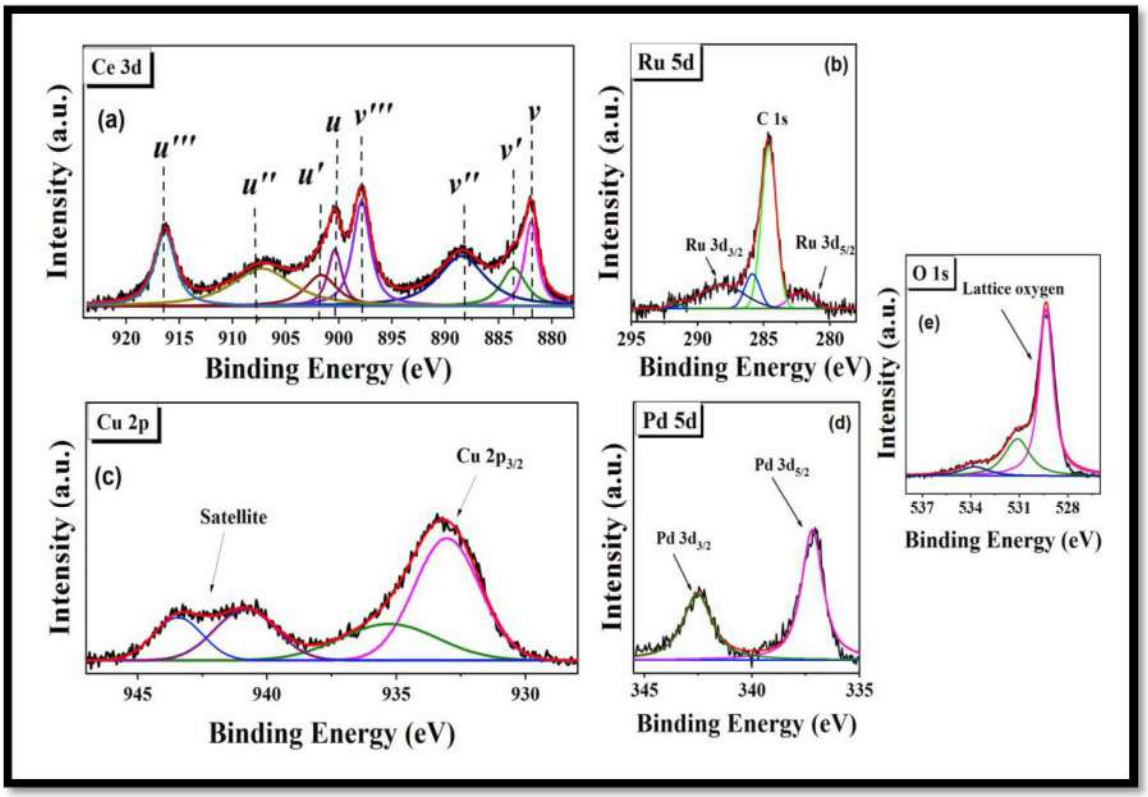

Fig. 4.32: *XPS spectra of (a) Ce 3d, (b) Ru 5d, (c) Cu 2p (d) Pd 5d and (e) O 1s from* $Ce_{0.95}Ru_{0.05}O_2$-$Cu_{0.95}Pd_{0.05}O$.

The Fig. 4.32b and Fig. 4.32d shows the photoelectron spectra of Ru and Pd from prepared composite system. After de-convolution of XPS spectra, Ru and Pd revealed the presence of Ru in +4 and Pd in +2 oxidation state. As shown in Fig. 4.32d, the Pd 3d splits into Pd $3d_{5/2}$ and Pd $3d_{3/2}$ at a binding energy of 337.18 eV and 342.55 eV which is a characteristic of Pd^{+2} oxidation state.

XPS spectrum of O 1s from the composite catalyst was depicted in Fig. 4.32e. Spectral fitting of the peak showed the existence of three different kinds of oxygen. The peak observed at a binding energy of 529.32 eV is denoted for the lattice oxygen and the second peak at binding energy of 531.12 eV corresponds to the defect oxygen species which occurs due to non-stoichiometric arrangement. It was observed that the such defect oxygen has a higher mobility than that of lattice one [155].

4.5 Scanning Electron Microscopy studies

SEM images were recorded to analyze the surface morphology of the prepared samples. Figure 4.33 represents SEM images of Cr_2O_3 and $Cr_{1.96}Cu_{0.04}O_3$ which was synthesized using combustion route. The porous-sponge like morphology of Cr_2O_3 can be observed from its SEM image (Fig. 4.33a). Also, copper incorporation in Cr_2O_3 (Fig. 4.33b) shows similar morphology and size of the particles as that of pure Cr_2O_3.

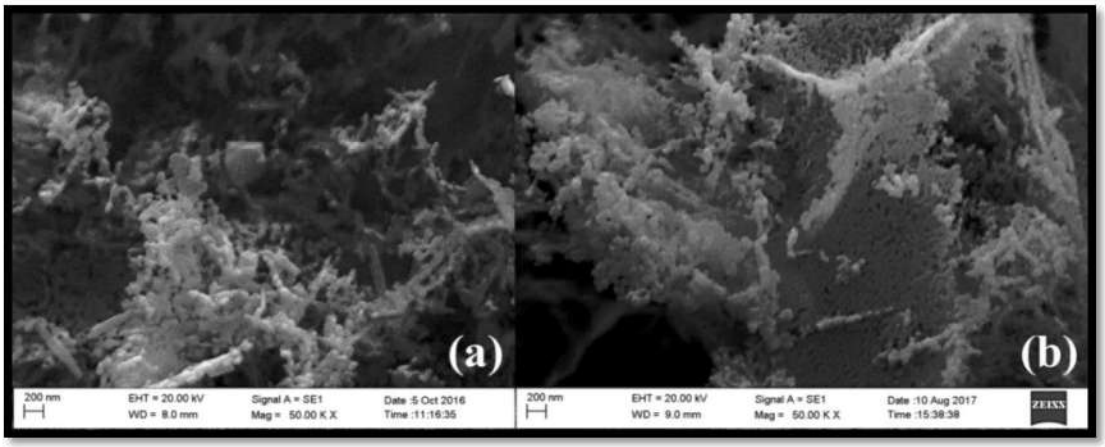

Fig. 4.33: *SEM image of (a) Cr_2O_3 and (b) $Cr_{1.96}Cu_{0.04}O_3$.*

Figure 4.34a shows the SEM image of CeO_2 which displays a porous morphology of the samples having particles in spherical shape. Also, the SEM image of $Ce_{0.95}Mn_{0.02}Cu_{0.02}Ag_{0.01}O_2$ was recorded and the same is presented in Fig. 4.34b. Comparing the morphological view of both CeO_2 and $Ce_{0.95}Mn_{0.02}Cu_{0.02}Ag_{0.01}O_2$ it is observed that CeO_2 has smaller particle size than that of $Ce_{0.95}Mn_{0.02}Cu_{0.02}Ag_{0.01}O_2$.

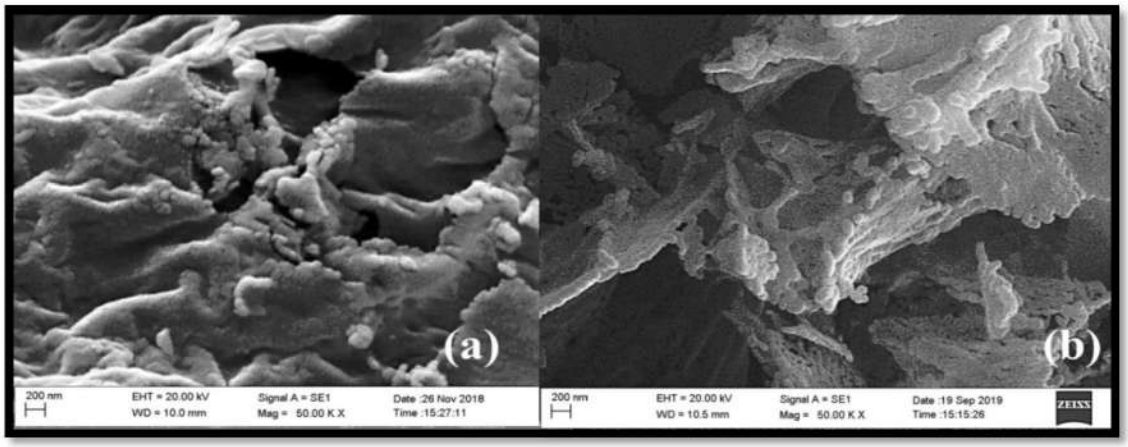

Fig. 4.34: *SEM image of (a) CeO_2 and (b) $Ce_{0.95}Mn_{0.02}Cu_{0.02}Ag_{0.01}O_3$.*

Figure 4.35 (a, b) and (c, d) represents the SEM images of CeO_2 and $Ce_{0.95}Ru_{0.05}O_2$, respectively.

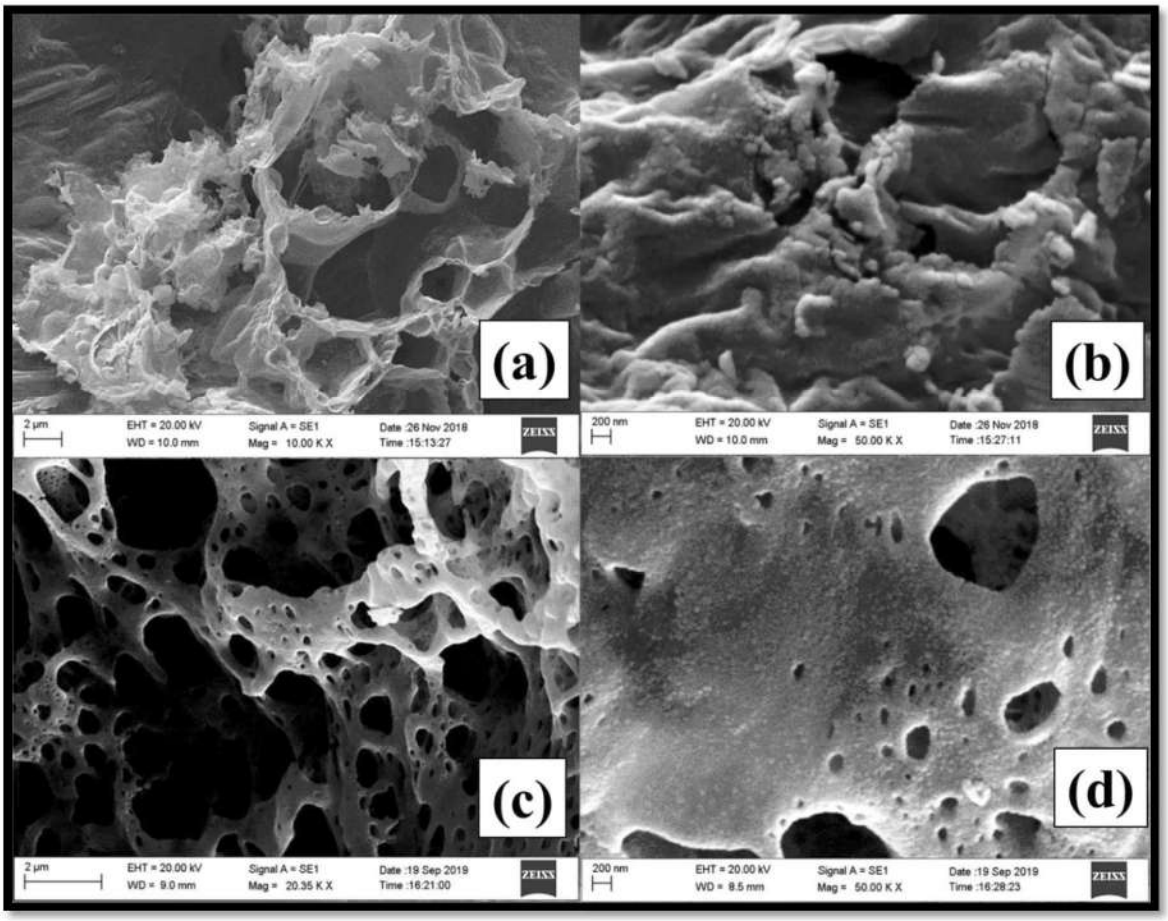

Fig. 4.35: *SEM image of (a) CeO_2 – 2 µm, (b) CeO_2 – 200 nm, (c) $Ce_{0.95}Mn_{0.02}Cu_{0.02}Ag_{0.01}O_2$ – 2 µm and (d) $Ce_{0.95}Mn_{0.02}Cu_{0.02}Ag_{0.01}O_2$ – 200 nm.*

The micrograph which has been taken at 2 µm scale (Fig. 4.35a and Fig. 4.35c) depicts the porous morphology for both the composition. Further, at 200 nm scale, the agglomerated nanoparticles were observed which constitute the observed porous structure of the samples.

SEM micrograph of MM′ and MM′-5% PdO oxide catalyst are presented in Fig. 4.36. As shown in Fig. 4.36a and Fig. 4.36b, SEM image reveals the porous appearance of this material with some agglomeration of the particles.

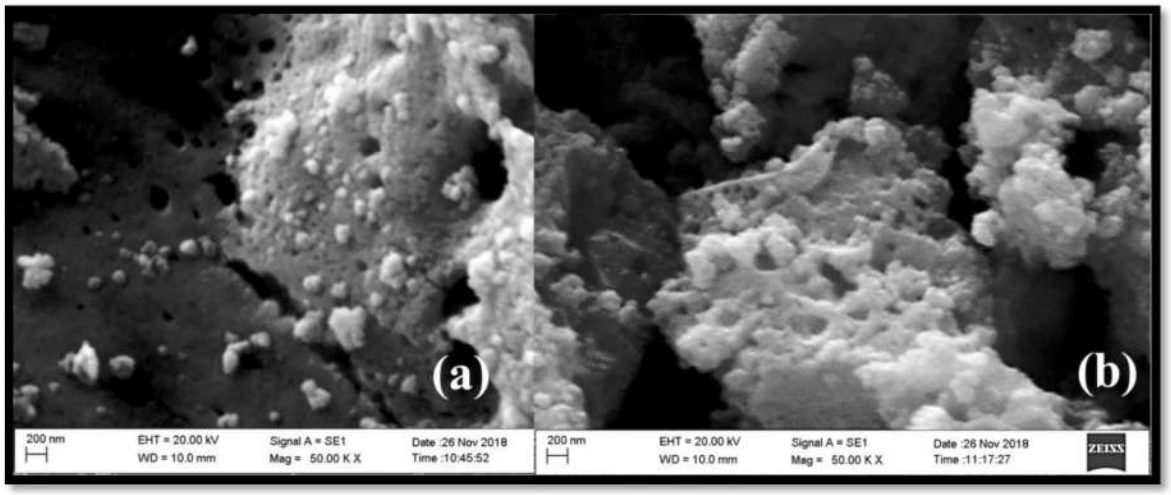

Fig. 4.36: *SEM image of MM′ (a) and MM′ -5% PdO (b).*

The SEM micrographs of the MM′ and MM′-5%Ag-1%Rh was obtained to explore the surface morphology and particle size of the composite oxide. Images of the same are presented in Fig. 4.37.

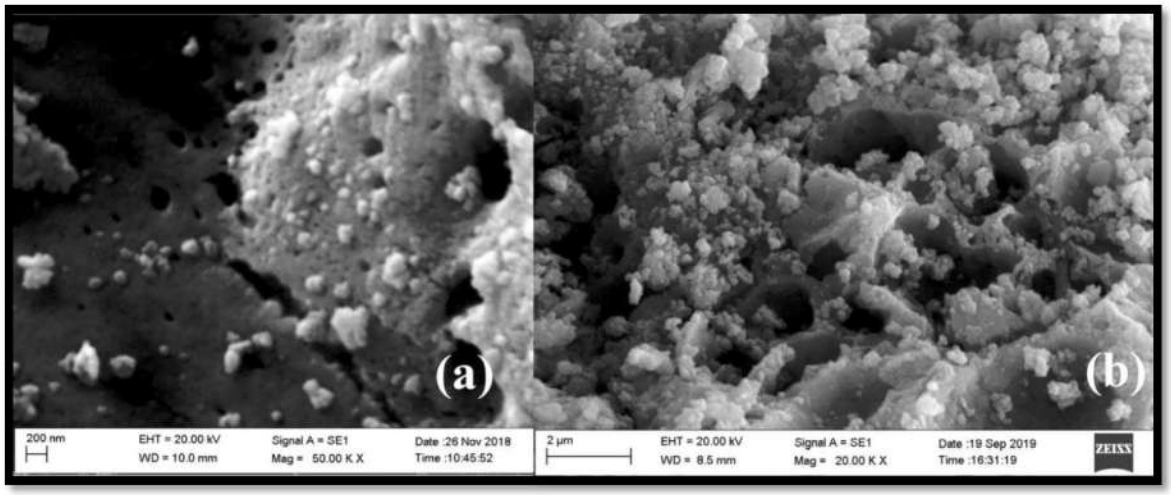

Fig. 4.37: *SEM image of MM′ (a) and MM′ -5% Ag – 1%Rh (b).*

The SEM image of CoO_x-MnO_x (MM′) as depicted in Fig. 4.37a shows a spongy porous like morphology. Also, SEM studies of Rh and Ag containing CoO_x-MnO_x (MM′-5%Ag-1%Rh) showed similar morphology as that of CoO_x-MnO_x as depicted in Fig. 4.37b. Such types of structure are characteristic of the method employed for the preparation of the catalyst. From literature, it has been observed that similar kinds of SEM data can be obtained when fuel like glycine [91, 234] was used during the preparation of metal oxide. The formations of pores

in the prepared catalysts are mostly due to the evolution of the gases which develop during the combustion process.

SEM studies were carried out on Cu-Mn-10%Al - 5%Pd composite oxide sample and the micrograph is shown in Fig. 4.38.

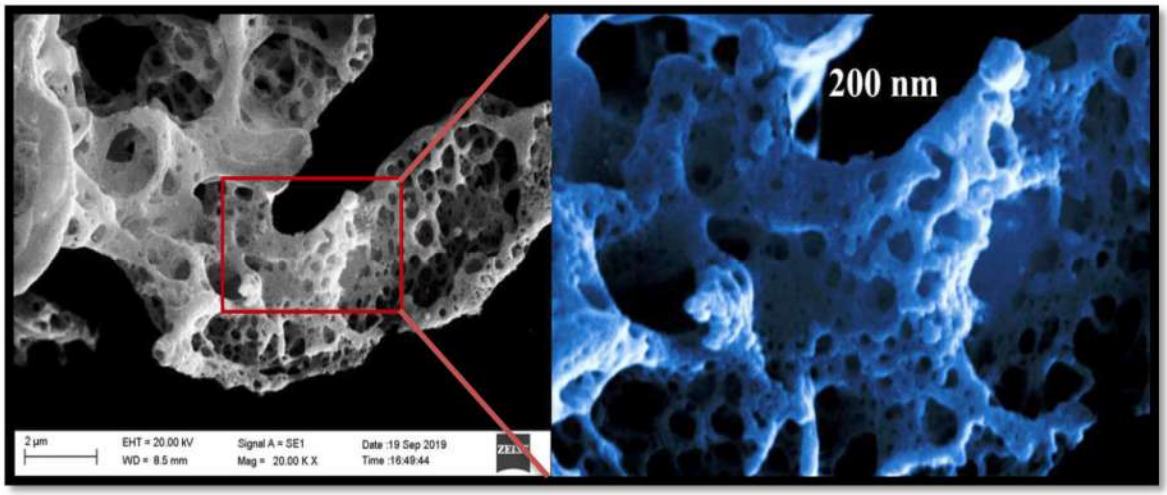

Fig. 4.38: *SEM image of Cu-Mn-10%Al- 5% Pd composite oxide.*

The image reveals the porous nature of the samples which is caused due to agglomeration of the nanoparticles. This porous appearance of the sample mostly occurs via evolution of the gas during the combustion synthesis. Particles forming these structures are not clearly visualized, owing to their nano-nature.

Figure 4.39 represents the SEM micrograph of all the PdR1, PdR2, PdR3 and PdR2-PdR3 oxide samples. All the micrographs displays the particles agglomeration produced from nanoparticles. Change in the morphology is observed when Pd was supported on Pd substituted cobalt chromite as depicted in Fig. 4.39b. Further, the final compound i.e. PdR2-PdR3 (Fig. 4.39d) showed characteristic texture as that of PdR3 (Fig. 4.39c) confirming the presence of PdR3 in it.

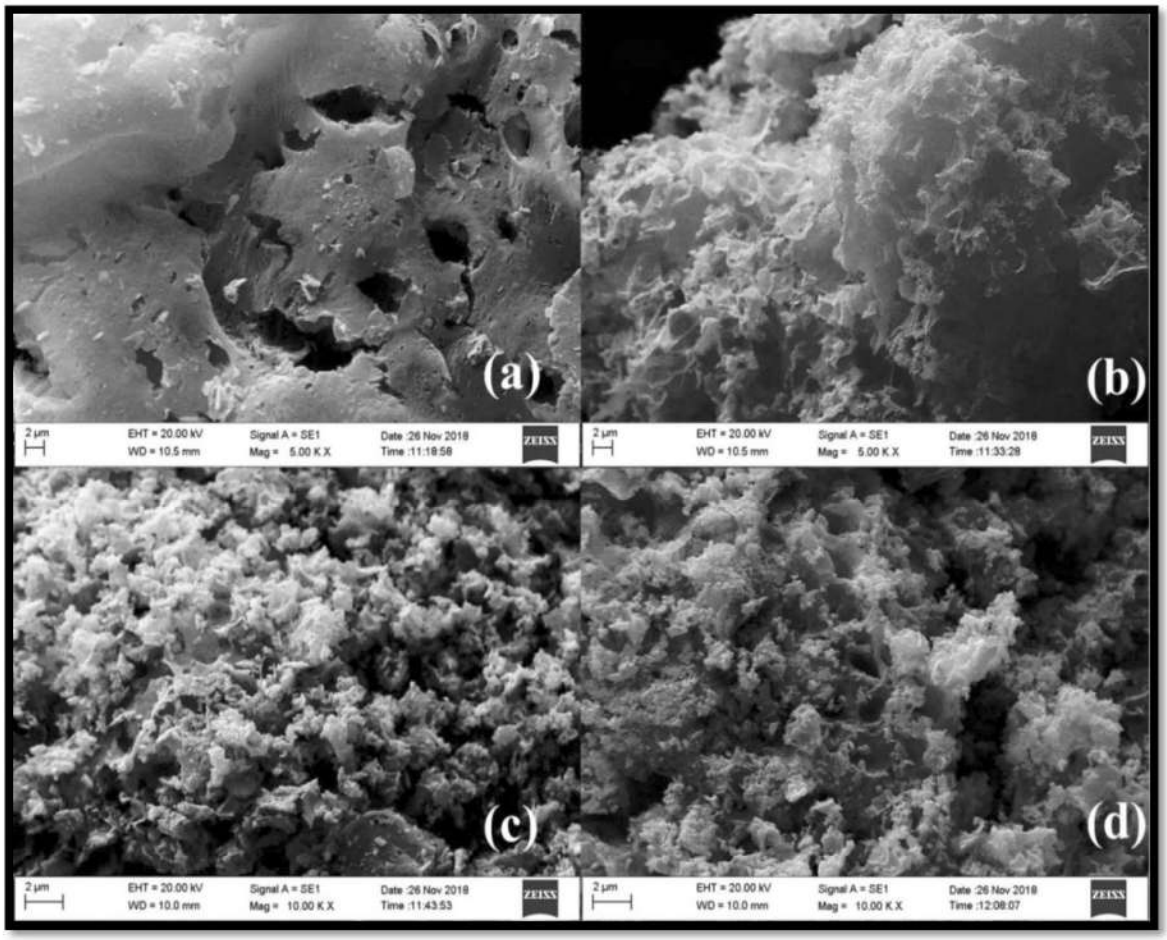

Fig. 4.39: *SEM image of (a) PdR1, (b) PdR2, (c) PdR3 and (d) PdR2-PdR3.*

The recorded SEM images of the $Cu_{0.95}Pd_{0.05}O$, 20Al/ $Cu_{0.95}Pd_{0.05}O$ and 10- $Cu_{0.95}Pd_{0.05}O$ are given in Fig. 4.40.

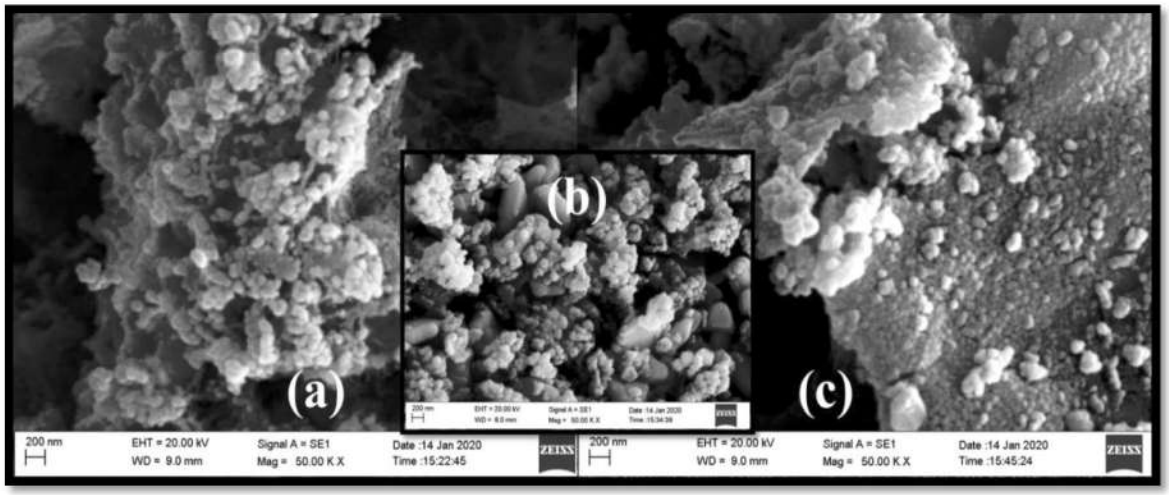

Fig. 4.40: *SEM image of (a) $Cu_{0.95}Pd_{0.05}O$, (b) 20Al/$Cu_{0.95}Pd_{0.05}O$ and (c) 10Al-$Cu_{0.95}Pd_{0.05}O$.*

The image of $Cu_{0.95}Pd_{0.05}O$ suggests the agglomeration of nanoparticles which resulted in a porous architect. As seen from Fig. 4.40b, addition of Al revealed the formation of distinct cubic particles in between $Cu_{0.95}Pd_{0.05}O$ structure emphasizing the presence of Al oxide. Later this structure has not been seen in 10- $Cu_{0.95}Pd_{0.05}O$ as depicted in Fig. 4.40c this shows the masking of Al in $Cu_{0.95}Pd_{0.05}O$.

Figure 4.41 shows the surface morphology and the elemental mapping of CeO_2-CuO nano composite prepared by simple grinding method.

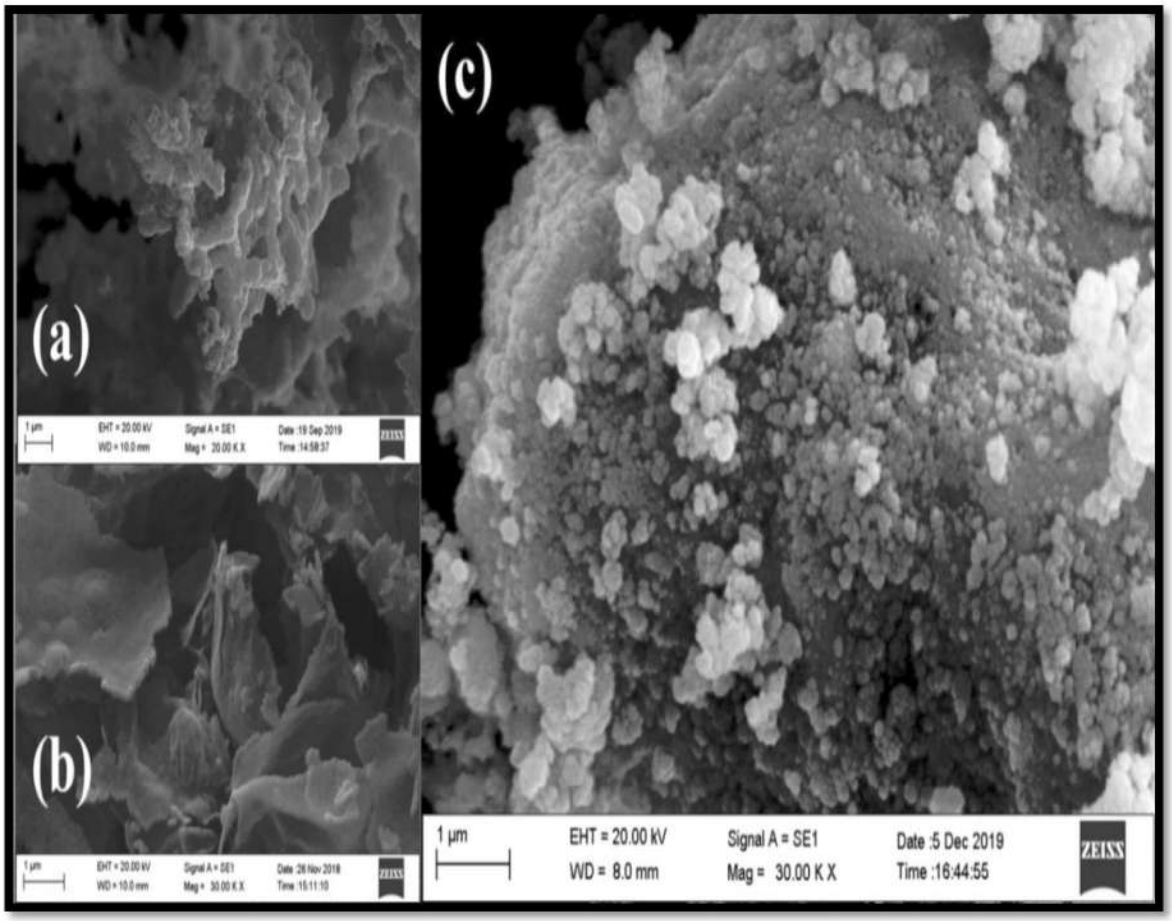

Fig. 4.41: *SEM images of CuO (a), CeO_2 (b) and Ce-Cu-O (c).*

SEM image of CeO_2 shows smaller particles than CuO and appears porous in nature. Although, more agglomeration can be seen from the CeO_2 morphological view (Fig. 4.41b), mixing it with CuO (Fig. 4.41a) leads in changing its agglomerated view which is clearly observed in Fig. 4.41c showing both CeO_2 and CuO particles.

Homogenous dispersion of the oxide was observed as can be seen from the elemental mapping images. Figure 4.42a-d shows the highly dispersed Ce, Cu and O over the catalyst surface. The amount of Ce (Fig. 4.42a) dispersion is higher as compared to Cu (Fig. 4.42b) confirming the lesser concentration of Cu with very well dispersion in the CeO_2-CuO composite (Fig. 4.42d).

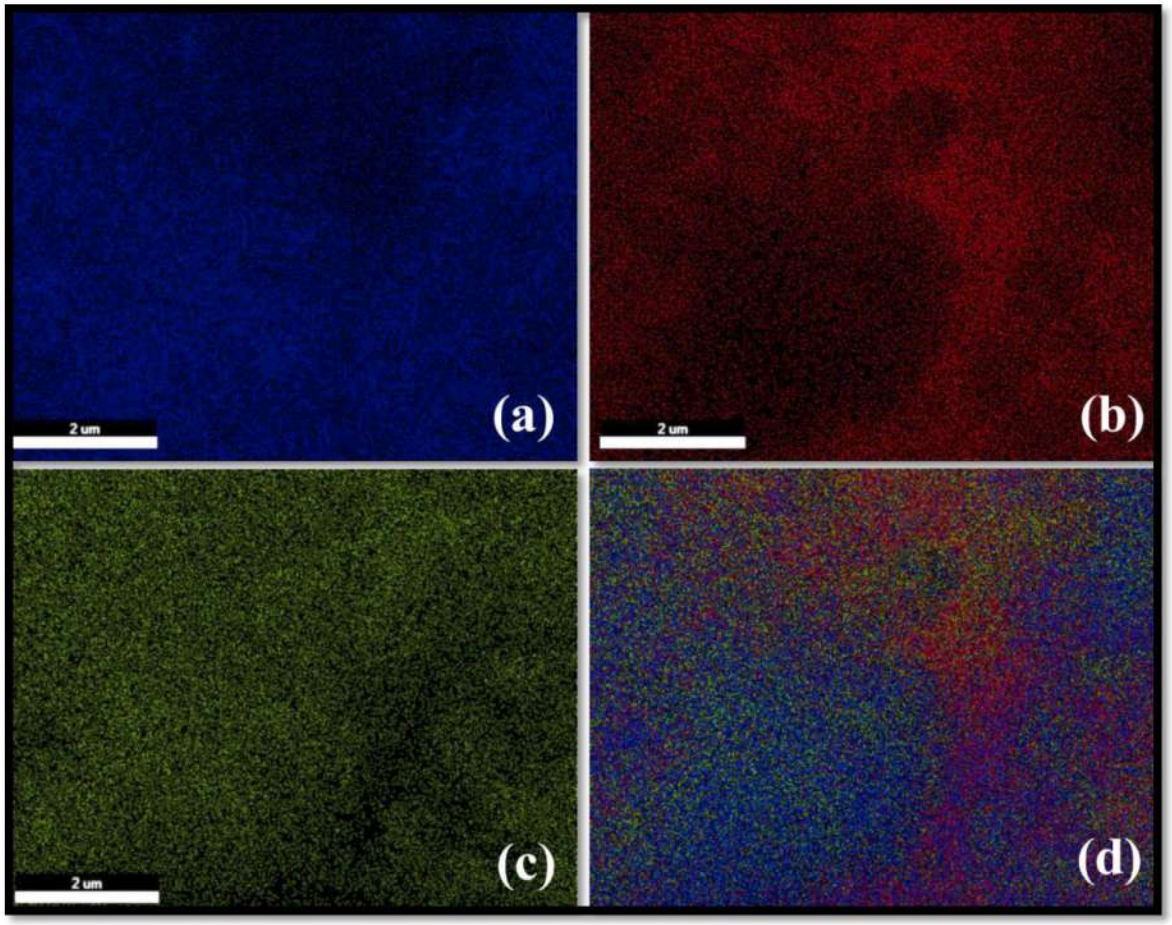

Fig. 4.42: *SEM elemental mapping of Ce (a) Cu (b) O (c) and Ce-Cu-O (d) in composite oxide.*

The morphology of the $Ce_{0.95}Ru_{0.05}O_2$, $Cu_{0.95}Pd_{0.05}O$ and CeRu-CuPd nano composite oxide were examined by SEM. $Ce_{0.95}Ru_{0.05}O$ shows spherical particles which shows agglomeration producing porous structure as seen from Fig. 4.43a.

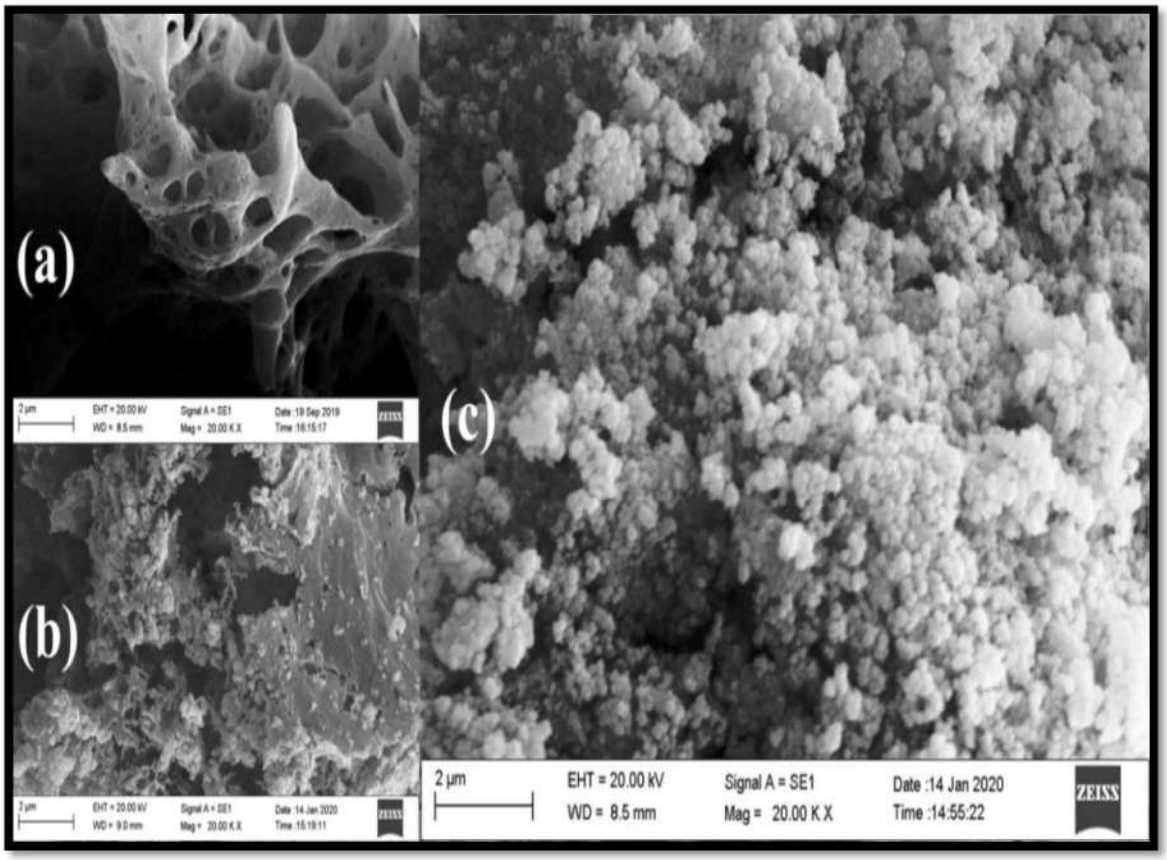

Fig. 4.43: *SEM image of $Ce_{0.95}Ru_{0.05}O$ (a), $Cu_{0.95}Pd_{0.05}O$ (b) and CeRu-CuPd composite oxide(c).*

Similarly, $Cu_{0.95}Pd_{0.05}O$ also showed agglomeration of the particles depicting different morphological view as that of $Ce_{0.95}Ru_{0.05}O$. Further, grinding both the compounds with 1:1 ratio projected different image showing change in particle agglomeration in the CeRu-CuPd nano-composite oxide.

4.6. Transmission electron microscopy studies

Figure 4.44 represents TEM micrographs and particle size distribution of Cr_2O_3 (a and b) and $Cr_{1.96}Cu_{0.04}O_3$ (c and d), which were synthesized using the combustion route. A TEM image of Cr_2O_3 reveals that these particles are in spherical form having size less than 50 nm. Copper incorporation in Cr_2O_3 lattice has not shown any change in shape and size of the particles. Additionally, particle size distribution studies showed the particles in the range of 20-100 nm having higher percentage of particles in 40-50 nm.

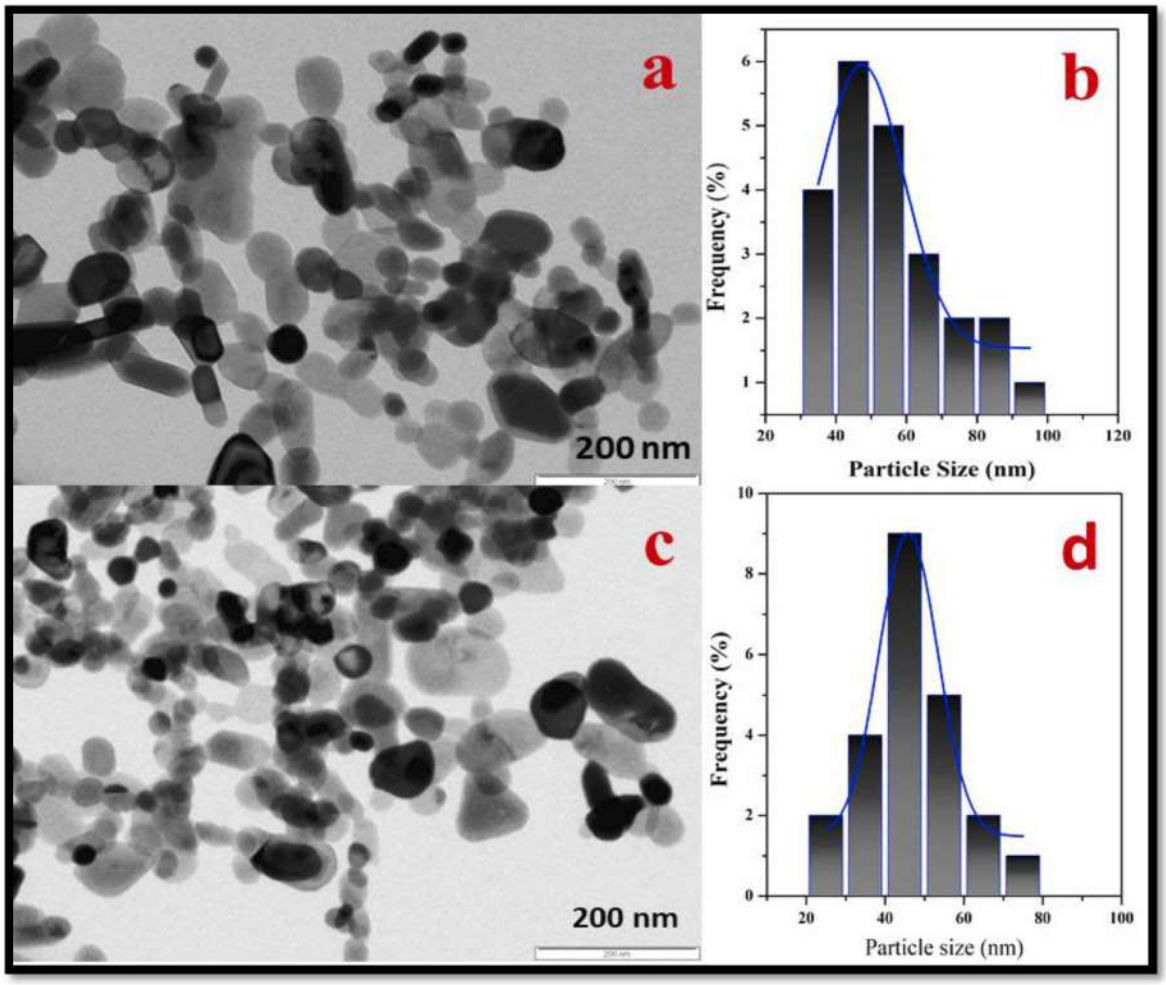

Fig. 4.44: *TEM image and particle size distribution of Cr_2O_3 (a and b) and $Cr_{1.96}Cu_{0.04}O_3$ (c and d).*

View of $Ce_{0.95}Mn_{0.02}Cu_{0.02}Ag_{0.01}O_2$ was studied using TEM and presented in Fig. 4.45. In Fig. 4.45, two images of $Ce_{0.95}Mn_{0.02}Cu_{0.02}Ag_{0.01}O_2$ were shown, one recorded at 50 nm and another at 20 nm scale. TEM image shows that the particles have a spherical view having size less than 50 nm. Additionally, agglomeration of the nanoparticles can also be seen from this TEM micrograph.

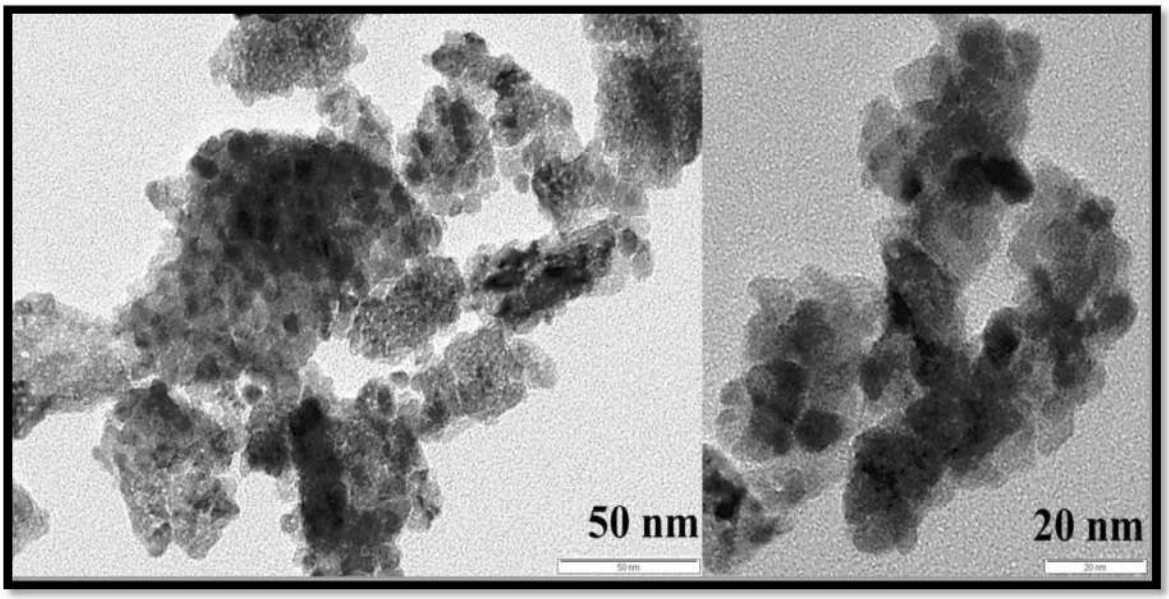

Fig. 4.45: *TEM image of* $Ce_{0.95}Mn_{0.02}Cu_{0.02}Ag_{0.01}O_2$.

A representative HRTEM image of $Ce_{0.95}Ru_{0.05}O_2$ has been studied for understanding the sample surface property at nano range scale. The image of the same is depicted in Fig. 4.46a.

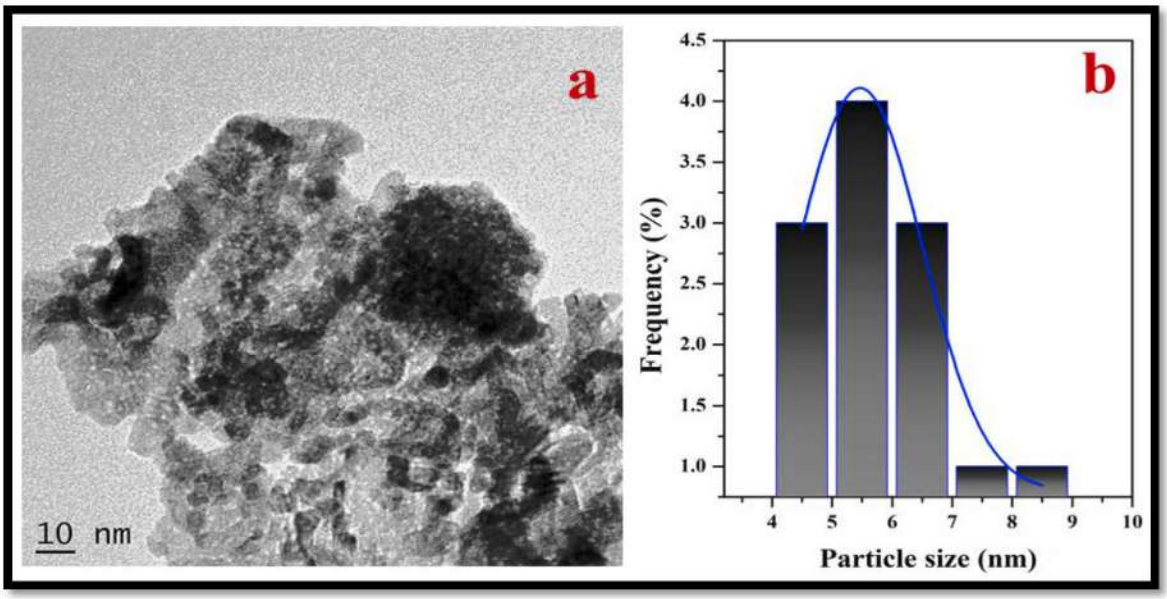

Fig. 4.46: *HRTEM image and Particle size distribution of* $Ce_{0.95}Ru_{0.05}O_2$.

Microscopic view at 10 nm confirmed the existence of nanoparticles showing spherical and cylindrical appearance. Also, histogram of particles size shows the dispersion below 10 nm having highest density of particle size from 5 to 6 nm.

A representative TEM image of MM′-5% PdO oxide catalyst is exhibited in Fig. 4.47. Aggregation of particles can be seen from the TEM view which may be the consequences of sample preparative method. Image reveals the formation of nano size particles below 20 nm, which is depicted in both 50 nm and 20 nm scale view.

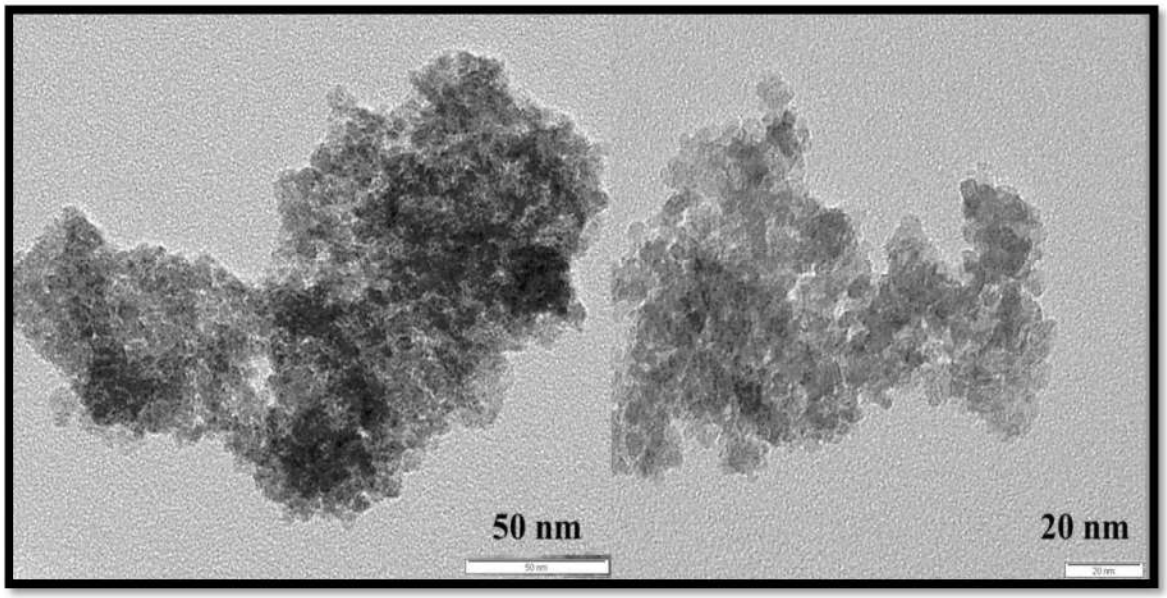

Fig. 4.47: *TEM image of MM′-5%PdO.*

Particle sizes and shapes of MM′-5% Ag-1% Rh determined through HRTEM is illustrated in Fig. 4.48a. At nanometer range, the HRTEM micrograph of MM′-5%Ag-1%Rh shows particles having spherical shapes with size less than 30 nm and this effect of nanoparticles had been reflected in broad peaks in XRD studies. Also, particle size distribution studies were carried out to examine the dispersion of particles in composite oxide and presented in Fig. 4.48b. According to distribution plot, particles are observed in the range of 10 to 45 nm.

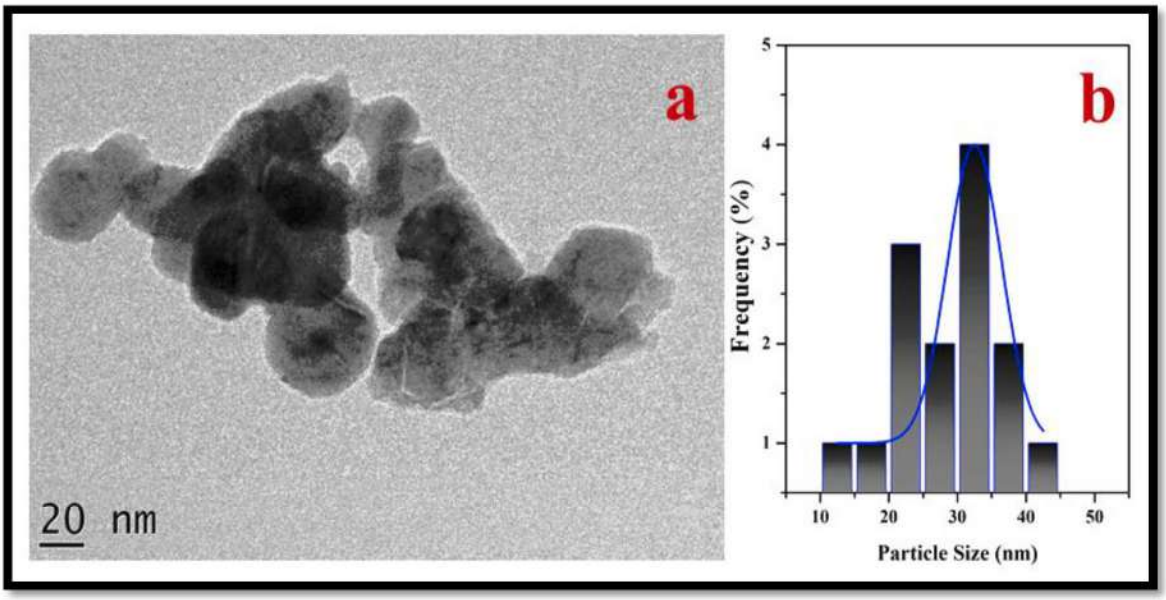

Fig. 4.48: *HRTEM image and particle size distribution of MM'-5% Ag-1% Rh.*

HRTEM studies were performed to capture the nanostructure of Cu-Mn-Al-Pd nano composite oxide and its image is illustrated in Fig. 4.49.

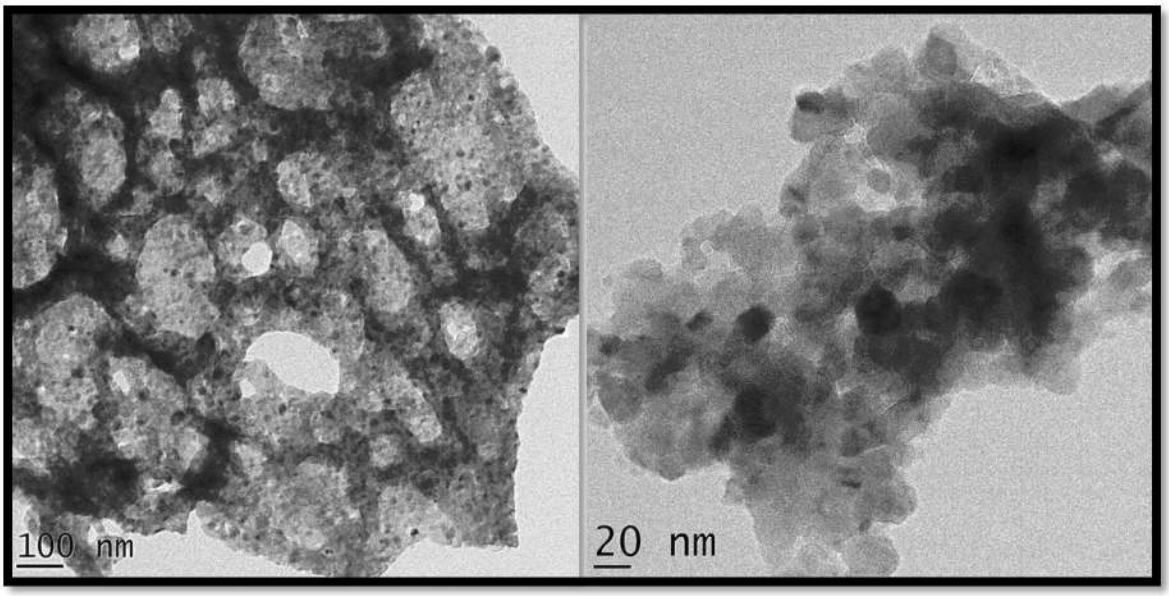

Fig. 4.49: *HRTEM images of Cu-Mn-Al-Pd composite oxide.*

Image at 100 nm scale clearly shows the porous nature of Cu-Mn-Al-Pd composite oxide which is also in agreement with the SEM studies. This porous structure is mostly obtained due

to the evaluation of gases during the sample preparation. Further, analyzing this image at 20 nm scale showed the spherical particles having sizes less than 20 nm.

The particle nature and size of the PdR3-PdR2 catalyst were observed through the TEM micrograph and also the particle size distribution was plotted to verify their size distribution. The result of the same is presented in Fig. 4.50. TEM analysis reveals that the particles formed are spherical in shape, having size less than 25 nm (Fig. 4.50a). Further, with the particle size distribution plotting it was confirmed that the particles from the PdR3-PdR2 samples are ranging from the 3 to 22 nm range (Fig. 4.50b).

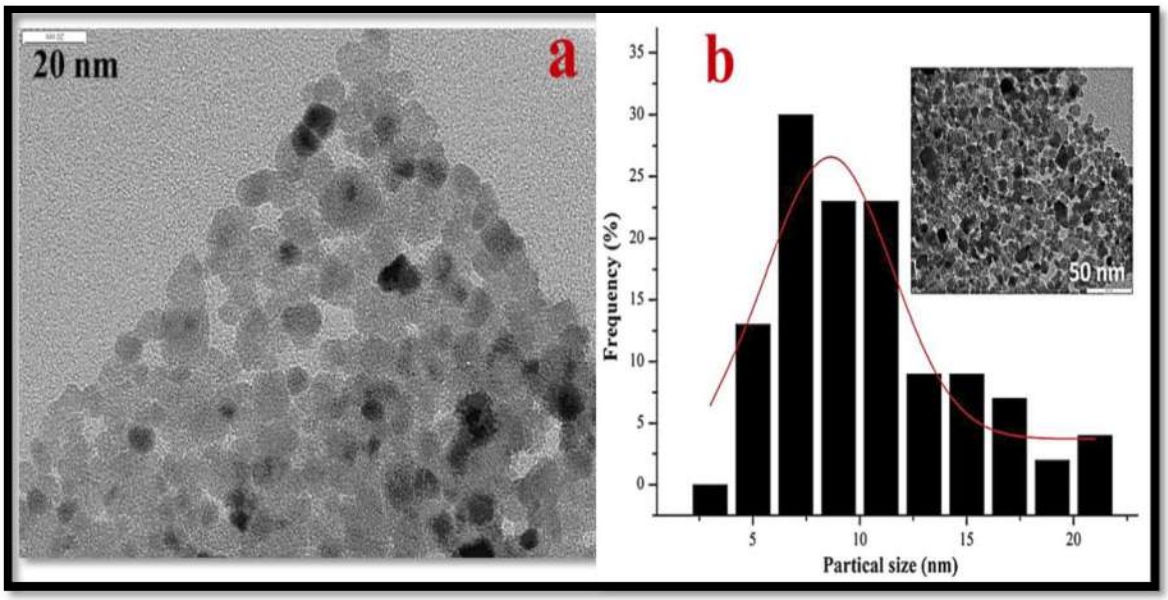

Fig. 4.50: *TEM image and Particle size distribution of PdR2-PdR3.*

Microscopic image of Cu-Co-10Mn oxide composite was obtained through HRTEM and depicted in Fig. 4.51a. The TEM image of Cu-Co-10Mn composite oxide shows spherical particles having size below 25 nm. Also, through histogram showing particle size distribution (Fig. 4.51b) it has been confirmed that the size of the particles are less than 25 nm. Histogram showed the particle dispersion below 24 nm showing high density in 12-14 nm scale.

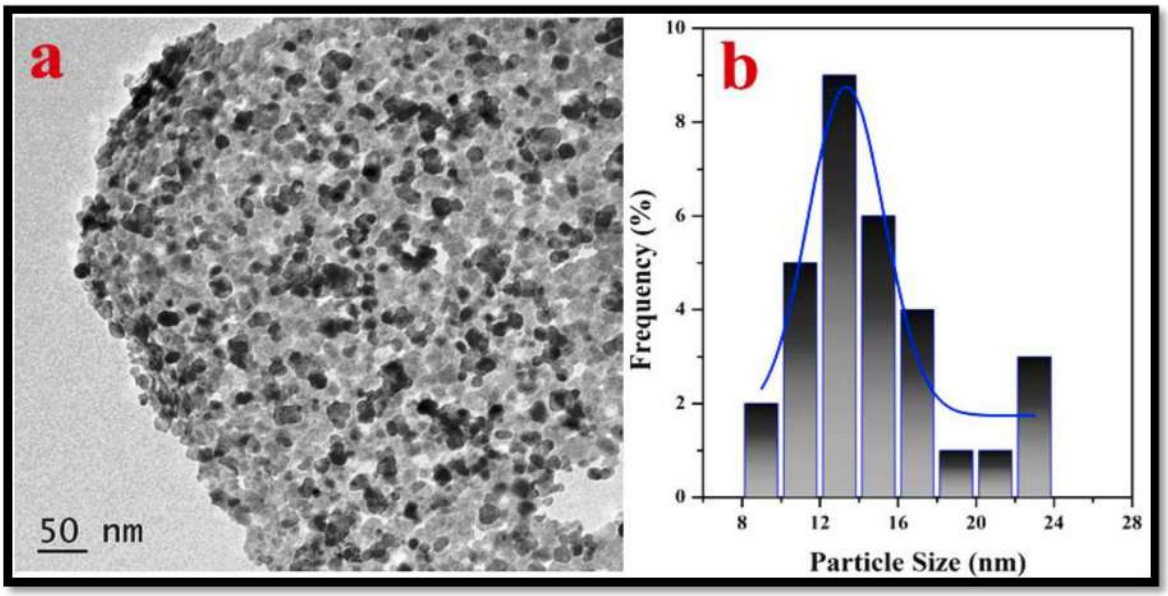

Fig. 4.51: *HRTEM image and Particle size distribution of Cu-Co-10Mn.*

5.1. N_2 - sorption studies

To determine the surface area, N_2 adsorption-desorption studies were performed at liquid N_2 temperature on copper substituted chromium (III) oxide. According to the International Union of Pure and applied Chemistry (IUPAC) rules, both the samples follow type II isotherm [235] having very small hysteresis. N_2 sorption isotherms of Cr_2O_3 and $Cr_{1.96}Cu_{0.04}O_3$ are given in Fig. 5.1.

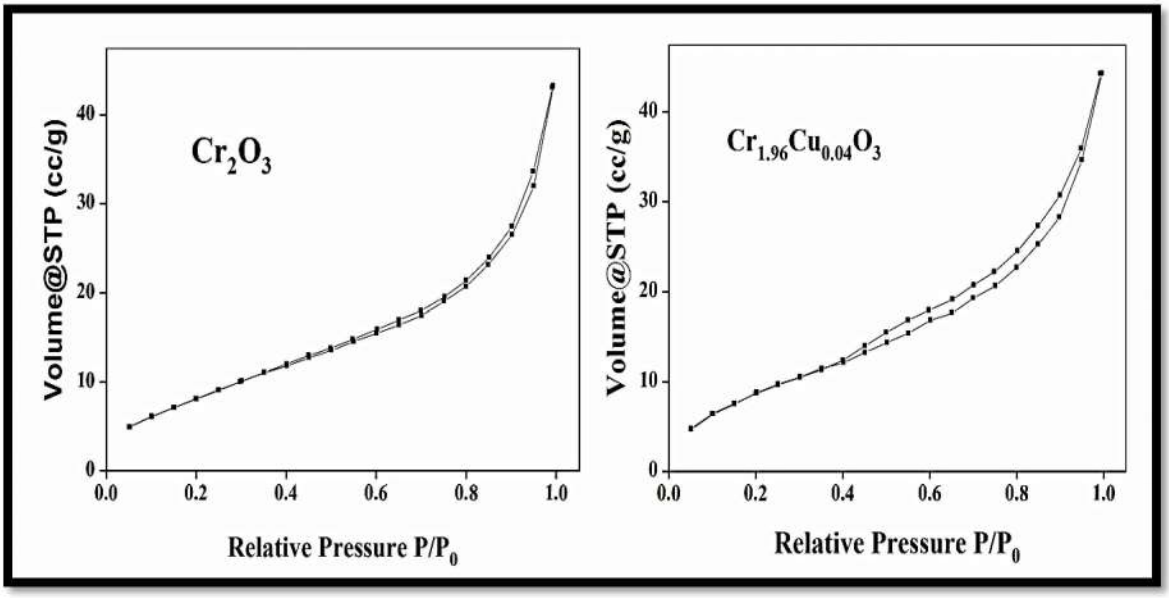

Fig. 5.1: *N_2 adsorption-desorption isotherm of Cr_2O_3 and $Cr_{1.96}Cu_{0.04}O_3$.*

The multi-point Brunauer-Emmett-Teller (BET) surface areas for Cr_2O_3 and Cu substituted Cr_2O_3 are found to be in range of 32 m^2/g to 36 m^2/g. Further, the resulted surface areas of all the prepared compounds from the series are tabulated in Table 5.1.

Table 5.1: *BET surface area of $Cr_{2-x}Cu_xO_3$.*

Sr. No.	Catalyst	BET surface area (m^2/g)
1	Cr_2O_3	32
2	$Cr_{1.96}Cu_{0.04}O_3$	34
3	$Cr_{1.92}Cu_{0.08}O_3$	33
4	$Cr_{1.84}Cu_{0.16}O_3$	36

N_2 adsorption-desorption isotherm of the prepared Mn, Cu and Ag substituted CeO_2 samples are demonstrated in Fig. 5.2. All the prepared samples exhibit same adsorption pattern like type II according to IUPAC rules [236, 237]. Further, it can be more precisely understood as type IIb isotherm [238].

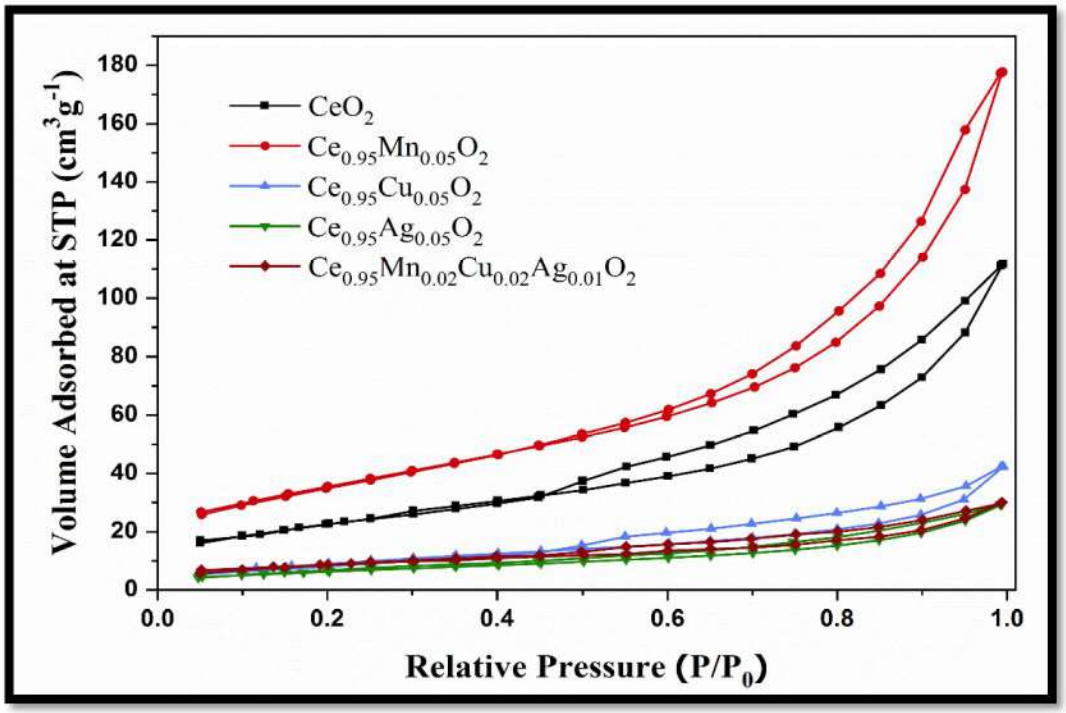

Fig. 5.2: *N_2 adsorption-desorption isotherm of Mn, Cu and Ag substituted CeO_2 series.*

The observed surface area values are summarized in Table 5.2. The formation of hysteresis loop can be accounted from the slit like pores formed by particle agglomeration, such particle agglomeration is also shown in SEM images. However, variation in the surface area was observed as dopant metal varies in CeO_2. The BET surface area for the Mn doped CeO_2 was found to be higher than the pristine CeO_2 (i.e. 128 m^2/g > 84 m^2/gm). The surface area of CeO_2 is found to decrease on doping with Cu or Ag and also with the co doping of Mn, Cu and Ag.

N_2 adsorption-desorption isotherm of Ru substituted CeO_2 are shown in Fig. 5.3. From Fig 5.3, it can be seen that the isotherm of the prepared oxides appears as Type II isotherm which is in accordance with IUPAC classification.

Table 5.2: *BET surface area of Mn, Cu and Ag substituted CeO_2.*

Sr. No.	Catalyst	BET surface area (m^2/g)
1	CeO_2	83
2	$Ce_{0.95}Mn_{0.05}O_2$	128
3	$Ce_{0.95}Cu_{0.05}O_2$	34
4	$Ce_{0.95}Ag_{0.05}O_2$	23
5	$Ce_{0.95}Mn_{0.02}Cu_{0.02}Ag_{0.01}O_2$	30

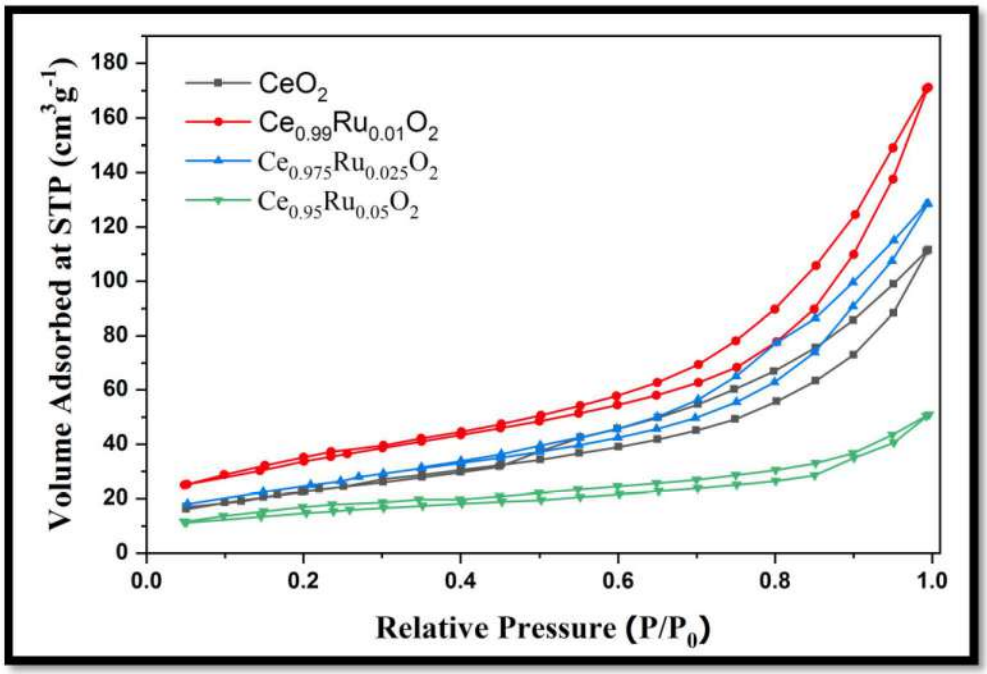

Fig. 5.3: *N_2 adsorption-desorption isotherm of $Ce_{1-x}Ru_xO_2$ (x = 0.01, 0.025, and 0.05).*

BET surface area values of all the studied catalyst are given in Table 5.3. Introduction of 1% Ru showed an increase in the surface area but further increase in Ru concentration in CeO_2 lead in reduction in surface area. This increase may be due to formation of more pores in $Ce_{0.99}Ru_{0.01}O_2$ which has not been observed in $Ce_{0.95}Ru_{0.05}O_2$ thereby dropping off its overall surface area.

Table 5.3: *BET surface area of $Ce_{1-x}Ru_xO_2$ (x = 0.01, 0.025, and 0.05).*

Sr. No.	Catalyst	BET surface area (m^2/g)
1	CeO_2	83
2	$Ce_{0.99}Ru_{0.01}O_2$	121
3	$Ce_{0.975}Ru_{0.025}O_2$	91
4	$Ce_{0.95}Ru_{0.05}O_2$	51

N_2 adsorption-desorption isotherms of the prepared Pd composed MM′ composite oxide catalysts are depicted in Fig. 5.4. It can be illustrated from this figure that the N_2-adsorption desorption are typical of type II isotherms having the resemblance of H_3 hysteresis loop.

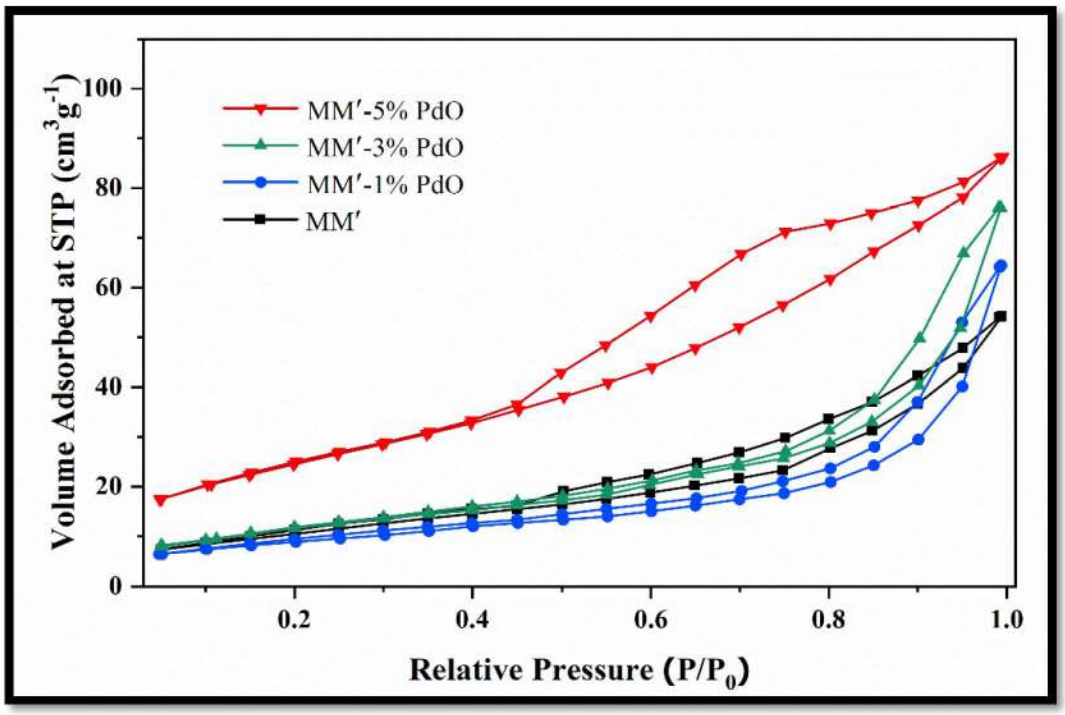

Fig. 5.4: *N_2 adsorption-desorption isotherm of Pd composed MM′ composite oxide series.*

The BET surface area shows rise from 40 to 90 m^2/g when the concentration of palladium in cobalt manganese composite oxides increases. Results of the same are tabulated in Table 5.4. A linear increase in surface area was observed with increase in Pd concentration. This may be due to the presence of palladium in the Co-Mn system which alters its structural

property leading to change in surface area. From literature studies, it is evident that the variation in surface area is observed when foreign material is incorporated in host system [239, 240]. Y. Kuwahara et al. studied the catalytic combustion reaction over iron-manganese oxide wherein variation in Fe concentration causes the enhancement in surface area of the system [39].

Table 5.4: *BET surface area of Pd composed MM′ composite oxide series.*

Sr. No.	Catalyst	BET surface area(m^2/g)
1	MM′	40
2	MM′ - 1% PdO	43
3	MM′ - 3% PdO	59
4	MM′ - 5% PdO	90

The BET surface area and pore size distribution were studied through N_2 adsorption-desorption isotherm over a series of Ag and Rh composed Co-Mn composite oxides prepared and are depicted in Fig 5.5. Observed isotherms presented in Fig. 5.5a are typical type II having a hysteresis loop of H3 type, which is mostly observed for mesoporous or macro-porous structure [241, 146]. These porous structures can be formed during the combustion process as the evolution of gases leads in generating the porous structure of the catalysts. The BET surface area for MM′, MM′-5%Ag, and MM′-5%Ag-1%Rh are 40 m^2/g, 38 m^2/g, and 80 m^2/g, respectively. The incorporation of Rh in the composite system leads in drastic increase of surface area from 38 m^2/g to 80 m^2/g. Further, the BJH distribution was done to evaluate the pore sizes and their distribution in the catalyst prepared (Fig. 5.5b).

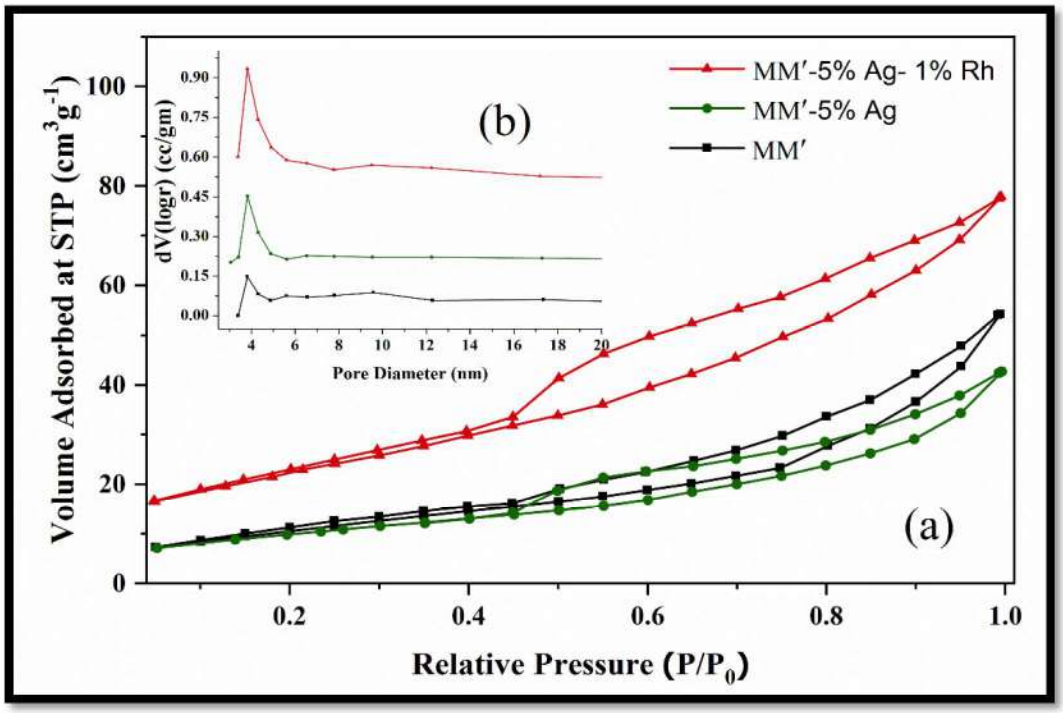

Fig. 5.5: *N_2 adsorption-desorption isotherm and BJH pore size distribution of MM′, MM′-5%Ag and MM′-5%Ag-1%Rh.*

All the prepared composites showed the mesoporous pores, which are ranging from 2 nm to 50 nm in size. MM′ catalyst showed the pore size of 3.8 nm having a pore volume of 0.078 cc/g whereas an increase in the pore volume was seen after the addition of Ag and Rh in MM′ composite oxide system, i.e. 0.108 cc/g (Detailed values are tabulated in Table 5.5).

Table 5.5: *BET surface area, pore volume and pore size of MM′, MM′-5%Ag and MM′-5%Ag-1%Rh.*

Sr. No.	Catalyst	BET surface area (m^2/g)	Pore volume (cc/g)	Pore Size (nm)
1	MM′	40	0.078	3.829
2	MM′ - 5% Ag	38	0.065	3.817
3	MM′ - 5% Ag- 1%Rh	80	0.108	3.827

Figure 5.6 shows the N_2 sorption studies of CuMn, CuMn-Pd and CuMn-Al-Pd composite oxide which were prepared via combustion route. According to the IUPAC classification, all

studied isotherm from Fig. 5.6a shows type II isotherm pattern. In addition, BJH pore size distribution curve are also determined and presented in Fig. 5.6b. The N_2 adsorption-desorption curve shows the lesser uptake of N_2 in CuMn and CuMn-Pd composite oxide whereas CuMn-Al-Pd composite oxide showed large amount of N_2 adsorption.

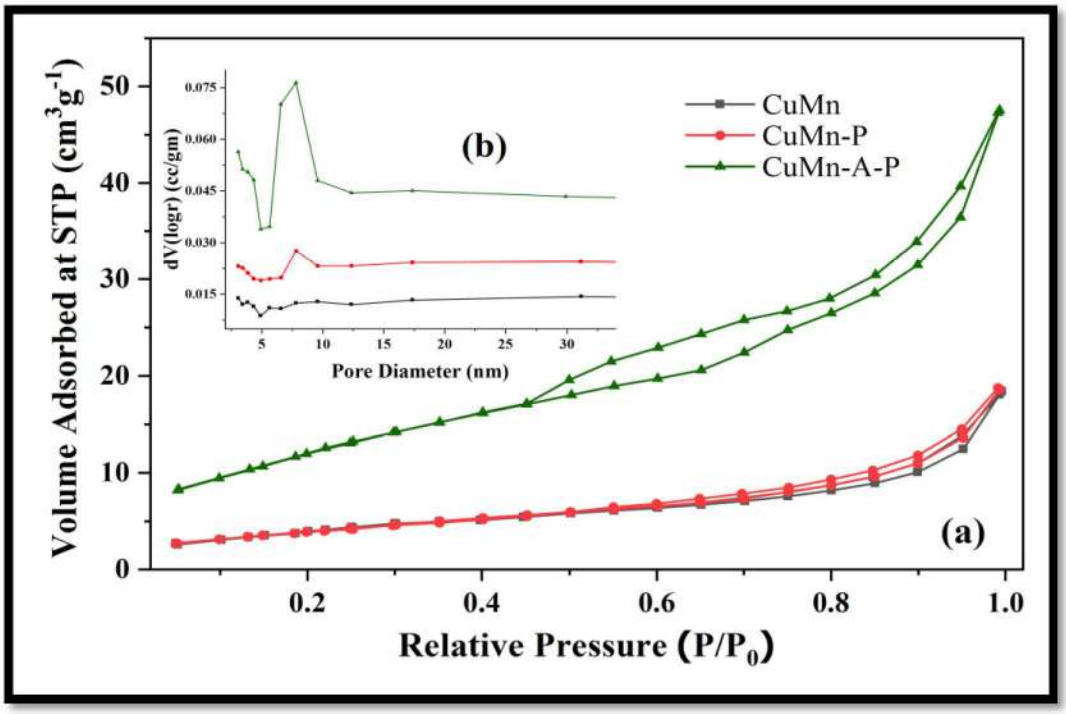

Fig. 5.6: *N_2 adsorption-desorption isotherm and BJH pore size distribution of CuMn, CuMn-Pd, and CuMn-Al-Pd composite oxide series.*

The result of BET surface area, pore volume and pore radius are listed in Table 5.6. The observed BET surface area of CuMn and CuMn-Pd are relatively low, which showed similar values i.e. 14.8 m^2/g and 14.4 m^2/g. In CuMn-Al-Pd composite oxide, profound increase in surface area can be seen on addition of Al (i.e. 45.4 m^2/g) and this increase is mostly because of pore formation as ascribed from its hysteresis loop. Furthermore, the hysteresis loop was formed by the capillary condensation of nitrogen in the pore which was later fitted with BJH method. Figure 5.6b shows that the pores are below 15 nm i.e. 3.06 nm for all the studied catalysts which is characteristic of mesoporous structure. With the addition of Aluminum, increase in mesoporous volume is seen which raises to 0.061 cc/g and this surface enlargement can be related to the increased surface area of CuMn-Al-Pd composite oxide.

Table 5.6: *BET surface area, pore volume and pore size of CuMn, CuMn-Pd, and CuMn-Al-Pd composite oxide series.*

Sr. No.	Catalyst	BET surface area (m^2/g)	Pore volume (cc/g)	Pore Size (nm)
1	CuMn	14.8	0.024	3.06
2	CuMn-P	14.4	0.025	3.06
3	CuMn-A-P	45.4	0.061	3.06

Figure 5.7 represents the nitrogen adsorption-desorption isotherms of manganese containing cobalt-copper composite oxide series. Type II isotherms have been observed for all the composite catalyst which were prepared via glycine combustion route.

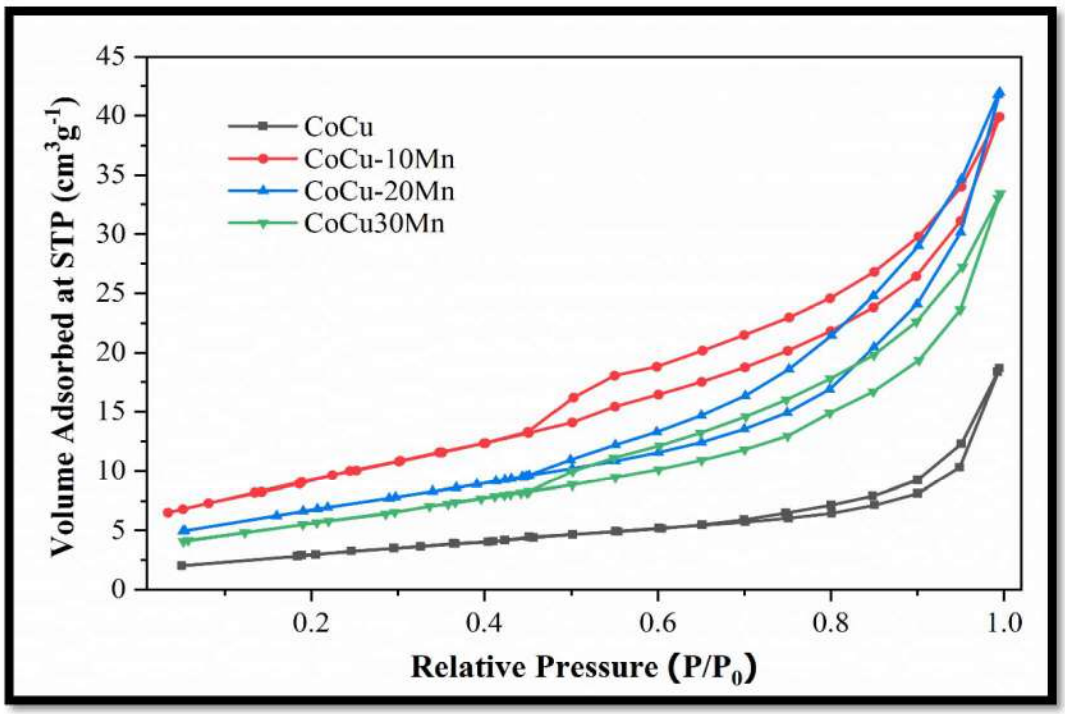

Fig. 5.7: *N_2 adsorption-desorption isotherm of Mn containing Co-Cu composite oxide series.*

The combustion process introduced the porous character in the composite catalyst as confirmed by the hysteresis loop. The BET surface area of all the prepared composite catalyst is given in Table 5.7. The surface area of Co-Cu composite oxide is found to be 11.1 m^2/g,

which is lowest in the prepared series. Further, the addition of 10% Mn in Co-Cu composite oxide has greatly enhanced the surface area to 33.5 m^2/g. However, increasing the concentration of Mn in Co-Cu composite oxide i.e. Co-Cu-20Mn and Co-Cu-30Mn has not shown the increase in BET surface area as that of CoCu-10Mn catalyst. The order of BET surface area is Co-Cu-10Mn > Co-Cu-20Mn > Co-Cu-30Mn > Co-Cu.

Table 5.7: *BET surface area of Mn containing Co-Cu composite oxide series.*

Sr. No.	Catalyst	BET surface area (m^2/g)
1	Cu-Co	11.1
2	Cu-Co-10Mn	33.7
3	Cu-Co-20Mn	24.5
4	Cu-Co-30Mn	20.6

BET surface areas of the prepared PdR1, PdR2, PdR3 and PdR3-PdR2 catalysts were calculated through N_2 sorption isotherm. The Adsorption-desorption plots of the prepared catalysts are shown in Fig. 5.8. From adsorption-desorption isotherm, we can conclude that the samples show type IV isotherm [237]. The highest surface area is observed for PdR1 while the lowest is observed for PdR3, i.e. 143 m^2/g and 22 m^2/g, respectively, in the prepared series. BET surface area of all the prepared oxide catalyst is tabulated in Table 5.8. The above observed pattern may be a result of their synthesis route and their surface occurrence. When $Co_{0.95}Pd_{0.05}Cr_2O_4$ is supported with PdO, a small decrease in surface area was observed, which can be seen from the N_2 adsorption-desorption isotherm of PdR2. In PdR3-PdR2, the surface area was found to be still lesser but was higher than PdR3, i.e. 56 m^2/g. Such a decrease in surface area of PdR3 can be due to the agglomeration of particles wherein a combination of PdR3-PdR2 prevents them from agglomeration compared to PdR3.

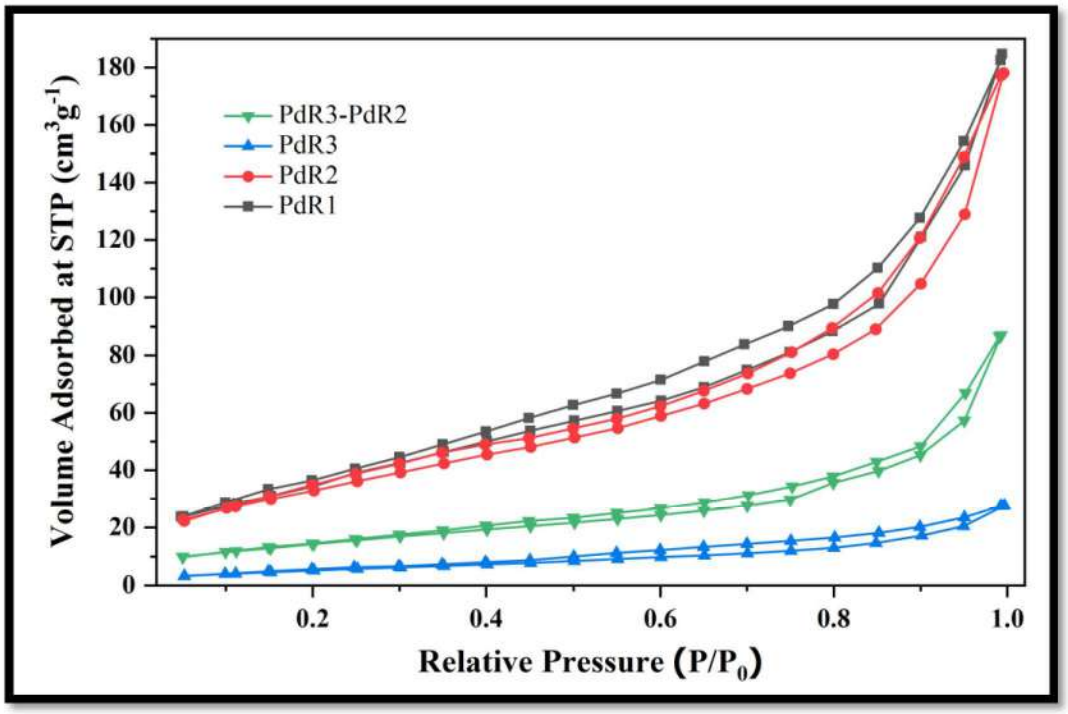

Fig. 5.8: *N_2 adsorption-desorption isotherm of PdR1, PdR2, PdR3 and PdR3-PdR2.*

Table 5.8: *BET surface area of PdR1, PdR2, PdR3 and PdR3-PdR2.*

Sr. No.	Catalyst	BET surface area (m^2/g)
1	PdR1	143
2	PdR2	130
3	PdR3	22
4	PdR3-PdR2	56

The BET surface area of $Cu_{0.95}Pd_{0.05}O$, $20Al/Cu_{0.95}Pd_{0.05}O$ and $10Al\text{-}Cu_{0.95}Pd_{0.05}O$ were measured with N_2 adsorption studies and are given in Table 5.9. The BET surface area of $Cu_{0.95}Pd_{0.05}O$ was observed to be 12 m^2/g, which is lowest surface area in the prepared series. With the addition of 20% Al_2O_3 on $Cu_{0.95}Pd_{0.05}O$ ($20Al/Cu_{0.95}Pd_{0.05}O$), the surface area was seen increasing to 17 m^2/g, which after addition of $Cu_{0.95}Pd_{0.05}O$ on the previously prepared $20Al/Cu_{0.95}Pd_{0.05}O$ (i.e. $10Al\text{-}Cu_{0.95}Pd_{0.05}O$) increased to 30 m^2/g. During the catalyst

modification with alumina, the surface changes its particle arrangement which thereby increases the surface area of the catalyst. The order for the surface area is as follows: $Cu_{0.95}Pd_{0.05}O$ > $20Al/Cu_{0.95}Pd_{0.05}O$ > $10Al\text{-}Cu_{0.95}Pd_{0.05}O$.

Table 5.9: *BET surface area of $Cu_{0.95}Pd_{0.05}O$, $20Al/Cu_{0.95}Pd_{0.05}O$ and $10Al\text{-}Cu_{0.95}Pd_{0.05}O$.*

Sr. No.	Catalyst	BET surface area (m^2/g)
1	$Cu_{0.95}Pd_{0.05}O$	12
2	$20Al/Cu_{0.95}Pd_{0.05}O$	17
3	$10Al\text{-}Cu_{0.95}Pd_{0.05}O$	30

Nitrogen sorption studies were employed to examine the BET surface area of all the prepared samples and its isotherms are depicted in Fig. 5.9a. According to IUPAC classification, prepared oxides samples showed typical Type IV isotherm having H3 type hysteresis [230, 237]. The BET surface area of the cerium oxide was observed to be 84 m^2/g whereas the pure CuO showed the surface area of 10 m^2/g. After the physical mixing of both CeO_2 and CuO, the average surface area was found to be 45 m^2/g. Such variable surface area of CeO_2, CuO and CeO_2-CuO composite can be easily related with their porosity nature as ascribed from hysteresis loop in Fig. 5.9a. Further, BJH pore size distribution studies were also performed using the N_2 adsorption-desorption isotherm over prepared series (Fig. 5.9b). The BJH pore size distribution showed the presence of pores in the mesoporous region and obtained values for pore volume and pore size are tabularized in Table 5.10. Pore volume for the CeO_2 was observed to be higher i.e. 0.167 cc/g having the pore diameter of around 3.8 nm whereas for CuO, it showed pore volume of around 0.020 cc/g with pore size of 4.3 nm. Such high pore volume in prepared cerium oxide may result in high amount of N_2 uptake as a consequence of capillary condensation [242]. This observed value showed the high mesoporous nature of CeO_2 oxides.

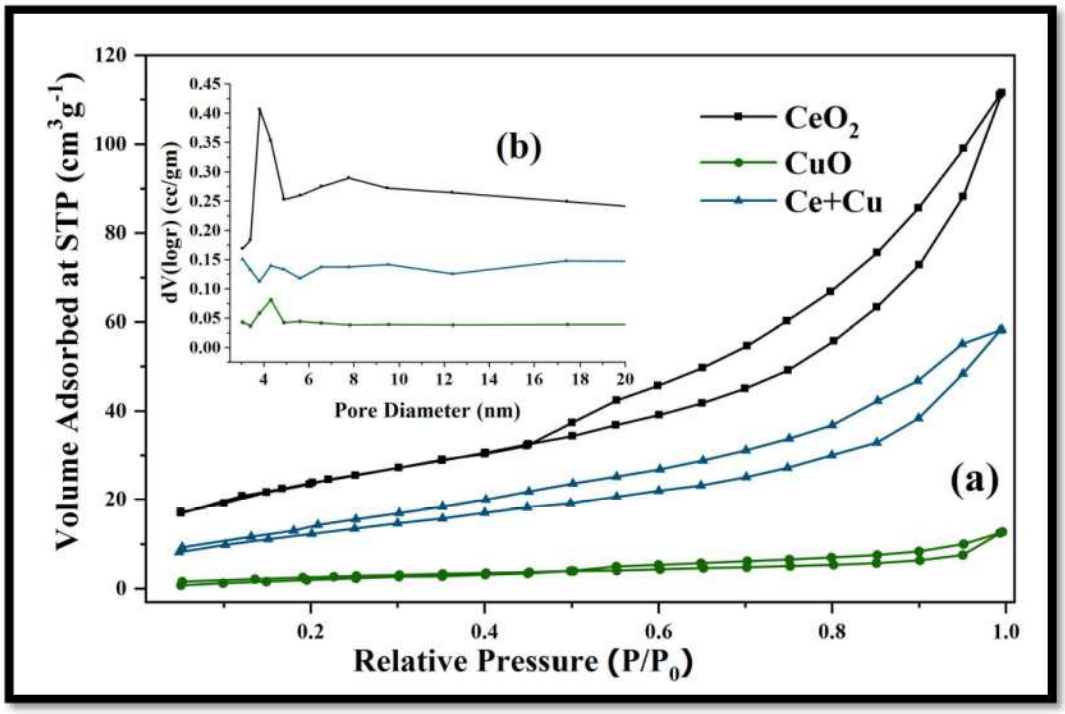

Fig. 5.9: *N_2 adsorption-desorption isotherm and BJH pore size distribution of CeO_2, CuO and Ce-Cu composite oxide*

Table 5.10: *BET surface area and BJH pore size distribution of CeO_2, CuO and Ce-Cu composite oxide.*

Sr. No.	Catalyst	BET surface area (m^2/g)	Pore volume (cc/g)	Pore Size (nm)
1	CeO_2	84	0.167	3.8
2	CuO	10	0.020	4.3
3	Ce - Cu	45	0.080	3.06

The BET surface area of prepared $Ce_{0.95}Ru_{0.05}O_2$, $Cu_{0.95}Pd_{0.05}O$ and CeRu-CuPd composite oxide are summarized in Table 5.11. The BET surface area of $Ce_{0.95}Ru_{0.05}O_2$ and $Cu_{0.95}Pd_{0.05}O$ were calculated at liquid nitrogen temperature which was found to be 51 m^2/g and 12 m^2/g, respectively. After physical grinding and further giving the heat treatment to the produced

mixture, the surface area was observed to increase to 64 m^2/g. This increase in the surface area may occur due to the interaction between the metals present in the mixture.

Table 5.11: *BET surface area of $Ce_{0.95}Ru_{0.05}O_2$, $Cu_{0.95}Pd_{0.05}O$ and CeRu-CuPd composite oxide.*

Sr. No.	Catalyst	BET surface area(m^2/g)
1	$Ce_{0.95}Ru_{0.05}O_2$	51
2	$Cu_{0.95}Pd_{0.05}O$	12
3	CeRu-CuPd	64

5.2. Temperature programmed Reduction studies using Hydrogen (H_2-TPR)

H_2-TPR studies were performed to examine the reducibility of the prepared catalyst. Figure 5.10 shows H_2 consumption profile of Cr_2O_3 and $Cr_{1.96}Cu_{0.04}O_3$ in the temperature range from 50 °C – 500 °C.

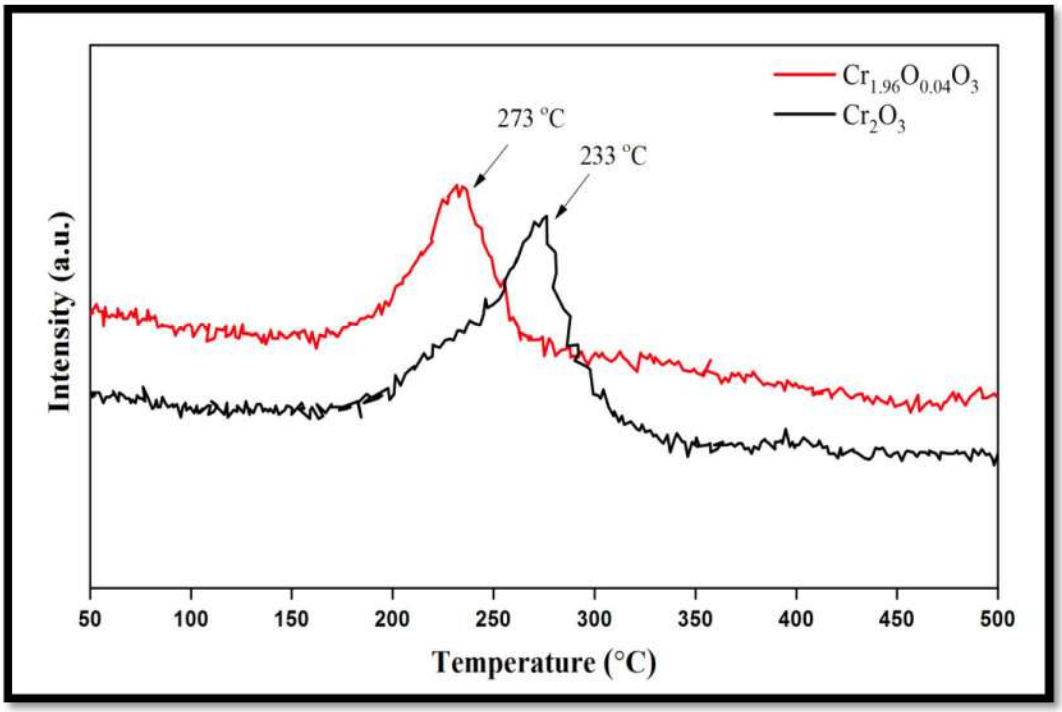

Fig. 5.10: *H_2-temperature programmed reduction studies over Cr_2O_3 and $Cr_{1.96}Cu_{0.04}O_3$.*

Oxygen uptake at a lower temperature region was observed when copper is substituted in Chromium oxide. Maximum reduction of Cr_2O_3 surface was observed at 273 °C whereas Cu substituted Cr_2O_3 shows reduction peak at 233 °C. M. Kocon et. al. also found maximum hydrogen uptake at 270 °C [243]. Presence of strongly bound oxygen in Cr_2O_3 catalyst makes it to reduce at higher temperature. In $Cr_{1.96}Cu_{0.04}O_3$, it is seen that the copper doping has increased oxygen mobility of Cr_2O_3 by weakening the metal oxygen bond. Also, literature showed excellent oxygen mobility in mixed metal oxide system compared to pure oxide [244, 245].

Temperature programmed reduction with hydrogen (H_2-TPR) is employed to assess the reducibility of the catalysts. TPR studies of CeO_2, $Ce_{0.95}Mn_{0.05}O_2$, $Ce_{0.95}Cu_{0.05}O_2$, $Ce_{0.95}Ag_{0.05}O_2$, and $Ce_{0.95}Mn_{0.02}Cu_{0.02}Ag_{0.01}O_2$ were carried out in temperature range of 50 - 500 °C and their profiles are presented in Fig. 5.11. The reduction pattern of CeO_2 shows a

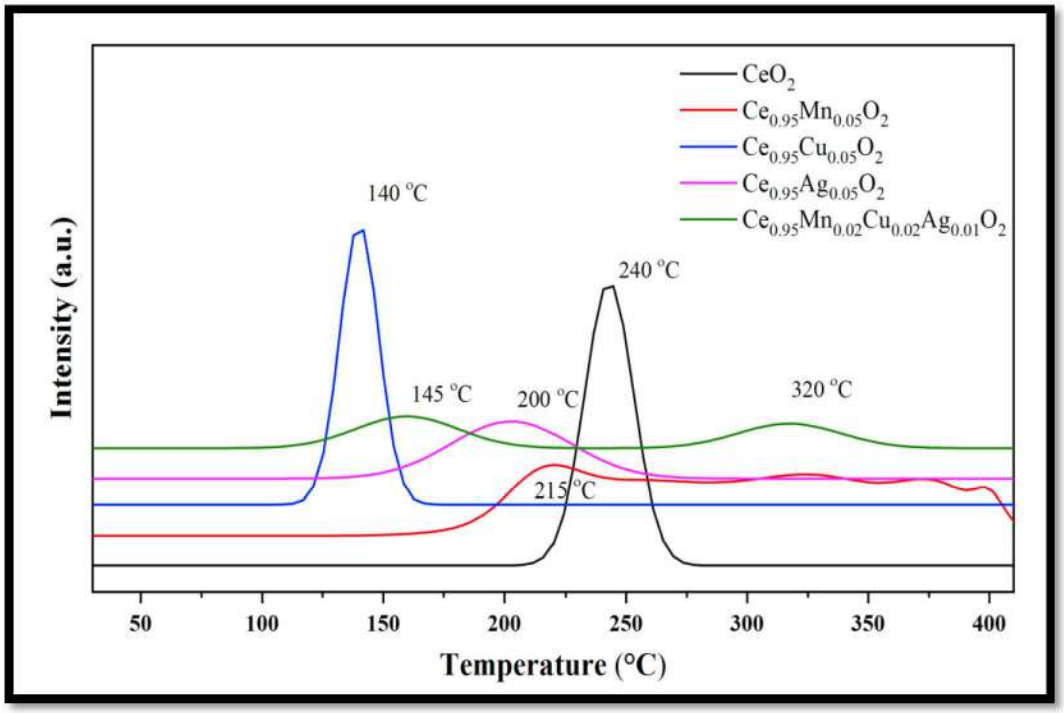

Fig. 5.11: *H_2-temperature programmed reduction studies over Mn, Cu and Ag substituted CeO_2 series.*

peak at around 240 °C that can be accounted for the oxygen consumption from the surface of cerium. Mn incorporation facilitates CeO_2 by enhancing its O_2 mobility, although intense peak

of oxygen consumption was not seen but the oxygen releasing capability was seen at much lower temperature (i.e. 185 °C) than pristine CeO_2 and it further continued till 400 °C. However, highly mobile oxygen was observed in $Ce_{0.95}Cu_{0.05}O_2$ showing a high rate of oxygen transfer by producing a reduction peak at a lower temperature region i.e. 140 °C. In $Ce_{0.95}Ag_{0.05}O_2$, it is observed to have lesser reactivity towards surface of the catalyst and showed a peak at 200 °C. Further, co-doping of Mn, Cu and Ag showed two peaks at 145 °C and 320 °C but the lesser amount of oxygen consumption were seen.

The reduction pattern of CeO_2 and Ru substituted CeO_2 catalysts are displayed in Fig. 5.12. The pure cerium oxide exhibit a reduction peak at around 240 ºC which may corresponds to the easily reducible cerium species from CeO_2 structure [175, 246]. Remarkably, the incorporation of 1% Ru in CeO_2 showed the improvement in its surface reduction pattern, which has been indicated by two reduction peaks at 117 ºC and 143 ºC.

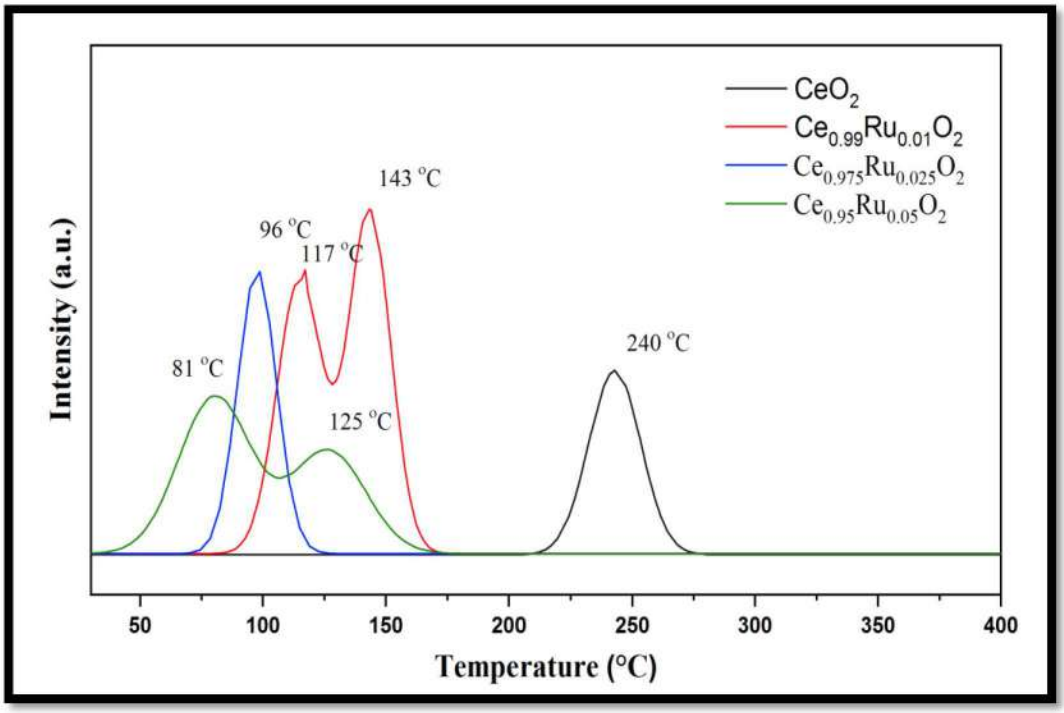

Fig. 5.12: *H_2-temperature programmed reduction studies over $Ce_{1-x}Ru_xO_2$ (x=0.01, 0.025 and 0.05).*

Also, in $Ce_{0.975}Ru_{0.025}O_2$ the formation of more mobile oxygen can be inferred which creates the sharp reduction peak at 96 ºC due to increasing oxygen mobility by presence of

more Ru species. Further, increase in Ru in ceria ($Ce_{0.95}Ru_{0.05}O_2$) showed the highest oxygen release at 81 ºC and 125 ºC which was observed to be a great achievement obtained within the series of catalyst prepared with respect to temperature. This shifting of the reduction pattern by addition of Ru is mainly due to weakening of Ce-O bond by Ru doping which alters the mobility of oxygen and also its redox character [247]. The increase in oxygen mobility with respect to temperature is in the order of $Ce_{0.95}Ru_{0.05}O_2$ > $Ce_{0.975}Ru_{0.025}O_2$ > $Ce_{0.99}Ru_{0.01}O_2$ > CeO_2.

H_2-TPR measurements were carried out to evaluate the reduction phenomenon of the Co-Mn composite oxide catalyst series. The profile for MM′ oxide series in temperature region of 50 to 500 °C are presented in Fig. 5.13. According to TPR pattern of the catalysts it is observed that MM′ composite having two reduction peaks exhibit comparatively less H_2 reactivity that too in the higher temperature region (at 270 °C and 385 °C). As Pd content increases in the system, increase in oxygen releasing property by catalyst was observed.

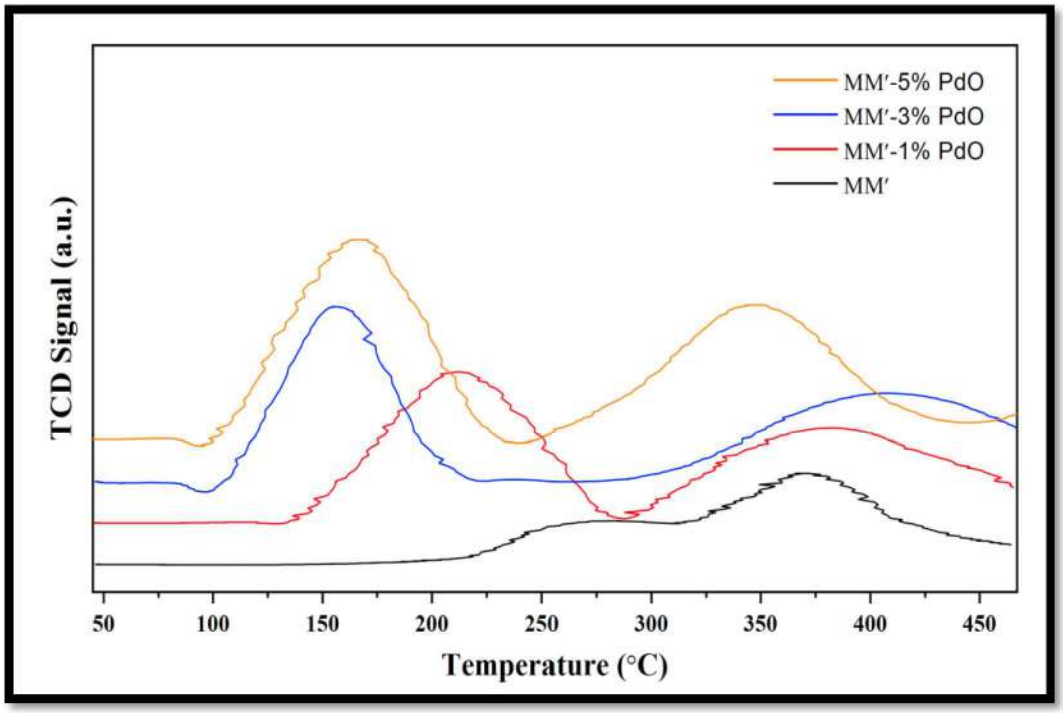

Fig. 5.13: *H_2-temperature programmed reduction studies over Pd composed MM′ composite oxide series.*

Also, surface reduction was achieved at lower temperature. When 5% palladium was introduced into Co-Mn mixed metal oxides, the oxygen reactivity was seen to increase and that too at lower temperature i.e. 150 °C and 349 °C. Observed trend of reduction temperature which was seen in H_2-TPR is directly in accordance with the catalytic conversion of CO and NO studies. Hydrogen consumption is controlled by mobility of oxygen in the system, which is seen to be increased when Pd content in Co-Mn composite is increased. It is well known fact that beside concentration of Pd, size of the particles also plays a vital role in surface reduction phenomenon. Compared to bulk particles, nano size material will have more exposed surface which result in more surface reduction. Denge et al. showed that the strong synergistic effects results in lowering reduction temperature and increase in oxygen mobility from advancement effect of precious metal [36]. Literature results showed that the presence of precious metal in mixed-metal system enhances oxygen mobility as compared to precious metal deficient systems [248][70].

Surface reductions over Ag and Rh composed catalysts were studied using H_2 and the resulted patterns are depicted in Fig. 5.14. The TPR plot of MM′ showed the presence of two peaks at 272 °C and 371 °C conveying the presence of two different stages of reduction processes in the composite.

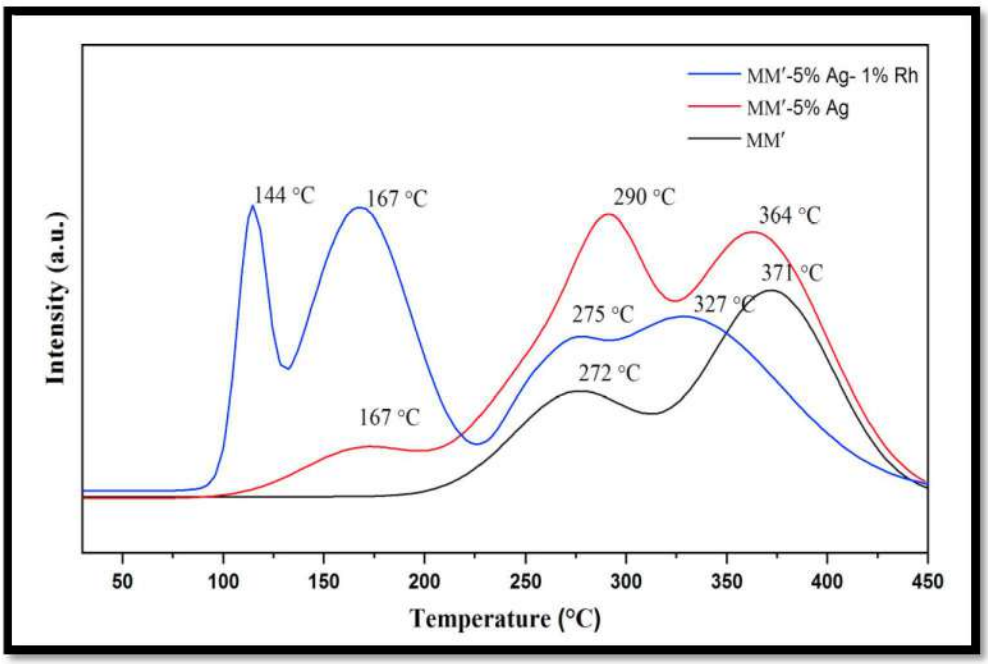

Fig. 5.14: *H_2-TPR studies over MM′, MM′ - 5% Ag and MM′-5%Ag-1%Rh composite oxide.*

As Ag was introduced in MM′ composite system, increased oxygen mobility was seen, which may be due to the enhancement in synergistic effect by the Ag addition. Also, a weak TPR signal was detected due to consumption of surface oxygen at 167 °C, portraying the development of mobile oxygen. Further, in MM′-5%Ag-1%Rh composite material, four reduction peaks were detected, out of which, two were appearing below 200 °C (114 °C and 167 °C) and two were above 200 °C (275 °C and 327 °C). Result demonstrates that, incorporation of Ag in MM′ composite along with Rh effectively increases the amount of oxygen mobility as compared to the rest of the prepared composite catalyst. The oxygen associated with the precious metal-containing system is easy to consume than a non-precious metal oxide system [249]. This may be the reason for the increase in oxygen mobility after incorporation of Ag and Rh in MM′ composite.

Surface reduction studies were employed on Pd and Al composed Cu-Mn composite series to understand the effect of Pd and Al in Cu-Mn composite and the results of the same are presented in Fig. 5.15.

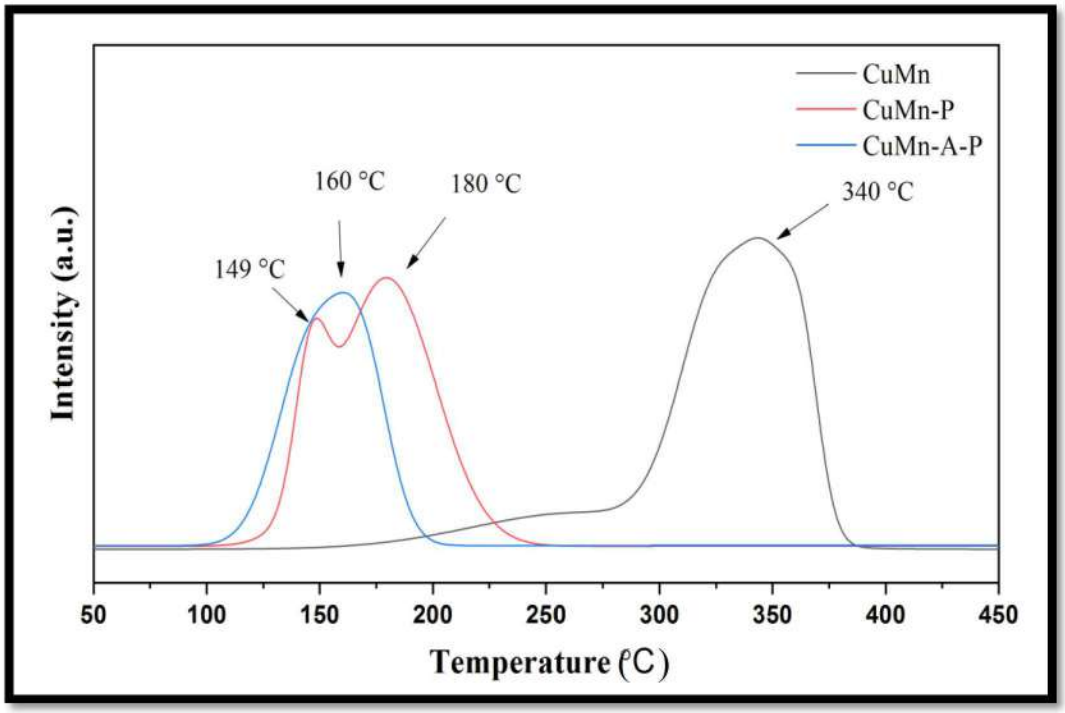

Fig. 5.15: *H_2-temperature programmed reduction studies over CuMn, CuMn-P and CuMn-A-P composite oxide.*

In Cu-Mn catalyst, a broad peak at 340 °C of H_2 consumption was seen with a shoulder peak at around 240 °C implying the surface reduction of Cu and Mn species. When Pd was added, the increase in oxygen mobility in Cu-Mn composite intern produces two reduction peaks at lower temperature i.e. 149 ºC and 180 ºC. For Cu-Mn-Al-Pd, the noticeable change in reduction pattern occurs by releasing its oxygen from 100 ºC till 200 ºC. This indicates the promotional effect of Al which helps in triggering the surface reduction property.

A series of Mn containing Cu-Co composite oxide were studied for their reduction pattern and curves obtained are illustrated in Fig. 5.16. From TPR pattern of Cu-Co oxide, a broad peak can be seen which starts its oxygen release at around 175 ºC and shows highest release at 270 ºC.

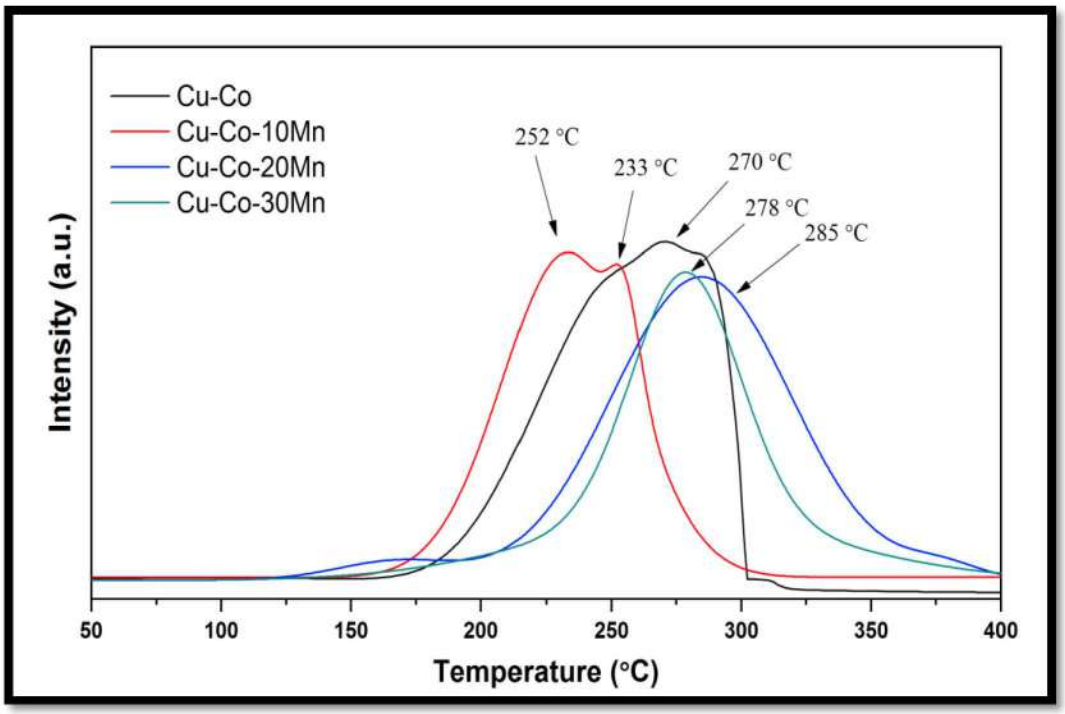

Fig. 5.16: *H_2-temperature programmed reduction studies over CoCu, CoCu-10Mn, CoCu-20Mn and CoCu-30Mn composite oxide series.*

After the incorporation of 10% Mn in Cu-Co oxide system, decrease in reduction temperature was observed, showing initiation of H_2 consumption at 160 ºC which may be provoked by systematic synergistic interaction of Cu, Co and Mn. Further, a raise in reduction temperature is seen with increase in Mn concentration to 20% and 30%. Such decrease in

oxygen mobility is mainly because of more strongly attached metal-oxygen bond which later makes the catalyst surface difficult to reduce.

Surface reducing-oxidizing properties of the catalyst are essential in completing any catalytic cycle. From the literature study, it is known that the availability of surface oxygen can efficiently be studied with H_2 temperature-programmed reduction studies [224, 246, 250].

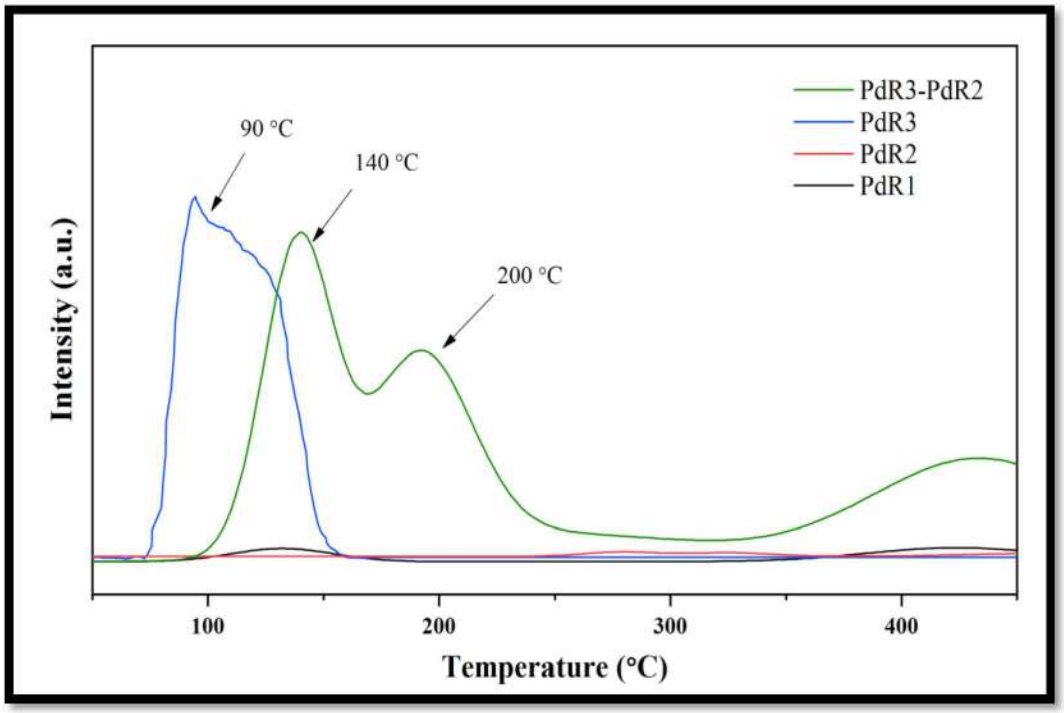

Fig. 5.17: *H_2-temperature programmed reduction studies over PdR1, PdR2, PdR3 and PdR3-PdR2.*

Figure 5.17 shows the H_2-TPR plot of prepared catalyst wherein different surface reducing patterns are seen. TPR profile shows very fewer reduction peaks for PdR1 and PdR2. Whereas in PdR3, strong reduction peak was observed at 90 °C and for PdR3-PdR2, peaks at 140 °C and 200 °C was observed which indicates that the interaction of PdR2 assists PdR3 to alter its reducing capability. When surface oxygen is removed, it is said that bulk oxygen moves to the surface and the defect moves in the opposite direction. [36] Such a surface phenomenon always depends on the reactivity of surface oxygen with H_2. When a surface possesses low oxygen mobility, it is very difficult to reduce the surface as it requires a high energy supply. In contrast, surface oxygen with high mobility can achieve a reduction to a greater extent.

The H_2-TPR profile of $Cu_{0.95}Pd_{0.05}O$ and Al_2O_3 modified $Cu_{0.95}Pd_{0.05}O$ catalysts are shown in Fig. 5.18. The H_2 TPR profile of $Cu_{0.95}Pd_{0.05}O$ shows reduction peak at 200 ºC with a shoulder peak at 157 ºC, which can be assigned for reduction of Cu^{+2} species that is present in vicinity of Pd. Also, additional peak was observed at 305 ºC which can be assigned to the tightly held oxygen from Cu-O, which has been confirmed from our previous report [175].

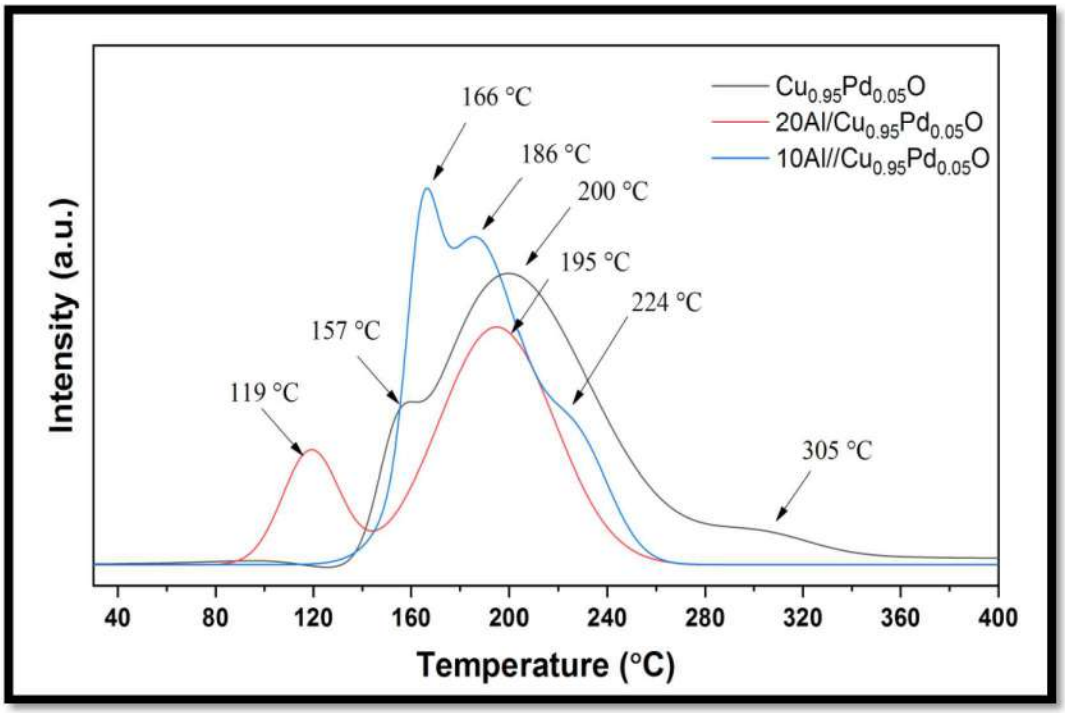

Fig. 5.18: *H_2-temperature programmed reduction studies over $Cu_{0.95}Pd_{0.05}O$, 20Al/ $Cu_{0.95}Pd_{0.05}O$ and 10Al-$Cu_{0.95}Pd_{0.05}O$.*

In 20%/$Cu_{0.95}Pd_{0.05}O$ catalyst, two H_2 consumption peaks at 119 ºC and 195 ºC are seen. The peak arising at higher temperature can be related to reduction of Cu^{+2} species from $Cu_{0.95}Pd_{0.05}O$ and the lower temperature peak of Cu^{+2} may be associated with the Al_2O_3 and Pd environment. Later, the catalyst has been designed in such a way that the exposed Al_2O_3 surface can be capped with Cu-Pd species from $Cu_{0.95}Pd_{0.05}O$. This modification resulted in three reduction peaks at 166 ºC, 186 ºC and 224 ºC showing an acting synergy between Cu, Pd and Al.

Surface oxygen mobility plays an important role in depicting the redox property of the catalyst. Surface reduction (H_2-TPR) with respect to temperature was examined over CeO_2, CuO and CeO_2-CuO composite oxide and their profile is given in Fig. 5.19. The pure CeO_2 starts reducing at around 215 °C and shows the small reduction peak having high reduction at 240 °C which may be due to the reducible CeO_2 surface [251]. On the other hand, a large peak in CuO profile indicates a huge release of oxygen from the CuO in the temperature range of 200 - 370 °C. During the analysis, it was observed that the catalyst turns its blackish brown appearance to reddish which may be due to CuO → Cu_2O transformation.

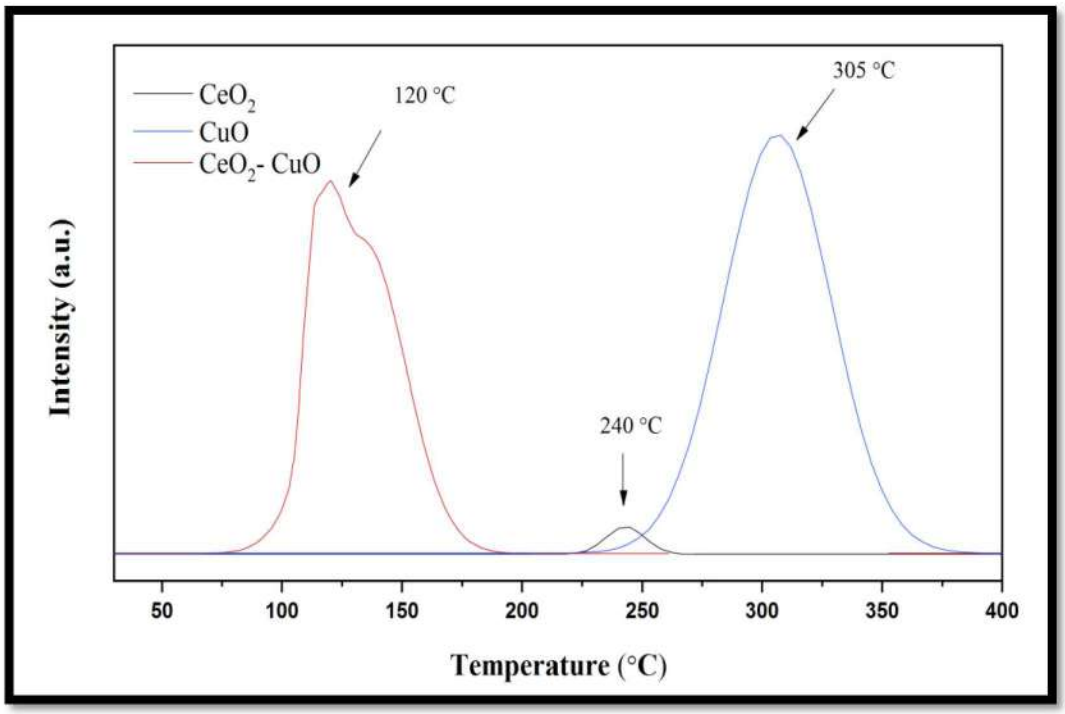

Fig. 5.19: *H_2-temperature programmed reduction studies over CeO_2, CuO and Ce-Cu composite oxide.*

When CeO_2 is combined with CuO to formulate CeO_2-CuO, strong peak of H_2 consumption was observed at lower temperature i.e. 80 - 200 °C. This may be the consequences of the interfaces generated by interaction between CeO_2 and CuO which helps in shifting the reduction temperature. Also, the higher dispersion rate of CeO_2 and CuO (as observed from the EDS mapping) is one of the promotional factor in deciding the catalyst reducing character. The literature reports shows that the addition of Cu in CeO_2 decreases the reduction temperature as a result of the strong interaction of copper with the ceria [100, 252, 253].

The H_2 TPR profile of $Ce_{0.95}Ru_{0.05}O_2$, $Cu_{0.95}Pd_{0.05}O$ and CeRu-CuPd composite oxide catalyst are shown in Fig. 5.20. A broad peak in TPR curve in $Cu_{0.95}Pd_{0.05}O$ at 200 ºC with two shoulders at 157 ºC and 305 ºC can be associated with the Cu^{+2} reduction. Such, H_2 consumption peaks in different temperature region is mostly due to the presence of Cu^{+2} in different electronic environment.

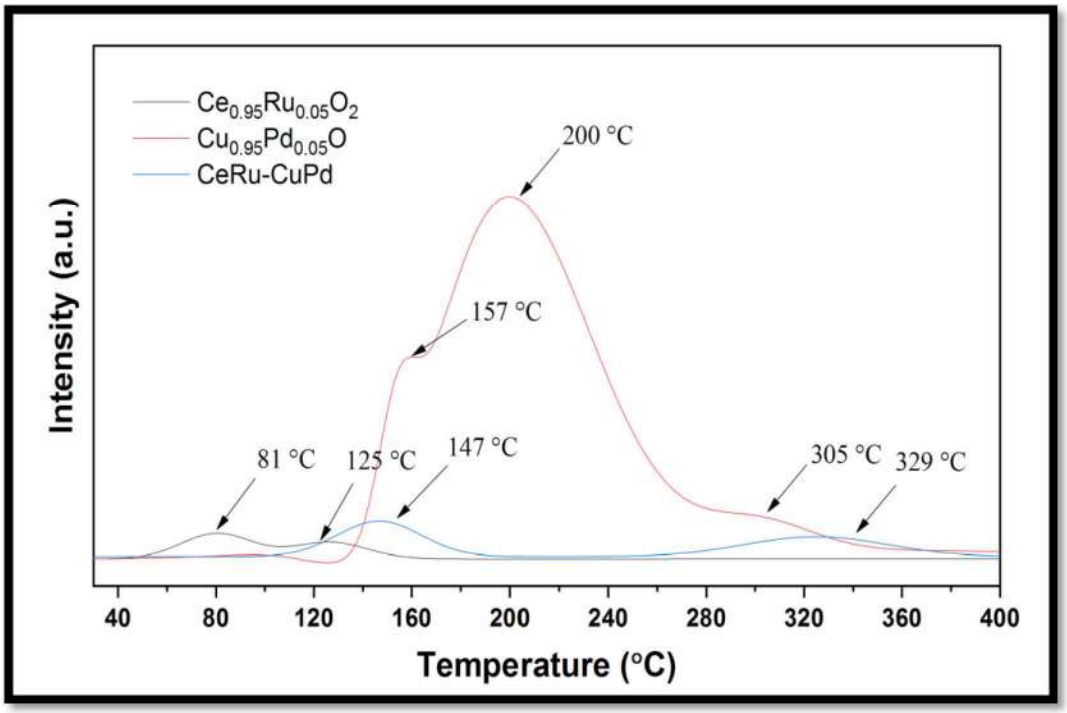

Fig. 5.20: *H_2-temperature programmed reduction studies over $Ce_{0.95}Ru_{0.05}O_2$, $Cu_{0.95}Pd_{0.05}O$ and CeRu-CuPd composite oxide.*

The pattern of reduction for Ru doped CeO_2 shows the release of oxygen in two different regions (i.e. 81 ºC and 125 ºC) which is at much lower temperature as compared to other catalyst from the series. With the systematic designing of CeRu-CuPd composite oxide through physical grinding, the release of huge amount of oxygen from $Cu_{0.95}Pd_{0.05}O$ and low temperature oxygen release from $Ce_{0.95}Ru_{0.05}O$ has been altered. As a result, two peaks with lower intensity and little lower oxygen mobility can be seen at 147 ºC and 329 ºC in CeRu-CuPd composite oxide system. Similar type of effect showing the variation in reduction pattern was also reported over CeO_2-CuO composite oxide [175].

5.3. Temperature programmed Oxidation studies using Oxygen (O_2-TPO)

O_2-TPO experiment was performed to investigate the oxidizing behaviour of the PdR1, PdR2, PdR3 and PdR3-PdR2 catalysts. O_2-TPO was studied in the temperature range of 30 °C to 500 °C and the profiles are presented in Fig. 5.21.

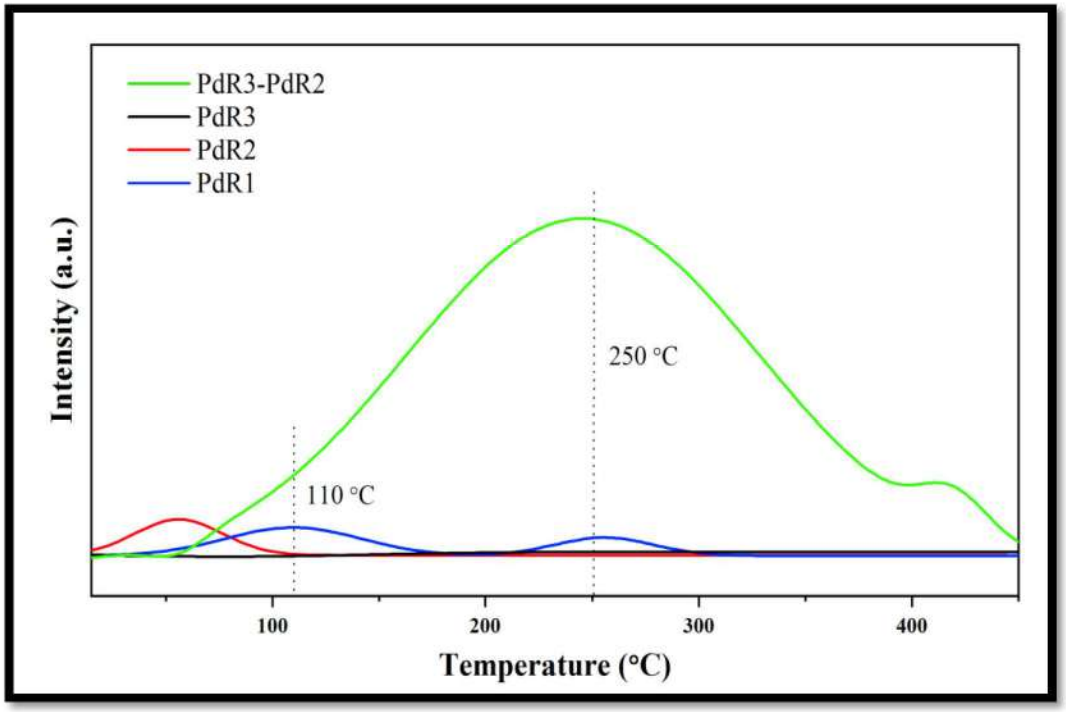

Fig. 5.21: *O_2-temperature programmed oxidation studies over PdR1, PdR2, PdR3 and PdR2-PdR3.*

The TPO results of PdR3 shows two small oxidation peaks at 110 °C and 250 °C showing its oxidizing nature at two different temperature regions. However, no peaks are observed for PdR1, also supporting PdO on it, as no change is seen a change in the TPO profile as ascribed from the PdR2 pattern. Further, combination effect is demonstrated in PdR3-PdR2 as seen from Fig. 5.21 wherein the enhancement in the surface oxidizing property has been observed. This increase in peak area shows the influence of support-support interaction in oxygen storage performance.

To investigate the oxidation behavior of the catalyst, O_2 temperature programmed oxidation (O_2-TPO) studies were performed after the H_2-TPR study over CeO_2, CuO and CeO_2-CuO catalyst. As depicted from Fig. 5.22, absence of oxidation peak during analysis

over CeO_2 implies the poor redox property of cerium oxide whereas CuO showed the two peaks at 137 °C and 285 °C. The sharp peak at 137 °C may be the resultant of highly exposed reduced copper oxide species which is considered to be very unstable and when it comes in contact with oxygen it directly converts to Cu (II) oxide.

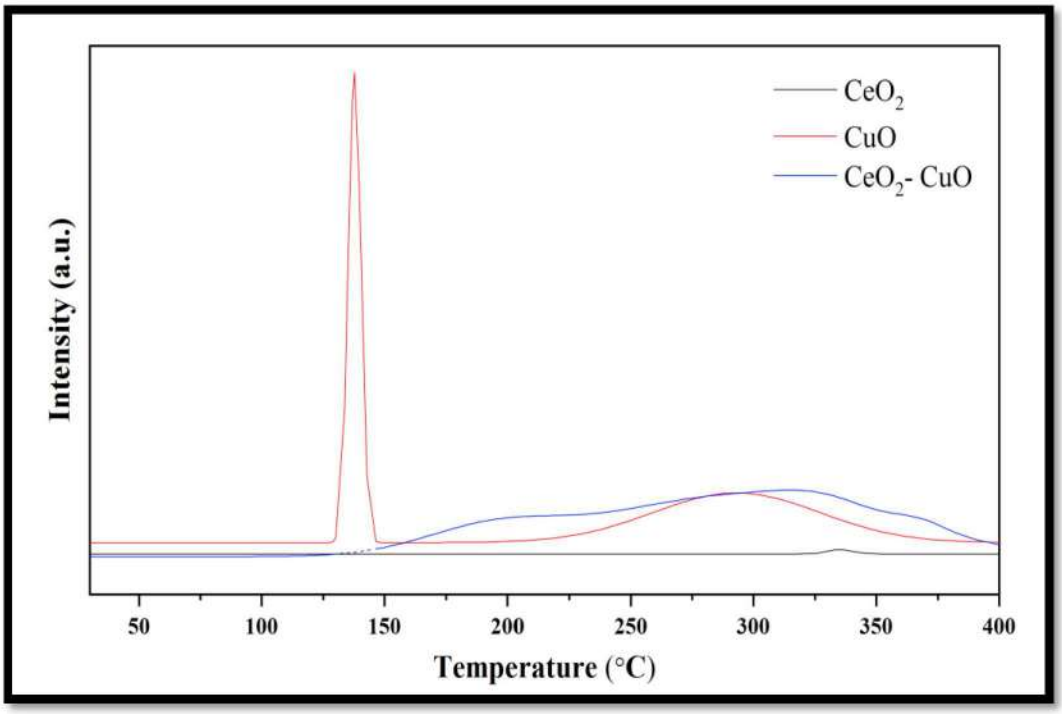

Fig. 5.22: *O_2-temperature programmed oxidation studies over CeO_2, CuO and Ce-Cu composite oxide.*

The presence of Cu_2O (reddish color) [254] was also evident from the TPR studies performed. The O_2-TPO profiles for CeO_2-CuO shows a broad peak starting at 150 °C and continues till 400 °C, displaying the oxidation of composite oxide in the controlled manner.

5.4. CO - Temperature programmed Desorption studies (CO-TPD)

Figure 5.23 represents the CO-TPD profile of Ru substituted CeO_2 series. In TPD profile, two peaks can be observed, out of which one is positioned at lower temperature (from 50-125 ºC) and another at higher temperature region (from 250-350 ºC). The peak originated at lower temperature can be attributed to weakly adsorbed CO and the one at higher temperature is associated with the strongly adsorbed CO [159]. For pure CeO_2, absence of desorption peak clarifies the lack of CO affinity towards the CeO_2. While, with the addition of Ru in cerium

oxide, the adsorption of CO is observed and found increasing linearly with increase in the Ru concentration. From the prepared series, $Ce_{0.95}Ru_{0.05}O_2$ showed higher CO concentration as compared to other compounds from the series and the order of CO desorption is observed as $Ce_{0.95}Ru_{0.05}O_2 > Ce_{0.975}Ru_{0.025}O_2 > Ce_{0.99}Ru_{0.01}O_2 > CeO_2$.

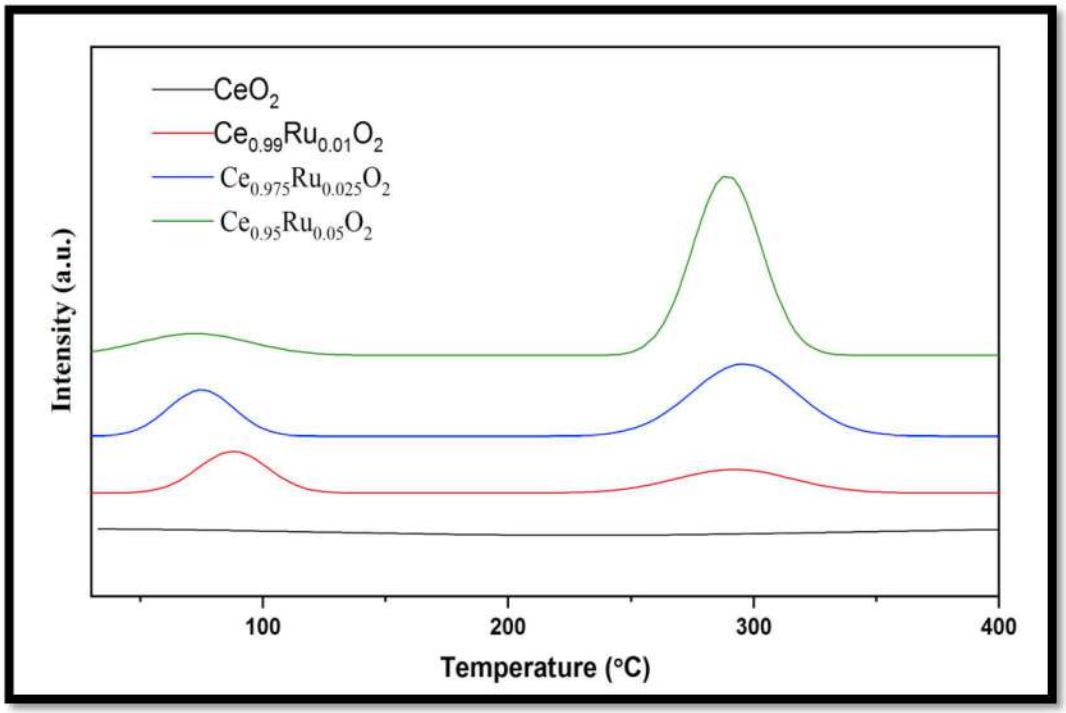

Fig. 5.23: *CO - Temperature programmed Desorption studies over CeO_2, $Ce_{0.99}Ru_{0.01}O_2$ $Ce_{0.975}Ru_{0.025}O_2$ and $Ce_{0.95}Ru_{0.05}O_2$.*

In order to examine the relationship between the studied catalytic reaction and chemical reactivity of CO with Ag and Rh composed Co-Mn surface, the CO desorption studies were performed with CO-TPD method. Figure 5.24 shows the CO-TPD profile of the prepared MM′, MM′ - 5% Ag and MM′-5%Ag-1%Rh composite oxide catalysts. MM′ catalyst shows only strongly adsorbed CO whereas MM′-5%Ag and MM′-5%Ag-1%Rh showed both weakly chemisorbed CO as well as strongly adsorbed CO species. Two desorption peaks at 97 °C and 236 °C was seen as Ag was introduced in MM′ catalyst system. This weak CO adsorption over the catalyst surface was observed to be increasing as Rh was added to Ag containing MM′ composite systems (64 °C and 264 °C). It is observed from the TPD profile that MM′-5%Ag-1%Rh catalyst system contains more amount of weak CO adsorption site, which is considered to be a key factor during the NO-CO redox reaction. Such surface phenomenon of

CO with the catalyst surface can be strongly accepted for Mars-Krevelen mechanism [33, 255, 256] wherein, surface oxygen plays a role in catalytic process.

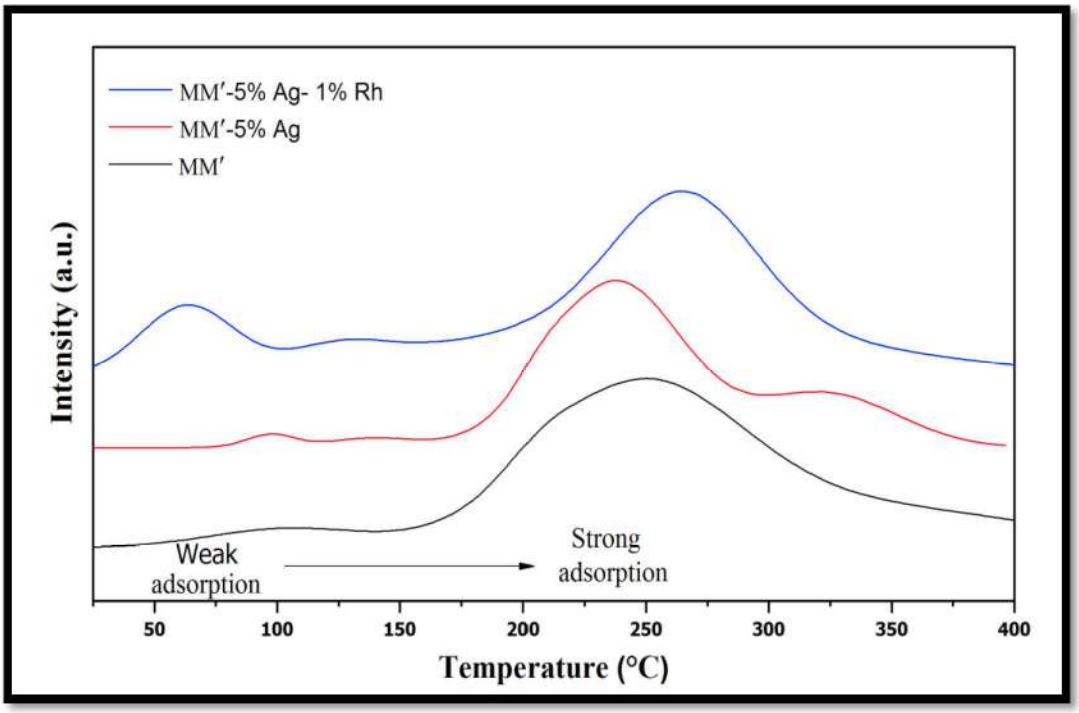

Fig. 5.24: *CO - Temperature programmed Desorption studies over MM', MM' - 5% Ag and MM'-5%Ag-1%Rh composite oxide series.*

To evaluate the amount of CO adsorbed and CO bonding strength toward the catalyst surface, CO-TPD studies were conducted over Mn containing Co-Cu composite oxide and the results of the same are presented in Fig. 5.25. In all the studied samples, CO desorption has been observed in the temperature range of 165 ºC to 330 ºC. In the case of Cu-Co composite oxide, a broad peak of CO desorption is found having highest CO desorption at 265 ºC. When 10% of Mn was added to Cu-Mn composite, a shift in CO desorption to lower temperature was detected which can be clearly seen from the TPD profile of Cu-Co-10Mn. Later, addition of higher concentration of Mn (i.e. 20 and 30%) decrease in peak intensity was seen with the increase in Mn concentration, conveying the lesser CO adsorption capacity of Cu-Co-20Mn and Cu-Co-30Mn composite oxide.

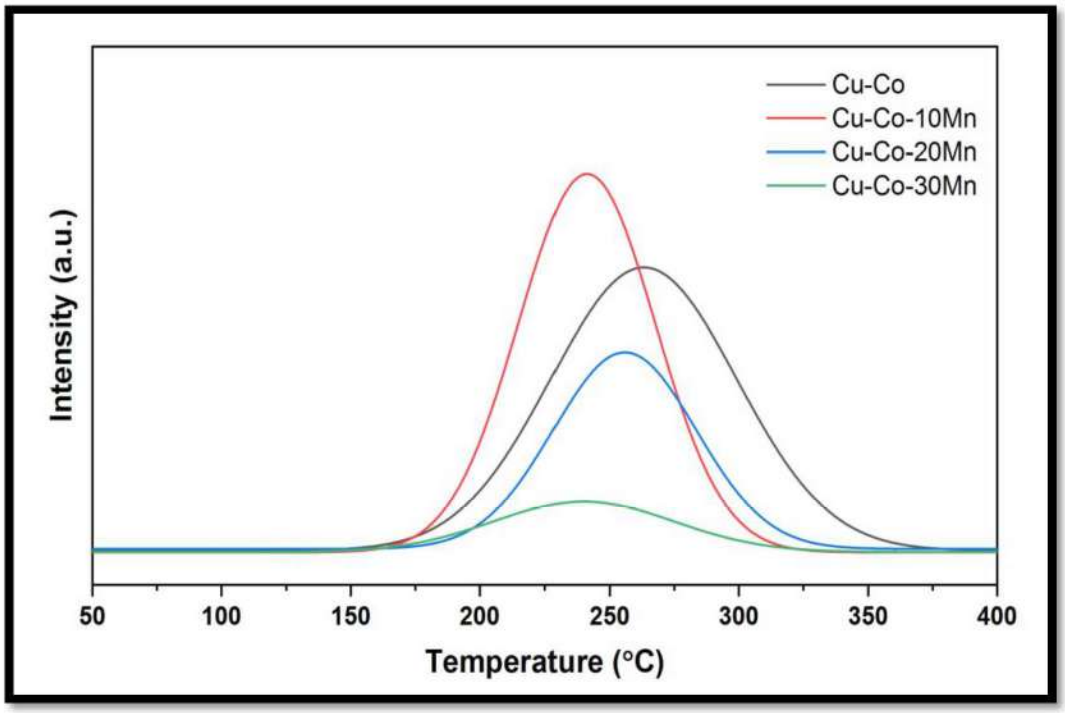

Fig. 5.25: *CO - Temperature programmed Desorption studies over Mn containing Co-Cu composite oxide series.*

Temperature programmed desorption (TPD) studies is an important tool to understand the surface reactivity towards the reacting gas in the catalysis area. The CO desorption profiles (CO-TPD) of the prepared catalyst are exhibited in Fig. 5.26. This Fig. illustrates two types of peaks having a large difference in CO desorption pattern in the studied temperature region. The peak at a lower temperature can be ascribed to the weak CO adsorption on the catalyst. In contrast, the peak at higher temperature corresponds to strongly adsorbed CO [20]. It can be perceived that PdR1 and PdO supported PdR1 (i.e. PdR2) has a weak chemisorbed CO whereas for PdR3 comparatively stronger CO chemisorption was observed with desorption in the range of ~200 - 400 °C. Further, increase in peak intensity of CO desorption was seen when PdR3 was combined with PdR2 indicating more intake of CO by the catalyst surface (CO-TPD pattern of PdR3-PdR2). According to studies reported, mobility of lattice oxygen and surface reactivity towards CO is a key factor in designing the desorption profile of CO, which can be altered by combining different metals in the catalyst system [241, 74]. Such alteration in O_2 mobility and surface reactivity was created by allowing PdR3 to combine with

PdR2 making its surface more active by adsorbing the CO for a longer period which is an important factor in a redox reaction.

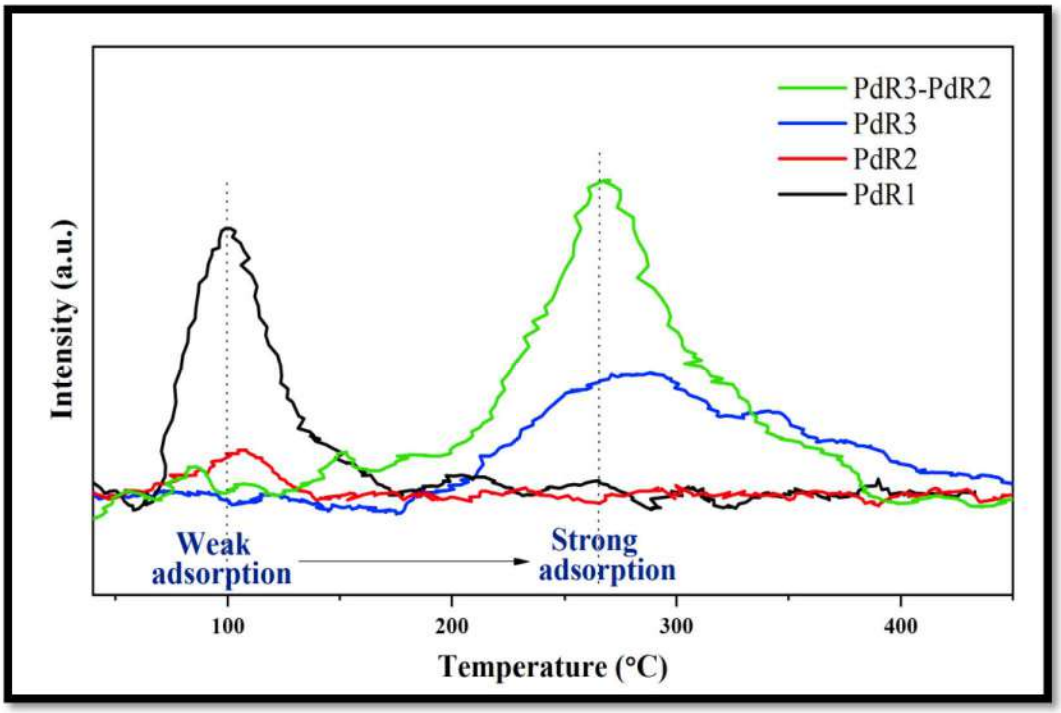

Fig. 5.26: *CO - Temperature programmed Desorption studies over PdR1, PdR2, PdR3 and PdR3-PdR2.*

Figure 5.27 shows the TPD spectra of Al_2O_3 modified $Cu_{0.95}Pd_{0.05}O$ series. In these measurements CO was adsorbed at room temperature and desorption was carried out with raising the sample temperature. The reactivity of CO towards the catalyst surface is known to be directly proportional to the active sites present on the catalyst surface. In $Cu_{0.95}Pd_{0.05}O$, desorption of CO starts at 167 ºC and completes desorption at 350 ºC, having a maximum at 255 ºC. In the case of $20Al/Cu_{0.95}Pd_{0.05}O$, addition of 20% Al_2O_3 to $Cu_{0.95}Pd_{0.05}O$ species, the adsorption of CO appeared with a greater peak area as compared to $Cu_{0.95}Pd_{0.05}O$ which shows CO desorption from 158 to 395 ºC. Further modifying the 20%Al/ $Cu_{0.95}Pd_{0.05}O$ to 10Al- Cu-Pd shows the improved CO adsorption as illustrated by desorption of CO from 147 to 395 ºC. This desorption is comparatively in greater amount as rest of the compounds from the series. Such improved CO adsorption is mostly due to the increment in the active site in $10Al/Cu_{0.95}Pd_{0.05}O$, which is achieved by more exposed Cu-Pd surfaces.

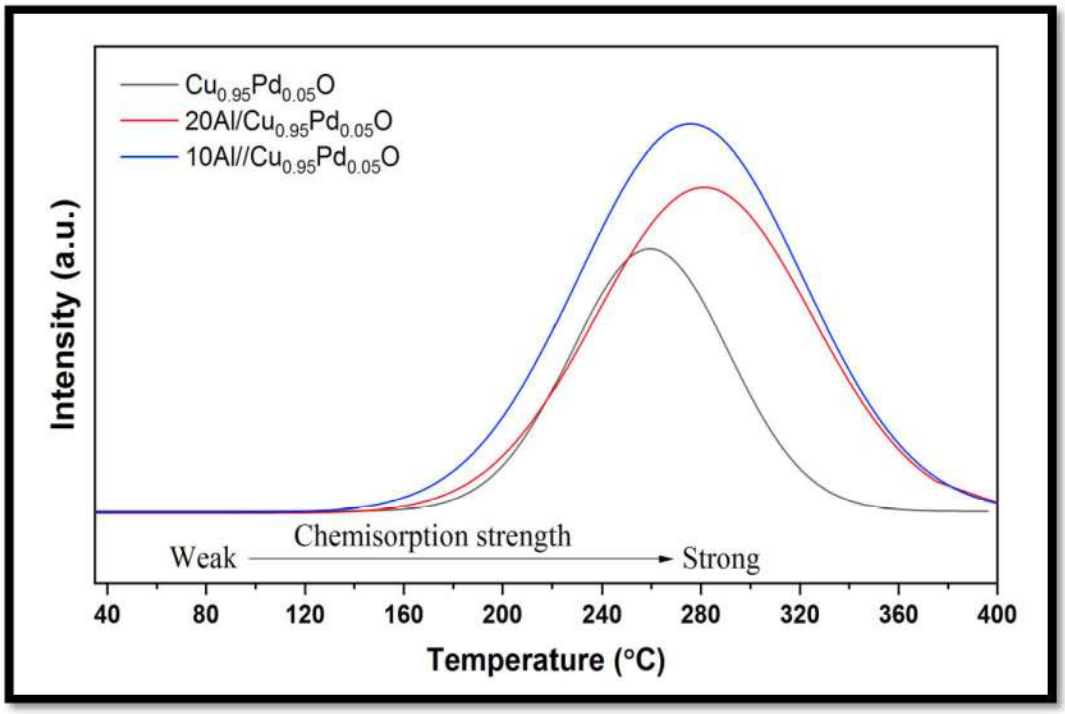

Fig. 5.27: *CO - Temperature programmed Desorption studies over $Cu_{0.95}Pd_{0.05}O$, 20Al/ $Cu_{0.95}Pd_{0.05}O$ and 10-$Cu_{0.95}Pd_{0.05}O$.*

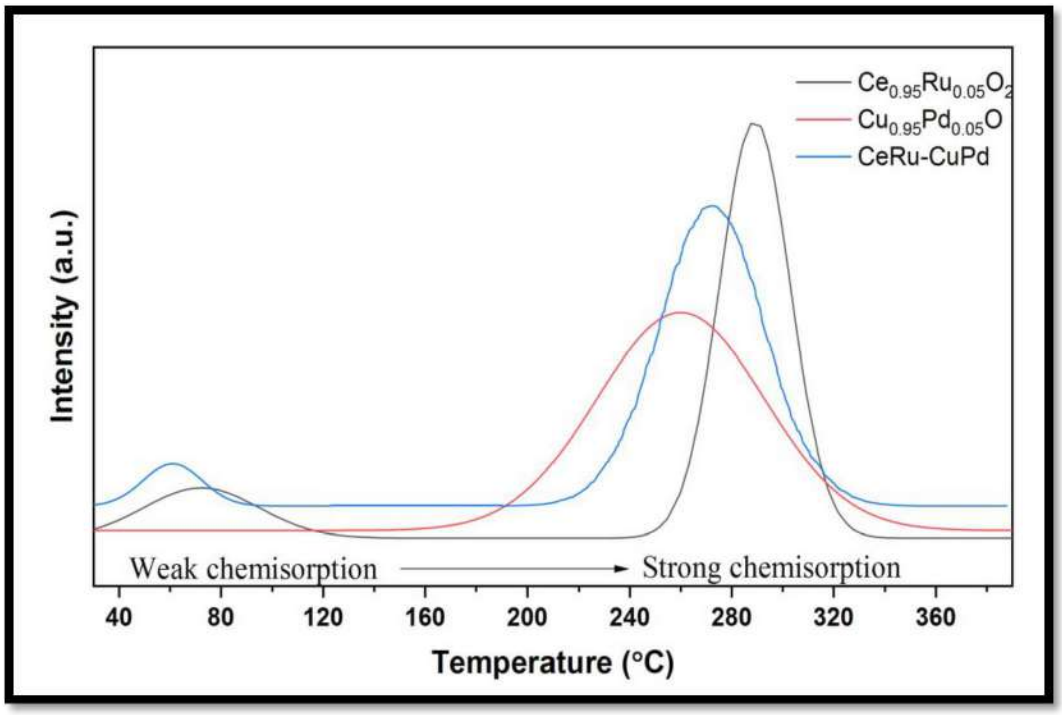

Fig. 5.28: *CO - Temperature programmed Desorption studies over $Ce_{0.95}Ru_{0.05}O_2$, $Cu_{0.95}Pd_{0.05}O$ and CeRu-CuPd composite oxide.*

The CO TPD profile of $Ce_{0.95}Ru_{0.05}O_2$, $Cu_{0.95}Pd_{0.05}O$ and CeRu-CuPd composite oxide are presented in Fig. 5.28. The TPD profile shows the desorption of CO in two temperature region, one in range of 50-120 ºC and the other one is between 180-340 ºC. The peak generated at lower temperature can be attributed to the desorption of weak chemisorbed CO, whereas the peak situated at higher temperature zone corresponds to the strongly adsorbed CO species [257]. The CO-TPD profile of Ru substituted CeO_2 showed two CO desorption peaks at 73 ºC (weakly chemisorbed CO) and 289 ºC (strongly chemisorbed CO), while for Pd doped CuO only one broad peak has been observed which is situated in strong chemisorbed region. On the other hand, in CeRu-CuPd composite system both types of CO chemisorption sites were observed with a slight shift in peak position (271 ºC and 60 ºC). Such observed shift may be the result of synergistic interaction between the Ce, Ru, Pd and Cu which thereby decreases its hold on CO and releasing the CO at much lower temperature.

5.5. NH_3 - Temperature programmed desorption studies (NH_3 - TPD)

NH_3 desorption studies (NH_3-TPD) were carried out to investigate the effect of Al_2O_3 on the surface acidity of the prepared composite catalyst. The results obtained for desorption of NH_3 are shown in the Fig. 5.29. NH_3 desorption profile shows evolution of NH_3 in two different regions, one at below 150 °C and other from 200-400 °C. The small peaks from 50-150 °C corresponds to the weakly adsorbed ammonia, therefore requires lesser energy to desorb from the catalyst surface. In addition, the desorption peak observed at higher temperature conveys the strongly adsorbed NH_3 which requires more energy to desorb from the surface [156, 258]. As depicted from Fig. 5.29, the overall acidic sites present over Pd containing Cu-Mn composite are observed to be in highest amount as that of Al-Pd containing Cu-Mn composite. While, the amount of weak acid sites observed in Cu-Mn-Al-Pd are high as that of Cu-Mn-Pd composite oxide catalyst and are least in Cu-Mn composite oxide.

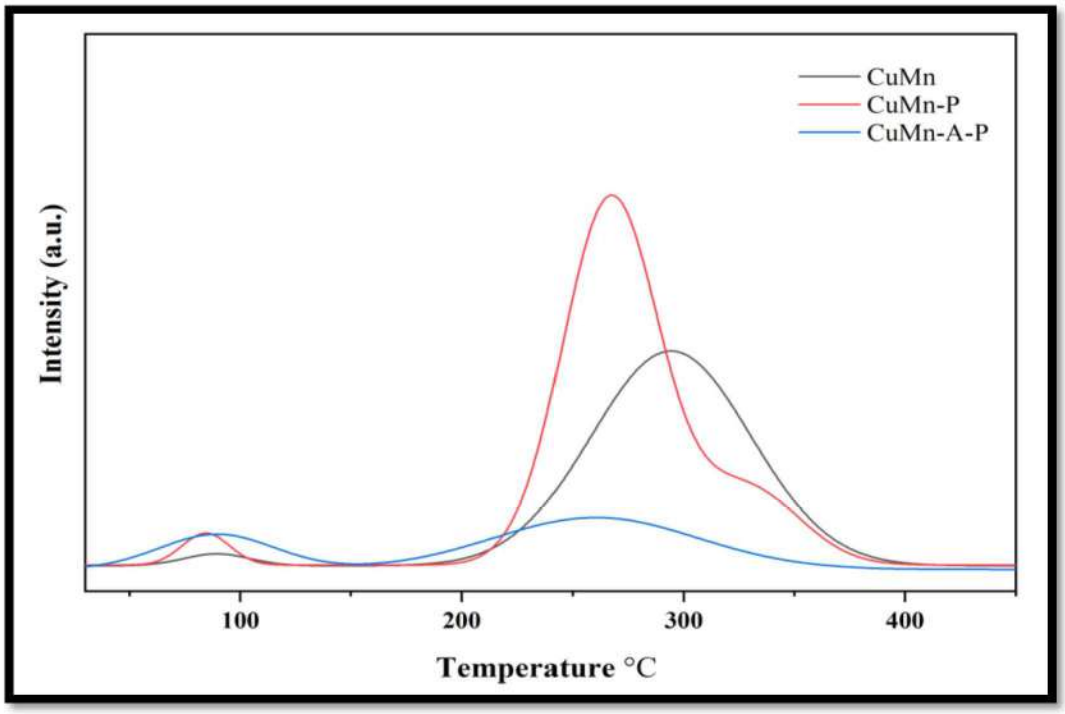

Fig. 5.29: *NH_3 - Temperature programmed Desorption studies over CuMn, CuMn-P and CuMn-A-P composite oxide*

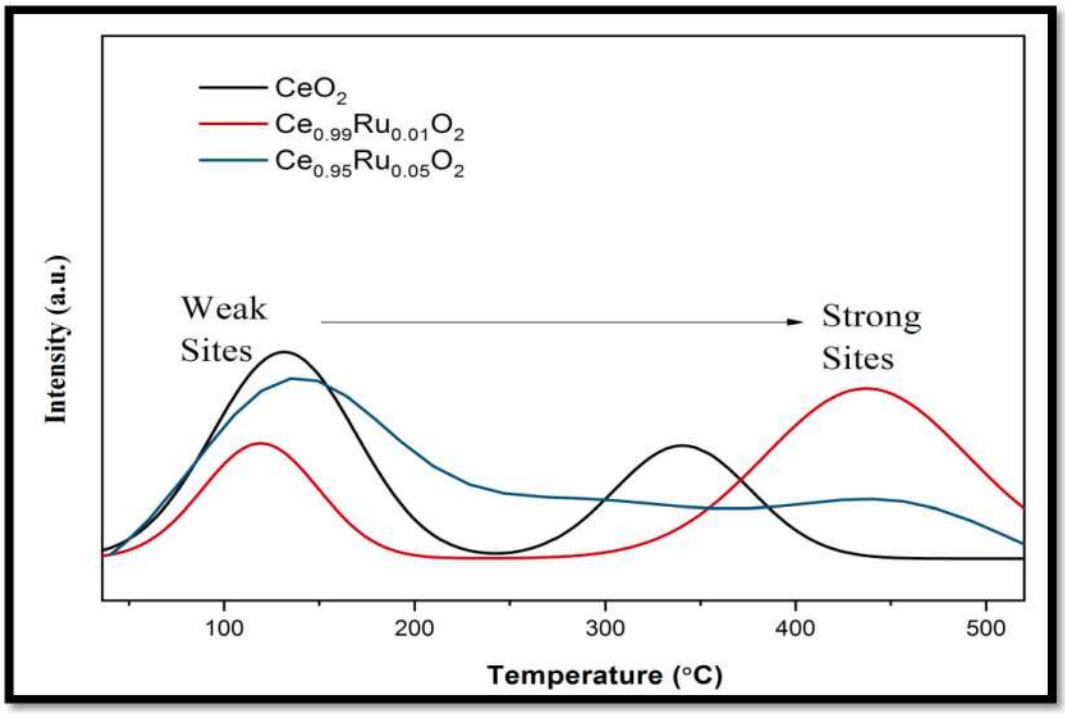

Fig. 5.30: *NH_3 - Temperature programmed Desorption studies over CeO_2, $Ce_{0.99}Ru_{0.01}O_2$ and $Ce_{0.95}Ru_{0.05}O_2$.*

The influence of ruthenium with respect to surface acidic property of cerium oxide has been investigated with ammonia desorption studies. Figure 5.30 shows the NH_3-temperature programmed desorption (NH_3-TPD) pattern of CeO_2, $Ce_{0.99}Ru_{0.01}O_2$ and $Ce_{0.95}Ru_{0.05}O_2$. In CeO_2 , two desorption peaks of ammonia are observed, one at 130 °C and the other at 340 °C which can be ascribed for weak acidic and moderate acidic site, respectively. After substitution of 1% Ru in CeO_2, increase in ammonia-ceria bond strength has been observed which results in lesser desorption of NH_3 at lower temperature. This increased bond strength produced higher amount of strong acidic sites in $Ce_{0.99}Ru_{0.01}O_2$. However in $Ce_{0.95}Ru_{0.05}O_2$, continuous desorption of ammonia has been observed which shows the presence of acidic character at entire studied temperature.

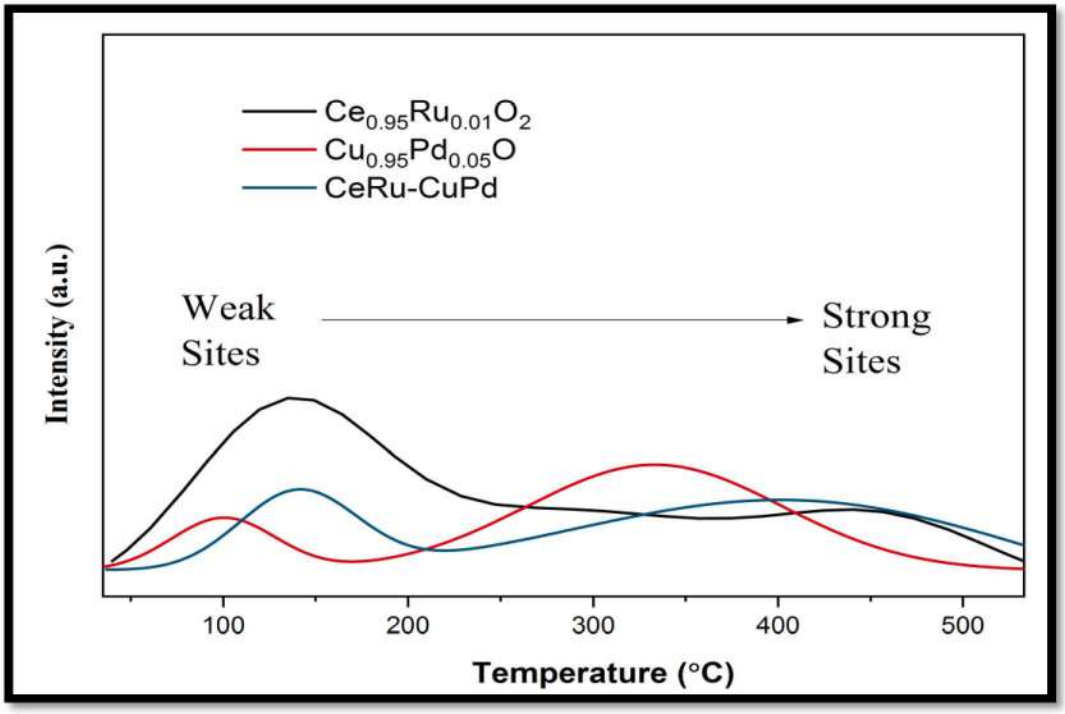

Fig. 5.31: *NH_3 - Temperature programmed Desorption studies over $Ce_{0.95}Ru_{0.05}O_2$, $Cu_{0.95}Pd_{0.05}O$ and CeRu-CuPd composite oxide.*

NH_3-temperature programmed desorption (NH_3-TPD) profile of $Ce_{0.95}Ru_{0.05}O_2$, $Cu_{0.95}Pd_{0.05}O$ and CeRu – CuPd composite oxide are shown in Fig. 5.31. According to the literature, different adsorption sites for ammonia are known and depending on its surface binding strength, it has been divided as weak, moderate and strong acidic sites [258, 259] . As depicted from Fig. 5.31, $Ce_{0.95}Ru_{0.05}O_2$ shows highest amount of acidic sites in the catalyst

series. $Ce_{0.95}Ru_{0.05}O_2$ shows high intensity peak at around 130 °C which can be attributed to the weak acidic sites and also there is presence of moderate and strong acidic sites. In $Cu_{0.95}Pd_{0.05}O$, lesser amount of physically bonded ammonia was observed as compared to chemisorbed ammonia. Further, in the composite of $Ce_{0.95}Ru_{0.05}O_2$ and $Cu_{0.95}Pd_{0.05}O$ i.e. CeRu-CuPd, decrease in overall acidity has been observed, which can be the consequence of the combination effect produced between Ce, Ru, Cu and Pd.

5.6. CO_2 - Temperature programmed desorption studies (CO_2 - TPD)

CO_2 desorption studies after the adsorption of CO_2 are performed on Cu-Mn composite oxide and the result of the same is depicted in Fig. 5.32. On comparing the results of the prepared catalyst it is observed that Cu-Mn composite oxide showed a minimum amount of basic site. This basic site tends to intensify with Pd addition and was observed maximum for Cu-Mn-Al-Pd composite oxide.

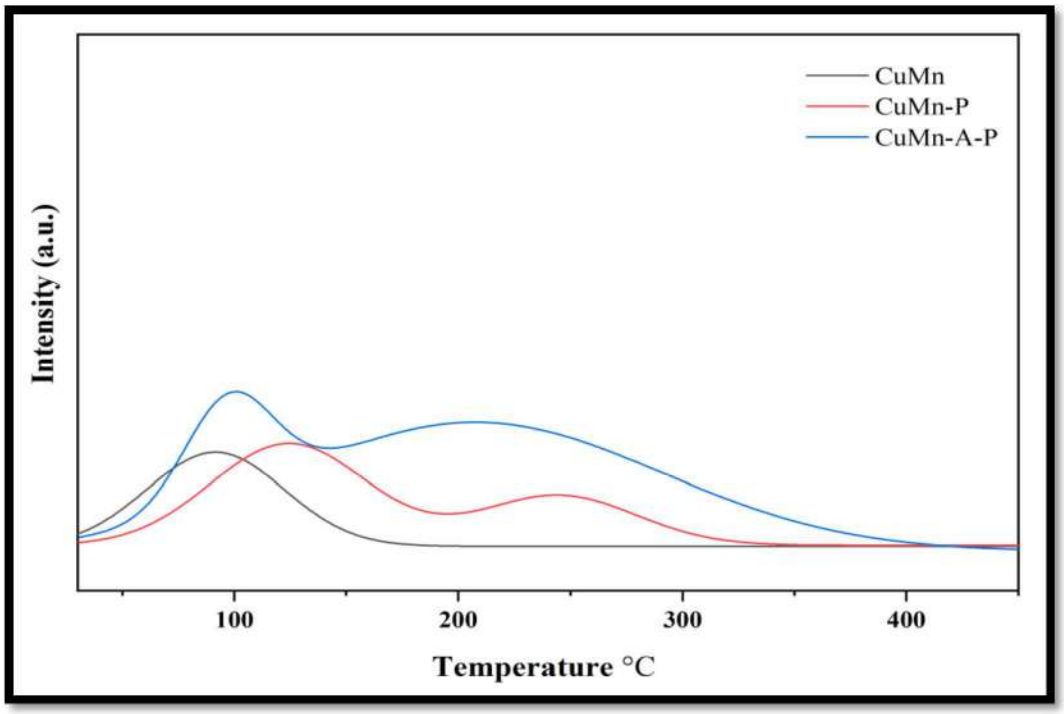

Fig. 5.32: *CO_2 - Temperature programmed Desorption studies over CuMn, CuMn-P and CuMn-A-P.*

TPD profile shows two peaks, one at a lower temperature region (i.e. 40-150 ºC in Cu-Mn & Cu-Mn-Al-Pd and 50-180 ºC for CuMn-Pd composite) corresponding to the weak basic

sites and the other one at higher temperature region corresponding to strong basic sites [260]. This strong basic site was found to be maximum in Al and Pd containing Cu-Mn oxide in which it got extended till 400 ºC.

5.7. CO Pulse Titration Studies

The CO pulse titration is the most suitable analytical technique to determine the CO adsorption capability of the catalyst surface. CO chemisorption profile for CeO_2, $Ce_{0.95}Mn_{0.05}O_2$, $Ce_{0.95}Cu_{0.05}O_2$, $Ce_{0.95}Ag_{0.05}O_2$, and $Ce_{0.95}Mn_{0.02}Cu_{0.02}Ag_{0.01}O_2$ are recorded at 50 °C and its representation is shown in Fig. 5.33. All the prepared catalyst showed affinity towards CO, as it is clearly seen from the CO chemisorption profile. Pristine CeO_2 showed the consumption of 85 µL/100 mg of CO.

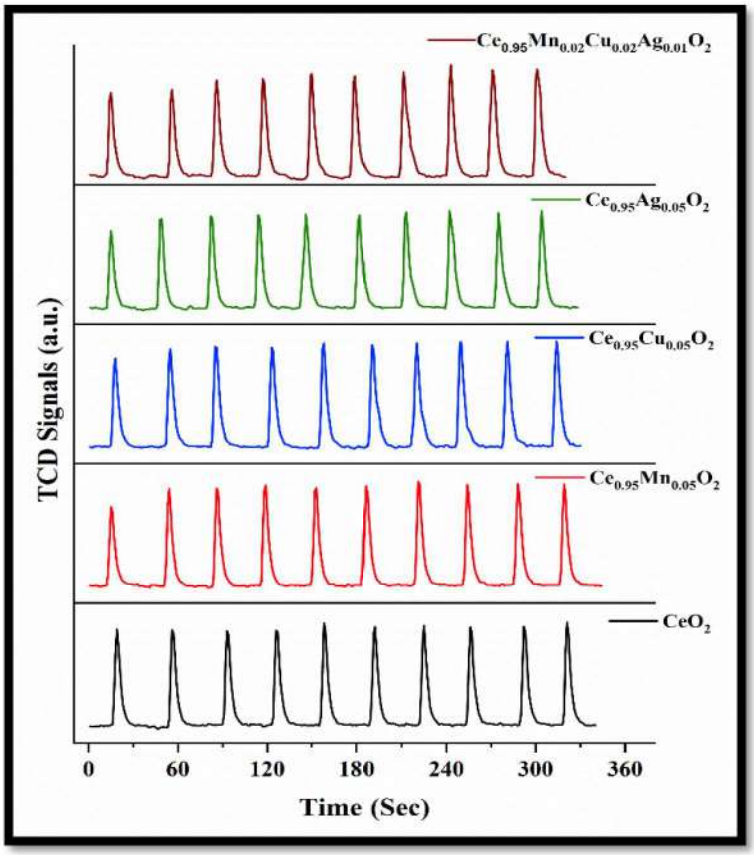

Fig. 5.33: *CO-pulse titration studies of the CeO_2, $Ce_{0.95}Mn_{0.05}O_2$, $Ce_{0.95}Cu_{0.05}O_2$, $Ce_{0.95}Ag_{0.05}O_2$, and $Ce_{0.95}Mn_{0.02}Cu_{0.02}Ag_{0.01}O_2$.*

The chemical adsorption of CO is found to increase when small amount of Mn, Cu and Ag are substituted in CeO_2. Amount of CO adsorbed for $Ce_{0.95}Mn_{0.05}O_2$, $Ce_{0.95}Cu_{0.05}O_2$ and

$Ce_{0.95}Ag_{0.05}O_2$ was observed as 123 µL/100 mg, 102 µL/100 mg and 125 µL/100 mg, respectively. Further enhancement in CO chemisorption (169 µL/100mg) was seen in multi ion doped CeO_2 ($Ce_{0.95}Mn_{0.02}Cu_{0.02}Ag_{0.01}O_2$), which could be a good example of proven synergistic interaction within Ce, Mn, Cu and Ag.

CO pulse titration was employed to understand the structural reactivity and surface chemistry of composite oxides catalyst towards carbon monoxide. CO pulse titration profile for MM', MM'-1% PdO, MM'-3% PdO and MM'-5% PdO are presented in Fig. 5.34.

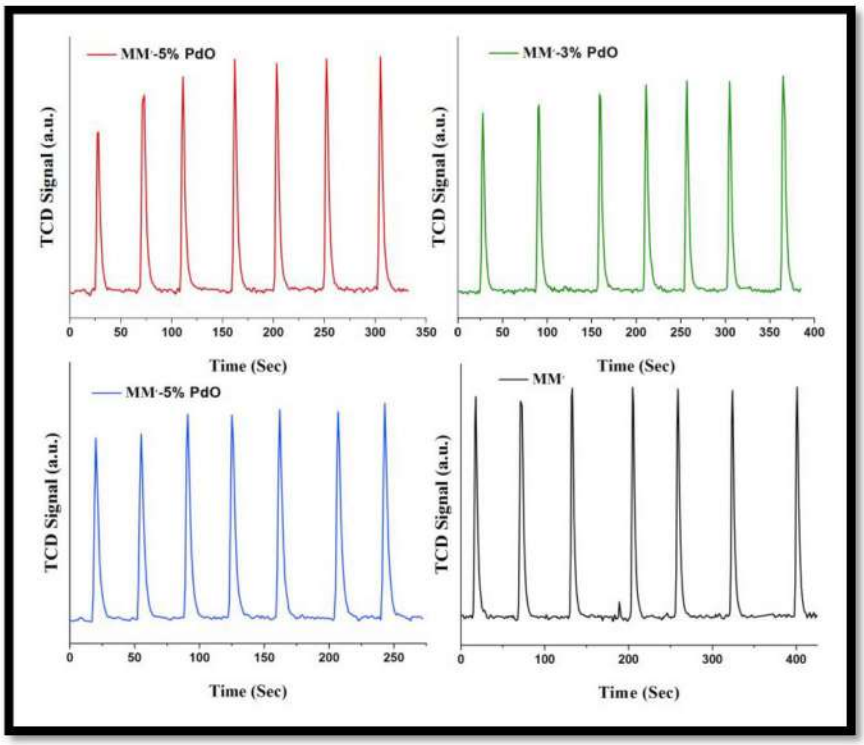

Fig. 5.34: *CO-pulse titration studies of Pd containing MM' composite oxide series.*

MM' shows chemical adsorption of 24 µL/100 mg whereas improved chemisorption is seen in MM'-5% PdO with 114 µL/100 mg. According to the chemisorption study pattern, a saturation point was detected above which no chemical adsorption of CO was seen. Gradual increase in adsorption was observed with variable Pd loading. Order for chemisorbed CO is organized as MM' (24 µL/100 mg) < MM'-1% PdO (56 µL/100 mg) < MM'-3% PdO (68 µL/100 mg) < MM'-5% PdO (114 µL/100 mg) which shows similar order in NO-CO and CO-O_2 reaction studies. Thus improved adsorption of MM' upon loading of Pd is mainly attributed

to interaction of palladium with Co-Mn composite oxide system. Such type of enhanced interaction by precious metal in host system are well known phenomenon cited in the literature [158, 249].

CO pulse chemisorption study was employed to understand the surface reactivity of CO in support of any CO related catalytic reaction. Active sites for CO adsorption can directly be related to the amount of CO chemisorbed. Here, the CO consumption studies over CeO_2, CuO and CeO_2-CuO nano composite were carried out and its profile is presented in Fig. 5.35.

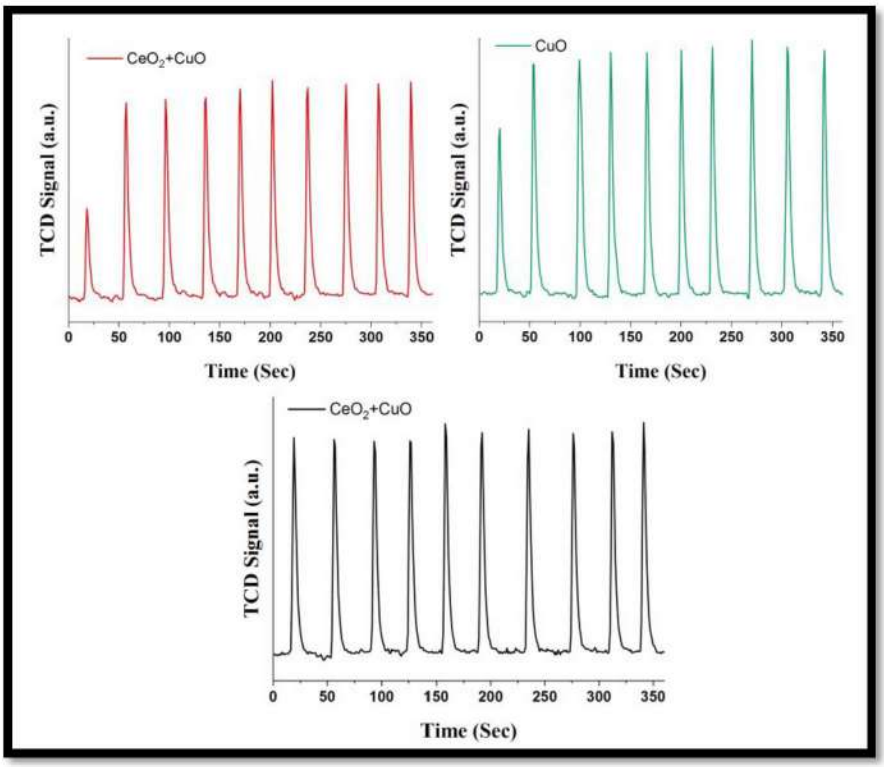

Fig. 5.35: *CO-pulse titration studies of the CeO_2, CuO and Ce-Cu composite oxide.*

During the CO pulse analysis, it was observed that the consumption of CO by the ceria surface was very less and uptake was found to be around 85 µL/100 mg. While on copper oxide surface, CO reactivity was about 147 µL/100 mg. Further, the chemical adsorption of CO on the CeO_2-CuO composite increased to 175 µL/100 mg as compared to pristine CeO_2 and CuO. Therefore, the amount of active sites produced can be directly seen from the CO chemisorption result and it proves the development of more active sites in bimetallic oxide system.

5.8 Catalytic Activity

5.8.1 CO oxidation using O_2 (CO-O_2)

A series of transition metal substituted CeO_2 was studied for the catalytic CO conversion as a function of temperature. As presented in Fig. 5.36, all the prepared catalyst shows increase in the CO oxidation as temperature rises. Pristine CeO_2 showed very poor conversion and could convert only ~ 30% of CO in the studied temperature range. This deprived activity of CeO_2 towards CO to CO_2 conversion can be attributed for its poor oxygen exchanging ability.

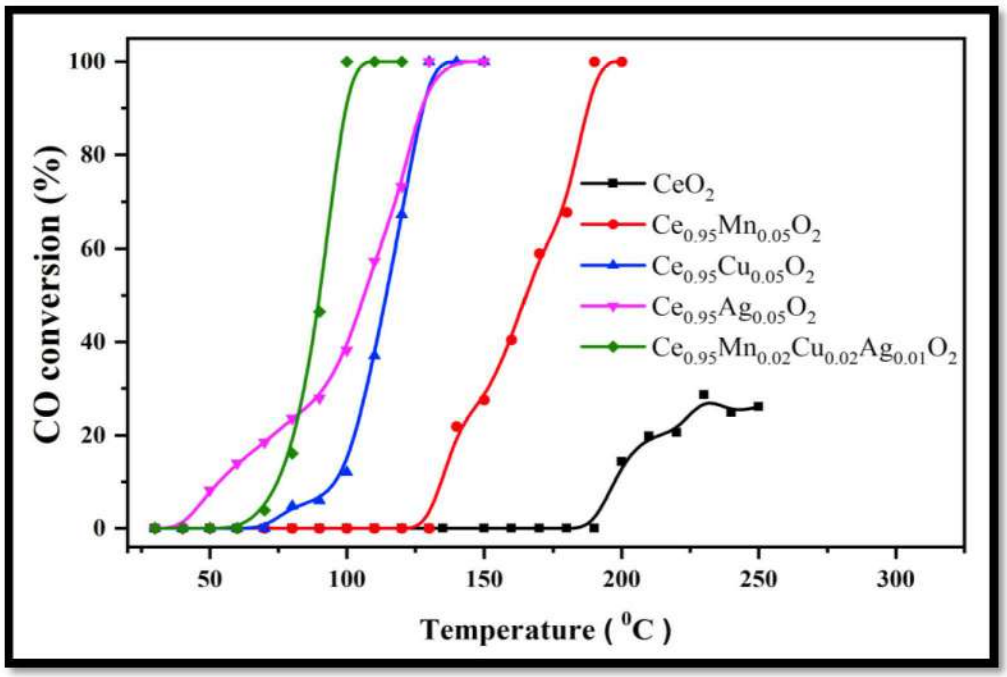

Fig. 5.36: *CO–O_2 conversion over CeO_2, $Ce_{0.95}Mn_{0.05}O_2$, $Ce_{0.95}Cu_{0.05}O_2$, $Ce_{0.95}Ag_{0.05}O_2$, and $Ce_{0.95}Mn_{0.02}Cu_{0.02}Ag_{0.01}O_2$ (5% CO and 5% O_2 in N_2 at flow rate of 5000 ml h^{-1}).*

Substituting 5% Mn, Cu and Ag in CeO_2 showed improved CO conversion at a much lower temperature as that of pristine CeO_2 showing T_{100} at 190 °C, 130 °C and 130 °C, respectively. Further, the combined substitution of Mn, Cu and Ag has greatly improved the reaction performance by converting CO to CO_2 at 95 °C, thus confirming the high adsorption capability and oxygen mobility produced within the catalyst system. Such multi substitution in the host system is an essential criterion to develop synergistic effect in the catalyst. The trend observed for CO/O_2 reaction is $Ce_{0.95}Mn_{0.02}Cu_{0.02}Ag_{0.01}O_2$ > $Ce_{0.95}Ag_{0.05}O_2$ ≈ $Ce_{0.95}Cu_{0.05}O_2$ > $Ce_{0.95}Mn_{0.05}O_2$ > CeO_2.

As per performance of H_2-TPR and CO adsorption studies showed good oxygen mobility with good CO adsorption which thereby tends to give better CO conversion reaction. Similar case is observed in the case of Mn substituted CeO_2. However, in $Ce_{0.95}Mn_{0.02}Cu_{0.02}Ag_{0.01}O_2$ system it is observed to have a very good CO adsorption, also reduction patter makes it a good redox platform at a lower temperature region.

CO oxidation studies over Ru substituted CeO_2 was performed and the result of the same are given in Fig. 5.37. As presented in Fig. 5.37, around 30% of CO conversion can be seen till 250 °C using pristine CeO_2.

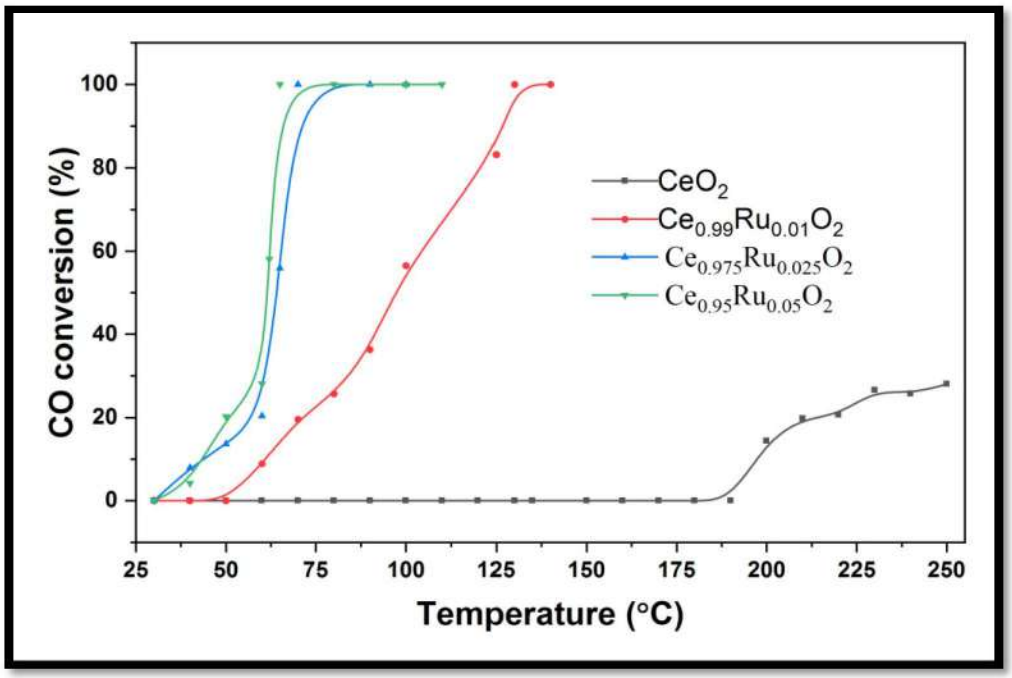

Fig. 5.37: *CO–O_2 conversion over CeO_2, $Ce_{0.99}Ru_{0.01}O_2$, $Ce_{0.925}Ru_{0.025}O_2$ and $Ce_{0.95}Ru_{0.05}O_2$ (5% CO and 5% O_2 in N_2 at flow rate of 5000 ml h^{-1}).*

However, CO oxidation for Ru substituted CeO_2 increased with the increase in Ru concentration in CeO_2. From the prepared series, $Ce_{0.99}Ru_{0.01}O_2$ showed CO conversion (T_{100}) at 130 °C and as concentration of Ru increases, the CO conversion was obtained at 65 °C in $Ce_{0.95}Ru_{0.05}O_2$. The trend for complete oxidation of CO is given as CeO_2 (T_{30}=250 °C) < $Ce_{0.99}Ru_{0.01}O_2$ (T_{100}=130 °C) < $Ce_{0.975}Ru_{0.025}O_2$ (70 °C) < $Ce_{0.95}Ru_{0.05}O_2$ (65 °C). This obtained result can be directly related towards the synergetic increase in the catalytic property of Ce with the incorporation of Ru.

As known from the various literatures that the Ru has very good affinity towars the CO and from CO-TPD studies it thus confirms the raise in CO chemisorption after concentration of Ru increases. Also, lower temperature reduction of a surface was observed from H_2-TPR study which proves the availability of surface oxygen at a lower temperature and can easily utilized in CO oxidation process.

Oxidation of CO is an important reaction in automobile and many industries [14, 261]. The activities of Co-Mn composite oxides were studied to highlight the importance of Pd incorporation in Co-Mn composite oxides to achieve the CO oxidation at lower temperature. Figure 5.38 shows the CO-O_2 reaction over MM′ and MM′-x% PdO (x= 1, 3, and 5) as a function of catalyst temperature. Based on the graphical representation, it is observed that Pd loading increases the CO oxidation and also decreases the reaction temperature.

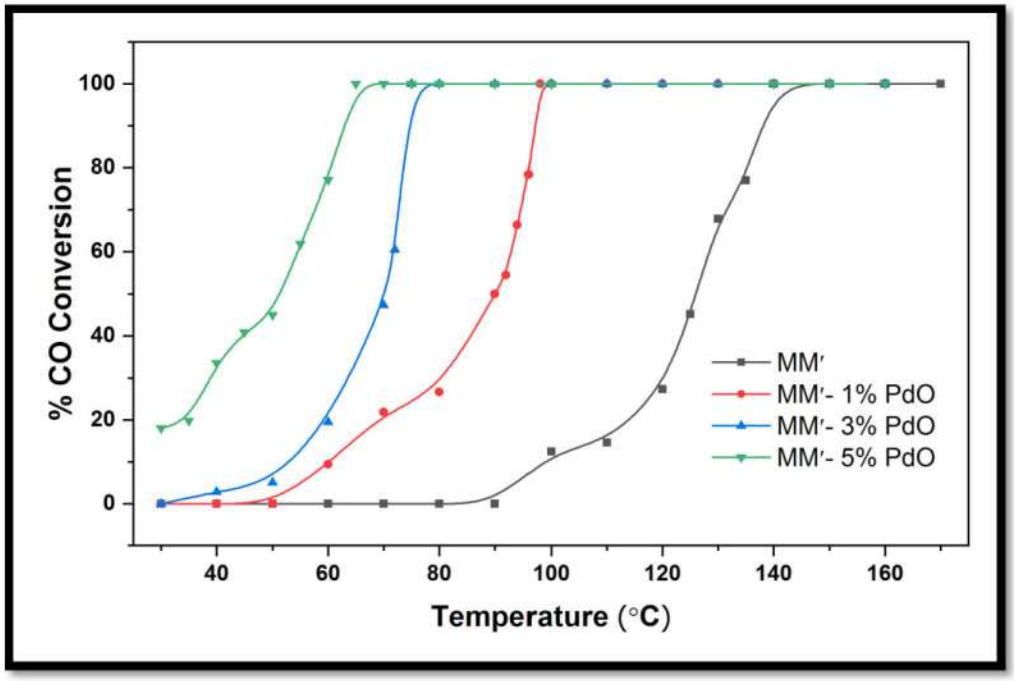

Fig. 5.38: *CO–O_2 conversion over MM′, MM′-1% PdO, MM′-3% PdO and MM′-5% PdO (5% CO and 5% O_2 in N_2 at flow 5000 ml h^{-1}).*

Catalytic oxidation over MM′ showed lowest activity with complete CO oxidation (T_{100}) taking place at 140 °C while in case of MM′-5% PdO, the oxidation reaction was starting at room temperature and achieved T_{100} at 65 °C. The trend for complete CO oxidation (T_{100}) is MM′ (140 °C) < MM′-1% PdO (100 °C) < MM′-3% PdO (75 °C) < MM′-5% PdO (65 °C).

Thus confirming that, although the composite oxides have good catalytic activity, incorporation of Pd increases the synergistic effect in host system thereby achieving the activity at lower temperature [64].

CO oxidation studies using O_2 over copper-manganese composite oxide (MM′) and precious metal containing copper-manganese composite oxide (MM′-Ag and MM′-Ag-Rh) are shown in Fig. 5.39. Addition of precious metal in composite oxide is found to increase the catalytic property of the composite oxide. The Cu-Mn composite oxide showed 100 % conversion of CO at 140 °C. Presence of Ag in composite system has lowered the catalyzing temperature of the composite catalyst from 140 °C to 95 °C.

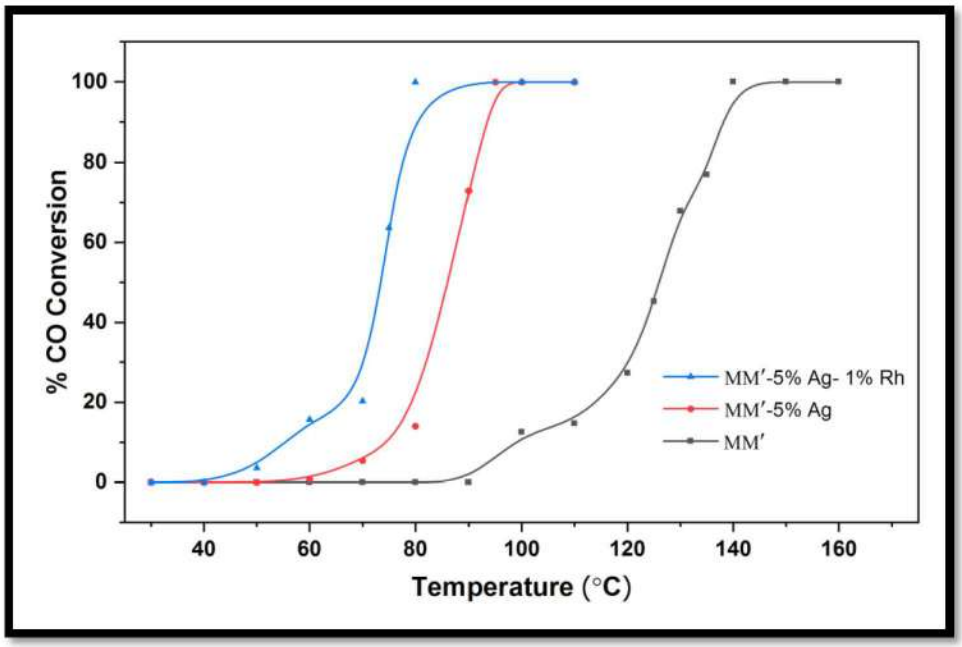

Fig. 5.39: *CO–O_2 conversion over MM′, MM′-5% Ag and MM′-5%Ag-1%Rh (5% CO and 5% O_2 in N_2 at flow rate of 5000 ml h^{-1}).*

This may be due to the electron rich character of silver facilitating the reaction at much lower temperature. Further, this catalyzing temperature has been still lowered by the addition of Ag and Rh in Cu-Mn composite oxide to 72 °C and this has been achieved by formation of synergistic effect when electron cloud from Ag is oscillated towards the Rh.

The effect of Al substitution in the composite oxide is studied for the catalytic conversion of CO and the obtained results are displayed in Fig. 5.40. CO to CO_2 conversion over Al

composed Cu-Mn-Pd oxide showed similar conversion as that of Cu-Mn-Pd composite oxide. Among the prepared composite oxides, Cu-Mn composite oxide showed 100% CO conversion at 135 °C whereas the Cu-Mn-Pd and Cu-Mn-Al-Pd showed 100% CO oxidation at 80 °C. Even after possessing a high surface area by Al addition in Cu-Mn oxide which can be seen from BET surface area studies, no obvious effect was seen in the CO conversion reaction. The order obtained for CO to CO_2 conversion is Cu-Mn < Cu-Mn-Pd ≈ Cu-Mn-Al-Pd. Here, again the electron rich nature of precious metal plays an important role in catalyzing the carbon monoxide at a lower temperature window.

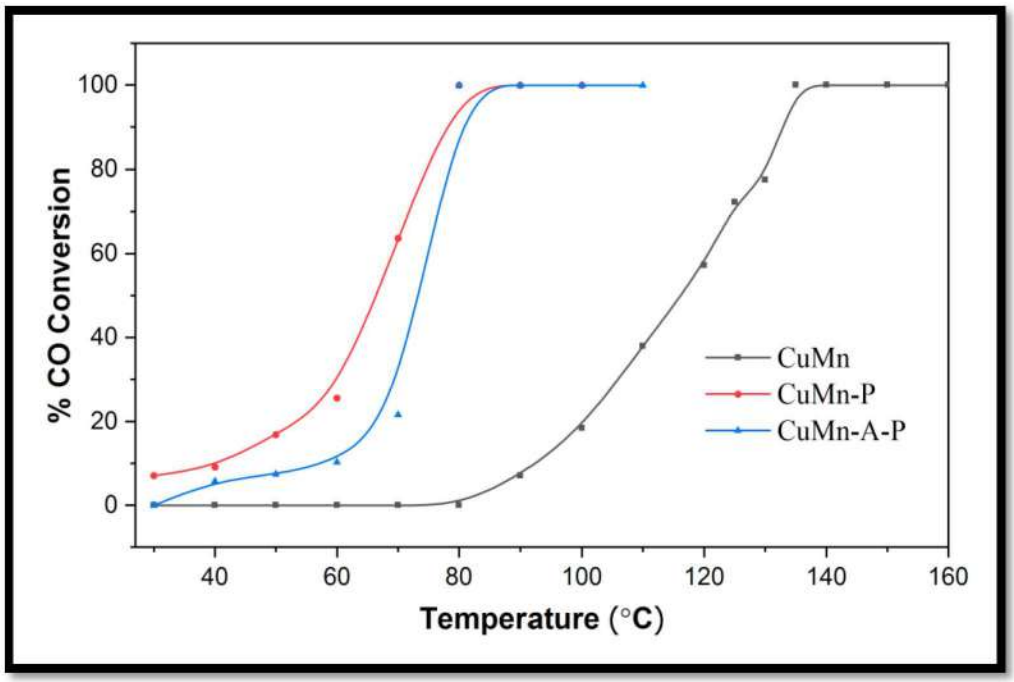

Fig. 5.40: *CO–O_2 conversion over CuMn, CuMn-P and CuMn-A-P (5% CO and 5% O_2 in N_2 at flow rate of 5000 ml h^{-1}).*

The CO oxidation reaction by O_2 was evaluated on Cu-Co composite oxide by varying the Mn concentration. Figure 5.41 shows the CO oxidation curve of the prepared composite oxides series. The Cu-Co composite oxide showed its highest activity at 90 °C which is converting 100% CO to CO_2. Further addition of 10%, 20% and 30% Mn in Cu-Co composite oxide exhibited CO conversion at 38 °C, 60 °C and 60 °C, respectively. This revealed a beneficial effect of Mn in improving the Cu-Co composite oxide, which could convert CO to CO_2 at much lower temperature. Besides presence of Mn, concentration effect was also

observed on the catalytic performance of the catalyst. Considering the Mn concentration, only 10 % Mn showed the improvement in catalytic property and further increasing the Mn concentration exhibited shift in temperature from 38 °C to 60 °C. This is possibly due to the excess Mn usage may perhaps suppress the active sites resulting in degradation of catalytic activity.

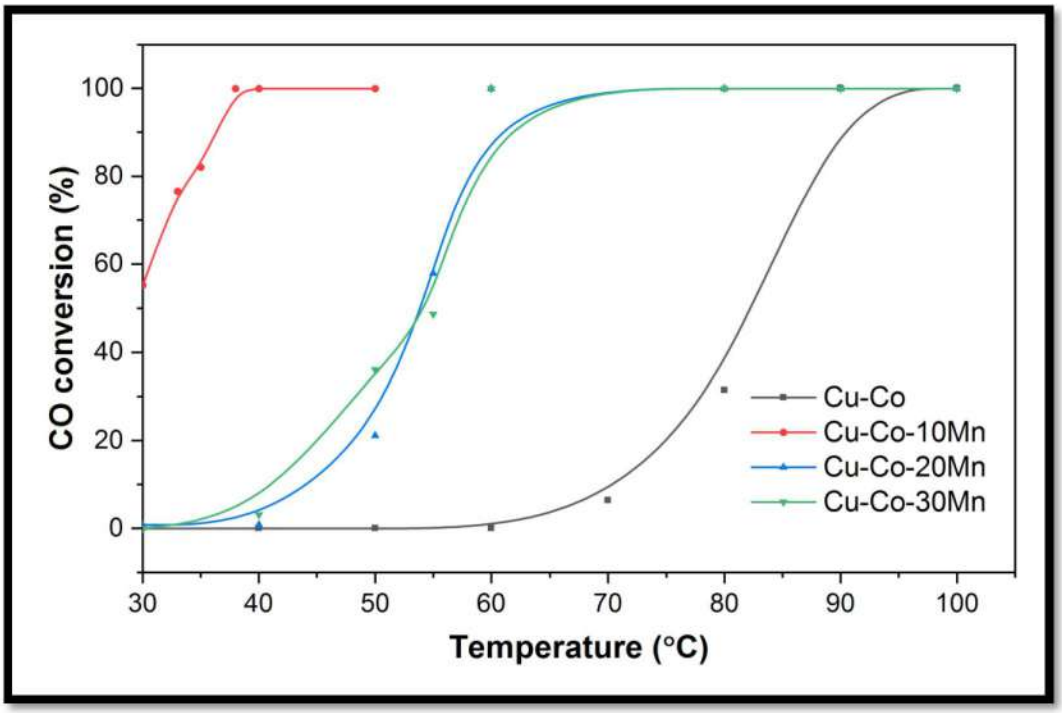

Fig. 5.41: *CO–O_2 conversion over Co-Cu, Co-Cu-10Mn, Co-Cu-20Mn and Co-Cu-30Mn (5% CO and 5% O_2 in N_2 at flow rate of 5000 ml h^{-1}).*

The catalytic performance of prepared Pd modified oxide catalysts were studied for CO oxidation as a function of temperature and the result achieved are presented in Fig. 5.42. As seen from Fig. 5.42, Pd incorporated cobalt chromite showed the complete oxidation of CO at 115 °C and also Pd supported $Co_{0.95}Pd_{0.05}Cr_2O_4$ (PdR2) displayed similar results showing no effect of the Pd support. Further, PdR3 was also studied for the CO oxidation which showed 100% conversion below 100 °C i.e. 95 °C. Finally, preparing the catalyst by architecting PdR3 and PdR2 composition could accomplish the reaction at 75 °C. This enhancement in the catalytic conversion of CO at a lower temperature window is due to the presence of Pd in different electronic environment which results in high synergistic effect.

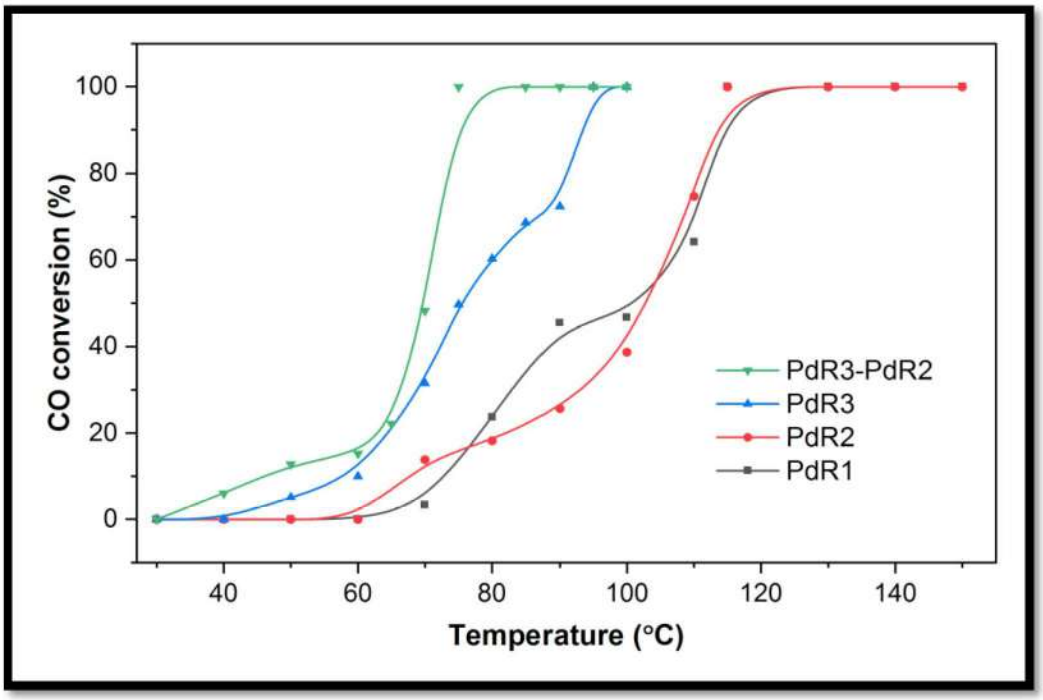

Fig. 5.42: *CO–O_2 conversion over PdR1, PdR2, PdR3 and PdR3-PdR2 (5% CO and 5% O_2 in N_2)*

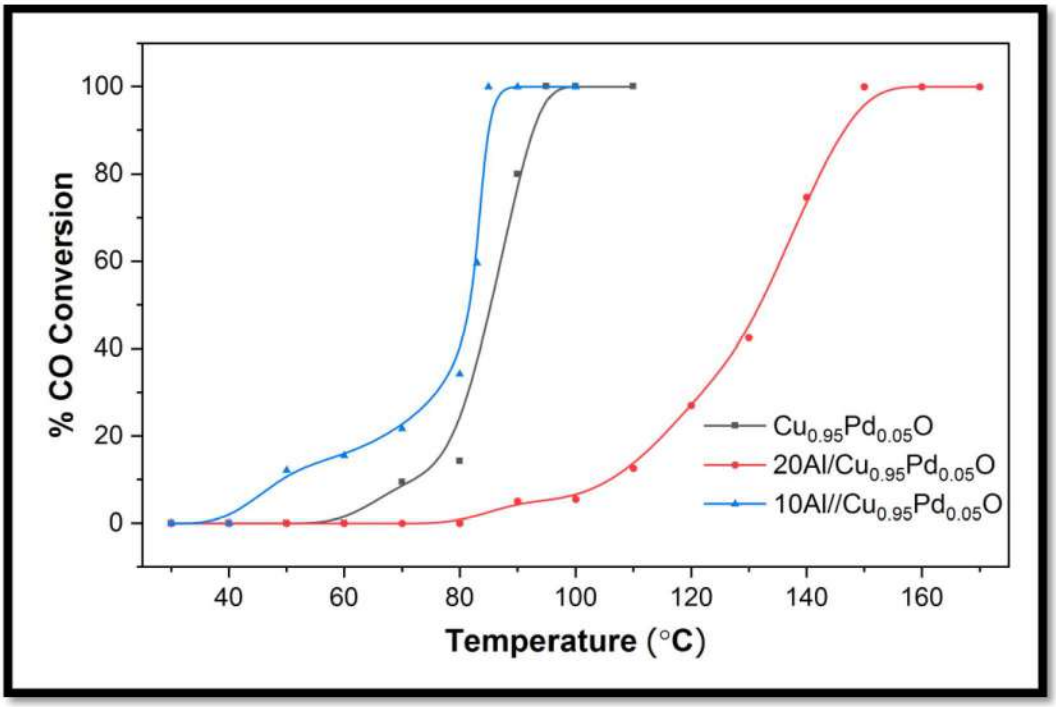

Fig. 5.43: *CO–O_2 conversion over $Cu_{0.95}Pd_{0.05}O$, 20Al/ $Cu_{0.95}Pd_{0.05}O$ and 10- $Cu_{0.95}Pd_{0.05}O$ (5% CO and 5% O_2 in N_2 at flow rate of 5000 ml h^{-1}).*

The catalytic conversion of CO to CO_2 was investigated on Al_2O_3 modified $Cu_{0.95}Pd_{0.05}O$ as a function of reaction temperature and the conversion result are depicted in Fig. 5.43. The $Cu_{0.95}Pd_{0.05}O$ showed maximum conversion at below 100 °C i.e. 100% activity at 95 °C. Later, addition of 20% Al_2O_3 to $Cu_{0.95}Pd_{0.05}O$ (20Al/ $Cu_{0.95}Pd_{0.05}O$) via impregnation method showed decrease in the catalytic activity of the catalyst (CO oxidation at 150 °C). This may be due to the capping of active Cu^{+2} and Pd^{+2} with Al_2O_3 resulting in unavailability of CO to the surface. However, modifying 20Al/$Cu_{0.95}Pd_{0.05}O$ to 10Al-$Cu_{0.95}Pd_{0.05}O$ gave a 100% conversion at 85 °C wherein Al surface will be covered with the $Cu_{0.95}Pd_{0.05}O$. This result suggest the promising effect of Al in $Cu_{0.95}Pd_{0.05}O$ system which activates the Cu and Pd species to convert CO to CO_2 at much lower temperature as that of $Cu_{0.95}Pd_{0.05}O$.

Oxidation of CO to CO_2 over CeO_2, CuO and CeO_2-CuO nano composite are shown in Fig. 5.44. The pure CeO_2 shows around 30% of CO conversion till 250 °C whereas CuO exhibited a complete conversion at 150 °C. Further, the catalytic oxidation of CO over the composite of CeO_2-CuO prepared by grinding route showed 100% conversion (T_{100}) at around 95 °C.

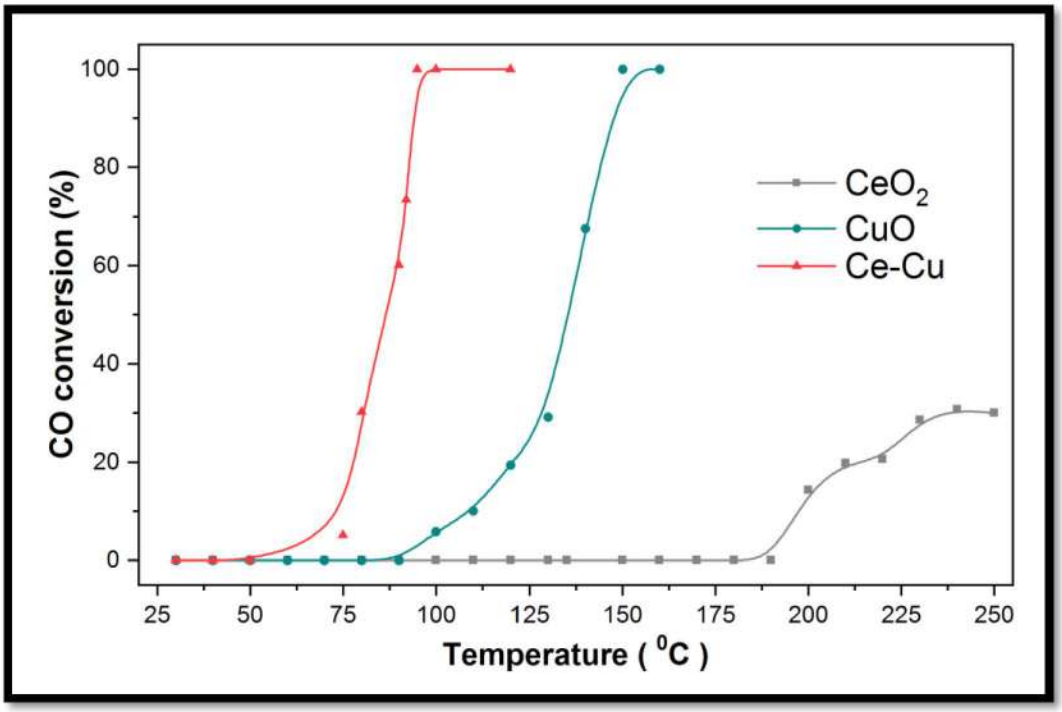

Fig. 5.44: *$CO–O_2$ conversion over CeO_2, CuO and Ce-Cu composite oxide (5% CO and 5% O_2 in N_2 at flow rate of 5000 ml h^{-1}).*

The addition of CuO in CeO_2 significantly improved the catalytic oxidation of CO showing a drastic change in CO conversion temperature. Similar type of result was also seen when Cu is added in cerium system which showed enhancement in CO oxidation studies as observed by Yin Wang and others [12, 228]. The trend for CO conversion reaction is observed as CeO_2 < CuO < CeO_2-CuO. Although, the surface area of composite decreases as compared to Cerium oxide, no reduction in catalytic activity is observed. On the contrary, increase in activity was seen. Such phenomenon was also observed by Zhang et al. wherein Cu addition in CeO_2 decreases the surface area compared to CeO_2 [38]. This result clearly indicates the promotional effect of nano composite produced within the CeO_2 and CuO which makes CeO_2-CuO composite catalyst more active at lower temperature and helps CO to oxidize at a faster rate. A surface reactivity study also gives reasonable evidence in support of the reaction.

To evaluate the effect of composite oxide prepared by physical grinding method, catalytic oxidation of CO was performed. In Fig. 5.45, CO oxidation results are presented with respect to the temperature over all the prepared catalyst. The composite prepared from $Ce_{0.95}Ru_{0.05}O_2$

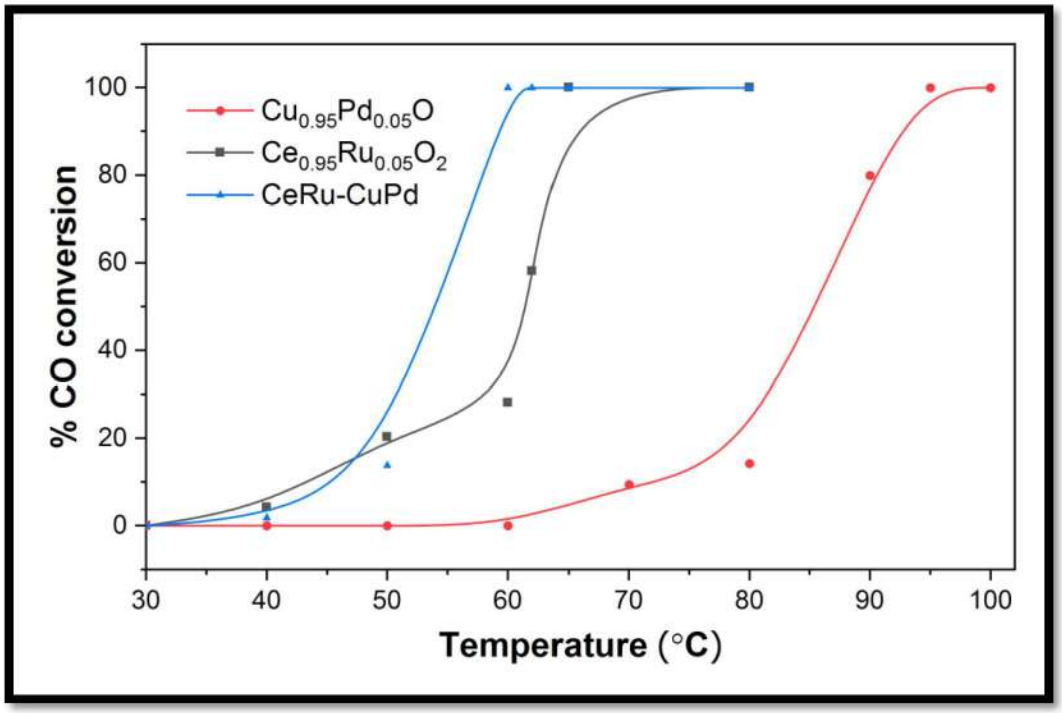

Fig. 5.45: *CO–O_2 conversion over $Ce_{0.95}Ru_{0.05}O_2$, $Cu_{0.95}Pd_{0.05}O$ and Ce-Ru composite oxide (5% CO and 5% O_2 in N_2 at flow rate of 5000 ml h^{-1}).*

and $Cu_{0.95}Pd_{0.05}O$ (CeRu-CuPd) showed an excellent conversion at a working temperature of 58 ºC whereas the 100% CO conversion over $Ce_{0.95}Ru_{0.05}O_2$ was observed at 65 °C and $Cu_{0.95}Pd_{0.05}O$ showed at 95 °C. It was remarkable to know that oxidation of CO on CeRu-CuPd was higher than $Ce_{0.95}Ru_{0.05}O_2$ and $Cu_{0.95}Pd_{0.05}O$ catalyst. This result clarifies the synergistic property of composite oxides which has been achieved by physical grinding of $Ce_{0.95}Ru_{0.05}O_2$ and $Cu_{0.95}Pd_{0.05}O$. Similar studies was also reported on enhancement of catalytic property using physical grinding method, wherein composite oxide prepared from CuO and CeO_2 had shown exceptional conversion of CO to CO_2 below 100 °C [175].

5.8.2 Catalyst Stability for CO oxidation reaction

The stability of catalyst is very much important to detoxify the CO effectively. The CO-O_2 reaction was further studied to check the stability of the catalyst in the presence and absence

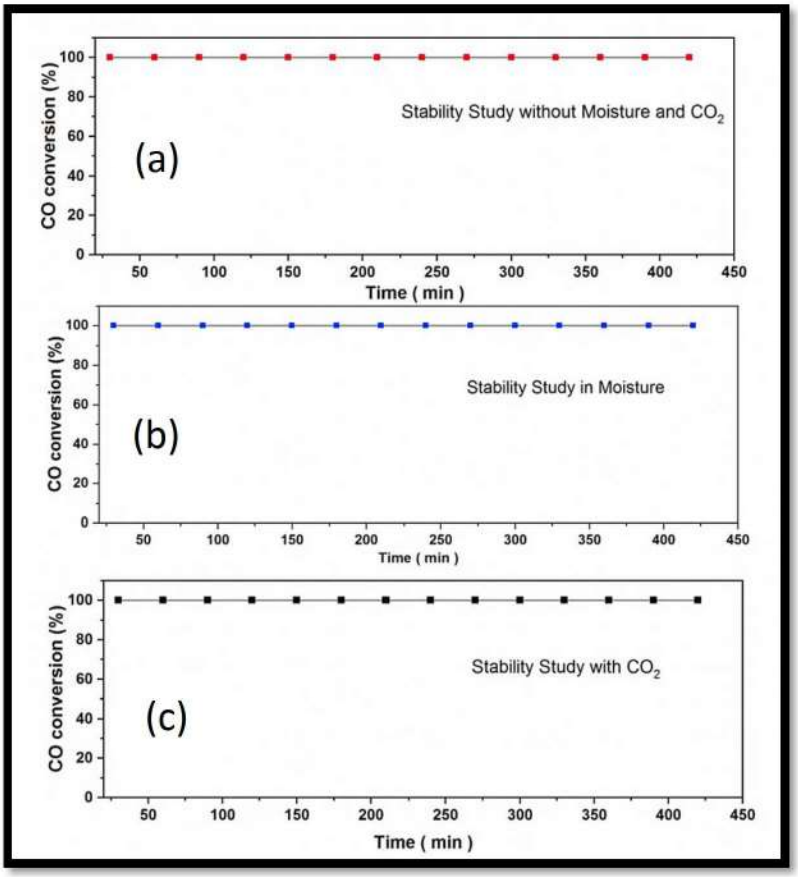

Fig. 5.46: *CO–O_2 reaction stability study over $Ce_{0.95}Mn_{0.02}Cu_{0.02}Ag_{0.01}O_2$ (a) without moisture and CO_2, (b) with moisture and (c) with CO_2.*

of moisture and carbon dioxide over a period of 7 h at 100 °C. Different catalysts were described in the literature to be having a promising activity but lacks in its stability and tend to deactivate easily [262, 263]. Figure 5.46a shows a good stability in the absence of moisture and CO_2 over $Ce_{0.95}Mn_{0.02}Cu_{0.02}Ag_{0.01}O_2$ catalyst for a period of 7 h. Figure 5.46b represents the CO oxidation with 4.714 X 10^{21} molecules h^{-1} of water and Fig. 5.46c depicts CO oxidation in 5% CO_2 concentration. In the presence of moisture and CO_2, catalyst showed a very good tolerant behavior, which can be ascribed from Fig. 5.46b and 5.46c, respectively.

The stability tests were performed on the CeO_2-CuO composite in presence and absence of moisture for 7 h and the plot of CO conversion v/s Time is presented in Fig. 5.47. The performance of composite catalyst was evaluated supplying 4.714 X 10^{21} molecules of water h^{-1} at 110 °C. During the analysis, catalyst showed stable behavior in both absence and presence of moisture. This stable CO oxidation activity is very important as many catalyst shows negative effect over a period of time and in presence of moisture. From the study, it is evident that the CeO_2-CuO has a superior behavior not only in the absence of moisture but also in moisture containing environment.

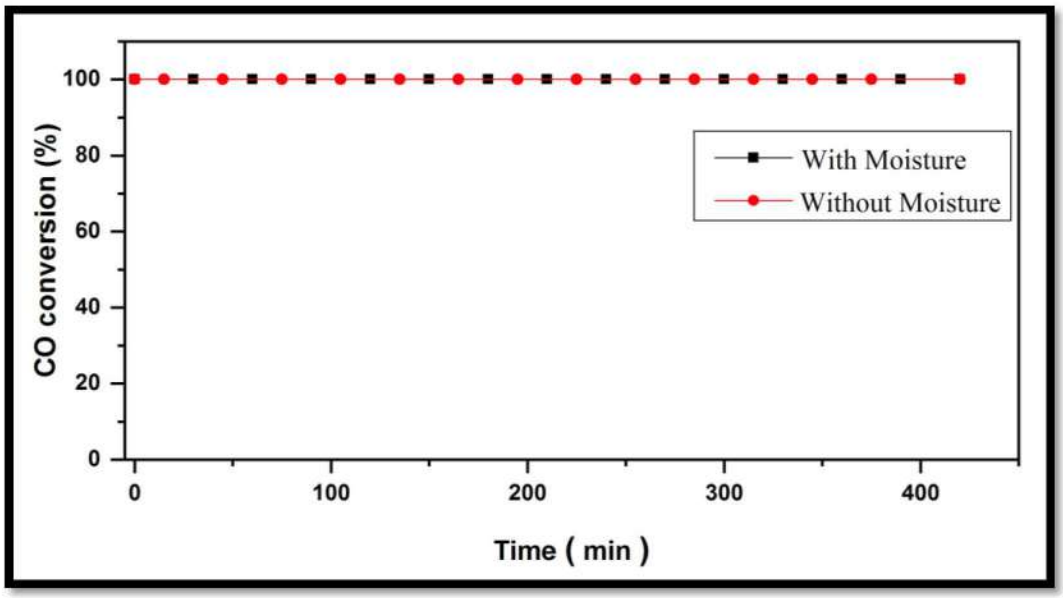

Fig. 5.47: *$CO–O_2$ reaction stability study over Ce-Cu composite oxide in the absence and presence of moisture.*

5.8.3 NO-CO redox reaction

Simultaneous reduction-oxidation reaction of NO-CO was carried out over freshly prepared Cr_2O_3 and Cu substituted Cr_2O_3 catalysts. Trend for NO-CO redox reaction is given in Fig. 5.48.

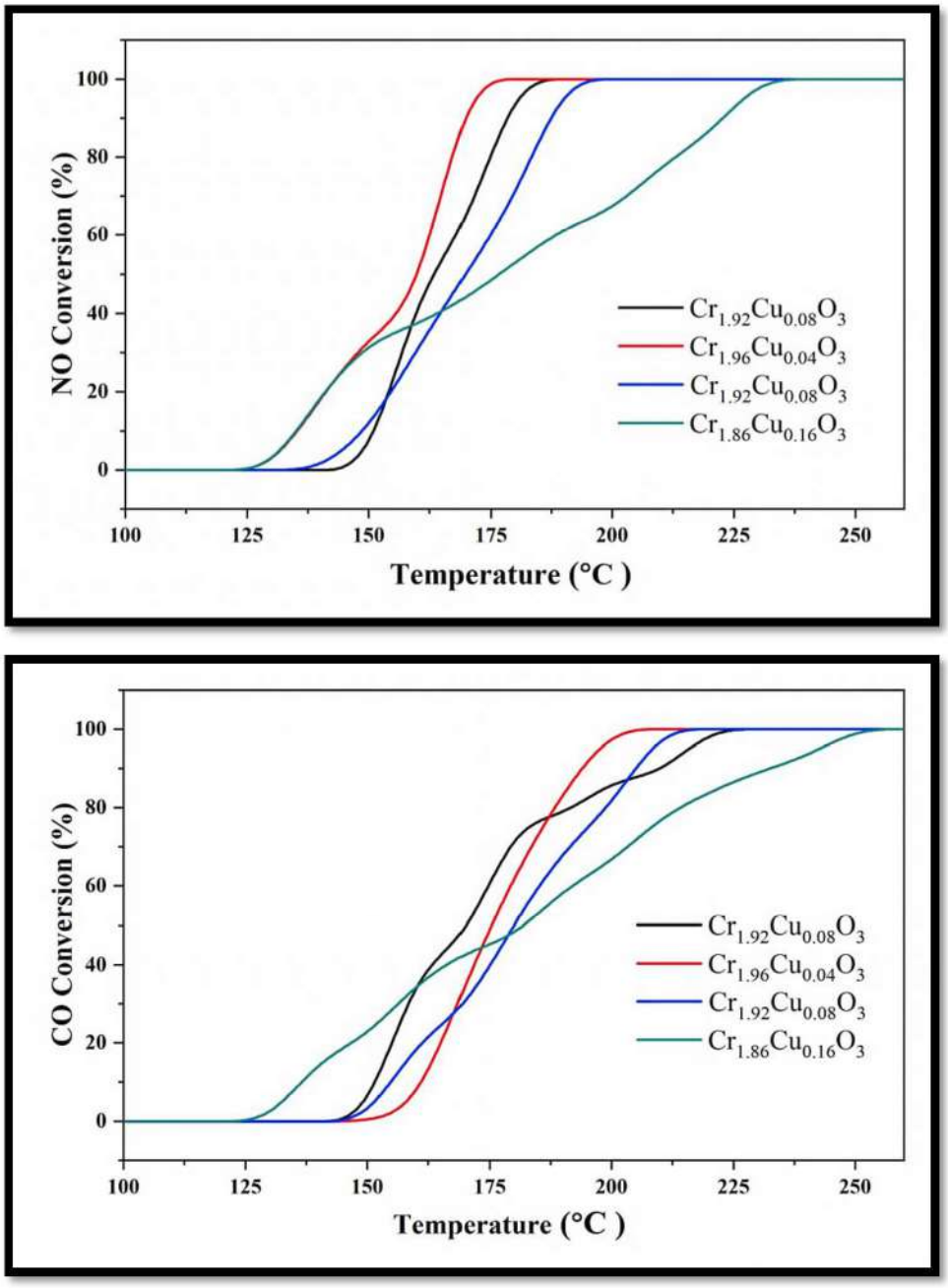

Fig. 5.48: *NO—CO redox reaction over Cr_2O_3, $Cr_{1.96}Cu_{0.04}O_3$ $Cr_{1.92}Cu_{0.08}O_3$ and $Cr_{1.84}Cu_{0.16}O_3$ (5% NO and 5% CO in Ar at flow rate of 5000 mL h−1).*

Catalytic NO reduction was seen at 180 °C for pristine and 170 °C for 2% Cu doped catalyst indicating novelty, whereas increasing the Cu concentration from 4% to 8% leads in increasing the conversion temperature compared to pure Cr_2O_3. It is very essential to completely reduce NO below 300 °C as the stability of NO increases above 350 °C. The CO oxidation occurs at higher temperature and observed temperature for CO to CO_2 transformation over Cr_2O_3, $Cr_{1.96}Cu_{0.04}O_3$, $Cr_{1.92}Cu_{0.08}O_3$ and $Cr_{1.86}Cu_{0.14}O_3$ are found to be at 220 °C, 200 °C, 210 °C and 250 °C, respectively. Higher concentration of Cu substitution i.e. $Cr_{1.84}Cu_{0.16}O_3$ showed decrease in catalytic activity and this may be due to biphasic nature as confirmed through XRD studies. While a small amount of Cu incorporation in Cr_2O_3 has shown enhancement in catalytic activity in case of $Cr_{1.96}Cu_{0.04}O_3$. Also, from the literature it has been found that the presence of copper enhances the adsorption property of Cr_2O_3 making this catalyst active at lower temperature [62, 264]. Moreover, increase in the surface redox behavior with the addition of Cu was seen from the H_2-TPR pattern. Therefore, significant increase in the NO-CO reaction in $Cr_{1.96}Cu_{0.04}O_3$ can be very much correlated with its surface property.

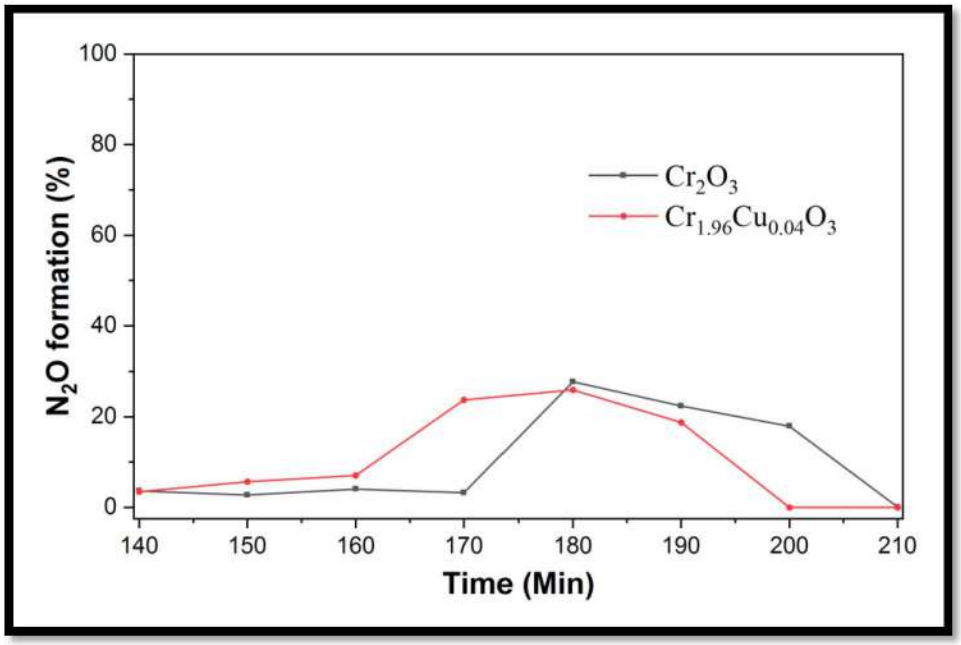

Fig. 5.49: *N_2O formation over Cr_2O_3 and $Cr_{1.96}Cu_{0.04}O_3$.*

During the reaction period, both N_2O and N_2 were detected. N_2O formation over Cr_2O_3 and $Cr_{1.96}Cu_{0.4}O_3$ was found to be similar in range as can be observed from Fig. 5.49. Initially,

very small amount of N_2O was produced which slowly decompose to give N_2. N_2O formation was observed due to the surface reduction by NO. At high temperature, NO reacts on the surface giving N_2O and O (ads) on surface [264]. From the reaction, it was observed that NO conversion occurs prior to CO oxidation, may be due to transformation of NO to N_2O to N_2 and oxidation of CO using surface oxygen. With the increase in temperature, CO desorbs by reacting with surface oxygen to form CO_2. On this reduced surface, dissociative adsorption-desorption pattern of NO is followed [20].

Catalytic decomposition of NO and CO simultaneously over Ru substituted CeO_2 has been studied and the result are presented in terms of percent CO and NO conversion in Fig. 5.50. The obtained result clearly indicates the promising effect of ruthenium in the CeO_2 for catalytic conversion of NO and CO. Pure cerium oxide showed unresponsive behavior with respect to NO-CO catalytic conversion wherein no conversion of NO and CO was observed in the temperature range of 30-250 °C. Such response is obvious in CeO_2 as it requires higher activation energy to take part in NO-CO catalytic process. Also, from the literature studies it has been clear that the reduction of NO on CeO_2 initiates above 250 °C [265]. Later, catalytic activity of CeO_2 was found increasing gradually by addition of Ru. In the case of $Ce_{0.99}Ru_{0.01}O_2$, addition of 1% Ru showed the 19% NO-CO conversion at 250 °C and this conversion rate has been increased up to 70% as concentration of Ru is increased ($Ce_{0.975}Ru_{0.025}O_2$). Further, improved NO-CO conversion ability is achieved by $Ce_{0.95}Ru_{0.05}O_2$, giving 100% conversion at 150 °C, which is highest amount the series of catalyst prepared. The trend observed in NO-CO catalytic conversion can be represented as CeO_2 < $Ce_{0.99}Ru_{0.01}O_2$ < $Ce_{0.975}Ru_{0.025}O_2$ < $Ce_{0.95}Ru_{0.05}O_2$. Such improvement in the catalytic conversion can be directly related to the advanced effect of electron rich Ru when it is added to CeO_2 system thereby providing effective synergy in catalytic process.

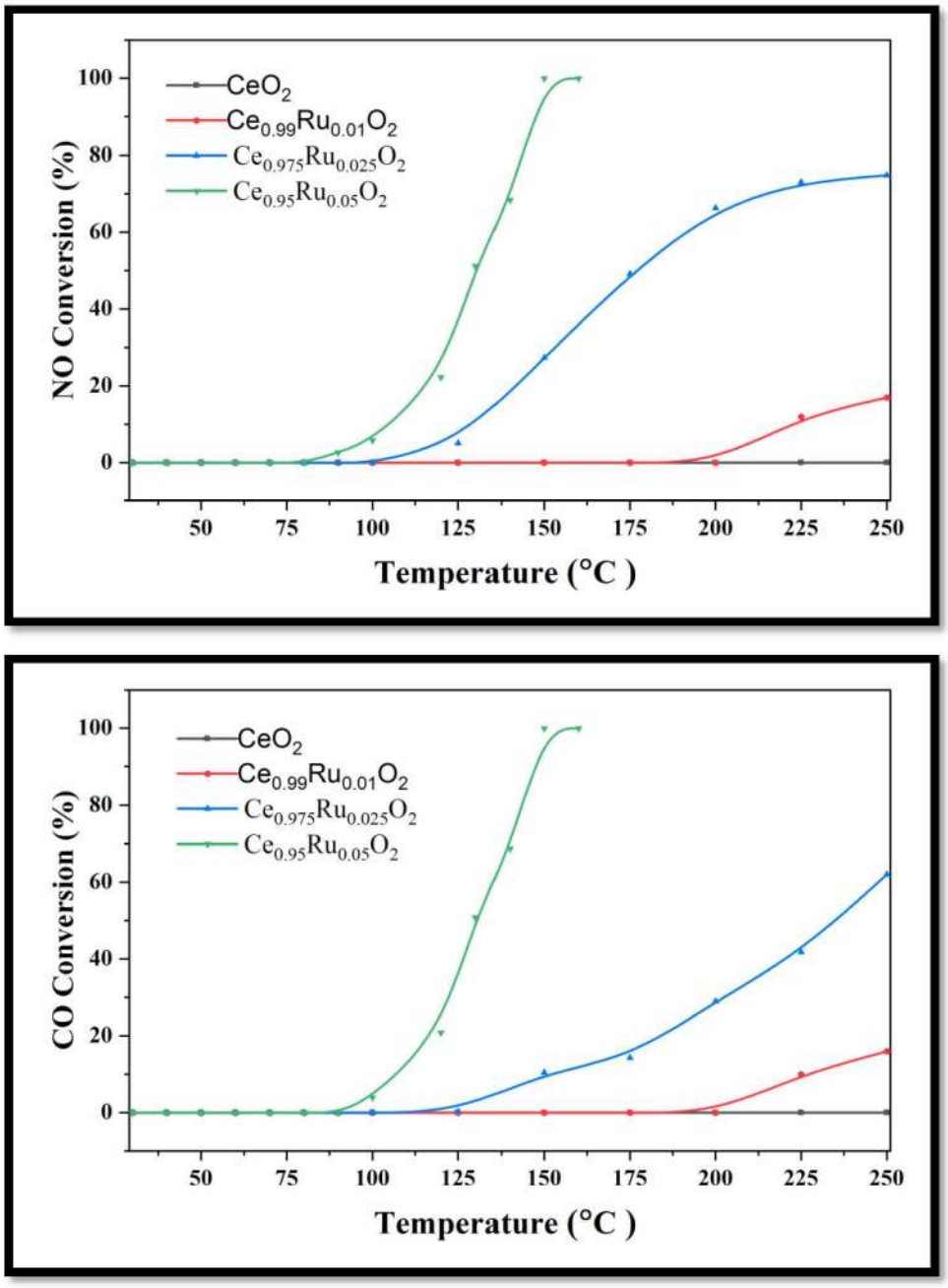

Fig. 5.50: *NO - CO redox reaction over CeO_2, $Ce_{0.99}Ru_{0.01}O_2$, $Ce_{0.975}Ru_{0.025}O_2$ and $Ce_{0.95}Ru_{0.05}O_2$. (5% NO and 5% CO in Ar at flow rate of 5000 mL h−1).*

NO-CO conversion plot over MM' and MM'-x% PdO (x = 1, 3 and 5) as a function of catalyst temperature are presented in Fig. 5.51. It can be seen that NO conversion on MM' is less than 40% in temperature range of 30 – 250 °C, while 100% conversion is achieved in case of MM'-3% PdO (180 °C) and MM'-5% PdO (170 °C). This clearly shows the enhanced effect

of precious metal concentration. The trend for NO-CO reaction is MM' < MM'-1% PdO < MM'-3% PdO < MM'-5% PdO which was similar to the CO-O_2 reaction with MM'-5% PdO showing 100% conversion at lower temperature.

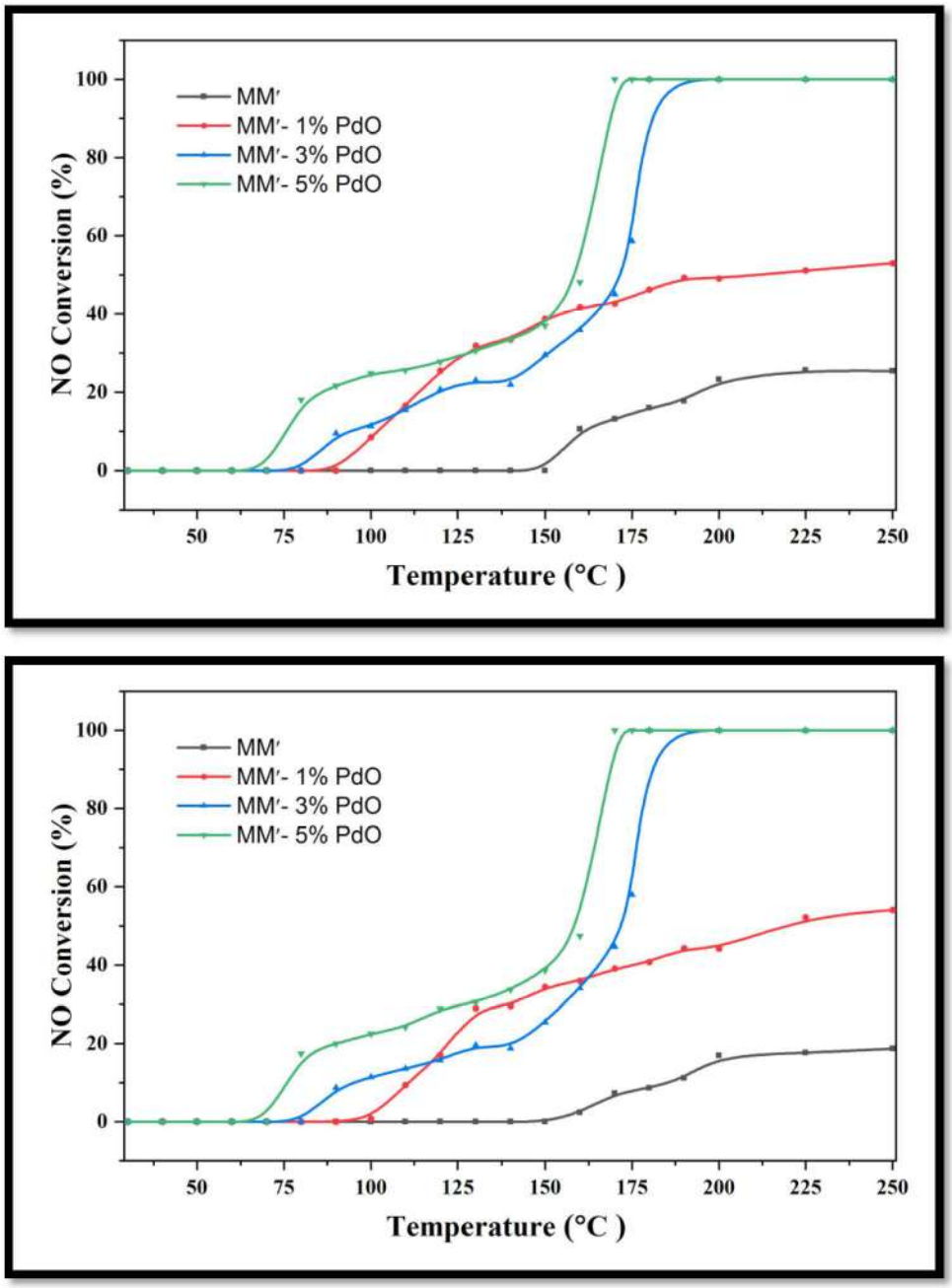

Fig. 5.51: *NO - CO redox reaction over MM', MM'-1%PdO, MM'-3%PdO and MM'-5%PdO. (5% NO and 5% CO in Ar at flow rate of 5000 mL h−1).*

N_2O formation was also observed during the conversion process. By increasing the Pd concentration, amount of N_2O production decreased gradually as seen from Fig. 5.52. This shows a promising effect of Pd which helps in reducing the N_2O formation. A very good oxidizing – reducing property of precious metal helps in enhancing the NO-CO reaction catalytically [81, 266].

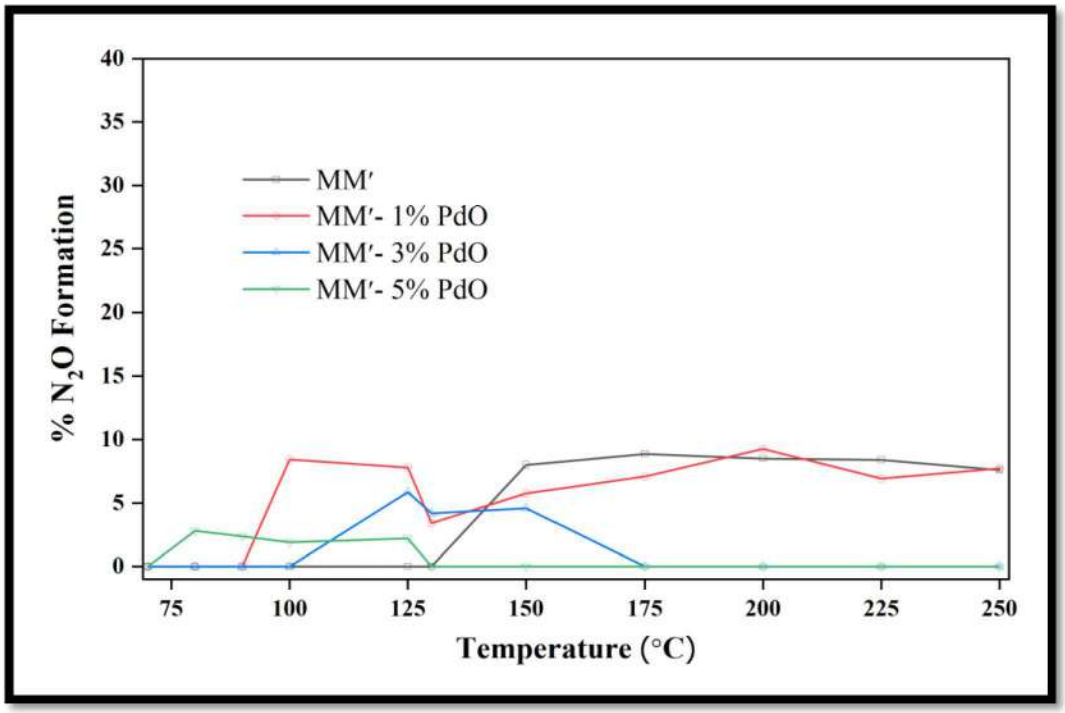

Fig. 5.52: *N_2O formation over MM', MM'-1%PdO, MM'-3%PdO and MM'-5%PdO.*

It was also established that the samples containing smaller amount of Ag and Pd manifest a higher conversion of NO and CO [84]. The synergy produced between Pd and Co-Mn composite oxides makes the system more active at lower temperature. Based on the result obtained from XPS, N_2 adsorption – desorption , H_2-TPR and CO-pulse titration, related with the MM'-5% PdO for NO-CO reaction can be attributed to their mix valances, increasing surface area, high surface reducibility and enhanced surface CO adsorption. Increase in surface area results in more surface exposing to reactant allowing more reactant to reduce as shown in H_2-TPR, also CO adsorption was greatly increased with increase in Pd addition and higher in MM'-5% PdO as ascribed by CO pulse titration study.

To explore the catalyst efficiency after the addition of Ag and Rh in MM′, the redox NO-CO reaction over the prepared composite oxide catalysts were studied and the plot of temperature verses % NO-CO conversion is given in Fig. 5.53.

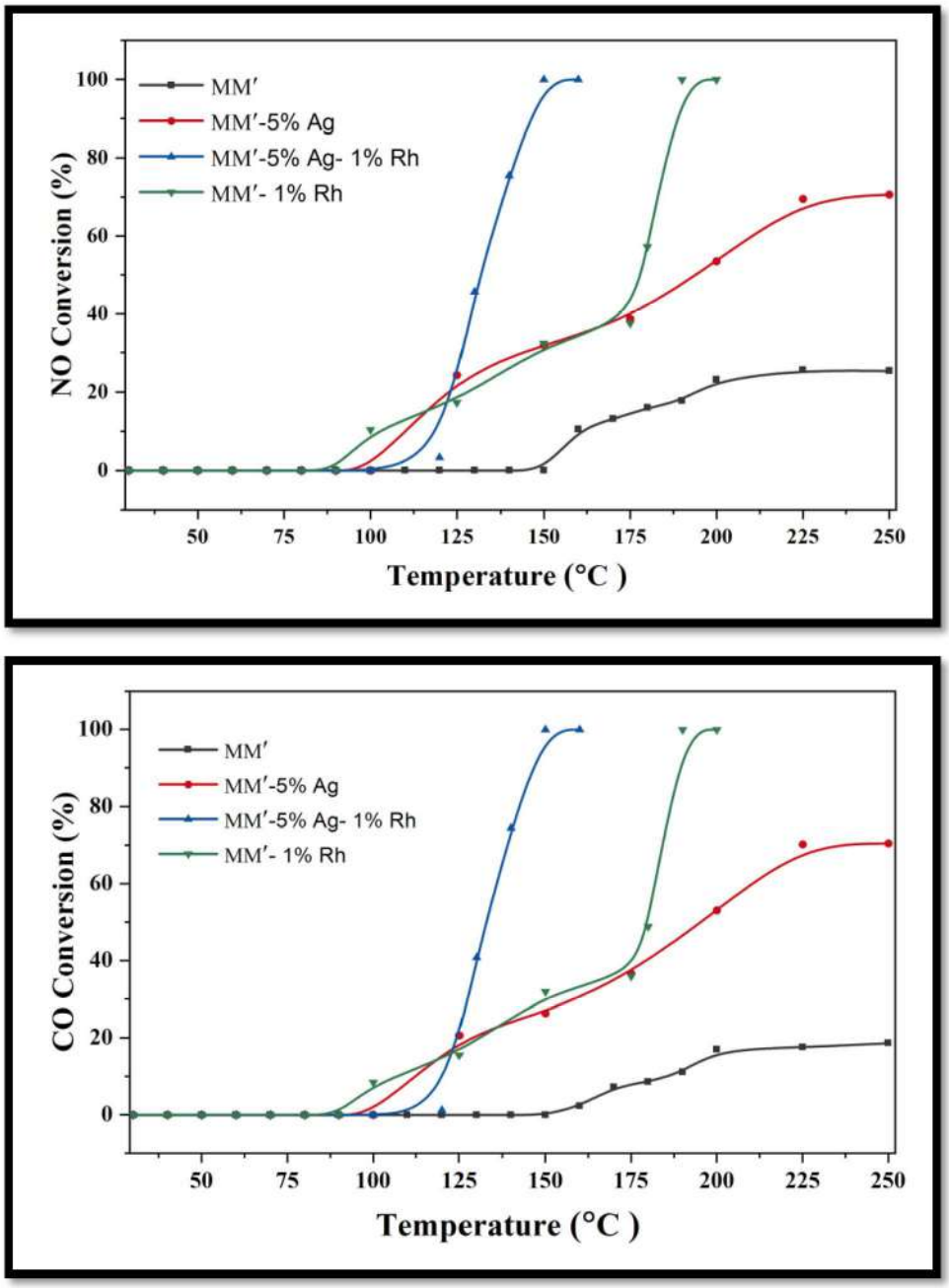

Fig. 5.53: *NO - CO redox reaction over MM′, MM′-5%Ag, MM′-5%Ag-1%Rh and MM′-1%Rh. (5% NO and 5% CO in Ar at flow rate of 5000 mL h−1).*

From the conversion plot, it can be seen that the insertion of Ag in MM′ composite oxide can slightly enhance its activity whereas addition of Rh along with the Ag in MM′ composite could achieve 100% conversion at a lower temperature region. The prepared MM′ composite showed only ~ 25% NO conversion in the temperature region of 50 °C to 250 °C. After the Ag addition (MM′-Ag), this reaction showed up to 70% NO-CO conversion till 250 °C, however, on multiple precious metal incorporation in composite oxide (i.e. MM′-5%Ag-1%Rh), 100% NO-CO conversion was observed at 150 °C which is a quite low temperature as compared to similar catalyst composed of Pd [222]. Such promising effect of binary system was also seen in existing exhaust reactor which is composed of Pt-Rh composition due to their higher activity in detoxification studies [163]. In addition, 1% Rh in MM' composite (MM'-Rh) was studied to understand the impact of Rh in catalytic performance, which showed 100% conversion at 190 °C. By observing result of MM'-Rh it was thus confirmed that the enhancement in the catalyst was not because of Rh. In fact, this enhancement in catalytic performance in MM′-5%Ag-1%Rh can be interpreted from the synergy interaction produced when Rh is in the vicinity of Ag in the Co- Mn composite oxide system. This synergy can be explained as consequences of the shift in electron cloud from silver to higher electronegative Rh, which is very important for the formation of good synergy. Such a synergistic effect of Ag and Rh was also discussed by J. Pandey et al. in context to catalytic dehydrogenation studies [164]. For prepared composite oxide series as illustrated from conversion plot the order of the activity is as follows MM′-5%Ag-1%Rh > MM′-5%Ag > MM′ wherein MM′-5%Ag-1%Rh is observed to be a highly active catalyst for NO-CO redox reaction.

The significant effect of Al in prepared composite was investigated through NO – CO conversion reaction. Figure 5.54 represents the NO – CO redox conversion pattern over Cu-Mn composite oxide composed of Pd and Al. The Cu-Mn composite oxide could achieve its maximum activity of up to 44% of NO – CO conversion. Also, addition of Pd in Cu- Mn composite fails to convert 100% of NO – CO but could elevate its activity to 65% in a temperature window of 100 – 250 °C. This rise in activity is due to presence of electron rich Pd in Cu-Mn system which provides greater active surface for simultaneous decomposition of NO and CO. Further, in Cu-Mn-Al-Pd composite catalyst, it has been seen that the incorporation of Al leads in 100 % conversion of NO and CO at 225° C. This result clearly

indicates that the presence of Al effectively promotes the catalytic performance of the composite oxide.

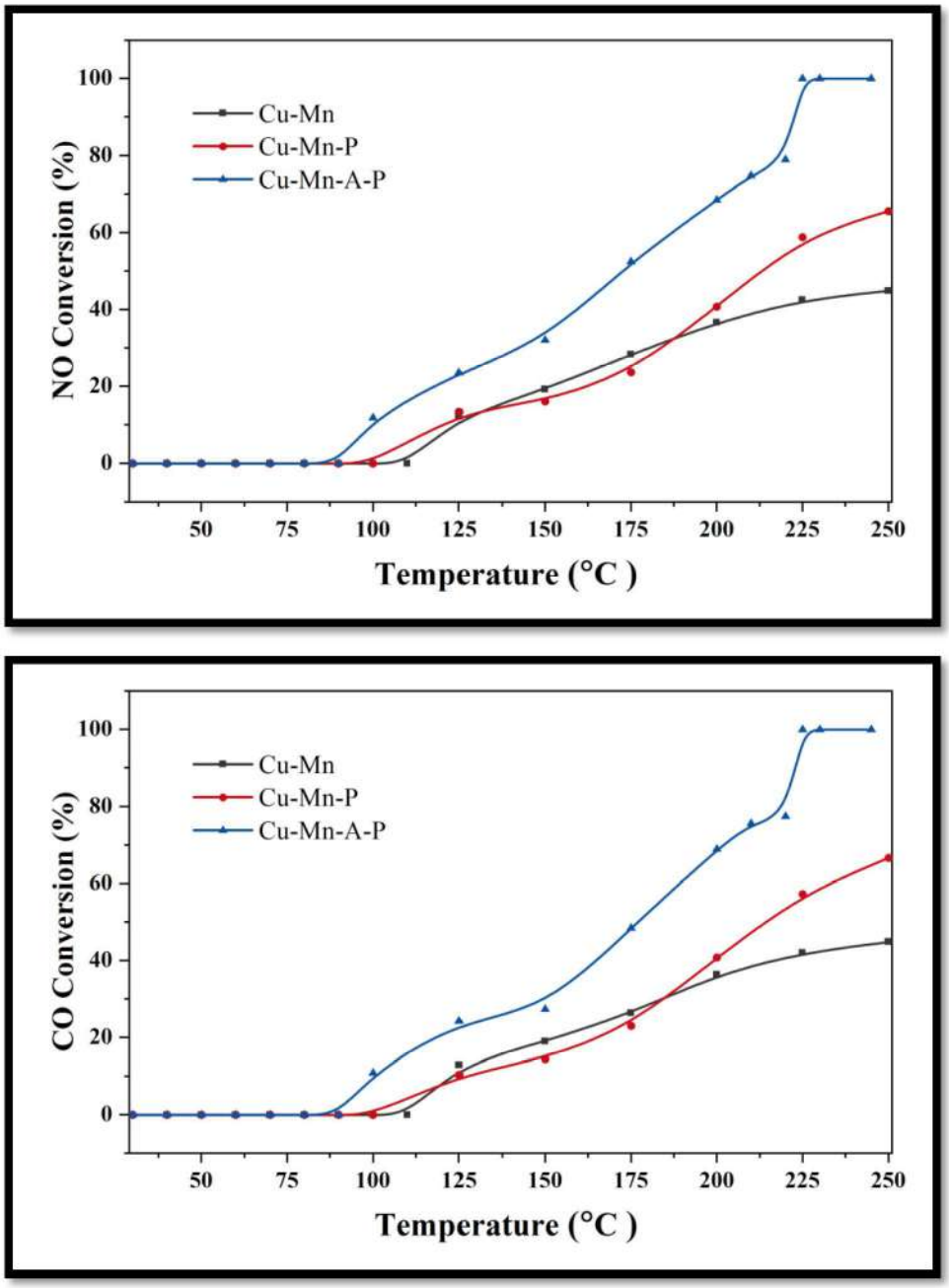

Fig. 5.54: *NO - CO redox reaction over CuMn, CuMn-P and CuMn-A-P. (5% NO and 5% CO in Ar at flow rate of 5000 mL h−1).*

Comparing the results of the BET surface area with catalyst performance, it has been clearly observed that the Cu-Mn-Al-Pd composite possesses the highest surface area whereas

Cu-Mn showed lowest and the same result is portrayed in NO-CO redox reaction. Although, Al_2O_3 is chemically inert, it has provided a good platform for the active metal like Cu, Mn and Pd in Cu-Mn-Al-Pd composite to act synergistically. Therefore it has been used as a support for many transition or precious metals in many chemical reactions for decades.

The influence of Mn in Cu-Co composite oxide was evaluated for simultaneous NO-CO redox reaction. The result of % NO and %CO conversion with respect to temperature in case of Co-Cu, Co-Cu-10Mn, Co-Cu-20Mn and Co-Cu-30Mn composite are displayed in Fig. 5.55. All the composite catalyst showed an increase in catalytic activity with the rise in temperature. The NO-CO conversion over Cu-Co composite oxide was initiated at 90 °C and yield to 100% conversion at 145 °C. In the case of Cu-Co-10Mn, Cu-Co-20Mn and Cu-Co-30Mn, the 100% catalytic conversion was achieved at 120 °C, 180 °C and 210 °C, respectively. This result clearly shows the promotional effect of 10% Mn in Cu-Co composite oxide, which is observed to be the best catalyst from the prepared catalyst. While, increase in the concentration of Mn in Cu-Co composite showed unexpectedly decrease in catalytic performance. The following is the order which has been observed for the simultaneous NO-CO conversion: Cu-Co-10Mn > Cu-Co > Cu-Co-20Mn > Cu-Co-30Mn. Such increase in the catalytic performance with the addition of 10% Mn may be due to the formation of active sites which plays a role of promoter in Cu-Co catalytic system. However, the further increase in Mn concentration can lead in suppressing these active sites by acting as a poison, which later results in decrease in the catalytic activity. Additionally, this explanation is well coinciding with the CO-TPD studies (Fig. 5.25) in which 10% Mn shows higher amount of CO desorption and as Mn concentration increases, the decline in CO peak was seen.

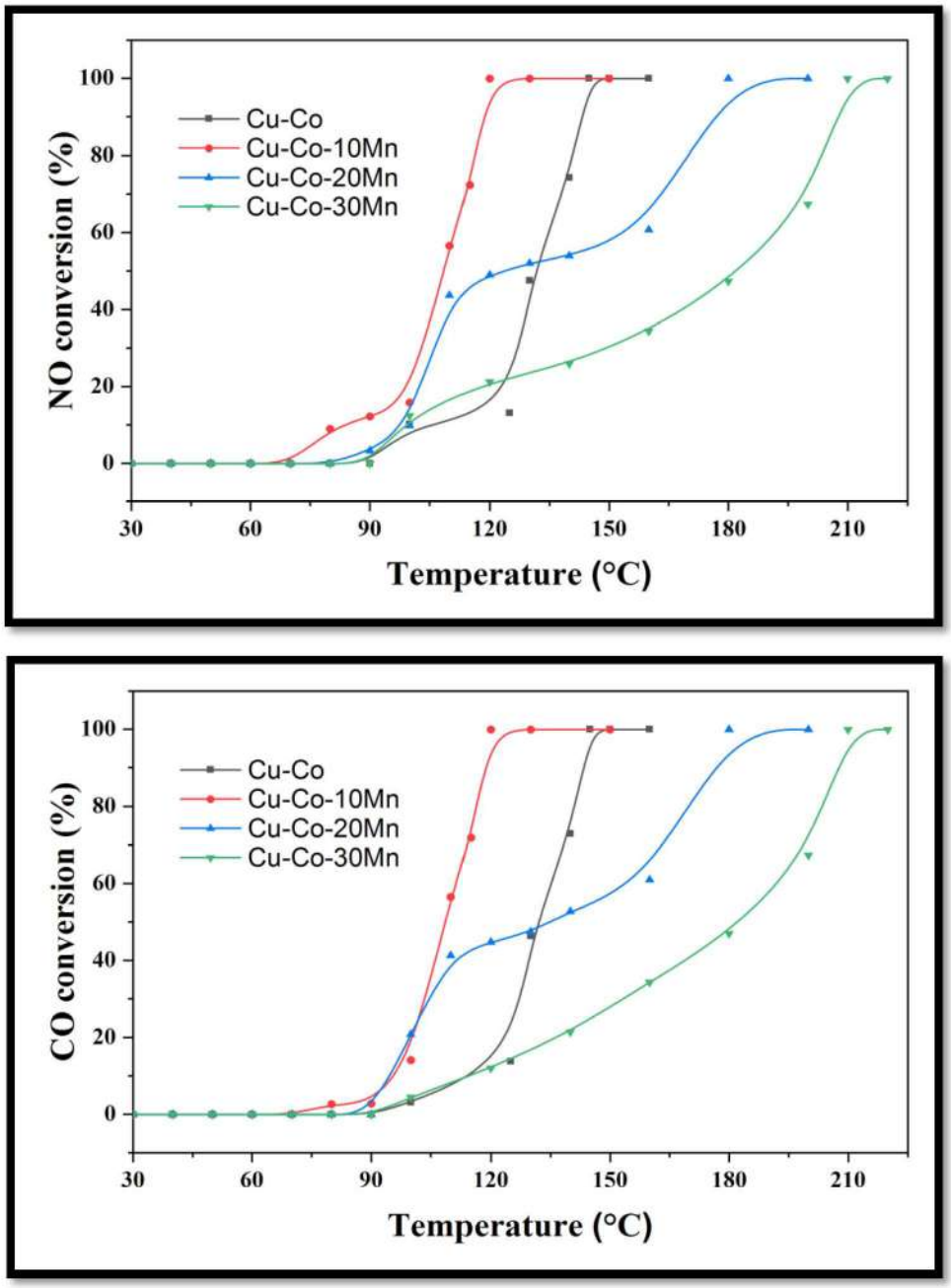

Fig. 5.55: *NO - CO redox reaction over Co-Cu, Co-Cu-10Mn, Co-Cu-20Mn and Co-Cu-30Mn (5% NO and 5% CO in Ar at flow rate of 5000 mL h−1).*

The performance of NO-CO redox reaction studied over different Pd containing oxide catalysts as a function of temperature is shown in Fig. 5.56. From Fig. 5.56, it can be understood that NO conversion using CO on Pd substituted cobalt chromite has poor activity among the prepared oxide catalysts (PdR1). The performance of PdR1 is increased by

supporting it with PdO but was unable to achieve the 100% conversion of NO to N_2 and CO to CO_2 as seen from PdR2.

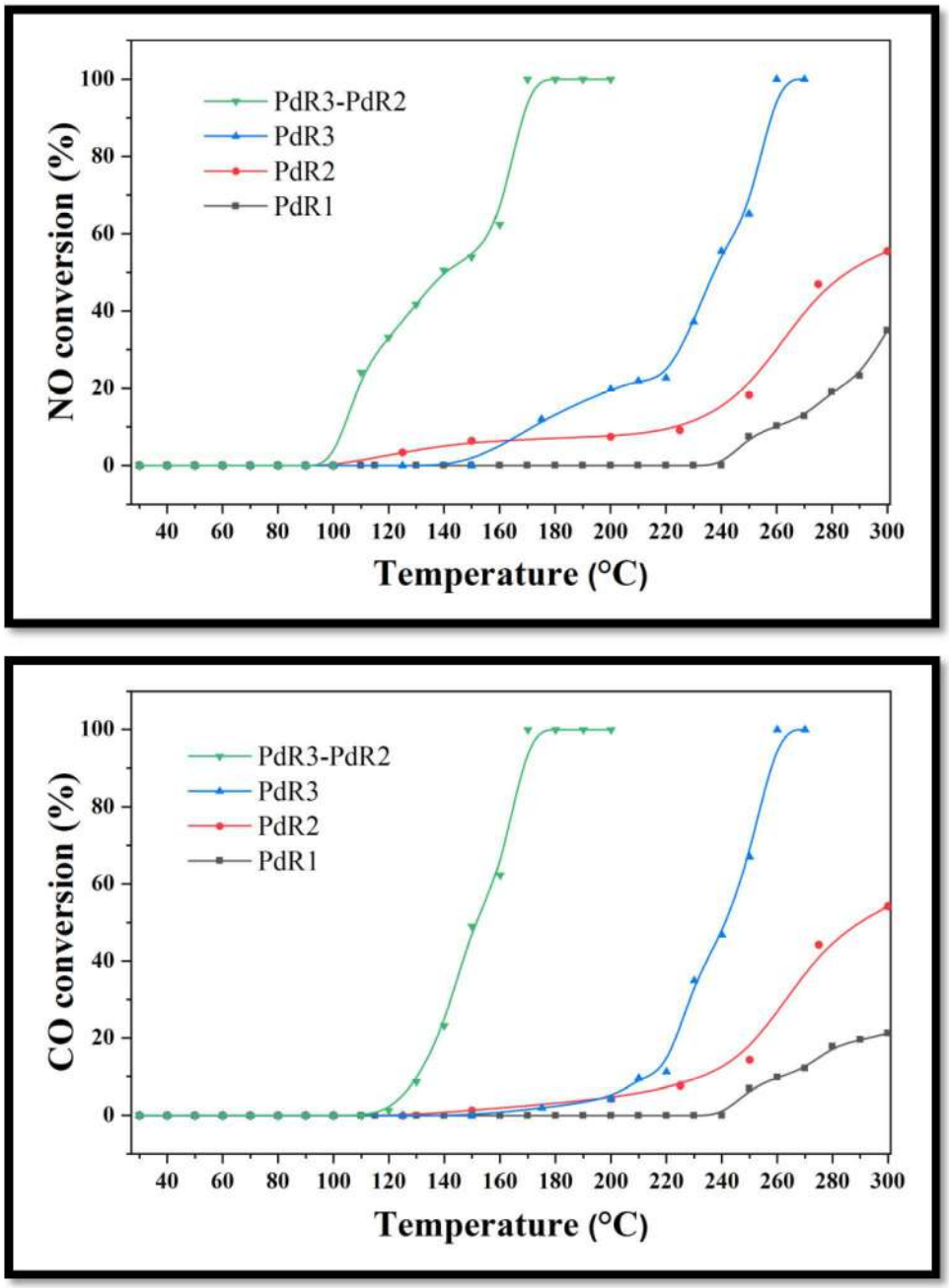

Fig. 5.56: *NO - CO redox reaction over PdR1, PdR2, PdR3 and PdR2-PdR3 (5% NO and 5% CO in Ar at flow rate of 5000 mL h−1).*

Also, the catalytic conversion over PdR3 was studied and showed T_{100} at 250 °C. Further, PdR3-PdR2 showed the enhancement in catalytic conversion when PdR3 was combined with

PdR2, gaining a 100% conversion of NO and CO at 170 °C. The reason for such a rise in conversion at a lower temperature is probably attributed to the presence of PdR2 producing synergy with the PdR3, which increases the overall redox property of the material. The percentage of Pd loading in 1 g of PdR1, PdR2, PdR3, and PdR3-PdR2 was calculated as 2.3%, 3.4%, 2.6%, and 2.9% by weight to compare the impact of Pd on the oxide system. The presence of a marginal Pd rise in the overall system may not be alone which helps in driving the NO-CO conversion but also can be greatly related to synergy interaction, which helps in lowering the reaction temperature. This significant increase in redox property of PdR3-PdR2 creates the active catalytic state at lower temperature on the surface of the catalyst, thereby allowing more reactant to catalyse on its surface.

During the reaction period, formation of N_2O was monitored over the catalysts and their results are shown in Fig. 5.57. From the results, it can be seen that N_2O formation was comparatively higher in PdR3 than the other studied materials, which was decreased in PdR3-PdR2. Additionally; N_2O was observed to be diminishing in a higher temperature region.

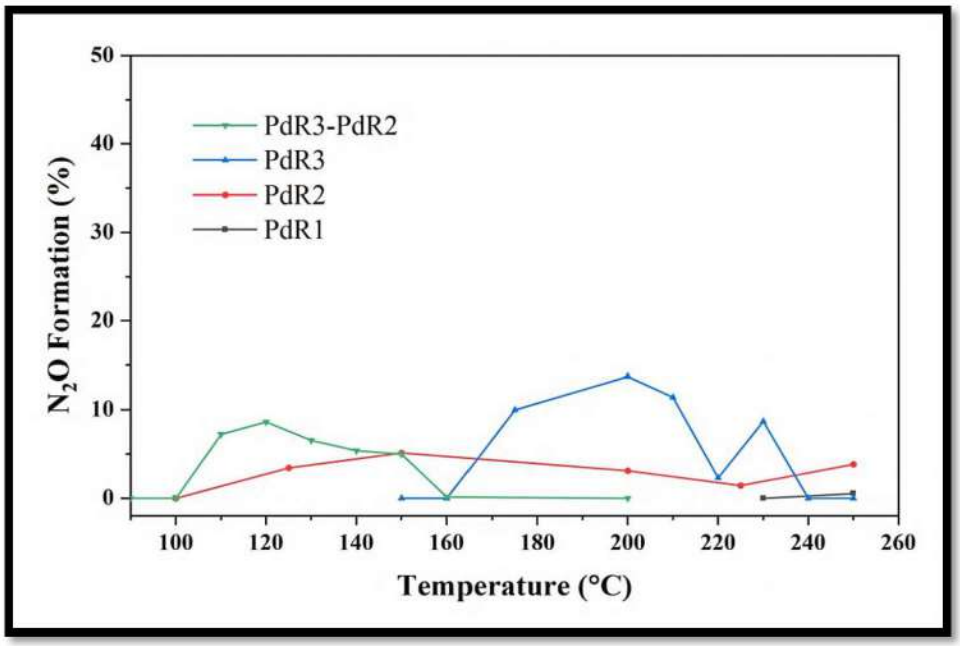

Fig. 5.57: *N_2O formation over PdR1, PdR2, PdR3 and PdR2-PdR3.*

Figure 5.58 shows the catalytic behavior of $Cu_{0.95}Pd_{0.05}O$ and Al_2O_3 modified $Cu_{0.95}Pd_{0.05}O$ with respect to NO – CO redox reaction. In the absence of Al, the $Cu_{0.95}Pd_{0.05}O$ showed poor conversion of NO and CO (i.e. 80% at 250 °C), whereas with the incorporation of Al a significant advancement is observed.

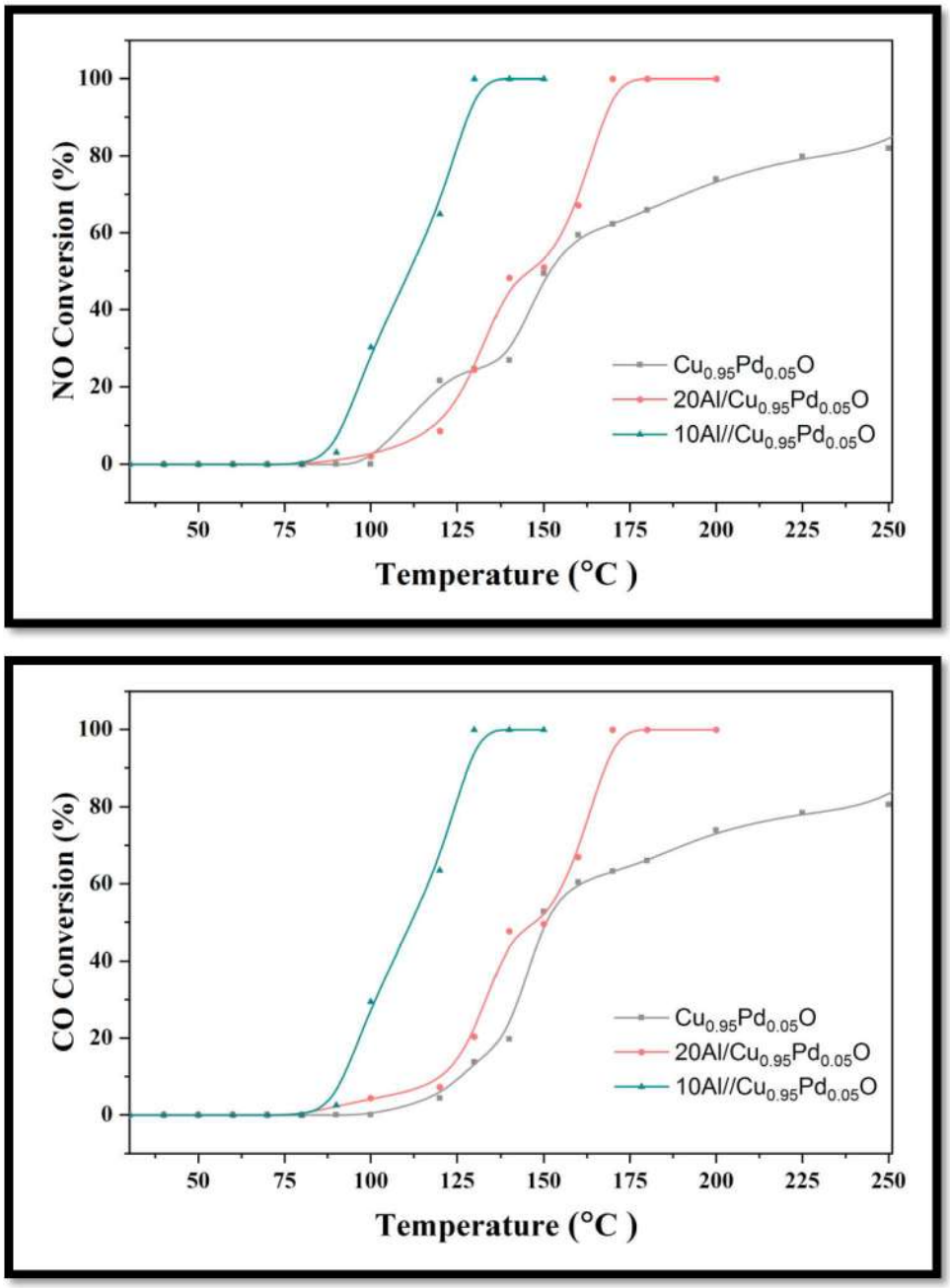

Fig. 5.58: *NO - CO redox reaction over $Cu_{0.95}Pd_{0.05}O$, 20Al $Cu_{0.95}Pd_{0.05}O$ and 10Al-$Cu_{0.95}Pd_{0.05}O$. (5% NO and 5% CO in Ar at flow rate of 5000 mL h−1).*

On monitoring the NO – CO conversion reaction on 20% Al_2O_3 crafted $Cu_{0.95}Pd_{0.05}O$, it displayed the improvement in catalytic process by giving 100% redox activity at 170 °C. This confirms the effect of Al addition in $Cu_{0.95}Pd_{0.05}O$, which makes the Cu-Pd more active. Similarly, it can be also correlated with CO-TPD profile, as quantum of CO adsorption was higher in 20Al/ $Cu_{0.95}Pd_{0.05}O$ than $Cu_{0.95}Pd_{0.05}O$. In contrast, just Al_2O_3 is inactive for such catalytic process but it can be used as good platform for active species by dispersing within the oxide system. Furthermore, simultaneous NO-CO conversion has been moved to lower temperature by architecting the Al_2O_3 and $Cu_{0.95}Pd_{0.05}O$ wherein more active species (i.e. Cu-Pd) was kept in exposed position. This designing of catalyst has attained the 100% conversion at lower temperature of 130 °C, which is again convincing with the CO TPD result as 10Al-$Cu_{0.95}Pd_{0.05}O$ holds more CO on its surface. Finally, the increasing trend obtained for the simultaneous NO – CO reaction is produced as 10Al-$Cu_{0.95}Pd_{0.05}O$ > 20Al/$Cu_{0.95}Pd_{0.05}O$ > $Cu_{0.95}Pd_{0.05}O$.

To examine the effect of physical grinding on simultaneous NO-CO conversion reaction, CeRu – CuPd composite oxide was prepared from $Ce_{0.95}Ru_{0.05}O_2$ and $Cu_{0.95}Pd_{0.05}O$. The result of % NO/CO conversion with respect to temperature gradient is presented in Fig. 5.59. The CuPdO, with a 5% Pd loading showed complete NO-CO detoxification at 275 °C, whereas the CeO_2 containing 5% Ru showed 100% conversion at 150 °C. This proves the significant effect of $CeRuO_2$ in detoxification of NO and CO at lower temperature as that of CuPdO. Further, the NO-CO testing on composite dropped the reaction temperature by 30 °C as that of CeRu and gave 100% conversion at 120 °C. Such performance of the CeRu-CuPd composite oxide is mostly due to the synergistic effect produced between CeRu and CuPd oxide system. The increasing trend observed in removal of NO and CO is CeRu–CuPd > $Ce_{0.95}Ru_{0.05}O_2$ > $Cu_{0.95}Pd_{0.05}O$. Similar type of studies was also reported wherein composite an oxide produces a greater impact in catalytic reaction than single phase oxide due to stoichiometric distortion.

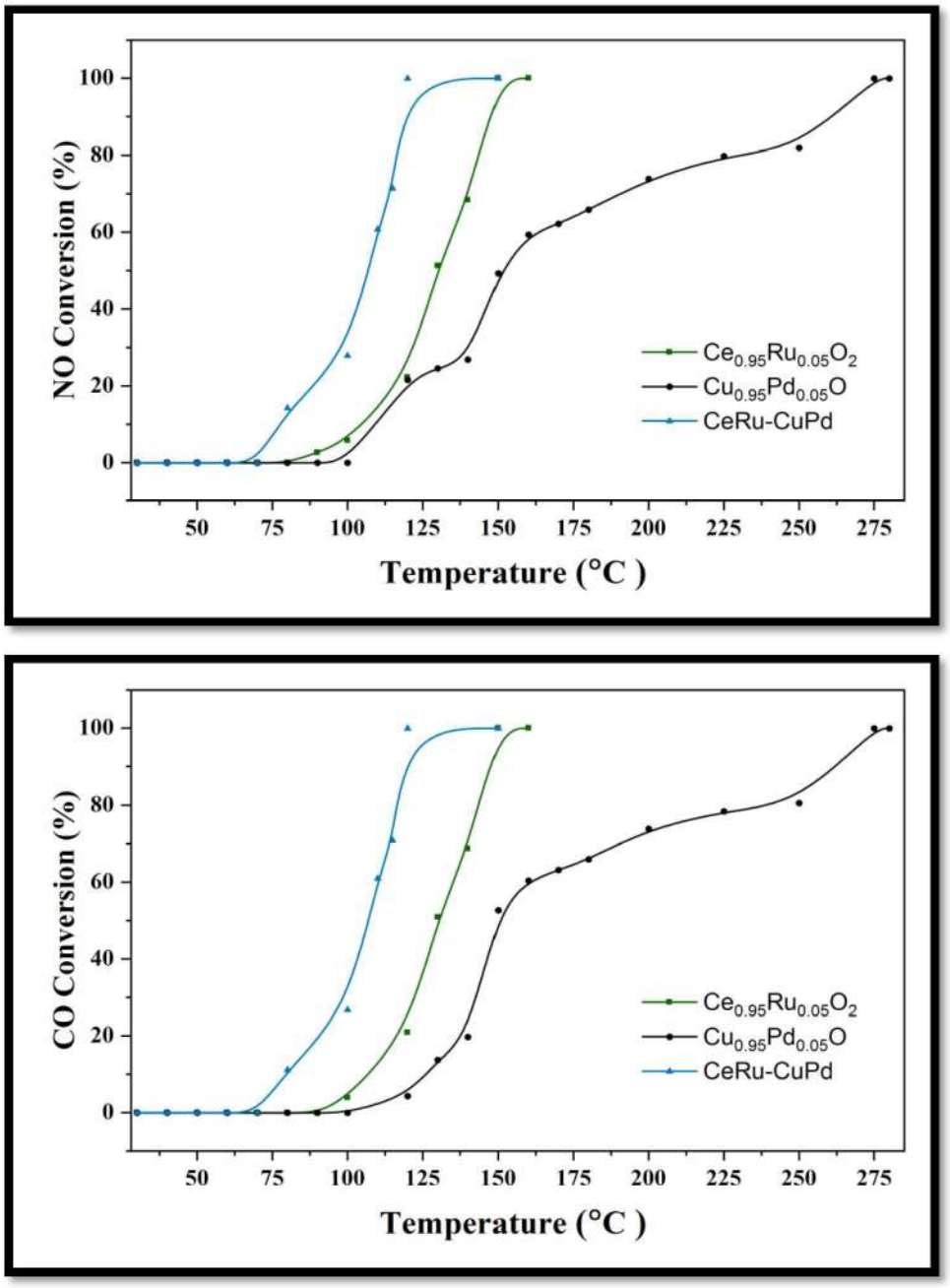

Fig. 5.59: *NO - CO redox reaction over $Ce_{0.95}Ru_{0.05}O_2$, $Cu_{0.95}Pd_{0.05}O$, and CeRu-CuPd composite (5% NO and 5% CO in Ar at flow rate of 5000 mL h−1).*

5.8.4. Catalyst Stability and recyclability for NO–CO redox reaction

Figure 5.60 shows the stability of the Cr_2O_3 and $Cr_{1.96}Cu_{0.04}O_3$ catalyst for NO conversion reaction. These catalysts were studied for 500 min in Ar atmosphere at a fixed temperature of

185 °C. A steady %NO conversion was seen during the studied time and result were consistent for 500 min. This shows the stability of the catalyst for 500 min run.

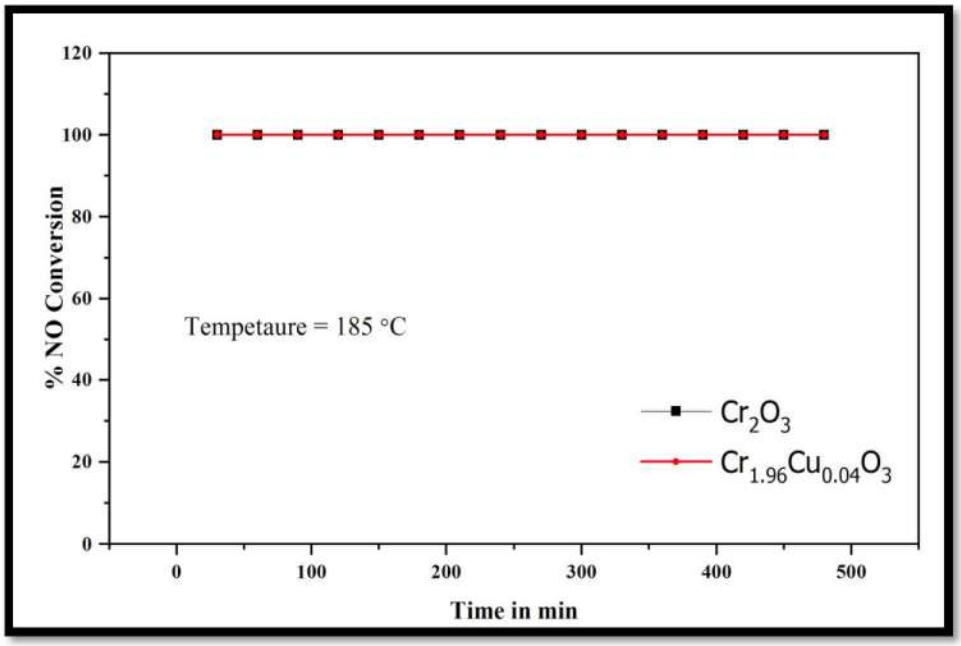

Fig. 5.60: *NO conversion stability over Cr_2O_3 and $Cr_{1.96}Cu_{0.04}O_3$ catalyst.*

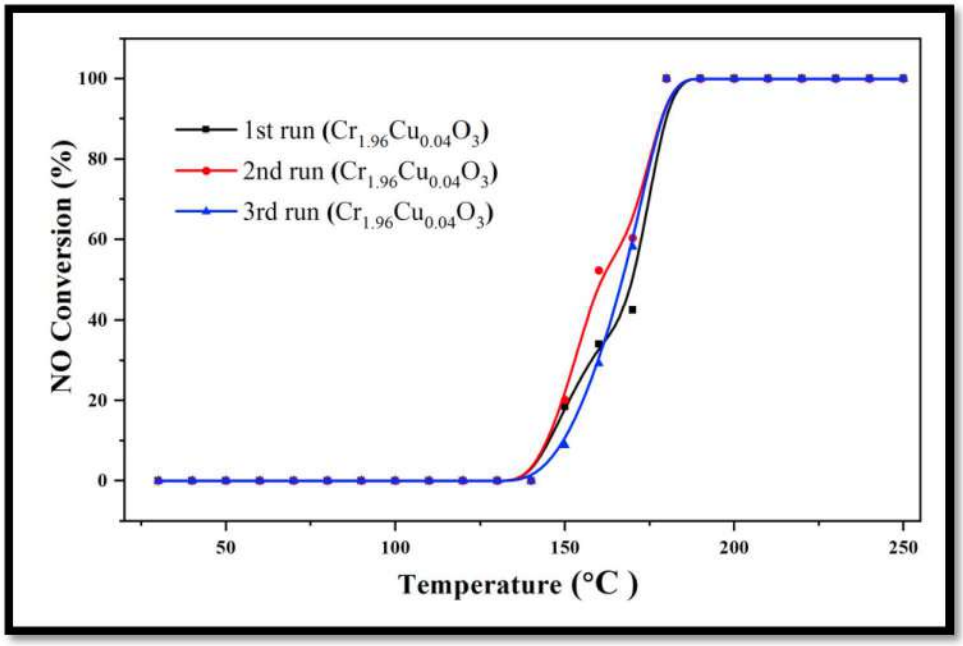

Fig. 5.61: *NO conversion over $Cr_{1.96}Cu_{0.04}O_3$ catalyst for three catalytic cycles.*

Also, the reproducibility study was carried out on the highly active catalyst ($Cr_{1.96}Cu_{0.04}O_3$) to understand the reusability of the catalyst prepared. The recyclability study was carried out for 3 catalytic cycles by taking 5% CO and 5% NO in Ar atmosphere and the obtained result is given in Fig. 5.61. The catalyst showed similar pattern for 3 catalytic cycles. This shows a good recyclability of the catalyst studied.

The reaction stability over MM'-5% PdO was studied and is displayed in Fig. 5.62. The reaction was carried out for a period of 7 h at a fixed temperature of 200 °C in Ar atmosphere. The studied condition was 5% CO, 5% NO and 90% Ar for 7 h and also stability was checked by introducing the moisture. MM'-5% PdO represents good stability in the run time of 7 h. The 71 mmols/h of H_2O was introduced in reaction mixture over MM'-5% PdO composite system at 200 °C shows stable conversion with marginal decrease in conversion. Further, this confirms the good stability of the catalyst and also moisture tolerant behavior of the MM'-5% PdO.

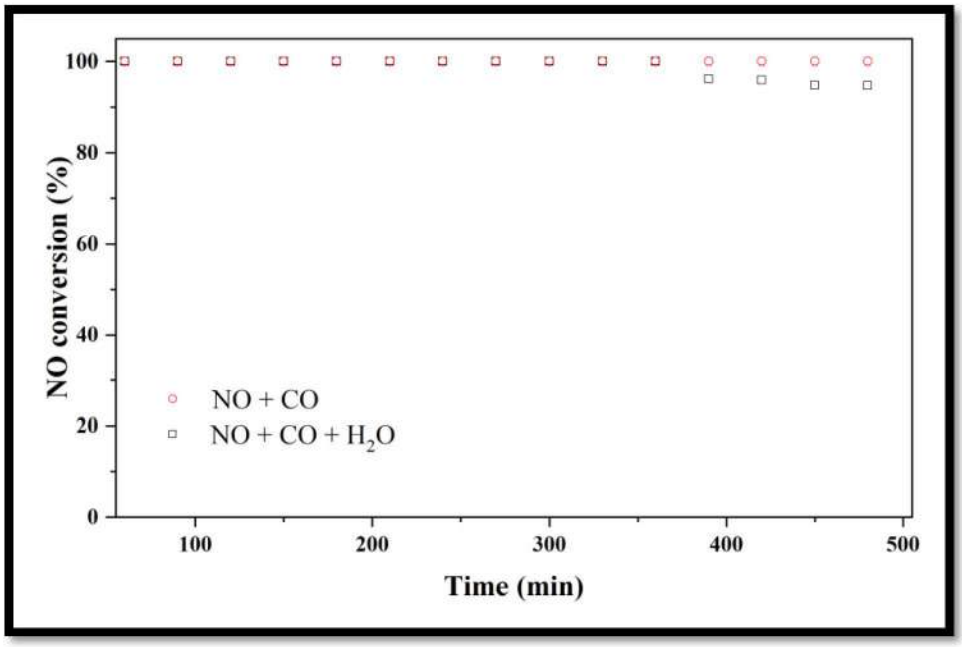

Fig. 5.62: *NO conversion stability over MM'-5%PdO in the absence and presence of moisture.*

As recyclability is one of the important criteria of the catalyst, reproducibility of MM'-5% PdO was checked for NO-CO reaction. The recyclability studies were carried out for three catalytic sets and the graph produced due to the same is displayed in Fig. 5.63. This result is in good agreement with each other and produces similar results for 3 continuous cycles. Therefore, a good reproducibility of the catalyst for NO-CO reaction is thus confirmed.

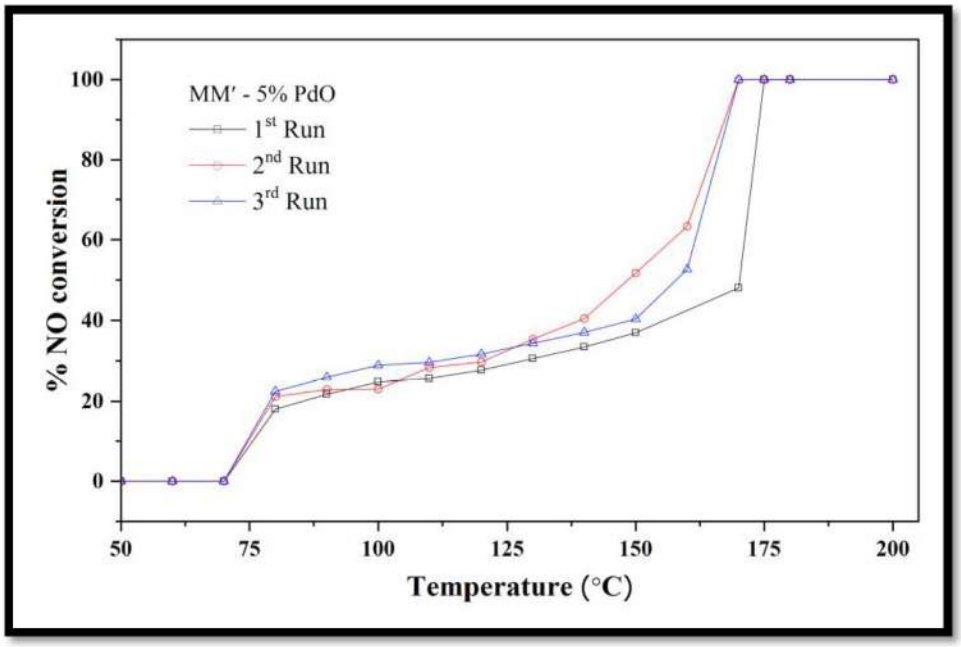

Fig. 5.63: *NO conversion over MM' - 5%PdO catalyst for three catalytic cycles.*

The Fig. 5.64 shows stability of the PdR3-PdR2 catalyst for 7 h at 180 °C. The reaction is composed of 5% NO, 5% CO and 90% Ar at a flow of 5000 ml/h. The consistent result was obtained during the 7 h run, which confirms the good stability of the catalyst towards simultaneous NO-CO conversion.

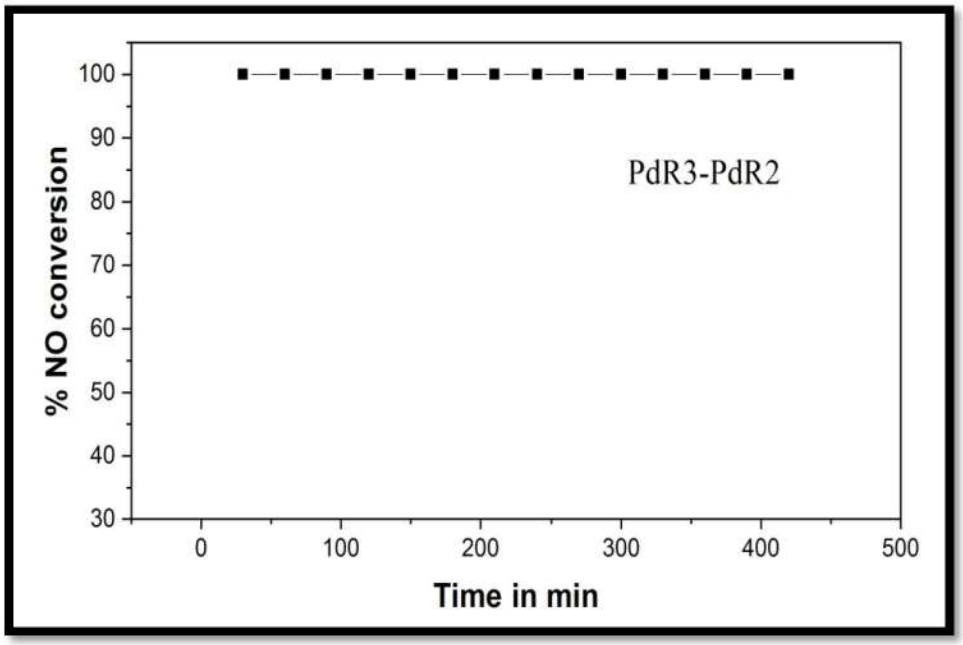

Fig. 5.64: *NO conversion stability over PdR3-PdR2 for 7 h.*

Catalyst reusability was performed over PdR3-PdR2 and the obtained data was presented in Fig. 5.65. Catalyst reproducibility was carried out from room temperature to 200 °C. This catalyst used for the catalytic run showed good performance for the repeated study.

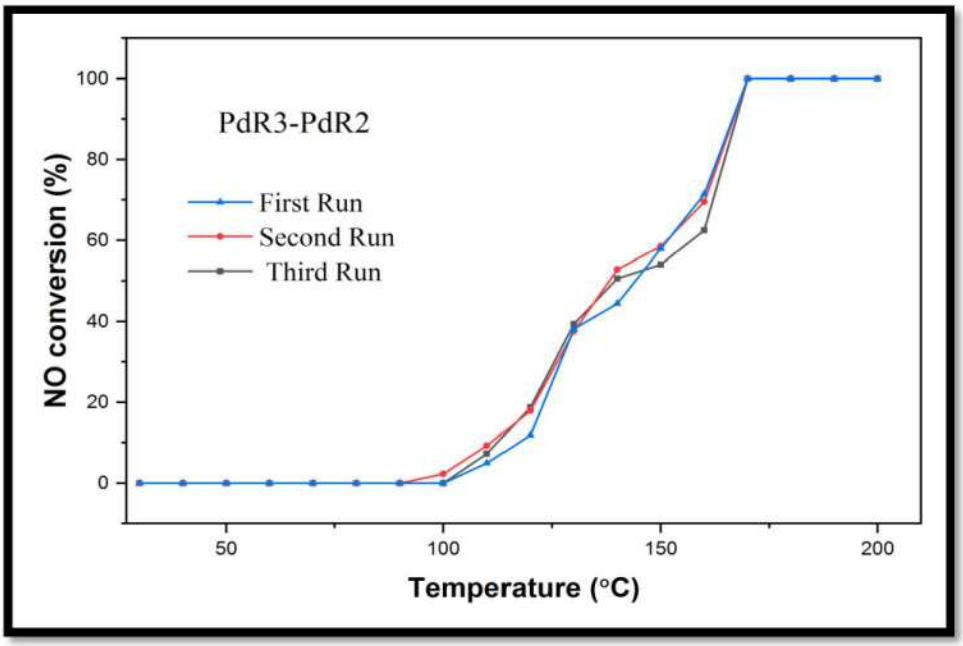

Fig. 5.65: *NO conversion over PdR3-PdR2 for 3 catalytic cycles.*

6.1 Summary

This Thesis is comprised of material designing and modification for detoxification of NO and CO pollutants. All the prepared catalysts were thoroughly characterized by different techniques to understand the properties of the catalysts. Thereafter, these catalysts were studied for the oxidation of CO with O_2. Similarly, simultaneous removal of NO and CO via NO-CO redox pathway was also studied. In this section, a brief overview of the work presented will be summarized.

Chapter 1 gives a brief introduction about the gaseous pollutants and its need for catalytic detoxification is highlighted. At the end of this chapter, highlights of overall thesis and its organization has been provided.

Chapter 2 describes the detailed literature survey in concern with nitrogen monoxide, carbon monoxide, overview of the catalysis and various methods for the catalyst preparation. In relation to CO-O_2 and NO-CO redox reaction mechanisms were discussed. In addition to this, a brief literature on various metal oxides with respect to CO-O_2 and NO-CO conversion were also discussed.

Chapter 3 describes the experimental details of the thesis work. A detailed procedure about the different types of the catalyst preparation and modification has been discussed. Similarly, procedures for catalytic reaction measurement over gas chromatography were presented. Thereafter, schematic representations of the catalytic set-up were also illustrated.

Chapter 4 contains characterization of all the catalyst materials using structural, morphological and spectroscopic tools. Thermal studies describe the decomposition of the metal precursor and also the stability of the prepared catalyst. Further, IR spectroscopy was implemented to clarify the complete decomposition of metal precursor by comparing IR data of metal-precursor with final metal oxide. XRD technique was employed to understand the crystallinity, phase purity and crystal structure of the prepared oxide catalyst. Catalysts were prepared using different methods, which therefore result in different morphological arrangements. The required information regarding sample morphology was gained through SEM technique. Also, elemental color mapping was depicted to provide focus on elemental distribution over the surface. As all the prepared metal oxide particles are obtained at a nano

scale, TEM technique was utilized to deduce their shape and to measure size of the particle. XPS analyses were conducted in order to understand the chemical valence state of the elements present. Since, binding energy is a characteristic feature of element, a representative compound from the series has been evaluated and discussed.

Chapter 5 consists of the surface and catalytic performance over all the various types of metal oxide catalysts. Surface studies such as N_2-sorption, H_2-TPR, O_2-TPO, CO-TPD, NH_3-TPD, CO_2-TPD and CO pulse titration which describes the surface area, surface redox property, surface affinity towards CO and surface acidity-basicity of the catalyst, respectively were discussed in detail. Likewise, CO-O_2 reaction and NO-CO redox reaction were performed and the obtained results were discussed in chapter 5. With respect to preformed reaction, catalyst stability, recyclability was also summarized. And finally in chapter 6 contain summary and conclusion.

6.2 Conclusion

- In conclusion of monophasic catalyst series, two host materials were selected for analyzing its catalytic property toward the oxidation of CO and NO-CO simultaneous conversion i.e. chromium oxide and cerium oxide. A successful preparation of chromium oxide and copper-substituted chromium oxide were carried out using glycine-combustion method, whereas for Ru, Ag, Cu, Mn substituted cerium oxide, tartaric acid mediated solution combustion route was employed. Complete combustion of metal-precursor to metal oxide was confirmed from IR spectra as no vibration bands in 4000 to 1000 cm^{-1} range was observed which corresponds to organic species. X-ray diffraction patterns of Cr_2O_3 and $Cr_{1.96}Cu_{0.04}O_3$ confirmed the rhombohedral phase and also, the presence of copper in Cu^{+2} was confirmed through XPS studies. In the case of cerium oxide, XRD revealed the formation of monophasic compounds and having cubic structure in all the substituted cerium oxides. Hydrogen reduction pattern of Cr_2O_3 and Cu substituted Cr_2O_3 showed low oxygen mobility in pristine Cr_2O_3 as compared to Cu substituted Cr_2O_3, thus decreasing the redox property of the Cr_2O_3. In TPR profile of Ru, Ag, Cu, Mn substituted cerium oxide, increase in the oxygen mobility were seen as compared to pure CeO_2. Similar pattern was seen in CO pulse studies on Ag, Cu, Mn substituted CeO_2 series, where multiple substitution showed highest CO adsorption in the series. But in the case of Ru substituted CeO_2, a gradual increase was shown by CO

desorption peak which intern confirms the higher amount of CO uptake with increase in Ru concentration in cerium oxide.

Foamy fibrous Cu substituted Cr_2O_3 series was studied for simultaneous NO-CO redox reaction which gave enhanced catalytic activity after substitution of copper in Cr_2O_3. This improved conversion by addition of copper can be associated to the enhanced redox nature in $Cr_{1.96}Cu_{0.04}O_3$. Also, good reaction stability and reusability of the chromium oxide catalyst was observed. In Ag, Cu, Mn substituted CeO_2 oxide series, the catalytic activity of the CeO_2 was significantly enhanced with the isomorph substitution exhibiting the highest conversion at 95 °C. Also, in moisture and CO_2 environment, a good moisture and CO_2 tolerance was observed. The highest catalytic conversion of the $Ce_{0.95}Mn_{0.02}Cu_{0.02}Ag_{0.01}O_2$ can be attributed to the synergy effect formed by co substitution of Mn, Cu and Ag in CeO_2 matrix. The TPR studies showed a good reduction property and high CO adsorption over $Ce_{0.95}Mn_{0.02}Cu_{0.02}Ag_{0.01}O_2$ which play important part in CO oxidation reaction. Likewise, Ru substitution in CeO_2 also showed enhanced catalytic activity in CO-O_2 and NO-CO redox reaction. The increase in the concentration of Ru in cerium oxide produced improvement in CO-O_2 and NO-CO conversion ability by giving 100% conversion at 150 °C, which is highest among the series of Ru substituted CeO_2 catalyst.

- The work on Co-Cu-Mn composite oxide and the precious metal containing Co-Mn and Cu-Mn composite oxide catalyst describes the promotional effect of composite oxide system towards the CO-O_2 and NO-CO redox reaction. Composite system having small amount of precious metal is an efficient and economical way to convert NO and CO to safer gases. A series of Pd containing cobalt–manganese oxide series, Ag and Rh composed cobalt-manganese oxide, Al and Pd, copper-manganese oxide nano-catalysts systems were successfully prepared by glycine - assisted combustion route. Similarly, Mn containing cobalt-copper composite oxide system was also designed via glycine assisted combustion synthesis. The metal-glycine precursors were characterized using thermal analytic tools for understanding their decomposition temperature and the temperature stability of prepared composite oxides were also confirmed. This complete removal of carbon moiety was thus investigated from the IR spectral studies. XRD peaks showed the low crystallinity in all the composite oxide samples which may be due to the formation of particles in nano-range. XPS revealed the presence of Co^{+2}/Co^{+3}, Mn^{+3}/Mn^{+4} and Pd^{+2} in the Pd composed Co-Mn oxide

and Co^{+2}/Co^{+3}, Mn^{+3}/Mn^{+4}, Ag^{+1} and Rh^{+3} in Ag-Rh containing Co-Mn oxide. Likewise, in Al and Pd containing Cu-Mn composite oxide, presence of copper in $Cu^{+1/+2}$, manganese in $Mn^{+2/+3/+4}$, aluminum in Al^{+3} and palladium in Pd^{+2} state was proved by XPS studies. The prepared composite oxide catalysts were found to show porous appearance in SEM and the formation of nanoparticles was confirmed through TEM analysis. BET surface area studies showed the increasing surface area trend in Co-Mn composite oxide with increasing Pd concentration in the series and with the addition of Ag and Rh together by providing more surface area. In the case of Cu-Mn composite oxide, addition of aluminum showed enhancement in the surface area, which is due to the formation of porous structure after addition of aluminum as confirmed through BJH studies. While in Co-Cu composite system, addition of 10% Mn showed increased surface area and later observed decrease in the surface area after addition of Mn. Surface oxygen mobility and the CO adsorption property of the Pd containing Co-Mn composite oxide catalysts were found in the order of MM′–5% PdO > MM′–3% PdO > MM′–1% PdO > MM′, similar in Ag-Rh composed series the observed order were MM′–5% Ag-1% Rh > MM′–1% Ag > MM′. This improvement was the consequence of the enhanced effect of the precious metal dilution in the Co-Mn composite system which helps in enhancement in surface property. From Cu-Mn composite oxide series, the promotional effect of Al was seen which helps in triggering the surface reduction property in Cu-Mn-Al-Pd composite oxide. Also, weakening of surface acidity and improvement in surface basicity was investigated in the presence of Al in Cu-Mn composite oxide system. H_2-TPR studies on 10% Mn addition in Co-Cu oxide showed the improvement in surface reduction which was further observed to decline with the increasing Mn concentration in Co-Cu composite oxide system. Similar pattern was also seen in CO TPD studies which showed desorption of CO at comparatively lower temperature as compared to other catalyst from the series.

Among the tested Pd containing Co-Mn catalysts, 5% PdO composed Co-Mn composite oxide exhibited improved catalytic reaction by completing CO–O_2 oxidation reaction at 65 °C and simultaneous NO–CO redox reaction at 170 °C, which was found to be the best catalyst for the studied reactions. The increase in Pd concentration in the composite oxides significantly decreases the N_2O formation and also showed excellent reproducibility for the reduction of nitric oxide to N_2. The catalysts showed very good stability for the simultaneous NO–CO redox reaction for 7 h. However, a marginal decrease was observed in NO reduction when

moisture was introduced into the reaction system, which is an observed pattern for most of the time. The work on Ag and Rh containing Co-Mn composite oxide describes the promotional effect of Rh-Ag pair towards the CO-O_2 and NO-CO redox reaction. This made MM′-5%Ag-1%Rh catalyst active at lower temperature, which results in 100% conversion of NO and CO at 150 °C in NO-CO reaction and 100% conversion of CO in CO-O_2 reaction thereby conveying the high efficiency of the catalyst as compared to many other catalysts. Among the prepared Cu-Mn composite series, addition of aluminum showed 100% conversion of NO and CO at 225 °C in Cu-Mn-Al-Pd composite oxide catalyst. In spite of inert nature of Al_2O_3, addition of Al has improved catalytic property, which showed the promotional effect of Al in composite oxide catalyst. In Co-Cu-Mn composite oxide catalyst, the order observed for the simultaneous NO-CO conversion was Cu-Co-10Mn > Cu-Co > Cu-Co-20Mn > Cu-Co-30Mn. Thereby showed enhancement in catalytic performance with the addition of 10% Mn. Similar trend was also observed in CO-O_2 reaction where 100% CO oxidation occurred below 40 °C.

- Systematically designed mixed metal oxide catalysts were prepared with glycine-combustion and wet impregnation method for oxidation of carbon monoxide and also simultaneous reduction of nitric oxide. Here two different mix metal oxide series were prepared, one comprised of Pd substituted $CoCr_2O_4$, PdO and Pd substituted Mn_2O_3 and other one includes Pd substituted CuO and Al_2O_3. Monophasic formation of Pd-substituted Mn_2O_3, $CoCr_2O_4$ and CuO was confirmed from their powder XRD patterns which were found to be matching with their standard JCPDS data card. N_2 sorption reveals the type IV isotherm of prepared nanoparticles and their variable oxidation states were analyzed through XPS studies. TPR- TPO studies were used to monitor the redox property of the catalyst which is in the order of PdR3-PdR2 > PdR3 > PdR2 > PdR1. Surface reactivity of CO studied using the temperature-programmed desorption showed two different adsorption regions, i.e., weakly chemisorbed and strongly chemisorbed on the surface, which is very well related to the reaction studied. In Al_2O_3 modified $Cu_{0.95}Pd_{0.05}O$ series, surface reduction was monitored through H_2-TPR studies which convey pre presence of active metal species in different surface environment. Likewise, in CO desorption studies 10% Al_2O_3 possessing $Cu_{0.95}Pd_{0.05}O$ showed larger desorption of CO indicating high amount of CO getting adsorbed on the catalyst surface.

Among these tested catalyst series, PdR3-PdR2 and 10Al-$Cu_{0.95}Pd_{0.05}O$ showed better activity with respect to simultaneous NO-CO conversion of 100% at 170 °C and 130 °C, respectively. Also, very good CO oxidation with O_2 was seen in 10Al-$Cu_{0.95}Pd_{0.05}O$ catalyst. Systematic designing of the catalyst produces a good synergy by metal-metal interaction, which helps in decreasing the reaction temperature. The catalyst showed good PdR3-PdR2 stability and reproducibility for NO-CO simultaneous conversion reaction.

- The physical grinding method was one of the routes to prepare composite oxide catalyst which is discussed in the thesis. A successful attempt was made to prepare CeO_2–CuO and $Ce_{0.95}Ru_{0.05}O_2$-$Cu_{0.95}Pd_{0.05}O$ composite oxide from the respective monophasic oxide. Comparing the XRD data of pure CeO_2 and CuO with CeO_2–CuO composite, no reflection of extra phases was seen. The surface morphology reveals the presence of porous agglomerated CeO_2 and CuO particles in the composite system which is observed to be well dispersed over the catalyst surface as shown in elemental mapping data. Likewise, $Ce_{0.95}Ru_{0.05}O$ and $Cu_{0.95}Pd_{0.05}O$ also showed porous structure with agglomerated particles which after grinding observed as agglomerated particles in SEM. The surface area and BJH pore size distribution of CeO_2–CuO composite was found to be lesser than that of pure cerium oxide. Elemental oxidation states studies were also carried out over composite wherein presence of Cu^{+1}/Cu^{+2} was seen in CeO_2-CuO composite oxide and the presence of Rh^{+4} and Pd^{+2} was seen in CeRu-CuPd composite oxide system. Further, the oxygen mobility and CO adsorptions over prepared CeO_2, CuO and CeO_2-CuO oxides were studied by means of H_2-TPR and CO pulse titration studies. These studies revealed the high oxygen mobility and CO adsorption over composite oxide which is an evidence for the strong synergy interaction generated within the composite system from Cu–Ce interaction. From $Ce_{0.95}Ru_{0.05}O_2$, $Cu_{0.95}Pd_{0.05}O$ and CeRu-CuPd composite oxide, $Cu_{0.95}Pd_{0.05}O$ showed higher surface reduction in the series thus proving large amount of movable oxygen in the temperature range of 130 °C- 320 °C. During CO desorption studies over CeRu-CuPd composite system, both types of CO chemisorption sites i.e. weak and strong sites were observed with a slight shift in peak position.

Catalytic oxidation of CO over CeO_2–CuO and CeRu-CuPd composite oxide showed better conversion than the respective monophasic oxides by expressing an enhanced effect of physical grinding. Similar result in NO-CO redox reaction was seen over CeRu-CuPd composite oxide wherein it showed a higher performance of catalytic activity with respect to

$Ce_{0.95}Ru_{0.05}O_2$, and $Cu_{0.95}Pd_{0.05}O$. This result was compared with the TPR and chemisorption studies and was found to be in the good agreement with the catalytic activity studies. Also, good reaction stability was seen in both absence and presence of moisture over CeO_2-CuO catalyst.

REFERENCES

[1] I.A. Reşitoglu, K. Altinişik, A. Keskin, Clean Technol. Environ. Policy 17 (2015) 15–27.

[2] W.M. Weigert, E. Koberstein, Angew. Chemie Int. Ed. English 15 (1976) 586–592.

[3] P.S. Myers, O.A. Uyehara, SAE Tech. Pap. (1968) 8–20.

[4] M. Brauer, M. Amann, R.T. Burnett, A. Cohen, F. Dentener, M. Ezzati, S.B. Henderson, M. Krzyzanowski, R. V. Martin, R. Van Dingenen, A. Van Donkelaar, G.D. Thurston, Environ. Sci. Technol. 46 (2012) 652–660.

[5] S.S. Lim, T. Vos, A.D. Flaxman, et al. Lancet 380 (2012) 2224–2260.

[6] Y. Tan, P. Henderick, S. Yoon, J. Herner, T. Montes, K. Boriboonsomsin, K. Johnson, G. Scora, D. Sandez, T.D. Durbin, Environ. Sci. Technol. 53 (2019) 5504–5511.

[7] A.S. Shote, E. Betiku, A.A. Asere, J. King Saud Univ. - Eng. Sci. 31 (2019) 178–183.

[8] P. Ning, Z. Song, H. Li, Q. Zhang, X. Liu, J. Zhang, X. Tang, Z. Huang, Appl. Surf. Sci. 332 (2015) 130–137.

[9] X. Li, H. Zhang, H. Lü, S. Zuo, Y. Zhang, C. Yao, Environ. Sci. Pollut. Res. 26 (2019) 12842–12850.

[10] Y. Jung, Y.J. Shin, Y.D. Pyo, C.P. Cho, J. Jang, G. Kim, Chem. Eng. J. 326 (2017) 853–862.

[11] D. Yin, J. Li, J. Wang, L. Ling, W. Qiao, Ind. Eng. Chem. Res. 57 (2018) 6842–6852.

[12] L. Wang, G. Yin, Y. Yang, X. Zhang, React. Kinet. Mech. Catal. 128 (2019) 193–204.

[13] Y. Park, S.K. Kim, D. Pradhan, Y. Sohn, Chem. Eng. J. 250 (2014) 25–34.

[14] R.K. Kunkalekar, A. V Salker, Catal. Commun. 12 (2010) 193–196.

[15] X. Zhang, X. Cheng, C. Ma, Z. Wang, Catal. Sci. Technol. 8 (2018) 3336–3345.

[16] S. Zhan, D. Zhu, M. Qiu, H. Yu, Y. Li, RSC Adv. (2016) 1–6.

[17] H.E. Curry-Hyde, H. Musch, A. Baiker, M. Schraml-Marth, A. Wokaun, J. Catal. 133 (1992) 397–414.

[18] L.A. Flores-Sanchez, J.M. Quintana-Melgoza, R. Valdez, A. Olivas, M. Avalos-Borja, React. Kinet. Mech. Catal. 117 (2016) 593–604.

[19] X. Cheng, X. Zhang, D. Su, Z. Wang, J. Chang, C. Ma, Appl. Catal. B Environ. 239 (2018) 485–501.

[20] A. V. Salker, M.S.F. Desai, Appl. Surf. Sci. 389 (2016) 344–353.

[21] R.K. Kunkalekar, A. V. Salker, React. Kinet. Mech. Catal. 106 (2012) 395–405.

[22] A. V. Salker, React. Kinet. Catal. Lett. 73 (2001) 209–216.

[23] H. Ha, S. Yoon, K. An, H.Y. Kim, ACS Catal. 8 (2018) 11491–11501.

[24] J.E. Kubsh, J.S. Rieck, N.D. Spencer, Stud. Surf. Sci. Catal. 71 (1991) 125–138.

[25] J.D. Butler, D.R. Davis, J. Chem. Soc. Dalt. Trans. (1976) 2249–2253.

[26] S. Roy, A. Marimuthu, M.S. Hegde, G. Madras, Catal. Commun. 9 (2008) 101–105.

[27] S. Castillo, M. Moran-Pineda, G. R, Catal. Commun. 2 (2001) 295–300.

[28] M. Boaro, M. Vicario, C. De Leitenburg, G. Dolcetti, A. Trovarelli, in: Catal. Today, 2003, pp. 407–417.

[29] S. Lin, X. Yang, L. Yang, R. Zhou, Appl. Surf. Sci. 327 (2015) 335–343.

[30] T. Boningari, S.M. Pavani, P.R. Ettireddy, S.S.C. Chuang, P.G. Smirniotis, Mol. Catal. 451 (2018) 33–42.

[31] S. Carlotto, M.M. Natile, A. Glisenti, A. Vittadini, J. Phys. Chem. C 122 (2018) 449–454.

[32] G. Gao, J.W. Shi, Z. Fan, C. Gao, C. Niu, Chem. Eng. J. 325 (2017) 91–100.

[33] K. Ramesh, L. Chen, F. Chen, Y. Liu, Z. Wang, Y.F. Han, Catal. Today 131 (2008) 477–482.

[34] M. Moreno, L. Bergamini, G.T. Baronetti, M.A. Laborde, F.J. Mariño, Int. J. Hydrogen Energy 35 (2010) 5918–5924.

[35] C. Liu, F. Li, J. Wu, X. Hou, W. Huang, Y. Zhang, X. Yang, J. Hazard. Mater. 363 (2019) 439–446.

[36] C. Deng, M. Li, J. Qian, Q. Hu, M. Huang, Q. Lin, Y. Ruan, L. Dong, B. Li, M. Fan, Chem. - An Asian J. 11 (2016) 2144–2156.

[37] C.D. Jones, Ambient Temperature Oxidation of Carbon Monoxide by Copper-Manganese Oxide Based Catalysts, 2006.

[38] X. Zhang, X. Zhang, L. Song, F. Hou, Y. Yang, Y. Wang, N. Liu, Int. J. Hydrogen Energy 43 (2018) 18279–18288.

[39] Y. Kuwahara, A. Fujibayashi, H. Uehara, K. Mori, H. Yamashita, Catal. Sci. Technol. 8 (2018) 1905–1914.

[40] A. V. Salker, M.S. Fal Desai, Catal. Sci. Technol. 6 (2016) 430–433.

[41] Y.A. Henry, A. Guissani, B. Ducastel, Nitric Oxide Research from Chemistry to Biology, Springer US, Boston, MA, 1997.

[42] Jack Lancaster, ed., Nitric Oxide: Principles and Actions, Elsevier, 1996.

[43] H. Bour, I.M. Ledingham, Carbon Monoxide Poisoning, Elsevier, 2006.

[44] A. Haynes, Concepts of Modern Catalysis and Kinetics, 2005.

[45] A. V Salker, R.K. Kunkalekar, Catal. Commun. 10 (2009) 1776–1780.

[46] N. Sahu, K.M. Parida, A.K. Tripathi, V.S. Kamble, Appl. Catal. A Gen. 399 (2011) 110–116.

[47] M. Gatica, S. Harti, M. Ouzzine, G.A. Cifredo, T. Chafik, H. Vidal, 342 (2008) 150–158.

[48] B. Shen, X. Zhang, H. Ma, Y. Yao, T. Liu, 2 (2013) 209–216.

[49] G. Qi, R.T. Yang, Chem. Commun. 3 (2003) 848–849.

[50] G. Wu, X. Feng, H. Zhang, Y. Zhang, J. Wang, Y. Chen, Y. Dan, Appl. Surf. Sci. 427 (2018) 24–36.

[51] J.A. Sullivan, Catal. Letters 79 (2002) 59–62.

[52] L. Wang, S. Zhang, Y. Zhu, A. Patlolla, J. Shan, H. Yoshida, S. Takeda, A.I. Frenkel, F. Tao, ACS Catal. 3 (2013) 1011–1019.

[53] G.G. Olympiou, A.M. Efstathiou, Chem. Eng. J. 170 (2011) 424–432.

[54] M. V. Twigg, Johnson Matthey Technol. Rev. 59 (2015) 221–232.

[55] Y. Liu, J. Zhao, J.M. Lee, ChemCatChem 10 (2018) 1499–1511.

[56] I. Nova, L. Lietti, L. Castoldi, E. Tronconi, P. Forzatti, 239 (2006) 244–254.

[57] S. Roy, A. Marimuthu, M.S. Hegde, G. Madras, Appl. Catal. B Environ. 73 (2007) 300–310.

[58] P. Bera, K.C. Patil, V. Jayaram, M.S. Hegde, G. Subbanna, J.Mater Chem. 9 (1999) 1801–1805.

[59] S. Shen, H. Weng, 3 (1998) 2654–2661.

[60] M. Kang, E.D. Park, J.M. Kim, J.E. Yie, Catal. Today 111 (2006) 236–241.

[61] G. Rothenberg, Catalysis, Wiley, 2008.

[62] M.I. Zaki, M.A. Hasan, L. Pasupulety, Appl. Catal. A Gen. 198 (2000) 247–259.

[63] W.B. Li, J.X. Wang, H. Gong, 148 (2009) 81–87.

[64] J.Y. Luo, M. Meng, J.S. Yao, X.G. Li, Y.Q. Zha, X. Wang, T.Y. Zhang, Appl. Catal. B Environ. 87 (2009) 92–103.

[65] T. Higo, Y. Omori, A. Shigemoto, K. Ueno, S. Ogo, Y. Sekine, Catal. Today 352 (2020) 192–197.

[66] M. Kantcheva, O. Samarskaya, L. Ilieva, G. Pantaleo, A.M. Venezia, D. Andreeva, Appl. Catal. B Environ. 88 (2009) 113–126.

[67] R.M. Lambert, Chemisorpt. React. Support. Clust. Thin Film. (1997) 1–26.

[68] V. Bratan, C. Munteanu, C. Hornoiu, F. Papa, N.I. Ionescu, React. Kinet. Mech. Catal. 112 (2014) 51–60.

[69] C. Anil, G. Madras, J. Mol. Catal. A Chem. 424 (2016) 106–114.

[70] Z. Han, J. Wang, H. Yan, M. Shen, J. Wang, W. Wang, M. Yang, Catal. Today 158 (2010) 481–489.

[71] S. Bobaru, Introd. to Theory Concern. CO Oxid. over Platin. Gr. Met., 2006, pp. 11–18.

[72] B. Han, T. Li, J. Zhang, C. Zeng, H. Matsumoto, Y. Su, B. Qiao, T. Zhang, Chem. Commun. 56 (2020) 4870–4873.

[73] A. Katsaounis, Z. Nikopoulou, X.E. Verykios, C.G. Vayenas, J. Catal. 226 (2004) 197–209.

[74] B. Penkala, D. Aubert, H. Kaper, C. Tardivat, K. Conder, W. Paulus, Catal. Sci. Technol. 5 (2015) 4839–4848.

[75] K. Morgan, K.J. Cole, A. Goguet, C. Hardacre, G.J. Hutchings, N. Maguire, S.O. Shekhtman, S.H. Taylor, J. Catal. 276 (2010) 38–48.

[76] M.D. Esrafili, Chem. Phys. Lett. 695 (2018) 131–137.

[77] A.K. Ladavos, P.J. Pomonis, Appl. Catal. A Gen. 165 (1997) 73–85.

[78] K. Lu, Nanoparticulate Materials, John Wiley & Sons, Inc., Hoboken, NJ, USA, 2012.

[79] S. V. Ganachari, N.R. Banapurmath, B. Salimath, J.S. Yaradoddi, A.S. Shettar, A.M. Hunashyal, A. Venkataraman, P. Patil, H. Shoba, G.B. Hiremath, Handb. Ecomater. 1 (2019) 83–103.

[80] B.A.T. Mehrabadi, S. Eskandari, U. Khan, R.D. White, J.R. Regalbuto, A Review of Preparation Methods for Supported Metal Catalysts, 1st ed., Elsevier Inc., 2017.

[81] M. Li, X. Wu, Y. Cao, S. Liu, D. Weng, R. Ran, J. Colloid Interface Sci. 408 (2013) 157–163.

[82] M. Behrens, I. Kasatkin, S. Kühl, G. Weinberg, Chem. Mater. 22 (2010) 386–397.

[83] A.S. Deshpande, D.G. Shchukin, E. Ustinovich, M. Antonietti, R.A. Caruso, Adv. Funct. Mater. 15 (2005) 239–245.

[84] L. Radev, M. Khristova, D. Mehandjiev, B. Samuneva, Catal. Letters 112 (2006) 181–

186.

[85] A. Tavakoli, M. Sohrabi, A. Kargari, Chem. Pap. 61 (2007) 151–170.

[86] A.P. Ferreira, D. Zanchet, R. Rinaldi, U. Schuchardt, S. Damyanova, J.M.C. Bueno, Appl. Catal. A Gen. 388 (2010) 45–56.

[87] U.G. Akpan, B.H. Hameed, Appl. Catal. A Gen. 375 (2010) 1–11.

[88] A. V Salker, S.J. Naik, Appl. Catal. B Environ. 89 (2009) 246–254.

[89] R. Rangel, L. Chávez-Chávez, E. Martínez, P. Bartolo-Pérez, Phys. Status Solidi Basic Res. 249 (2012) 1199–1205.

[90] L.S. Kaykan, J.S. Mazurenko, A.K. Sijo, V.I. Makovysyn, Appl. Nanosci. (2020).

[91] Y.T. Nien, M.R. Hu, T.W. Chiu, J.S. Chu, Mater. Chem. Phys. 179 (2016) 182–188.

[92] R. Krishnamurthy, S.S.C. Chuang, K. Ghosal, Appl. Catal. A, Gen. 114 (1994) 109–125.

[93] A. Boubnov, S. Dahl, E. Johnson, A.P. Molina, S.B. Simonsen, F.M. Cano, S. Helveg, L.J. Lemus-Yegres, J.D. Grunwaldt, Appl. Catal. B Environ. 126 (2012) 315–325.

[94] C. Suryanarayana, Mech. Alloy. Milling 46 (2004) 1–472.

[95] S.F. Tikhov, V.A. Sadykov, K.R. Valeev, A.N. Salanov, S.V. Cherepanova, Y.N. Bespalko, V.E. Ramanenkau, Y.Y. Piatsiushyk, S.V. Dimov, Catal. Today 246 (2015) 232–238.

[96] M. Nyoka, Y.E. Choonara, P. Kumar, P.P.D. Kondiah, V. Pillay, Nanomaterials 10 (2020) 242.

[97] A.A. Firsova, O.S. Morozova, A. V. Leonov, A.N. Streletskii, V.N. Korchak, Kinet. Catal. 55 (2014) 783–791.

[98] S. Rajadurai, J.J. Carberry, B. Li, C.B. Alcock, J. Catal. 131 (1991) 582–589.

[99] O. Cambon, J. Haines, Crystals 7 (2017) 1–13.

[100] G. Avgouropoulos, T. Ioannides, H. Matralis, Appl. Catal. B Environ. 56 (2005) 87–93.

[101] L. Wang, X. Cheng, Z. Wang, C. Ma, Y. Qin, Appl. Catal. B Environ. 201 (2017) 636–651.

[102] R. Charrad, H.E. Solt, A. Domján, F. Ayari, M. Mhamdi, J. Valyon, F. Lónyi, J. Catal. 385 (2020) 87–102.

[103] S. Zhang, J. Shan, Y. Zhu, L. Nguyen, W. Huang, H. Yoshida, S. Takeda, F. Tao, Nano Lett. 13 (2013) 3310–3314.

[104] I. V. Zagaynov, Appl. Nanosci. 7 (2017) 871–874.

[105] H. Einaga, N. Urahama, A. Tou, Y. Teraoka, Catal. Letters 144 (2014) 1653–1660.

[106] M. Shelef, K. Otto, H. Gandhi, J. Catal. 12 (1968) 361–375.

[107] Y. Ren, Z. Ma, L. Qian, S. Dai, H. He, P.G. Bruce, Catal. Letters 131 (2009) 146–154.

[108] E. Nasr, I. Mohamed, Zeitschrift Tur Phys. Chemie 203 (1998) 131–142.

[109] M.J.S. Farias, C. Busó-Rogero, F.J. Vidal-Iglesias, J. Solla-Gullón, G.A. Camara, J.M. Feliu, Langmuir 33 (2017) 865–871.

[110] M. Kobayashi, T. Kanno, J. Chem. Soc. Faraday Trans. I 85 (1989) 579–583.

[111] E. Moretti, A.I. Molina, G. Sponchia, A. Talon, R. Frattini, E. Rodriguez-Castellon, L. Storaro, Appl. Surf. Sci. 403 (2017) 612–622.

[112] T. Tsoncheva, K. Ivanov, D. Dimitrov, Can. J. Chem. 89 (2011) 583–589.

[113] P.W. Park, J.S. Ledford, Ind. Eng. Chem. Res. 37 (1998) 887–893.

[114] R. Eckert, M. Felderhoff, F. Schüth, Angew. Chemie 129 (2017) 2485–2488.

[115] S. Song, Y. Wu, S. Ge, L. Wang, Y. Wang, Y. Guo, W. Zhan, Y. Guo, ACS Catal. (2019) 6177–6187.

[116] Z. Qiu, X. Guo, J. Mao, R. Zhou, Appl. Surf. Sci. 481 (2019) 1072–1079.

[117] H. Zhu, Y. Chen, Y. Gao, W. Liu, Z. Wang, C. Cui, W. Liu, L. Wang, J. Rare Earths 37 (2019) 961–969.

[118] D. Li, K. Li, R. Xu, X. Zhu, Y. Wei, D. Tian, X. Cheng, H. Wang, ACS Appl. Mater. Interfaces 11 (2019) 19227–19241.

[119] Z. Guo, L. Song, T. Xu, D. Gao, C. Li, X. Hu, G. Chen, Mater. Chem. Phys. 226 (2019) 338–343.

[120] J. Yu, J. Yu, Z. Wei, X. Guo, H. Mao, D. Mao, Catal. Letters 149 (2019) 496–506.

[121] I. Spassova, N. Velichkova, D. Nihtianova, M. Khristova, J. Colloid Interface Sci. 354 (2011) 777–784.

[122] H. Wang, D. Mao, J. Qi, Q. Zhang, X. Ma, S. Song, L. Gu, R. Yu, D. Wang, Adv. Funct. Mater. 29 (2019) 1–9.

[123] X. Jin, Y. Duan, D. Liu, X. Feng, W. Li, Z. Zhang, Y. Zhang, ACS Appl. Nano Mater. 2 (2019) 5769–5778.

[124] L. Savereide, S.L. Nauert, C.A. Roberts, J.M. Notestein, J. Catal. 366 (2018) 150–158.

[125] A.N. Il'ichev, M.Y. Bykhovsky, Z.T. Fattakhova, D.P. Shashkin, Y.E. Fedorova, V.A. Matyshak, V.N. Korchak, Kinet. Catal. 60 (2019) 661–671.

[126] M. Piumetti, S. Bensaid, D. Fino, N. Russo, Appl. Catal. B Environ. 197 (2016) 35–46.

[127] P.E. Plyusnin, E.M. Slavinskaya, R.M. Kenzhin, A.K. Kirilovich, E. V. Makotchenko, O.A. Stonkus, Y. V. Shubin, A.A. Vedyagin, React. Kinet. Mech. Catal. 127 (2019) 69–83.

[128] H. Bao, X. Chen, J. Fang, Z. Jiang, W. Huang, Catal. Letters 125 (2008) 160–167.

[129] S. Roy, M.S. Hegde, Catal. Commun. 9 (2008) 811–815.

[130] R.D. Kerkar, A.V. Salker, Mater. Chem. Phys. 253 (2020) 123326.

[131] K. Murata, E. Eleeda, J. Ohyama, Y. Yamamoto, S. Arai, A. Satsuma, Phys. Chem. Chem. Phys. 21 (2019) 18128–18137.

[132] X. Yang, X. Cheng, J. Ma, Y. Zou, W. Luo, Y. Deng, Small 15 (2019) 1903058.

[133] X. Gu, H. Li, L. Liu, C. Tang, F. Gao, L. Dong, J. Rare Earths 32 (2014) 139–145.

[134] C.R. Jung, A. Kundu, S.W. Nam, H.I. Lee, Appl. Catal. A Gen. 331 (2007) 112–120.

[135] X. Guo, R. Zhou, Catal. Sci. Technol. 6 (2016) 3862–3871.

[136] L. Zhang, X. Yao, Y. Lu, C. Sun, C. Tang, F. Gao, L. Dong, J. Colloid Interface Sci. 509 (2018) 334–345.

[137] Q. Yu, X. Yao, H. Zhang, F. Gao, L. Dong, Appl. Catal. A Gen. 423–424 (2012) 42–51.

[138] J. Li, G. Luo, Y. Chu, F. Wei, Chem. Eng. J. 184 (2012) 168–175.

[139] H. Li, S. Wu, C.Y. Wu, J. Wang, L. Li, K. Shih, Environ. Sci. Technol. 49 (2015) 7373–7379.

[140] P.I. Kirienko, S.N. Orlik, P. Nauky, Theor. Exp. Chem. 46 (2010) 38–43.

[141] R.Q. Long, R.T. Yang, J. Phys. Chem. B 103 (1999) 2232–2238.

[142] M.S. Fal Desai, R.D. Kerkar, A.V.Salker, Int. J. Environ. Sci. Technol. 16 (2018) 1541–1550.

[143] G.G. Jernigan, G.. Somorjai, J. Catal. 147 (1994) 567–577.

[144] S. Poulston, P.M. Parlett, P. Stone, Surf. Interface Anal. 24 (1996) 811–820.

[145] A. Patel, P. Shukla, T. Rufford, S. Wang, J. Chen, V. Rudolph, Z. Zhu, Appl. Catal. A Gen. 409–410 (2011) 55–65.

[146] C. Deng, B. Li, L. Dong, F. Zhang, M. Fan, G. Jin, J. Gao, L. Gao, F. Zhang, X. Zhou, Phys. Chem. Chem. Phys. 17 (2015) 16092–16109.

[147] X. Niu, T. Zhao, F. Yuan, Y. Zhu, Sci. Rep. 5 (2015) 1–8.

[148] M. Zhou, L. Cai, M. Bajdich, M. García-Melchor, H. Li, J. He, J. Wilcox, W. Wu, A. Vojvodic, X. Zheng, ACS Catal. 5 (2015) 4485–4491.

[149] A. Glisenti, M. Pacella, M. Guiotto, M.M. Natile, P. Canu, Appl. Catal. B Environ. 180 (2016) 94–105.

[150] J. Gao, C. Jia, L. Zhang, H. Wang, Y. Yang, S. Hung, Y. Hsu, B. Liu, J. Catal. 341 (2016) 82–90.

[151] A. Srinivasan, C. Depcik, Catal. Rev. 52 (2010) 462–493.

[152] I. Twagirashema, M. Engelmann-Pirez, M. Frere, L. Burylo, L. Gengembre, C. Dujardin, P. Granger, Catal. Today 119 (2007) 100–105.

[153] H. Inomata, M. Shimokawabe, M. Arai, Appl. Catal. A Gen. 332 (2007) 146–152.

[154] T. Vinodkumar, D. Naga Durgasri, B.M. Reddy, I. Alxneit, Catal. Letters 144 (2014) 2033–2042.

[155] X. Shi, B. Chu, F. Wang, X. Wei, L. Teng, M. Fan, B. Li, L. Dong, L. Dong, ACS Appl. Mater. Interfaces 10 (2018) 40509–40522.

[156] Y. Jiang, C. Bao, Q. Liu, G. Liang, M. Lu, S. Ma, Catal. Commun. 103 (2018) 96–100.

[157] T. Liu, Y. Yao, L. Wei, Z. Shi, L. Han, H. Yuan, B. Li, L. Dong, F. Wang, C. Sun, J. Phys. Chem. C 121 (2017) 12757–12770.

[158] T. Zheng, J. He, Y. Zhao, W. Xia, J. He, J. Rare Earths 32 (2014) 97–107.

[159] Y. Zhou, Z. Wang, C. Liu, Catal. Sci. Technol. 5 (2015) 69–81.

[160] Y.J. Mergler, A. van Aalst, B.E. Nieuwenhuys, in: 1995, pp. 196–207.

[161] X.N. Li, Z.Y. Li, H.F. Li, S.G. He, Chem. - A Eur. J. 22 (2016) 9024–9029.

[162] O.A. Stonkus, T.Y. Kardash, E.M. Slavinskaya, V.I. Zaikovskii, A.I. Boronin, ChemCatChem 11 (2019) 3505–3521.

[163] R.M. Wolf, J. Siera, F.C.M.J.M. Van Delft, B.E. Nieuwenhuys, Faraday Discuss. Chem. Soc. 87 (1989) 275–289.

[164] J.V. Pande, A.B. Bindwal, Y.B. Pakade, R.B. Biniwale, Int. J. Hydrogen Energy 43 (2018) 7411–7423.

[165] X. Zheng, X. Zhang, X. Wang, S. Wang, S. Wu, Appl. Catal. A Gen. 295 (2005) 142–149.

[166] S. Zeng, W. Zhang, N. Liu, H. Su, Catal. Letters 143 (2013) 1018–1024.

[167] X. Yu, J. Wu, A. Zhang, L. Xue, Q. Wang, X. Tian, S. Shan, C.J. Zhong, S. Zeng, CrystEngComm 21 (2019) 3619–3626.

[168] G. Avgouropoulos, T. Ioannides, H.K. Matralis, J. Batista, S. Hocevar, Catal. Letters 73 (2001) 33–40.

[169] X. Xi, S. Ma, J.F. Chen, Y. Zhang, J. Environ. Chem. Eng. 2 (2014) 1011–1017.

[170] X. Zheng, X. Wang, X. Zhang, S. Wang, S. Wu, React. Kinet. Catal. Lett. 88 (2006) 57–63.

[171] S.C. Kim, W.G. Shim, Environ. Technol. 29 (2008) 535–542.

[172] C. Suryanarayana, Research 2019 (2019) 1–17.

[173] U. Kamolphop, S.F.R. Taylor, J.P. Breen, R. Burch, J.J. Delgado, S. Chansai, C. Hardacre, S. Hengrasmee, S.L. James, ACS Catal. 1 (2011) 1257–1262.

[174] F.C. Jentoft, H. Schmelz, H. Knözinger, Appl. Catal. A Gen. 161 (1997) 167–182.

[175] R.D. Kerkar, A. V. Salker, Catal. Letters (2020).

[176] A.A. Bunaciu, E. gabriela Udriştioiu, H.Y. Aboul-Enein, Crit. Rev. Anal. Chem. 45 (2015) 289–299.

[177] T. Hatakeyama, H. Hatakeyama, Hot Topics in Thermal Analysis and Calorimetry, 2005.

[178] Y.L. Bai, H. Bin Xu, Y. Zhang, Z.H. Li, J. Phys. Chem. Solids 67 (2006) 2589–2595.

[179] P. Li, Z. Zhou, H. Xu, Y. Zhang, Thermochim. Acta 544 (2012) 71–76.

[180] J.A. Cecilia, A. Arango-Díaz, V. Rico-Pérez, A. Bueno-López, E. Rodríguez-Castellón, Catal. Today 253 (2015) 115–125.

[181] M.A. Małecka, U. Burkhardt, D. Kaczorowski, M.P. Schmidt, D. Goran, L. Kępiński, J. Nanoparticle Res. 11 (2009) 2113–2124.

[182] S. Gnanam, V. Rajendran, J. Alloys Compd. 550 (2013) 463–470.

[183] F. Nawaz, Y. Xie, J. Xiao, H. Cao, Z.A. Ghazi, Z. Guo, Y. Chen, Catal. Sci. Technol. 6 (2016) 7875–7884.

[184] D. Gingasu, I. Mindru, D.C. Culita, L. Patron, J.M. Calderon-Moreno, P. Osiceanu, S. Preda, O. Oprea, V. Parvulescu, V. Teodorescu, J.P.S. Walsh, Mater. Res. Bull. 62 (2015) 52–64.

[185] P. Venkataswamy, D. Damma, D. Jampaiah, D. Mukherjee, M. Vithal, B.M. Reddy, Catal. Letters 150 (2020) 948–962.

[186] D. Zhang, Y. Qian, L. Shi, H. Mai, R. Gao, J. Zhang, W. Yu, W. Cao, Catal. Commun. 26 (2012) 164–168.

[187] K. Nagase, Y. Zheng, Y. Kodama, J. Kakuta, J. Catal. 187 (1999) 123–130.

[188] S. Palussiere, J. Cure, A. Nicollet, P. Fau, K. Fajerwerg, M.L. Kahn, A. Esteve, C. Rossi, Phys. Chem. Chem. Phys. 21 (2019) 16180–16189.

[189] S. Sakr, H. Elshafie, I. Camele, S. Sadeek, Molecules 23 (2018) 1182.

[190] R.D. Kerkar, M.S. Fal Desai, A. V. Salker, Surf. Interface Anal. 50 (2018) 1343–1348.

[191] S. Khamlich, V. V Srinivasu, A. Konkin, N. Cingo, F.T. Thema, A. Benyoussef, M. Maaza, J. Nanomater. 2015 (2015) 1–8.

[192] I. Banerjee, H.K.D. Kim, D. Pisani, K.P. Mohanchandra, G.P. Carman, J. Alloys Compd. 614 (2014) 305–309.

[193] D. Andreescu, E. Matijević, D. V. Goia, Colloids Surfaces A Physicochem. Eng. Asp. 291 (2006) 93–100.

[194] J. Calvache-Muñoz, F.A. Prado, J.E. Rodríguez-Páez, Colloids Surfaces A Physicochem. Eng. Asp. 529 (2017) 146–159.

[195] M. Hassel, I. Hemmerich, H. Kuhlenbeck, H. Freund, Surf. Sci. Spectra 4 (1998) 246.

[196] V. Balouria, A. Kumar, A. Singh, S. Samanta, A.K. Debnath, A. Mahajan, R.K. Bedi, D.K. Aswal, S.K. Gupta, J. V Yakhmi, Sensors Actuators, B Chem. 157 (2011) 466.

[197] B. Bao, J. Liu, H. Xu, B. Liu, K. Zhang, Z. Jin, RSC Adv. 7 (2017) 8589–8597.

[198] J.P. Espinós, J. Morales, A. Barranco, A. Caballero, J.P. Holgado, A.R. González-Elipe, J. Phys. Chem. B 106 (2002) 6921–6929.

[199] M.C. Biesinger, L.W.M. Lau, A.R. Gerson, R.S.C. Smart, Appl. Surf. Sci. 257 (2010) 887–898.

[200] X. Zhang, J. Qin, Y. Xue, P. Yu, B. Zhang, L. Wang, R. Liu, Sci. Rep. 4 (2014) 4–11.

[201] L. Guo, Y. Tian, J. Li, D. Zhao, X. Yu, T. Ding, Z. Jiang, X. Li, Catal. Today (2019).

[202] Y. Zhou, S. Xu, Y. Zhang, X. Hu, F. Li, X. Chen, H. Cai, J. Wang, L. Shi, X. Chen, Chem. Eng. J. 382 (2020).

[203] D. Gu, H. Zheng, Y. Ma, S. Xu, X. Zhou, J. Alloys Compd. 790 (2019) 602–609.

[204] M.C. Biesinger, B.P. Payne, A.P. Grosvenor, L.W.M. Lau, A.R. Gerson, R. St, C. Smart, Appl. Surf. Sci. 257 (2011) 2717–2730.

[205] X. Zhang, H. Li, F. Hou, Y. Yang, H. Dong, N. Liu, Y. Wang, L. Cui, Appl. Surf. Sci. 411 (2017) 27–33.

[206] X. Zhou, L. Zheng, R. Li, B. Li, S. Pillai, P. Xu, Y. Zhang, J. Mater. Chem. 22 (2012) 8862–8867.

[207] S. Yasmin, S. Cho, S. Jeon, Appl. Surf. Sci. 434 (2018) 905–912.

[208] L. Zhang, L. Shi, L. Huang, J. Zhang, R. Gao, D. Zhang, ACS Catal. 4 (2014) 1753–1763.

[209] Q. Wang, W. Wang, L. Zhang, Y. Su, K. Wang, H. Wu, J. Mater. Sci. Technol. 34 (2018) 2337–2341.

[210] B.A. Zaccheo, R.M. Crooks, Langmuir 27 (2011) 11591–11596.

[211] G.B. Hoflund, Z.F. Hazos, G.N. Salaita, Phys. Rev. B - Condens. Matter Mater. Phys. 62 (2000) 11126–11133.

[212] W.C. Liu, G. Melaet, W.T. Ralston, S. Alayoglu, Y. Horowitz, R. Ye, T. Hurlburt, B. Mao, E. Crumlin, M. Salmeron, G.A. Somorjai, Catal. Letters 146 (2016) 1574–1580.

[213] Y.V. Larichev, O.V. Netskina, O.V. Komova, V.I. Simagina, Int. J. Hydrogen Energy 35 (2010) 6501–6507.

[214] L.W.M. Lau, A.R. Gerson, B.P. Payne, R.S.C. Smart, M.C. Biesinger, A.P. Grosvenor, Appl. Surf. Sci. 257 (2010) 2717–2730.

[215] P. Mohanty, C.J. Sheppard, A.R.E. Prinsloo, W.D. Roos, L. Olivi, G. Aquilanti, J. Magn. Magn. Mater. 451 (2018) 20–28.

[216] N. Weidler, S. Paulus, J. Schuch, J. Klett, S. Hoch, P. Stenner, A. Maljusch, J. Brötz, C. Wittich, B. Kaiser, W. Jaegermann, Phys. Chem. Chem. Phys. 18 (2016) 10708–10718.

[217] L. Zhong, W. Cai, Y. Yu, Q. Zhong, Appl. Surf. Sci. 325 (2015) 52–63.

[218] X. Shao, J. Xu, Y. Huang, X. Su, H. Duan, X. Wang, T. Zhang, AIChE J. 62 (2016) 2410–2418.

[219] Z. Liu, Y. Li, T. Zhu, H. Su, J. Zhu, Ind. Eng. Chem. Res. 53 (2014) 12964–12970.

[220] W. Luo, L. Sun, Y. Yang, Y. Chen, Z. Zhou, J. Liu, F. Wang, Catal. Sci. Technol. 8 (2018) 6468–6477.

[221] G. Avgouropoulos, T. Ioannides, Appl. Catal. A Gen. 244 (2003) 155–167.

[222] R.D. Kerkar, A. V. Salker, Appl. Nanosci. 10 (2020) 141–149.

[223] F.E. López-Suárez, A. Bueno-López, M.J. Illán-Gómez, A. Adamski, B. Ura, J. Trawczynski, Environ. Sci. Technol. 42 (2008) 7670–7675.

[224] L. Mao, X. Zhao, Y. Xiao, G. Dong, New J. Chem. 43 (2019) 4196–4204.

[225] Y. Yang, H. Dong, Y. Wang, Y. Wang, N. Liu, D. Wang, X. Zhang, Inorg. Chem. Commun. 86 (2017) 74–77.

[226] M. Zhou, Z. Wang, Q. Sun, J. Wang, C. Zhang, D. Chen, X. Li, ACS Appl. Mater. Interfaces 11 (2019) 46875–46885.

[227] T. Cwele, N. Mahadevaiah, S. Singh, H.B. Friedrich, A.K. Yadav, S.N. Jha, D.

Bhattacharyya, N.K. Sahoo, Catal. Sci. Technol. 6 (2016) 8104–8116.

[228] Y. Wang, Y. Yang, N. Liu, Y. Wang, X. Zhang, RSC Adv. 8 (2018) 33096–33102.

[229] J. Ma, G. Jin, J. Gao, Y. Li, L. Dong, M. Huang, Q. Huang, B. Li, J. Mater. Chem. A 3 (2015) 24358–24370.

[230] X. Zhang, Y. Yang, L. Song, Y. Wang, C. He, Z. Wang, L. Cui, Mol. Catal. 447 (2018) 80–89.

[231] R.K. Kunkalekar, A. V. Salker, React. Kinet. Mech. Catal. 108 (2013) 173–182.

[232] X. Huang, Z. Ma, W. Lin, F. Liu, H. Yang, Catal. Commun. 91 (2017) 53–56.

[233] G. Córdoba, M. Viniegra, J.L.G. Fierro, J. Padilla, R. Arroyo, J. Solid State Chem. 138 (1998) 1–6.

[234] A.C.F.M. Costa, V.J. Silva, C.C. Xin, D.A. Vieira, D.R. Cornejo, R.H.G.A. Kiminami, J. Alloys Compd. 495 (2010) 503–505.

[235] K.S.W. Sing, Pure Appl. Chem. 57 (1985) 603–619.

[236] P. Venkataswamy, D. Jampaiah, D. Mukherjee, C.U. Aniz, B.M. Reddy, Catal. Letters 146 (2016) 2105–2118.

[237] M. Thommes, K. Kaneko, A. V. Neimark, J.P. Olivier, F. Rodriguez-Reinoso, J. Rouquerol, K.S.W. Sing, Pure Appl. Chem. 87 (2015) 1051–1069.

[238] I.R. and K.S. Francoise Rouquerol, Adsorption by Powder and Porous Solids, 1999.

[239] Y. Hilli, N.M. Kinnunen, M. Suvanto, A. Savimäki, K. Kallinen, T.A. Pakkanen, Appl. Catal. A Gen. 497 (2015) 85–95.

[240] X. Zhang, G. Li, S. Yang, X. Song, Z. Sun, Microporous Mesoporous Mater. 226 (2016) 61–70.

[241] J.Y. Luo, M. Meng, X. Li, X.G. Li, Y.Q. Zha, T.D. Hu, Y.N. Xie, J. Zhang, J. Catal. 254 (2008) 310–324.

[242] Z. Wang, Q. Sun, D. Wang, Z. Hong, Z. Qu, X. Li, Sep. Purif. Technol. 209 (2019) 1016–1026.

[243] M. Kocoń, P. Michorczyk, J. Ogonowski, Catal. Letters 101 (2005) 53–57.

[244] A. Laobuthee, C. Veranitisagul, N. Koonsaeng, V. Bhavakul, N. Laosiripojana, Catal. Commun. 12 (2010) 25–29.

[245] Y. Zheng, K. Li, H. Wang, X. Zhu, Y. Wei, M. Zheng, Y. Wang, Energy and Fuels 30 (2016) 638–647.

[246] J.M. López, A.L. Gilbank, T. García, B. Solsona, S. Agouram, L. Torrente-Murciano, Appl. Catal. B Environ. 174 (2015) 403–412.

[247] F. Sabaté, J.L. Jordá, M.J. Sabater, A. Corma, J. Mater. Chem. A 8 (2020) 3771–3784.

[248] T. Miki, T. Ogawa, M. Haneda, N. Kakuta, A. Ueno, S. Tateishi, S. Matsuura, M. Sato, J. Phys. Chem. 94 (1990) 6464–6467.

[249] S. Meiqing, M. Yang, J. Wang, J. Wen, M. Zhao, W. Wang, J. Phys. Chem. C 113 (2009) 3212–3221.

[250] K.J. Leary, J.N. Michaels, A.M. Stacy, J. Catal. 107 (1987) 393–406.

[251] Y. Zhang, Y. Zhao, H. Zhang, L. Zhang, H. Ma, P. Dong, D. Li, J. Yu, G. Cao, RSC Adv. 6 (2016) 70653–70659.

[252] S.A. Mock, E.T. Zell, S.T. Hossain, R. Wang, ChemCatChem 10 (2018) 311–319.

[253] C.G. MacIel, T.D.F. Silva, M.I. Hirooka, M.N. Belgacem, J.M. Assaf, Fuel 97 (2012) 245–252.

[254] P. Walker, W.H. Tarn, CRC Handbook of Metal Etchants, 1990.

[255] S. Hinokuma, H. Shimanoe, Y. Kawabata, S. Kiritoshi, K. Araki, M. Machida, Catal. Commun. 105 (2018) 48–51.

[256] W. Yang, R. Zhang, B. Chen, N. Bion, D. Duprez, S. Royer, J. Catal. 295 (2012)45–58.

[257] F. Meng, P. Zhong, Z. Li, X. Cui, H. Zheng, J. Chem. 2014 (2014) 1–7.

[258] L. Li, L. Zhang, K. Ma, W. Zou, Y. Cao, Y. Xiong, C. Tang, L. Dong, Appl. Catal. B Environ. 207 (2017) 366–375.

[259] Y. Shao, K. Sun, Q. Li, Q. Liu, S. Zhang, Q. Liu, G. Hu, X. Hu, Green Chem. 21 (2019) 4499–4511.

[260] T.A. Le, M.S. Kim, S.H. Lee, T.W. Kim, E.D. Park, Catal. Today 293–294 (2017) 89–96.

[261] X. Wang, J.S. Tian, Y.H. Zheng, X.L. Xu, W.M. Liu, X.Z. Fang, ChemCatChem 6 (2014) 1604–1611.

[262] R. Jain, E.S. Gnanakumar, C.S. Gopinath, ACS Omega 2 (2017) 828–834.

[263] S. Zhang, X.S. Li, B. Chen, X. Zhu, C. Shi, A.M. Zhu, ACS Catal. 4 (2014) 3481–3489.

[264] R.P. Gura, V.M. Vlasenko, V.A. Kuznetsov, V.V Raksha, Theor. Exp. Chem. 21 (1985) 338–343.

[265] X. Yao, C. Tang, Z. Ji, Y. Dai, Y. Cao, F. Gao, L. Dong, Y. Chen, Catal. Sci. Technol. 3 (2013) 688–698.

[266] A.A. Vedyagin, V.O. Stoyanovskii, P.E. Plyusnin, Y. V. Shubin, E.M. Slavinskaya, I. V. Mishakov, J. Alloys Compd. 749 (2018) 155–162.

Appendix I

Paper Published

1. **R.D. Kerkar**, M.S. Fal Desai and A.V. Salker,
   "Complete detoxification reaction by NO reduction with CO over nano-sized copper-substituted Cr_2O_3".
   Surf. Interface Analysis. 50 (2018) 1343–1348. doi:10.1002/sia.6528.

2. M.S. Fal Desai, **R.D. Kerkar** and A.V. Salker,
   "Detoxification of NO and CO gases over effectively substituted Pd and Rh in cupric oxide catalysts".
   Intl. J. Environ. Sci. Technol. 16 (2018) 1541–1550. doi:10.1007/s13762-018-1744-5

3. **R.D. Kerkar** and A.V. Salker
   "Nitric oxide reduction by carbon monoxide and carbon monoxide oxidation by O_2 over Co–Mn composite oxide material".
   Appl. Nanosci. 10 (2020) 141–149. doi:10.1007/s13204-019-01109-y.

4. **R.D. Kerkar** and A.V. Salker
   "A route to develop the synergy between CeO_2 and CuO for low temperature CO oxidation".
   Catal. Letters. 150 (2020) 2774-2783. doi:10.1007/s10562-020-03166-3.

5. **R.D. Kerkar** and A.V. Salker
   "Synergistic effect of modified Pd-based cobalt chromite and manganese oxide system towards NO-CO redox detoxification reaction".
   Environ. Sci. Pollut. Res.27 (2020) 27061-27071. doi:10.1007/s11356-020-09146-9

6. **R.D. Kerkar** and A.V. Salker
   "Significant effect of multi-doped cerium oxide for Carbon Monoxide oxidation Studies".
   Mater. Chem. Phys. 253 (2020) 123326. doi:10.1016/j.matchemphys.2020.123326

7. **R.D. Kerkar** and A.V. Salker

   "Promising effect of Ag/Rh paired mesoporous composite oxide for low temperature NO-CO reaction".

   Catal. Commun. 149 (2021) 106257 doi.10.1016/j.catcom.2020.106257

8. **R.D. Kerkar** and A.V. Salker

   "Superior advancement in NO/CO redox reaction over Cu-Mn composite oxide: the effect of Al^{+3} fabrication".

   (Communicated)

9. **R.D. Kerkar** and A.V. Salker

   "NO-CO redox reaction over Ru modified CeO_2: A low-temperature conversion with a mechanistic approach".

   (Communicated)

Appendix II

Conferences participated

1. Presented a poster entitled '**Catalytic oxidation of carbon monoxide over transition metal oxides**' at **2nd National Conference on New Frontiers in Chemistry- From Fundamentals to Applications- II (NFCFA 2017)** held at Department of Chemistry, BITS Pilani K.K. Birla Goa Campus on 28th-29th January 2017

2. Presented a poster entitled '**Thermal and catalytic study on pristine and substituted chromium oxide catalyst'** at DAE-BRNS sponsored **21st Workshop & Symposium on thermal analysis (THERMANS-2018)** organized by Department of Chemistry, Goa University, Goa and Indian Thermal Analysis Society Mumbai, held at Department of Chemistry, Goa University during January 16-20, 2018.

3. Presented a poster titled "**Catalytic detoxification of NO and CO over Indium oxide composite**" at **23rd National Symposium on Catalysis (CATSYMP-23)**, January 17 – 19, 2018, Catalysis Society of India – Bengaluru Chapter, Bengaluru.

4. Presented a poster entitled **'Synergic effect of Cerium oxide in catalytic oxidation of carbon monoxide'** at **National school on Computer-Assisted Spectroscopic Data Interpretation Techniques** organized by Department of Physics, Rashtrasant Tukadoji Maharaj Nagpur University, Nagpur, Jointly with Physics Promotion and Charitable Trust and Materials Research Society of India, Nagpur chapter from Jan 7-11,2019.

Workshop attended

1. Attended National workshop on "**Theory and practice of X-ray diffraction techniques (TPXRDT) 2017**" organized by Alagappa Chettiar Collage of Engineering and Technology, Karaikudi during 25th to 27th May 2017.

2. Attended a two week MHRD sponsored GIAN Course on "**Phase Transitions and their Technological Applications**" organized by Department of Physics, Goa University Taleigao Goa during 05^{th} to 19^{th} march 2018.

3. Attended course on "**Documentation Using LaTeX**" organized by Extra mural studies and Extension service, Goa university from 24 February to 24 March, 2018.